UNIVERSITÉ LAVAL

Non-destructive quality control of carbon anodes using modal analysis, acousto-ultrasonic and latent variable methods

Thèse

Moez Ben Boubaker

Doctorat en génie chimique
Philosophiæ doctor (Ph. D.)

Québec, Canada

Résumé

La performance des cuves d'électrolyse utilisées dans la production d'aluminium primaire par le procédé Hall-Héroult est fortement influencée par la qualité des anodes de carbone. Celles-ci sont de plus en plus variables en raison de la qualité décroissante des matières premières (coke et braie) et des changements de fournisseurs qui deviennent de plus en plus fréquents afin de réduire le coût d'achat et de rencontrer les spécifications des usines. En effet, les défauts des anodes, tels les fissures, les pores et les hétérogénéités, causés par cette variabilité, doivent être détectés le plus tôt possible afin d'éviter d'utiliser des anodes défectueuses dans les cuves et/ou d'apporter des ajustements au niveau du procédé de fabrication des anodes. Cependant, les fabricants d'anodes ne sont pas préparés pour réagir à cette situation afin de maintenir une qualité d'anode stable. Par conséquent, il devient prioritaire de développer des techniques permettant d'inspecter le volume complet de chaque anode individuelle afin d'améliorer le contrôle de la qualité des anodes et de compenser la variabilité provenant des matières premières.

Un système d'inspection basé sur les techniques d'analyse modale et d'acousto-ultrasonique est proposé pour contrôler la qualité des anodes de manière rapide et non destructive. Les données massives (modes de vibration et signaux acoustiques) ont été analysées à l'aide de méthodes statistiques à variables latentes, telles que l'Analyse en Composantes Principales (ACP) et la Projection sur les Structures Latentes (PSL), afin de regrouper les anodes testées en fonction de leurs signatures vibratoires et acousto-ultrasoniques. Le système d'inspection a été premièrement investigué sur des tranches d'anodes industrielles et ensuite testé sur plusieurs anodes pleine grandeur produites sous différentes conditions à l'usine de Alcoa Deschambault au Québec (ADQ). La méthode proposée a permis de distinguer les anodes saines de celles contenant des défauts ainsi que d'identifier le type et la sévérité des défauts, et de les localiser.

La méthode acousto-ultrasonique a été validée qualitativement par la tomographie à rayon-X, pour les analyses des tranches d'anodes. Pour les tests réalisés sur les blocs d'anode, la validation a été réalisée au moyen de photos recueillies après avoir coupé certaines anodes parmi celles testées.

Abstract

The performance of the Hall-Héroult electrolysis reduction process used for the industrial aluminium smelting is strongly influenced by the quality of carbon anodes, particularly by the presence of defects in their internal structure, such as cracks, pores and heterogeneities. This is partly due to the decreasing quality and increasing variability of the raw materials available on the market as well as the frequent suppliers changes made in order to meet the smelter's specifications and to reduce purchasing costs. However, the anode producers are not prepared to cope with these variations and in order to maintain consistent anode quality. Consequently, it becomes a priority to develop alternative methods for inspecting each anode block to improve quality control and maintain consistent anode quality in spite of the variability of incoming raw materials.

A rapid and non-destructive inspection system for anode quality control is proposed based on modal analysis and acousto-ultrasonic techniques. The large set of vibration and acousto-ultrasonic data collected from baked anode materials was analyzed using multivariate latent variable methods, such as Principal Component Analysis (PCA) and Partial Least Squares (PLS), in order to cluster the tested anodes based on vibration and their acousto-ultrasonic signatures. The inspection system was investigated first using slices collected from industrial anodes and then on several full size anodes produced under different conditions at the Alcoa Deschambault in Québec (ADQ). It is shown that the proposed method allows discriminating defect-free anodes from those containing various types of defects. In addition, the acousto-ultrasonic features obtained in different frequency ranges were found to be sensitive to the defects severities and were able to locate them in anode blocks.

The acousto-ultrasonic method was validated qualitatively using X-ray computed tomography, when studying the anode slices. The results obtained on the full size anode blocks were validated by means of images collected after cutting some tested anodes.

Table of contents

List of tables

List of figures

Nomenclature

ADQ	Alcoa Deschambault Quebec
AE	Acoustic emission
Al	Aluminium
AU	Acousto-ultrasonic
CAD	Computed-aided design
CCD	Charge-coupled device
Coif	Coiflet
CT	Computed tomography
CT-Scan	Computed tomography scan
CV	Cross-validation
CWT	Continuous wavelet transform
Db	Daubechies
DEM	Discrete element method
DFT	Discrete Fourier transform
DWT	Discrete wavelet transform
E	Energy
FEM	Finite element method
fn	Natural frequency
FRF	Frequency response function
FFT	Fast Fourier transform
FT	Fourier transform
GLCM	Gray-level co-occurrence matrix
IR	Infrared
IRT	Infrared thermography
K	Kurtosis
LV	Latent variable
MA	Modal analysis
MAX	Maximum
MLR	Multiple linear regression
MIA	Multivariate image analysis
MIREA	*Mesure Instantanée de la Résistivité Électrique Anodique*
MSC	Mauricie Sowing Center
NDT	Non-destructive testing
NDE	Non-destructive evaluation
PAC	Physical acoustic corporation
PCA	Principal component analysis
PLS	Projection to latent structures/partial least squares
RMS	Root mean squares
RTA	Rio Tinto Alcan
RGB	Red Green Blue
S	Skewness
SMB-PLS	Sequential multi-block-PLS
STD	Standard deviation
Sym	Symlet
UT	Ultrasonic testing
VBD	Vibrated bulk density
Voxel	Volumetric pixel
WPT	Wavelet packet transform

WTA	Wavelet texture analysis

Acknowledgements

بسم الله والحمد لله والصلاة والسلام على رسله ومن تبعهم بإحسان إلا يوم الدين

Here comes the moment of thanks. A daunting but essential task to express my deep respect and gratitude to the people who contributed to the completion of this PhD. I hope not to forget anyone.

This work was carried out within the Departments of Chemical, Mechanical and Civil Engineering at Laval University, and more precisely within laboratories: REGAL, structures and concrete (saw room). It was funded by Alcoa, Fonds de recherche du Québec–Nature et technologies (FRQNT), Aluminium Research Centre – REGAL, NSERC and Laval University.

I would like first to thank my supervisor, Professor Carl Duchesne for his availability, confidence, support, guidance and opportunities that strongly participate in the success of this project. Professor Houshang Alamdari of the department of mining, metallurgical and materials engineering, co-supervisor of this thesis, for his precious ideas, comments, suggestions and guidance all along my project. Prof. Mario Fafard of the department of civil and water engineering for his technical support. Dr. Jayson Tessier, my industry co-supervisor, for his professionalism, participation through all the industrial tasks as well as through the different coordination with Alcoa. Dr. Donald Picard and Dr. Hicham Chaouki, for their enthusiasm, dedications and respective knowledge of experimentation and modeling that have been profitable for the experimental set-up development as well as for the planning and execution of the experiments. Be assured of my great esteem and friendship.

My sincere thanks also go to the technicians and engineers who helped me during this PhD. Special thanks to Guillaume Gauvin, the man of “difficult missions”, who is always striving to overcome the industrial/academic coordination challenges, and who stayed with me during the majority of the laborious experimental tasks. I especially appreciate the availability, collaboration and technical assistance in the laboratory of my dear Sirs: Hugues Ferland, Pierre-André Tremblay, Mathieu Thomassin-Maillot, and Martin Lapointe. Finally, I would also like to thank the students and trainees, with whom I shared the laboratories, for their patience and tolerance vis-à-vis the cluttering of the place and the uncomfortable conditions caused by our big block of carbon. My thanks also go to my colleagues in the

office Kamran, Julien, Pierre-Marc, Massoud, Amélie, Wilinthon, Corinne, Alexandre, Jean-Pascal, Thierry, Mathias, Juliette, Karl, Simon, Shahab, Véronique and Adéline. All the moments shared and enjoyed together were profoundly appreciated.

I would like to thank all my fellow students at the Engineering schools and training centers, especially those we spent a lot of time together as volunteers in the associative framework. I will keep a wonderful memory of the fruitful scientific and human exchanges and the exciting discussions I had during breaks with all of you my friends.

In conclusion, I express my profound gratitude to my family for their unconditional encouragement and support. Especially my mom, dad, sisters and my wife, I could not have completed a Ph.D., raise our beautiful daughter “Sarah”, succeed several social and other projects and still have a normal life without you. To all my friends, with whom, I had the opportunities to live the best moments of my life and I would like to have new opportunities with.

Great THANKS everybody.

Foreword

This thesis consists of seven chapters and four appendices. In the first chapter, the recent progresses in anode quality control as well as non-destructive methods applied to the inspection of anode materials are described. In addition, the possible defects that may occur in the anodes and the different techniques that may be used to detect those are discussed and compared in order to select the best candidates. The second chapter focuses on the methods used in this thesis. The principles of modal analysis and acousto-ultrasonic are presented first, followed by the signal and image analysis methods, the numerical modal analysis, and a background on the multivariate latent variable methods. Chapters 3 to 6 consist of the four articles published or to be published in international scientific journals. The last chapter contains general conclusions, a discussion of industrial benefits, and recommendations for future work. The following subsections explain the contributions of each article in the field as well as the contribution of the candidate to each article.

Chapter 3:

The sensitivity of the acousto-ultrasonic signals to the various defects present in carbon anode materials is investigated in this chapter. This mainly concerns the detection and identification of internal defects like pores and cracks using the attenuation of the mechanical waves propagating through the material. The investigation was conducted on slices cut from a full-size baked anode. Each slice was virtually subdivided into 6 vertical corridors. The set of so-called corridors were excited by an acoustic (mechanical) wave at a given frequency and its response (attenuated wave) was recorded. This process was repeated sequentially using 7 different excitation frequencies. A method was proposed to process the acousto-ultrasonic response signals obtained from various anode slices in order to extract a large set of potentially relevant acoustic features representing the material's attenuation behavior. The approach used in this research was to compute as many features as possible to capture all aspects of the material response. Since the large number of features were highly collinear, multivariate statistical methods were used for analyzing them. Pruning of the set of features in order to simplify the analysis was not considered in this thesis, but should be examined in future work to simplify the practical application of the method. The presence of defects inside different parts and their identification was therefore

revealed by applying Principal Component Analysis (PCA) to the matrix of acoustic features, and by analyzing the clustering patterns of 6 different subsections (called corridors) within each anode slice. The acoustic features were found to be sensitive to the presence of cracks and pores within the materials and were able to discriminate between them. These results were validated qualitatively using images of X-ray computed tomography that revealed the internal morphology of each anode slice included in this work.

This work published in:

- M. Ben Boubaker, D. Picard, J. Tessier, H. Alamdari, M. Fafard, C. Duchesne, The Potential of Acousto-Ultrasonic Techniques for Inspection of Baked Carbon Anodes, Metals, Vol. 6 (7), 151, 2016, 1-13.

Some of the results were also presented in:

- M. Ben Boubaker, D. Picard, J. Tessier, H. Alamdari, M. Fafard, C. Duchesne, Inspection of baked carbon anodes using acoustic techniques, Proceedings of 33rd International ICSOBA Conference, Dubai, UAE, 2015, 467–476.

It is necessary to mention that the slices preparation including anode slicing and X-ray imaging was led by Dr. Donald Picard (Research assistant) to meet the objectives of another research project. The remaining slices were used in this PhD project. I carried out the ordering of missing equipment, cutting of additional slices, experimental set-up preparation, acousto-ultrasonic testing, signal analysis and features extraction by writing the necessary MATLAB codes. I also performed X-ray images preprocessing, and applied multivariate latent variable methods for data analysis. Finally, I wrote the first draft of the manuscript and corrected it under the guidance of my supervisors.

Chapter 4:

This chapter presents an improved acousto-ultrasonic method for testing the materials and analyzing their response in a more efficient way. Instead of exciting the materials sequentially at different frequencies, a single multi-spectral excitation signal was investigated as a mean of reducing the time required for inspecting each anode. The frequency modulated excitation signal spanned the same frequency range as that used in

the work reported in Chapter 3. Since the new excitation signal results in a more complex attenuation response (also containing several frequencies), the method for processing and analyzing the attenuation signals also required some modifications. Instead of computing acoustic features directly from the attenuated signal (as in Chapter 3), the latter was first decomposed into 4 different frequency bands using the 1D Discrete Wavelet Transform (DWT), followed by calculation of the acoustic features from each wavelet sub-signal (i.e., filtered signal in each frequency band). This new approach was applied on the same anode slices and corridors as described in Chapter 3. In addition to this, it was desired to build relationships between the CT-scan images of each anode slice and their acoustic attenuation features in order to provide a thorough quantitative analysis of the data (as opposed to the qualitative validation proposed in Chapter 3). To link material attenuation features and images, a vector of features was calculated from the latter in order to formulate a regression problem with two data matrices; **X** containing the acoustic features and **Y** the image data. The CT-scan image features were extracted by applying the 2-D Discrete Wavelet Transform to decompose the image signals in 4 frequency bands along three spatial directions within the images. The energy of the signal in each wavelet sub-image was used to form a row-vector of features of each image. These were found to extract information about the material structure (pores and cracks). After applying PLS regression using both data matrices, it was found that the multi-frequency excitation strategy led to very similar results as the sequential excitation but was much faster. Again, the corridors in each slice were discriminated based on the contained pores or cracks, and how severe these defects were.

This work was presented in:

- M. B. Boubaker., D. Picard, J. Tessier, H. Alamdari, M. Fafard, C. Duchesne, Inspection of Prebaked Carbon Anodes using Multi-Spectral Acousto-Ultrasonic signals, Wavelet Analysis and Multivariate Statistical Methods, Proceedings of 34rd International ICSOBA Conference, October 3-6, Québec City, Canada, 2016.

And will be submitted in the following journal:

- M. Ben Boubaker, D. Picard, J. Tessier, H. Alamdari, M. Fafard, C. Duchesne, Inspection of Prebaked Carbon Anodes using Multi-Spectral Acousto-Ultrasonic signals, Wavelet Analysis and Multivariate Statistical Methods, “to be submitted to Metals”.

Through communication with the manufacturer, I have adapted the acoustic system for a comparative multi-spectral analysis. This was achieved by adding some external components such as resistors and electrical connections. I have performed all the multi spectral acousto-ultrasonic tests and data analysis including the writing of the new MATLAB codes for signals and image analysis, as well as for modeling. I wrote the first draft of the manuscript and revised it under the guidance of my supervisors.

Chapter 5:

The acousto-ultrasonic inspection technique developed in Chapter 4 was then applied to full-size industrial anode blocks, the material ultimately targeted for the industrial application. A total of 27 anodes were sampled from the production line at the Alcoa Deschambault Quebec (ADQ) smelter, including some anodes containing known defects visible from their surface, and a larger set of anodes which had no visual defects but manufactured under different operating conditions (i.e., normal operation, start-up of the paste plant, and anodes baked in different positions within the furnace). The multi-frequency excitation strategy was applied to each anode at 29 different positions (21 along the anode height and 8 in the direction of its long side), and the attenuation signals were recorded for each. These response signals were preprocessed according to the method proposed in Chapter 4. The attenuation features in each position in each anode were organized in two different matrices in order to analyze the variability within each anode as well as the variability between all of them. The first data matrix was formed by concatenating all the attenuation features in all positions for a given anode in a row vector. Thus, each row of that matrix corresponds to the attenuation signature of one anode and allows for a comparison between the different anodes (between anode variability). Applying Principal Component Analysis (PCA) to that data matrix allowed clustering the anodes based on known defects or according to the process conditions under which they were produced. To analyze the within anode variability, each row of the second data matrix was filled with the attenuation features for a single position in a given anode, after which PCA was applied. Several case studies are presented, but all of them confirmed the sensitivity of acousto-ultrasonic signals to defects within the anode structure and changes in some manufacturing conditions. Qualitative validation of the results was performed by collecting images of internal surfaces of several anodes after cutting them along their long side.

This work was written in a manuscript format to be submitted to a scientific journal:

- M. Ben Boubaker, D. Picard, J. Tessier, H. Alamdari, M. Fafard, C. Duchesne, Quality inspection of carbon anodes with combination of acousto-ultrasonic technique and principal component analysis, (It will be submitted to a journal that will be determined soon).

One of the big challenges in this work was how to deal with the large industrial anodes including their selection from a large variety, testing them using acoustic methods and cutting them for result validation. The latter was conducted with the help of Mr Guillaume Gauvin (research assistant at REGAL centre) and collaboration with the ADQ smelter and the Mauricie Sowing Center (MSC). I performed all the experiments including anodes preparation, acousto-ultrasonic testing and numerical imaging after cutting some anodes followed by the data analysis. At this point, it is necessary to mention that part of tests were conducted at ADQ and the other part in the civil engineering labs. I wrote the first draft of the manuscript and revised it under the guidance of my supervisors.

Chapter 6:

In this chapter, an alternative approach to acousto-ultrasonic inspection of baked anode blocks, namely vibration modal analysis, was investigated. This technique was considered in this thesis because it could lead to a faster inspection compared to acousto-ultrasonic, and could be easier to implement in an industrial environment site. However, it cannot provide as much detailed information as the acoustic methods. A combination of both approaches may be considered in the future to improve inspection efficiency. Modal analysis would be applied to all manufactured anodes for the purpose of detecting defects. Acoustic inspection would be used to provide a detailed diagnosis of the defects (i.e., type, severity, location) only upon positive detection by modal analysis. Hence, modal analysis is studied in this chapter to determine its potential for defect detection. The same set of 27 anodes used in acoustic inspection (chapter 5) was also used for this part of the research work. These anodes were mechanically excited at several different positions on four faces of the block using a hammer, and the vibration signals of the blocks were measured by accelerometers also at different positions. Where to hit the block and to measure the vibrations was determined with the assistance of finite element modeling. The vibration signals were recorded by seven accelerometers after each excitation. A code was

developed to compute the first two vibration modes (natural frequencies) from each of the recorded signal. The frequency corresponding to these modes obtained for each excitation point and accelerometer were stored in a row vector. A modal feature matrix was formed by collecting the row vectors obtained for each anode. The data was then analyzed by PCA to cluster the anodes according to their vibration modes. It was shown that this approach could also discriminate the anodes based on known defects and/or the conditions under which they have been manufactured. Finally, the results were confirmed visually using some images collected after cutting some of the tested anodes (similarly as for the acoustic technique).

The results were presented and published in:

- M. Ben Boubaker, D. Picard, J. Tessier, H. Alamdari, M. Fafard, C. Duchesne, Non-destructive testing of baked anodes based on modal analysis and principle component analysis, TMS, Light Metals, 2017, 1289-1298.

I performed all experiments including sensor selection, ordering the missing equipment, set-up preparation, anodes fixing and vibration tests. In addition, I developed necessary MATLAB codes for natural mode identification and frequency selection. Finally I wrote the first draft of the paper under helpful ideas, comments, suggestions and modifications by my supervisors.

Appendices:

Appendices 1&2:

Due to word and page limitation imposed by ICSOBA proceedings and Metals journal, some parts of the work on the reliability of acousto-ultrasonic technique could not be included in the submitted manuscript presented in chapter 3 and 4. Hence, two appendices present additional results pertaining to the ‘similarity of the acousto-ultrasonic responses of the rods to those of their corresponding corridors’ and ‘the possibility to distinguish between corridors containing high density of pores and those containing different cracks’, respectively. These additional results are discussed in appendix 1 and appendix 2, respectively.

I performed all the experiments including sample preparation, acousto-ultrasonic tests, signal and image analysis, and reported the results under the guidance of my supervisors.

Appendix 3:

Since Chapter 5 was written in a manuscript format to be submitted to a scientific journal the attenuation maps of only three anodes (two anodes containing severe defects and a defect free anode) were presented for sake of conciseness. Therefore, the attenuation maps of all tested anodes are presented in Appendix 3.

I performed all the experiments, the corresponding analysis and the attenuation maps as well as reported the results under the guidance of my supervisors.

Appendix 4:

Due to the TMS paper-format restrictions the comparison between the numerical and the experimental modal responses of the anode, as well as details about the numerical model, such as the boundary conditions used, were omitted in chapter 6. These additional information are reported in Appendix 4.

I performed both of experimental and numerical modal analysis including the numerical simulation, preparation of experimental set-up and experimental measurements. Finally, I performed the corresponding statistical analysis and reported the results under the guidance of my supervisors.

Chapter 1 Introduction

Nowadays, global economic development is highly suffering by the increase of energy consumption in various sectors. In countries such as Canada, where the economy is mainly based on the exploitation of abundant natural resources, the energy consumption grows enormously. These large energy requirements are mostly concentrated in the industrial sector, especially those involved in metal refining, smelting and production of aluminium. To optimize these needs and their effects on global warming, the Canadian government is providing funding to meet the performance standards in order to help improve the energy efficiency of different sectors. According to the Office of Natural Resources Canada [1], these measures have helped the economy by saving more than 1 560 petajoules in 2010, which is equivalent to the energy consumption of all sectors throughout the province of Quebec during the same year. Figure 1-1 illustrates the efforts of Canadian primary aluminium producers in terms of both energy efficiency and production costs.

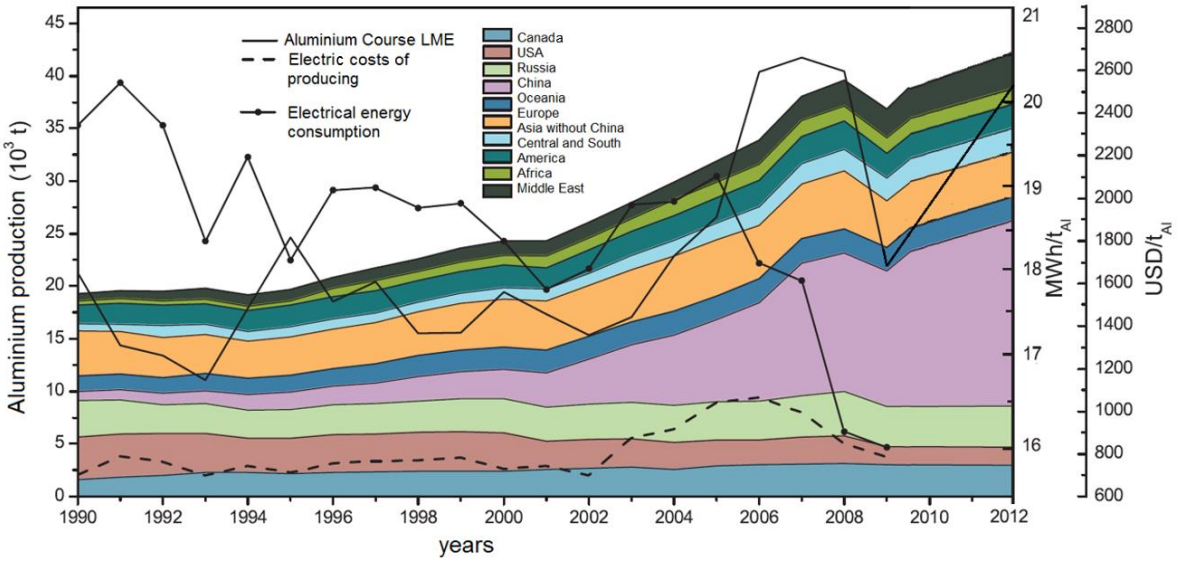

Figure 1-1 Representation of changes in the global primary aluminium production, energy consumption and electrical costs per ton of aluminium. The evolution of the LME aluminium price is also presented. Sources: Naturel Resources Canada [1], London Metal Exchange [2], USGS [3], I.E.A - Energy Prices and Taxes [4].

In the context of the strong increase in global primary aluminium production that reached 45Mt per year with a Canadian contribution around 7% [5-7], as illustrated in Figure 1-1, the industry must improve the performance and efficiency through the reduction

of the production cost and technological innovation. The significant increase in demand is explained by the intrinsic properties of aluminium that make it an interesting material to replace steel in a number of applications. This increment is offset by apparition of the new producers that simultaneously affect the economic and strategic issues. To maintain its competitiveness, primary aluminium producers rely today on a constant improvement of the manufacturing process control in their different smelters. Energy efficiency and carbon consumption during manufacturing processes are two important performance metrics that need to be optimized. However, these factors are hugely dependent on the carbon anode quality. Indeed, the worst-case scenario happens when the carbon anodes contain defects (i.e., heterogeneities, cracks, and pores). For such reason, carbon anode quality is becoming a well-known concern for aluminium producers. On the one hand, they have to deal with the decreasing quality and increasing variability of raw materials (petroleum coke and coal tar pitch) on the market. These raw materials are by-products of refineries, who have little incentive to better control their quality. On the other hand, the aluminium producers must mitigate the impact of changes in these raw material properties through appropriate adjustments to the anode manufacturing process parameters. Producing anodes with more consistent quality is therefore necessary.

1.1 Aluminium production

Aluminium is the third element and the first most abundant metal, constituting around 8% of the earth's crust [8]. It is produced via an electrochemical reaction, reducing alumina to metal aluminium. Alumina is mainly extracted from bauxite by the Bayer process [9]. Paul L.T. Héroult in France and Charles M. Hall in the United States of America both had independently discovered the electrochemical process for the manufacture of aluminium in the 19th century [10]. Until now, the dominant primary aluminium production technology is based on the Hall-Héroult process. A schematic of a modern aluminium-smelting cell is presented in Figure 1-2. The reactor (also called reduction cell or pot) is made of a steel shell internally covered with a lining of carbonaceous materials, acting as a thermal insulator and protecting the shell from the extremely harsh conditions prevailing in the cell. The electrical current enters the cell by a set of pre-baked carbon anodes (typically 40 anodes/cell). These are suspended in the cell by means of steel stubs, and float in a layer of cryolite (electrolyte also commonly called bath) containing dissolved alumina, continuously fed in the cell by point feeders. The overall alumina reduction, reaction taking place in the electrolyte layer, is represented in the following equation:

$$2Al_2O_3 + 3C + \text{electricity} \rightarrow 4Al + 3CO_2 \quad (1.1)$$

where alumina (Al_2O_3) is reduced to aluminium (Al) by applying an electrical current in the presence of a carbon source. Carbon dioxide (CO_2) is also released during the reaction. The aluminium produced by the reaction settles at the bottom of the cell and forms a metal pad. A cathode block made of a graphitic material is installed at the bottom of the cell. The electrical current exits the cell by the cathode after passing through the metal pad. Several hundreds of cells are electrically connected in series in a typical smelter, using a system of bus bars. The metallic aluminium is periodically tapped from the cells and sent to the cast house.

Although this technology is a century old, the energy efficiency of modern reduction cells is still relatively low, with roughly half of the electrical energy input that leaves, in some cases on purpose, the pots in the form of waste heat. Since the primary production of aluminium is a process that requires extensive amounts of electricity (~13-15 MWh per ton of Al produced), these energy losses are enormous considering the Al production capacity of 2.8 million tons per year in the province of Québec alone.

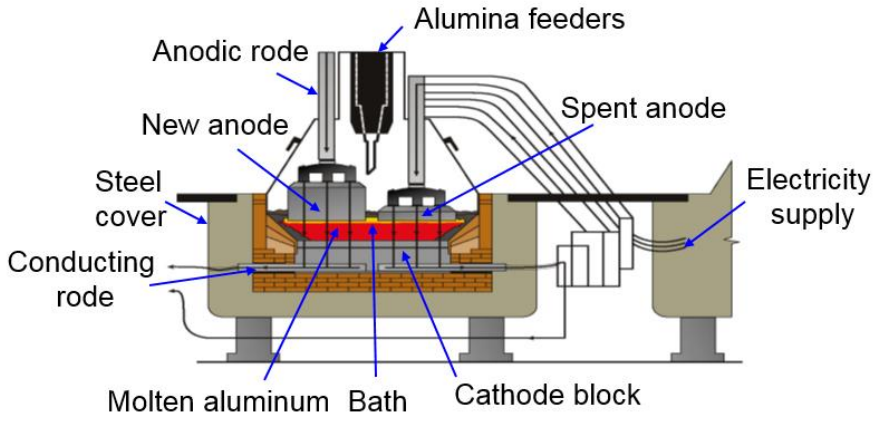

Figure 1-2 Cross section of a prebaked reduction cell technology (Courtesy of Alcoa).

Carbon anodes provide the carbon source for alumina reduction (i.e., they are consumed by the reaction) and are therefore considered as a consumables for the smelting process. Their quality affects the economic and environmental performance of the process. Approximately half of electrical energy passing through the anodes is converted into heat by means of Joule effect.

In spite of several improvements in the electromagnetic stability, in the chemical behavior of the bath, in electrode design, as well as the application of better process control schemes, the typical thermal loss of a modern electrolysis is still high. As mentioned previously, these heat losses comprise approximately half of the consumed electrical energy. A typical distribution of the heat loss for an electrolytic cell is illustrated in Figure 1-3.

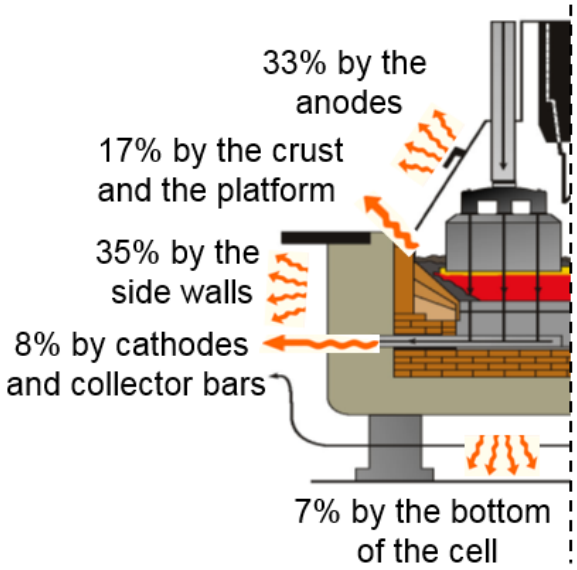

Figure 1-3 Heat loss distributions in an electrolytic cell during operation [75].

Basically, 96% of the electrical energy, consumed in a smelter, is used for aluminium electrolysis [11] and around 10% of such energy is consumed to overcome the electrical resistance of prebaked anode that can reach 60μΩm [12-14]. As shown in Figure 1-3, the thermal loss through the anode can reach up to 33% [15-16]. These losses are not only related to the nature of anode materials but also to the defects such as heterogeneities, cracks and porosity in the baked anodes. In addition, a low quality anode may result in a more reactive anode towards air and CO_2, which cause more material loss and dusting, low flexural strength and low thermal shock resistance [12]. Carbon consumption is also negatively correlated with the anode density, affecting its electrical resistivity [13, 17]. This explains the difference between theoretical and real carbon anode consumption of approximately 0.33 and 0.4kg/kg Al, respectively, as illustrated in Figure 1-4. Finally, in order to obtain a lasting service life and good energy efficiency in the electrolysis cell the anode quality have to be kept as high as possible in order to minimize the electrical resistivity, air permeability and carbon consumption.

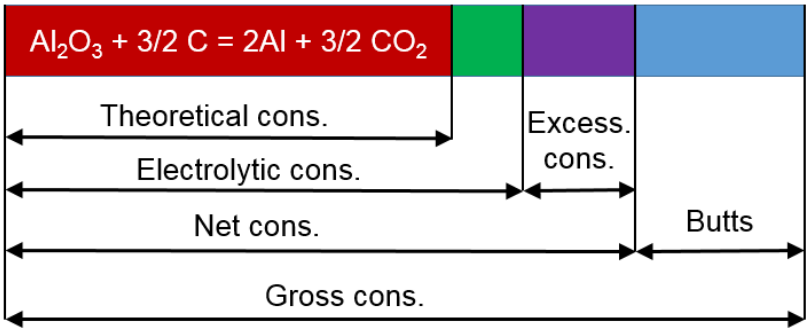

Figure 1-4 Anode consumption figures [43].

1.2 Anode production

The anode manufacturing process involves five main stages: formulation, blending, mixing and forming to obtain the so-called green anode, followed by baking (carbonizing) to obtain the so called baked anode [18]. A typical process flowsheet is shown in Figure 1-5. The raw materials (coal-tar pitch, petroleum coke and recycled butts) are preheated separately at around 200°C and introduced in the mixer or the kneader to produce the anode paste. The latter is then densified by pressing or vibro-compacting. Afterwards, the green anodes are baked in large open pit furnaces at 1100-1200°C. Lastly, the baked anodes are stored until rodding, and the conveyed to the electrolysis cells. The rods (aluminium/steel assembly) serve to suspend the anodes in the electrolytic bath and to transmit the electrical current to the cell through the anodes.

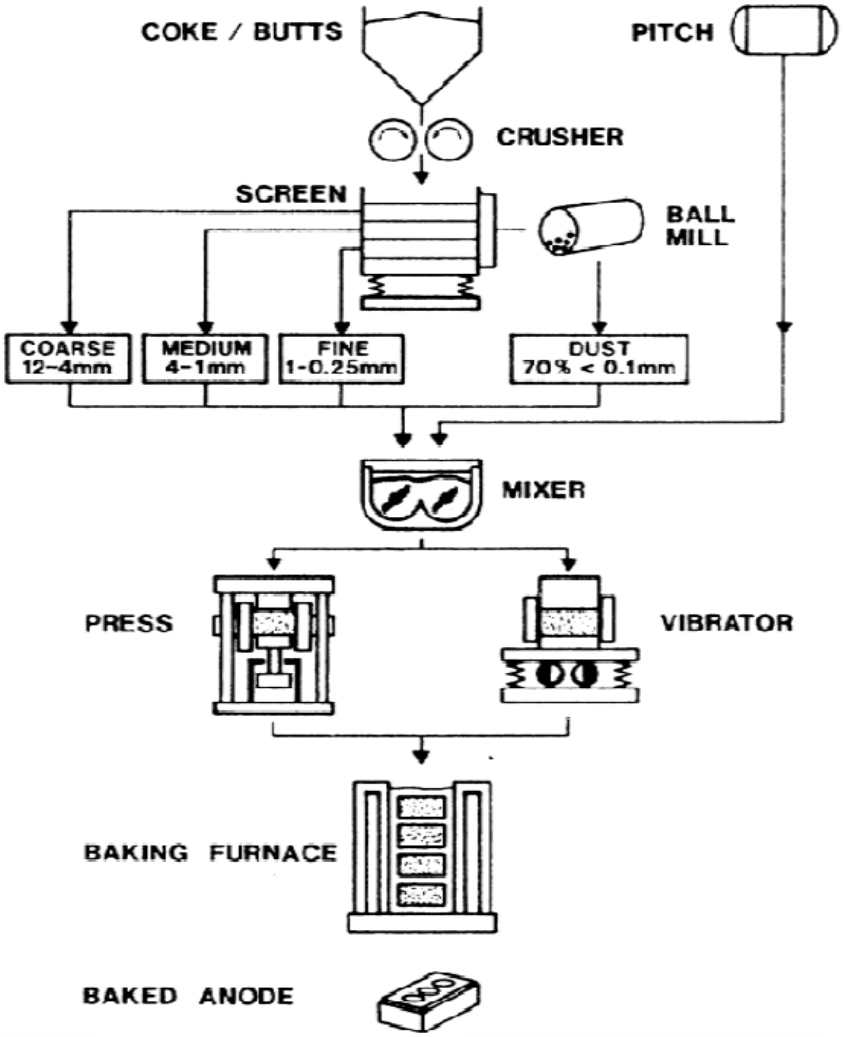

Figure 1-5 Schematic of anode manufacturing process [19].

The size of a typical anode is 1.4-1.6 m in length, 0.65-0.75 m in width and 0.6 to 0.65 m in height. The value of the density of the baked anode can reach up to 1.570 g.cm^{-3} and the Young modulus (compression) varies between 7000-11000 MPa [20-21]. The mass composition of a typical anode is 65% of petroleum coke, 15% of coal-tar pitch and 20% of anode butts (anode residues crushed and recycled after their use in the electrolysis cells). These components are distributed throughout the volume of the anode, sometimes heterogeneously. Compositional heterogeneities and variations in carbon structure may give rise to defect anodes. The baked anode volume also includes a high quantity of pores of different sizes. A normal anode typically contains about 25% of pore space. The typical size of these pores varies between 10-300 µm. Larger pores (> 300 µm) can also appear due to some variations in the anode process production parameters. The size at which pores become an issue for anode performance is still unclear at this point, and more research is

required to address this question. For more details about the baked and green anode structures as well as the porosity distribution the reader is referred to the thesis of Azari Dorcheh [43]. The raw materials (coke and pitch) are by-products of petroleum and coal, respectively. Coal-tar pitch is the much preferred binder in the industry. Coke and pitch are mostly composed of carbon but there are impurities, in particular, sulfur in petroleum coke that tends to increase in recent decades [21]. Recycled anode butts also add some impurities (e.g., fluorine, sodium and aluminium) in the anodes since they have been in contact with the electrolytic bath. Table 1-1 lists the typical chemical elements and physical properties of baked anodes.

Table 1-1 Chemical components and physical properties of baked anodes [30].

(a) Chemical composition

Element	Unit	Typical range
S	%	0,5-3,0
F	ppm	150-1500
Na	ppm	100-1000
Fe	ppm	100-800
Al	ppm	100-600
Ca	ppm	50-500
V	ppm	20-350
Si	ppm	5-300
Ni	ppm	40-250
K	ppm	5-50
Mg	ppm	5-50
Pb	ppm	5-50
Zn	ppm	5-50
P	ppm	1-30

(b) Physical properties

Property	Unit	Typical range
Apparent density	gcm^{-3}	1,5-1,62
Real density	gcm^{-3}	2,05-2,10
Thermal conductivity	$Wm^{-1}K^{-1}$	3-5
Electrical resistivity	μΩm	51-74
Air permeability	$10^{-13}m^2$	0,3-8
Thermal expansion coefficient	$10^{-6}K^{-1}$	3,6-4,6
Compressive strength	MPa	30-65
Bending strength	MPa	4-14
Young modules (static)	GPa	3-6,5
Porosity	%	20-30
Reactivity to CO_2 (ISO 12988-1) mass losses	%	4-15
Reactivity to air (ISO 12989-1) mass losses	%	4-35

The anode quality is defined in terms of the properties such as strength, density and electrical resistivity. These depend on the operating parameters of the manufacturing process as well as on the raw material properties. Any change in these properties or in the process is usually reflected in the process efficiency [21-28]. A bad combination of manufacturing conditions may decrease the process efficacy by introducing heterogeneities in the anode blocks or by increasing the chances of creating cracks. This thesis will elaborate the possibilities to identify such defects as well as some of their causes, using non-destructive techniques.

1.3 Factors affecting anode quality

The various factors that have an influence on the final quality of the anode are divided into three groups [29]; including the raw materials characteristics, the manufacturing parameters of green anode (mixing, compaction and cooling), and baking conditions. The knowledge of the physical and chemical properties of different anode components as well as their preparation process is necessary to understand how heterogeneities arise, and how cracks are formed in the anode blocks.

1.3.1 Anode raw materials

It is worth mentioning that the anode density, electrical resistivity, mechanical strength, and reactivity are determined by a number of characteristics such as types, portions and properties of raw materials as well as the dry particle sizes. It was mentioned previously that the green anode is obtained after molding a mixture of liquid binder coal tar pitch and dry aggregates, composed of calcined petroleum coke and recycled butts particles of different sizes. The three components and their impacts on the anode quality will be discussed in the next section.

Calcined coke is commonly used in the aluminium industry and is made from green petroleum coke, a by-product of the heavy oil refinery, by means of a calcining operation. It is the main carbonaceous material in the anodes and has the highest mass fraction in anode paste comprising more than 60%. Any problem in calcining conditions and green coke quality corresponding to the crude oil quality, refining operation and delayed coking operation parameters consequently reflects in the quality of the obtained calcined coke [19]. On the other hand, the refineries do not have benefits to improve the quality of low value by-products such as coke, since it is obtained from the residuals of raw petroleum that have low cost on the market. Some authors [31] addressed the classification of various coke categories and their effects on the anode characteristics such as cracking, density, CO_2 emission, metallic impurities and oxidation. Others have discussed about the impact of oil quality and process operation on green coke quality [32-33]. The study conducted by Rodenovc [34] shows that if the coke does not contain high amount of sodium, vanadium and sulfur (thermally unstable), good binding efficiency between coke and pitch can be obtained after baking. Presence of sulfur in an optimum amount assists in reducing reactivity. Contrariwise, sodium and vanadium increase the CO_2 and air reactivities.

The main role of coal tar pitch, second raw material, is to bind filler aggregates together and thus to provide sufficient strength in anode blocks especially after pyrolysis in the baking process. It consists of approximately 50% non-volatile fraction of coal-tar that remains in the down level of the column after vaporization of all contained oils [35-37]. At room temperature, it is presented as a black friable solid. It becomes fluid above its softening point (110-115 °C, depending on its chemical composition). The pitch is then subjected to various heat treatments to improve its quality before being used in the anode recipe [38]. Its quality depends on the constituents and the operation conditions in the cooking ovens. The pitch is also useful to penetrate in the coke pores to increase the anode density and consequently the electrical conductivity. Consequently, its quality can be defined in terms of wetting properties since less viscous pitch can penetrate in smaller voids and increase the anode density [39]. Moreover, after baking the amorphous pitch transforms into semi-crystalline coke that improves the mechanical properties.

Anode butts consist of the remained anode part after about 25 days operation in typical modern electrolysis bath since the anodes are not completely consumed to avoid metal contamination by the connection steel rods. They are crushed after cooling and cleaning from bath contaminants such as sodium. The crushed butts are then used with coke as dry aggregates in the anode paste and account for about 20 % of the green anode formulation [40]. The proportion, particle size, physical as well as chemical properties of butts are crucial for anode quality [40-42]. In the latter, Fischer, Perruchoud and Belitskus also found that an increment in butt content would result in an increase of baked apparent density, decrement in electrical resistivity and shrinkage during anode baking. In addition, it was found that carbon consumption depends also on butt particle size [40].

1.3.2 Green anode manufacturing process

The quality of carbon anodes depends on other various parameters of the manufacturing process such as the type of equipment used, methods of preparation, process conditions, and allotted time for each stage. The initial step is the preparation of aggregates where the coke particles sizes are reduced by a preheated crusher [43]. This is followed by a further refinement of the resulting particles that is defined by the used technology. Zhuchkov and Khramenko [44] provided a typical range of particles size distribution: 30% coarse particles (0.6-5 mm), 20% medium particles (0.3-0.6 mm), 20% the particles of small sizes (<0.3 mm) and finally 30% of dust. After crushing and screening, the

coke and butt aggregates must be heated, weighed and then blended with pitch to obtain the desired recipe. The preparation of the dry aggregates and paste directly influences the formation of defects in the anode, mainly the homogeneity of the block and the cracking phenomenon. It is therefore important to use an optimum dosing of different coke particle fractions (coarse, intermediate and fines) and the coarse butts as well as the liquid pitch in order to ensure a better particles distribution [19,44].

The last step to prepare the anode paste is the mixing of the blended raw materials. The power, time and temperature of mixing are the most important parameters determining the mixing effectiveness. The efficient mixing is defined in terms of homogenous distribution of the anode contents [45-49] and lower porosity in the paste in order to obtain anodes with high density [49] and thermal shock resistance [46]. The moderate mixing energy is important because low energy leads to poor distribution of pitch and therefore inhomogeneous paste while high-energy risks to break the large particles [26]. Moreover, this must be conducted under a specific temperature (around 170°C) since the pitch characteristics such as viscosity and wetting capacity have significant effects on the anode-cracking phenomenon [48, 51]. Certain properties of the anode such as density and porosity can be correlated with mixing temperature and its duration since these parameters have an effect on the visual appearance of the paste [53-54]. Therefore, the optimization of all parameters mentioned above is necessary to obtain a good anode quality.

The anode forming can be done in two ways: by pressing or vibro-compacting. The processes that are using the vibro-compactor are preferred as they allow a more homogeneous distribution in the anode by decreasing the paste viscosity. The anode geometry is important as well, because the degassing of volatile components in the pitch depends on the anode dimensions. A bigger anode is more likely to undergo cracking because the volatiles have to travel a longer distance to exit the block. Insufficient heating during anode forming can cause an heterogeneous distribution of pitch and may lead to formation of cracks and porous areas during baking [55]. In addition, the forming temperature must not be too high (implies too low paste viscosity) in order to avoid the anode collapse when removed from the mold. Lastly, since the non-uniform density distribution within the anode can occur when the anode paste is filled in the mold, it is very important to ensure a balanced filling [55].

After extraction from the mold, the anode undergoes either a slow cooling over 540 minutes in ambient air or an accelerated cooling by spraying or immersing in water, at a temperature approaching 70°C, which takes about only 90 minutes to cool down the green anode [18]. Generally, the vibro-compacted anodes need a longer cooling time than those formed by presses because of the higher forming temperature [30]. However, in both cases, the temperature should be suitably adjusted in order to avoid the development of high temperature gradient between the cooling fluid and the anode surfaces. When using a low cooling temperature, the anode is exposed to significant thermal stresses, which may exceed the limit supported by the anode. Furthermore, small cracks may appears during a rapid cooling caused of the excessive contraction in the anode surface since a high temperature gradient between the surface and the anode center can be produced. If the anode is already holding defects especially cracks, the thermal stresses are more likely to cause further propagation of the horizontal pre-existing cracks, regardless of the uniformity of the cooling (uniform or variable) [26]. Finally, the transportation, handling and storage of the green anodes after forming should be completed with care because the hot anodes are more vulnerable to damages.

1.3.3 Anode baking process

The most important step in the anode production process is the anode baking since the anode mechanical and physical properties develop during this process. In this step, part of the pitch is released as volatiles and the other part is coked to give the anode its rigid form. The baking process is very complex because there are several parameters that can change the anode structure. It is also the most expensive step in the anode production line. The anodes are staked vertically in the pits of an open ring furnace and are covered with fine particles of coke in order to fill the empty spaces and avoid anode burning during baking at high temperatures reaching up to 1200°C [19, 30]. Meanwhile, the heat is provided by burning a fuel during all baking operation that takes around two weeks. The furnace design, the heat-up rate, the final temperature, the temperature gradient, and the soaking time at such temperature are the important baking parameters [60-62]. In addition, the way to inject the fuel into the furnace also affects the baking process efficiency in a considerable way and consequently affects the quality of baked anodes [63].

At the beginning of baking, an anode expansion phenomenon occurs, at about 200°C, due to the pressure (induced by the anode expansion) that is accumulated during the

previous process: mixing and green block cooling. However, if the resulting stress exceeds a critical limit, a vertical crack may appear at the center of the anode [25, 26]. At a temperature higher than 200°C, the release of volatiles generates an evolution of the pressure in the whole anode block. If this pressure is not efficiently removed by degassing, the same vertical cracking phenomenon can result. When the temperature exceeds the boiling point of the pitch, the volatiles emerge through micro-pores and provoke the apparition of micro-cracks by interconnecting these pores. For these reasons, it is important to operate the furnace with an optimal heating rate to avoid the pressure increase and thus to decrease the crack development. In addition, when a high heating rate is used, the operation requires more energy (i.e. fuel) especially at the beginning of baking [64]. According to Dagoberto et al. [65], the heating rate must not be exceed 15°C/h to avoid the formation of this kind of cracks.

Other types of cracking are caused by the stresses already present within the anode, which is accumulated during compacting and green anode block cooling, if they reach a certain threshold. The overpressure accumulated inside the anode is quickly stopped when the cooling is accelerated by water, which increases the pressure in the anode. However, in the case where the cooling is performed by air, the heating rate during firing can be done at a higher speed [58]. The better distribution of the pitch in the anode block causes a reduction of the internal pressure during de-volatilization, which leads to an anode with less cracks.

Moreover, the lifetime of the anode and their consumption in the electrolysis are directly related to the final cooking temperature [66]. Liu et al. [67] highlighted this by means of studying the influence of the plant parameters and anode properties. The results show that the major causes of this problem is the propagation of pre-existing cracks. The latter are created during the baking process when a density gradient is accumulated in the green anode. The release of induced stress, which is formed by both compaction and cooling process, leads to the creation of vertical cracks by de-volatilization of pitch during the baking process [68].

In conclusion, it is clear from the above that the appearance of defects can be caused either by different anode manufacturing processes or by the quality of raw materials. Although these mechanisms are completely different and independent of each other, some form of defects, such as vertical cracks, can be caused by different factors. This makes the exact origin of these cracks difficult to identify.

1.4 Common anode defects

The carbon anodes, used in the modern electrolysis, are consumables and therefore have to be replaced periodically. Indeed, the high temperature of the electrolysis causes a thermal shock to the new anode which may favour the development of microscopic cracks that may lead to large cracks with different forms (inclined at the corner, horizontal in the mid-plane under stub-holes or vertical everywhere in the block) [42,44,69]. The propagation of such cracks during electrolysis operation may cause the anode degradation as it is illustrated in Figure 1-6.

Figure 1-6 Cracked carbon anode due to the thermal shock in the electrolysis cell [50].

The anode manufacturing objective is to maximize the mechanical strength and density in order to reduce the electrical resistivity and the carbon lost caused by the thermal chocks. The mechanical strength and density of the anodes are highly influenced by the nature of the raw materials (coke, pitch and butts), paste composition, different parameters of the production process, the baking parameters in particular, as well as the equipment technology. As shown in Figure 1-7, the common defects found in the baked anodes, discussed in more details in section 1.4, include:

- Porosity: it appears due to the exclusion of air, solvents and other contaminants during mixing and anode forming. Pores in general belong to two groups, closed pores or open pores. These two groups have very different shapes and sizes. They are randomly distributed in the anode block. These pores can also be classified into

three different types based on their size [291]: micropores (width less than 0.1µm), mesopores (width between 0.1 and 10µm) and macropores (width greater that 10µm). The increasing number of any type of these pores as well as the increasing size of macropores may become problematic since this could increase the electrical resistivity of the anode;

- Inclusions: impurities accidentally included in the raw material or introduced by production process. These inclusions increase the risk of degradation of the anode sides and corners, mainly in the electrolysis, because they are made of different materials and show a different behavior, and consequently create more stress around their locations;
- Cracks: Generally cracking in dense carbon anodes begins at the microscopic scale and then expands to provide macro-cracks by cyclic thermal loads (i.e., heating and cooling). These cracks are distributed throughout the block but more concentrated in the median plane under the stub-holes; their length can reach the anode dimensions and their width may vary between 1.4–2.1 mm [292]. Depending on their positions in the anode, they can occur in three different directions; vertical, horizontal and diagonal (corner cracks). Both of micro and macro-cracks have to be considered as a defect because as soon as they appear in the anode block they may increase the electrical resistivity as well as the anode degradation risk during thermal shocks;
- Burning: This kind of defect generally appears in the baking process. It results from the chemical reactions of oxidation, reactivity to air, which is thermally activated process, especially when the oxygen is diffused around carbon.

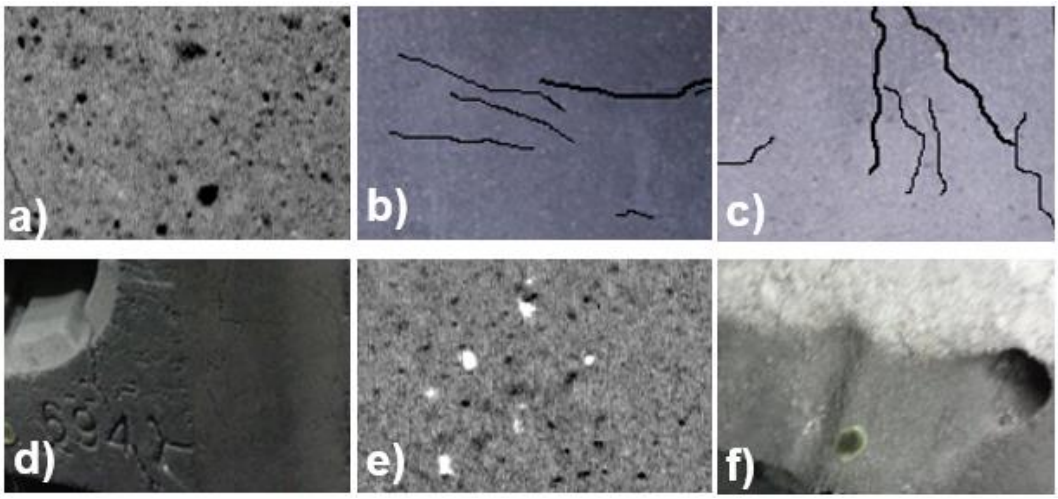

Figure 1-7 Common anode defects a) pore (inhomogeneity), b) horizontal cracks, c) vertical cracks, d) corner cracks, e) impurities, f) over baking.

Selecting adequate feedback corrective actions to implement on the anode manufacturing process requires an accurate diagnostic of the defects present in an anode (identification of their type, location and severity). It is also essential to have a good understanding of which part of the process could be responsible for a specific anode defect. This helps to know which process parameters could be adjusted to correct the problem. In this context, the degree of influence of various factors on common anode defects is summarized in Table 1-2 [74].

Table 1-2 Degree of influence of the factors provoking common defects in anodes [74].

	Inhomogeneity (pores)	Burning	Vertical cracking	Horizontal cracking	Slant cracking	Impurities (inclusions)
Raw materials	+	-	+	+	++	++
Composition of the anode paste	++	-	+	-	++	+
Mixing of the anode paste	++	-	+	-	+	+
Anode forming (Compacting)	+	-	+	++	+	-
Baking Parameters	+	++	++	-	-	-
Rod sealing and handling	-	-	++	-	-	-
Thermal shock	-	-	++	+	++	-
(-) have no influence		(+) little influence			(++) lot of influence	

1.5 Problems

High quality carbon anodes contribute to optimal performance of aluminium reduction cells. The currently increasing variability of anode raw materials (coke and pitch) makes it challenging to manufacture anodes with consistent quality. Intercepting faulty anodes (i.e., damaged due to internal cracks and voids) before they are set in reduction cells is therefore important. However, this is a difficult task even in modern and well-instrumented anode plants because their best quality control strategies consist of characterising only a small portion of anode core samples. Typically, less than 1% of produced anodes are cored and just half of these cores are fully characterized because the nature of the measurement techniques is destructive and the lab characterizations are labour intensive. The measured characteristics are divided into four groups: mechanical properties, physical properties, chemical composition and reactivity. Laboratory analyses are detailed in [19]. Sinclair and Sadler [69, 74] listed the most important problems associated with such anodes quality control method:

- Core samples are not representative of the population, for economic reasons (tests and analysis cost) only a small proportion of anodes from which samples are typically cored and characterized;
- Each core sample is not necessarily representative of the whole anode block to which it belongs due to the too small size of the sample comparing to the entire anode block and the little number of anodes from which these samples have been cored;
- Long delay (2-4 weeks) for obtaining the laboratory analysis results. The baked anodes are often set in the reduction cells before these lab results are available;
- Only major defects or deviations from targeted properties affecting the entire anode blocks over a sufficient long period of time can be detected by core sampling and characterization scheme.

Developing methods for anode health monitoring in a non-intrusive way has become fundamental since the majority of defects are located within the anode block and are often not visible from the external surfaces. In fact, there are at least three engineering problems that need to be addressed before achieving a successful quality control system. First, the techniques have to be non-destructive to preserve the product, to be rapid in order to be consistent with the plant production rate, and to be able to acquire volumetric information. The severity, type, and location of the defects should be evaluated based on information contained in the data collected from the material. It is thus necessary to care about several concerns such as the time consuming and the computational effort involved for arriving at the solution. The data collection, processing and analysis techniques must therefore be efficient. The last and most important aspect is how to pave the way for the industrial application. It is usually a big challenge to move from lab testing on small samples to real tests conditions on full scale samples since we have to deal with new difficult parameters and environment conditions (i.e. testing an anode blocks is not as easy as testing a samples).

The following sections present an overview of the different strategies and methods that have been proposed to control the anodes quality. Meanwhile, a literature review of the non-destructive techniques (NDT) is also presented to select the best methods that satisfy the requirements of the primary aluminium industry.

1.6 Methods for green and baked anode quality control

1.6.1 Empirical and numerical models for predicting anode properties

The mixing, forming, baking, particle fineness, quality of coke and pitch, and electrolysis operation are the main factors that have been widely investigated over the last decades in order to develop correlations for predicting the final anode properties. Keller and Fischer [73] and McClung and Ross [78] were the first to develop empirical models for predicting the net carbon consumption in the pot using, respectively, raw materials and anode properties. Jones [44] has implemented the difference between the net and the real carbon consumptions (excessive consumption) to correlate the carbon reactivity to the anode mechanical failure under thermal shock. Other mechanistic models of the baking furnace have been also proposed to predict anode temperature [81-83], but all of them require long computing times. Moreover, an overview of the relationships that have been established between the raw materials properties, baked anodes properties and process parameters is available in [84]. Hume et al. [85], for example, have measured the influence of sodium and sulfur contamination on the CO_2 reactivity of the anodes. Fischer and Perruchoud [42] also highlighted the impact of contamination by sodium as well as the hardness of the anode butts on the bulk density, air permeability, resistance to bending and reactivity to air and CO_2. Fischer et al. [87] evaluated the evolution of electrical resistivity, flexural strength, reactivity to air and CO_2 and thermal conductivity versus baking parameters. However, all these studies focusing on only one or few properties.

Recently, Lauzon-Gauthier et al. [90] have proposed an empirical soft-sensor model to predict anode core properties directly after the baking cycle. This includes all the available plant data such as raw materials properties, paste plant measurements , baking data and anode cores properties, etc. The model has shown good predictions for most of the measured properties, but only for anodes baked at the coldest and hottest positions in the furnace, due to the constraints of the core sampling strategy. In order to improve this work and based on the relation between baking conditions and anode quality discussed in [81-82], the impact of any baking position was investigated by Dufour et al. [93]. After combining different categorical variables, it was possible to accurately predict the temperature history of anodes baked in different positions, which is typically not measured during normal operation.

1.6.2 Machine vision techniques

Bogoya-Forero et al. [97] proposed a non-destructive machine vision sensor to predict Vibrated Bulk Density (VBD) of coke aggregate samples based on their surface textural characteristics that are obtained by imaging. In this work, coke mixture properties such as particle size, proportion and quality were predicted. They have benefited from the wavelet decomposition of the images that helps in model interpretations since it was already demonstrated in several industrial product quality control applications [99]. Particle mixture samples were collected from the dry aggregate mix from industrial conveyor belts just before adding pitch and thus VBD is typically measured according a standard procedure involving a vibration table [100]. Since the VBD is a function of the real coke density and its internal porosity, it is possible to make an appropriate link to the mixture quality. Furthermore, the pitch demand and anode density are highly related to the coke porosity which is one of the most important physical properties [98].

Recently, a machine vision sensor was designed by Lauzon-Gauthier et al. [54, 102] for real-time monitoring of anode paste texture prior to forming. Since the visual textural appearance of the paste is influenced by the particle size distribution, coke particle porosity and pitch distribution, it was thus a good indicator of the anode quality. This method was investigated at a laboratory scale and then the final machine vision sensor robustness was successfully validated at the industrial scale at the ADQ carbon plant. In addition, the visualization and interpretation of the models for large and complex industrial datasets were improved according to the suggestions of previous works [90, 103] through a development of a new sequential multi-block PLS algorithm (SMB-PLS). This algorithm allows the integration of all data related to anode quality such as raw materials properties, process operating conditions, some real-time non-destructive measurements of the paste, green and baked anodes quality related features, baking furnace operation data, and more into one single model.

1.6.3 Electrical resistivity measurements

The electrical resistivity is an important anode property, and its distribution in the anode could provide indications about the presence of defects and therefore evaluate the anode quality. During the last decades, several studies have proven the effectiveness of the electrical measurements to generate information on several porous material properties.

Electrical impedance tomography [105], for example, has been applied in quality control and defects detection for various materials [106-108]. Unfortunately, this method is sensitive to the uncertainties and the inaccuracies of the implemented models. In addition, it does not take into account the spatial variations of materials conductivity [109]. Such a technique is an extension of the electrical resistance tomography technique, which has been used in defects cartography and cracks detection for inspecting concrete and composite materials [110, 111]. However, since these methods use the experimental measurements as inputs to numerical models, the effects of heterogeneities cannot be taken into account, mainly in the case of carbon anodes since the material is orthotropic.

Seger [112, 113] published the earliest application of resistivity measurements for baked anodes, in the early 1970's. The measurement system allows, firstly, the current circulation through the anode height. The current and the voltage drop between the stub-holes and the bottom are then measured by mean of several probes for finally predicting the average resistivity value of the anode. Since that time, this same principle was extensively employed in the field of carbon anode quality control. Recently, a commercial on-line equipment named MIREA [114-115] was successfully implemented by Rio Tinto Alcan (RTA) in order to estimate the current distribution in anode block. According to the industrial operation, the current was effectively applied to the lateral surfaces of the stub-holes using metallic brushes. The anode resistivity distribution is then estimated by using a numerical model, which is calibrated by the voltage drop data measured between the top surface and the lateral anode surface at different heights. This system can extract the morphological information concealed in the voltage drops collected from different locations. Therefore, to obtain the spatial distribution of defects, it is necessary to collect the voltage drop in different directions. However, due to the size of anode block, the time consuming of the measurements remains high.

The principle of eddy current has also been implemented by Haldemann and Fawzi [116] in order to measure the induced current losses in the surfaces of carbon samples. The anode sample quality was then predicted by the combination of the current attenuation and the electrical resistivity. The main drawback of the apparatus is the limitation of its magnetic field, which cannot penetrate deeply in the object. For such reason, the apparatus does not seem promising to inspect large objects such as industrial anodes. Furthermore, a comparative study between the average electrical conductivity of homogenous and defect green anode has been proposed in [117] to evaluate their quality. However, the test bench

provides a limited thickness of impedance measurement since the magnetic field created by the corresponding coil allowed a penetration of about only ten centimeters in the top anode layer. Unfortunately, this depth is not sufficient to evaluate the quality of the whole anode block.

In order to cope with the limitations of the previous techniques, and to eliminate the useless baking of defective anodes, a non-intrusive measurement of green anode electrical resistivity has been developed by Kocaefe et al. [118-119]. Interesting results were found after conducting preliminary tests on anode samples and then on industrial anodes using a first generation measurement system. A second generation is now being developed in order to provide a more robust prototype, adapted to the industrial application. The main advantage of this on-line anode quality control technique is to allow earlier detection of the defective green anodes and thus effective use of the fuel in the baking furnace since the baking of defective anodes is circumvented. Even though it should be possible to measure the resistivity distribution in the whole anode block, it is not clear if these measurements could be used to discriminate between the various types of anode defects (e.g., cracks, group of pores, etc.). This identification of defects is necessary for taking timely feedback corrective actions on the anode manufacturing process. Finally, Alcoa has also proposed its own technology for measuring the green anode resistivity based on a 4 points probe (4PP) device [327].

1.6.4 Characterization of baked anodes and anode paste

Recently, several characterization tests have been conducted on many anode parts to measure the mechanical properties of the anode material and thus directly evaluate its quality. Eliassen [20, 88] has proposed some correlations between mechanical properties, such as fracture toughness, tensile strength and fracture strain and physical properties such as density at different temperatures in order to simulate the anode cracking behavior in the electrolysis. Since the established relationships have limitation on crack size and part dimensions, a new relationship using a finite element numerical modelling approach was investigated [89]. However, due to the very little change relative to the variance of the measured values, a dependency to the temperature for the Young's modulus was not established.

Furthermore, Azari et al. [94-96] proposed a method to reduce the inconsistency in the baked anode quality by controlling materials variations and process parameters and

provide a feedback to tune the subsequent production steps. In this work, the compaction behavior of green anode paste was used as an intermediate quality index to reduce the large number of variables that are associated to the anode quality. The measurements include the evaluation of density, porosity, pore size distribution and particles shape factors. Good paste characteristics such as effective mixing, maximum density, minimum air permeability and specific surface area were defined via both optimum mixing time and mixing temperature.

1.7 Other relevant NDT techniques

The first part of the literature review showed that numerous research activities are being conducted to develop tools and techniques for monitoring the anode manufacturing. However, few works have directly focused on the anode block inspection. Although there are many experimental set-ups and some equipment that have been developed to characterize the anode material, it seems that very few attempts were made to develop a real-time quality control systems for baked industrial anodes, except the MIREA system that may not be able to locate and identify the defects. Consequently, the lack of on-line quantitative measurements makes it very difficult to face the increase in raw material variability and variations in anode manufacturing process, which increases the energy and carbon consumption. Therefore, alternative non-destructive testing techniques (NDT) need to be investigated. Indeed, since the electrical connection of the anodes is initiated from the center (stub-holes) and in order to expose its internal morphology, the concern of this work is the volumetric inspection of the anode block. Finally, the industrial application requires a quick but a detailed method that can solicit the whole anode block.

1.7.1 Visual inspection

Visual inspection is the most widely used NDT method. Indeed, the operator can directly identify the large defects of the surface. Furthermore, this kind of test provides information on which complementary control method to be used. There are two types of visual control for the detection of surface defects: direct and indirect. The direct control uses the naked eye but the indirect control uses some devices, such as endoscopes [120] and Charge-Coupled Device (CCD) cameras [121] that produce more rigorous control because of their recording ability. The limitations of this method are the different perceptions and the low accuracy of human being that cause the non-reproducibility of events. In addition, only

defects in accessible surface can be analyzed. This ancient and simple method reveals the presence of open discontinuities on surface such as scratches, macro and micro cracks, inclusion, wells, etc. It is applicable to all porous materials and its accuracy is as much as that of the visual system. In the context of a traditional quality control, this method has already been established in two different places in anode plants. The first one is during transferring anode on the conveyor and directly after the baking process to measure the different anode sizes. The second system is installed at the end in order to analyze the shape of anode butts.

1.7.2 Electromagnetic or Eddy current testing

This method involves the creation of induced currents in a conductive material by varying a magnetic flux, as shown in Figure 1-8. These induced currents flow locally in the material with a distribution that is dependent on the excitation of the magnetic field, sample geometry and electrical conductivity as well as magnetic permeability of the examined material. The presence of abnormalities in the tested material disturbs the current circulation. Consequently, by measuring the variation of the apparent impedance of the measurement sensor, it is possible to detect and identify the defects since such disturbances are correlated to the nature of these defects. The analysis is usually based on a comparison between the related apparent impedance signals and the signals measured from defect-less material. Notice that the eddy currents are mostly concentrated near the surface of the material because the electromagnetic field decreases exponentially with depth [122]. Although the penetration depth of the eddy currents in the material can be increased by reducing the excitation frequency (penetration depth is inversely proportional to the excitation frequency), using a too low frequency reduces the sensitivity of the method. Therefore, it is possible to use this method to detect only surface and sub-surface defects within conductive materials.

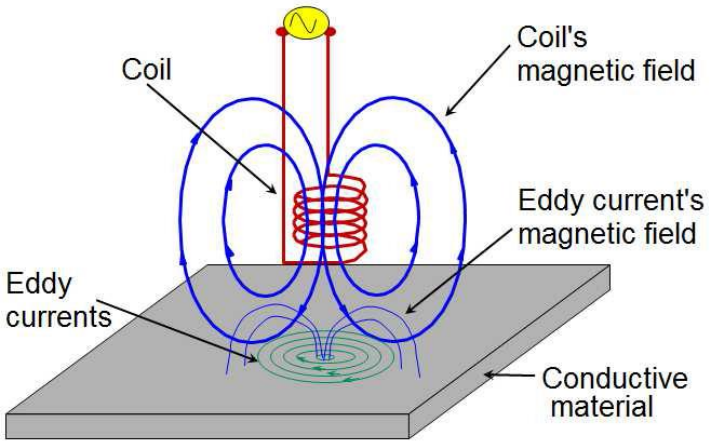

Figure 1-8 Eddy current testing procedure [52].

Haldemann and Fawzi have developed a system for controlling the electrical quality of carbon anodes in an automatic fashion, including detection of internal defects by measuring an eddy-current loss and resistivity in the block. A patent was published in this context [116], in which these authors have detailed the approach as well as the functioning of the system. The method consists of determining the electrical efficiency of anodes by determining their electrical resistivity after baking. It aims to detect internal defects such as cracks, voids, and heterogeneities in the carbon block. A combination of two electrical measurements was used to evaluate the quality of laboratory scale carbon anodes. First, a four-point probe was used to measure the electrical resistivity. Second, a large coil, surrounding the blocks with parallel capacitor, was used to measure the resistance of two groups of ten carbon blocks. The coil size has to be as close as possible to that of the carbon block and the electrical current intensity has to be optimal. The main drawback of the tool developed here is the limitation of the magnetic field and the resulting eddy-current penetration. For this reason, the developed tool does not seem promising for industrial anodes application.

1.7.3 Ultrasound

Ultrasonic Testing (UT) involves the propagation of ultrasonic waves in the material to be tested. In most common UT applications, very short ultrasonic pulse-waves, with center frequencies ranging from 0.1-15 MHz and occasionally up to 50 MHz, are transmitted through materials to characterize them or detect their internal flaws. It can be performed based on two configurations: transmission or reflection. The image shown in Figure 1-9, represents the principle of reflection ultrasonic testing. The transducers used in UT consist

of a transmitter and receiver, which are available as a separate units or embedded together as a single unit. Because of its effectiveness, this technique has become widely used in industry. Moreover, it can be used to quickly scan the entire volume of a part and then assess its state. Indeed, the presence of porosity strongly disturbs the propagation of ultrasonic waves [124-127]. The estimation of porosities in the material can be determined through evaluating the ratio of input and output signals [128-130].

This technique also relies on the comparison of the measured attenuation through various materials versus that measured on standard test specimens. There is also the mode conversion technique that is quite useful in the field of characterization of porous materials. It involves immersing of the material in a viscous liquid to allow shear waves propagation after water saturating using the vacuum impregnation technique. The sample must be placed between two ultrasonic transducers for acquisitions under several angles of incidence. Depending on the chosen incidence angles, the transmitted wave is divided into two parts: slow and fast waves. By calculating the ratio between the speeds of these two produced waves, which is inversely proportional to the density, the porosity percentage of the examined material can be obtained. The main advantage of ultrasonic technique is that it allows for a multi-site assessment examination even in objects that have only one accessible surface. The measurements of the material properties can be provided based on the estimation of wave propagation speed through such material [131-134].

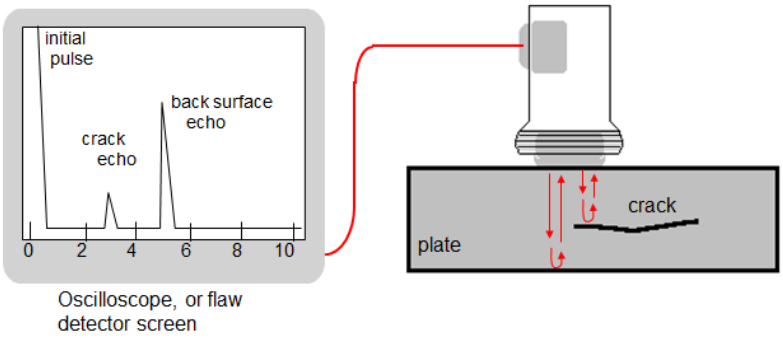

Figure 1-9 Schematic representation of Ultrasonic testing set-up (pulse-echo mode) [56].

The ultrasonic technique was applied in characterization and controlling of several heterogeneous materials in various fields that include the Young's modulus estimation of human bone [135], measuring dynamic elastic modulus of the porous titanium [136], damage evaluation and characterization for concrete, mortars and cement [137-145] and rocks, [146] determining the wood's Young modulus [147] and characterization of ceramic

[148-149]. Since the method has been successfully applied on all the materials cited above, it may be effective in the porous carbon anode inspection. However, the anodes have larger dimensions, and this will increase the attenuation of signals in the entire blocks. Thus, having a powerful tool (acoustic wave generator, transducers) that is able to send high-energy waves is required to cross the large block that measures over 1.5 m.

The ultrasonic reflection based method (i.e., pitch-catch) has been proposed by Haldemann and Fawzi for detecting cracks in the carbon anode center [116]. However, it was impossible to discriminate random backscatter caused by several irregularities (i.e., different kinds of pores) from that caused by actual defects. The random scattering also attenuates the signal rapidly when crossing the anode sample. Random back scattering from a region close to the transducer may hide the signal from a defect located in the body of the carbon block. In addition, this strong attenuation requires a large amount of energy to be coupled into the carbon block, which in turn produces more random back scattering. As a result, the pitch-catch configuration is useless for carbon anode inspection. Other configuration such as transmission (i.e., pitch-catch) could thus cope with the scattering problem since the transmitted signal will be measured rather than the reflected one, and thus the attenuation caused by defects will be evaluated. Furthermore, it would be more beneficial if the implemented generator can produce very low frequency waves with high amplitudes.

1.7.4 Acoustic emission

The quality control using acoustic emission (AE) testing refers to the evaluation of transient elastic waves generated after stressing the material. One difference between AE and other NDE methods is that AE inspection can be used either with active excitation, such as pulse impact, or with passive excitation, such as spontaneous phenomenon relying on energy released from damage formation within the material undergoing the test [152]. Figure 1-10 shows a typical installation of acoustic emission test. AE wave propagation properties are highly correlated with the material composition and structural component characteristics. There are various acoustic excitation tools like AE generators [150-151], pencil lead break fractures [153], and excitation with balls surrounded by a variable number of metal rings [152].

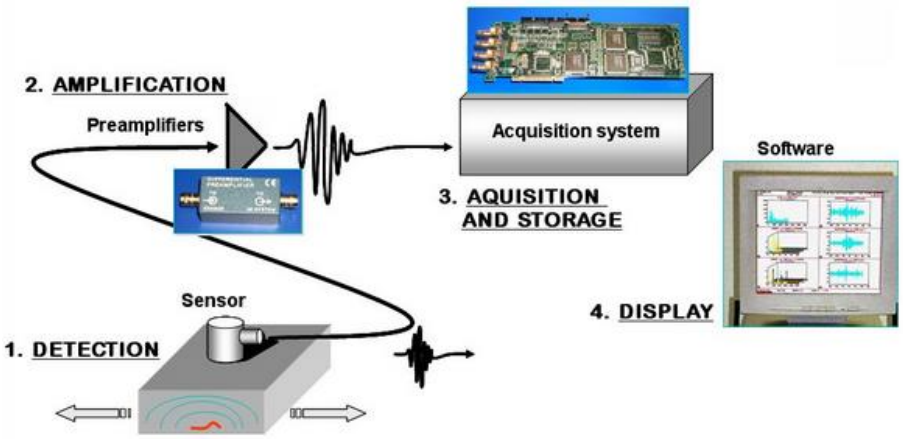

Figure 1-10 Typical mounting of acoustic emission testing [57].

Acoustic emission monitoring is a recognized non-destructive test (NDT) method commonly used to detect and locate several defects in materials. In recent years, the AE technique has rapidly developed and has become a very important research tool in porous materials since the signals generated by this method can deliver abundant information. By means of AE monitoring techniques, several materials quality problems leading to industrial instabilities, have been successfully solved. Early use of the AE method in porous material inspection was for laboratory specimens and simple concrete structures [154-155] before being extended to reinforced concrete, concrete composites and bridges [156-159].

Since AE can be generated under the fracture stress level, it can be used to detect defects in fragile materials such as ceramics, silicon carbide, and sintered glass as well as different composites [160-163]. Other scientists have carried out extensive research of AE phenomena in rock and expanded this to coal rock [164-167]. In the carbon anode field, some analyses of preliminary measurements have been conducted on anode block samples [116]. The audio sound measurements after hitting different samples using a metallic hammer resulted in good discrimination between all sound signatures. However, after they easily convert the time domain signatures for each carbon block into frequency spectra, some difficulties arose, mainly to determine which part of the spectrum corresponds to flaws. Consequently, the authors have abandoned the technique for two reasons (according to their opinions). First, this technique requires a homogeneous graphite block to calibrate the sound measurement device, and obtain good results with this technique. However, this type of calibration material is difficult to obtain. Second, the calibration experiment would have to be conducted in an anechoic chamber, which is relatively expensive, in order to protect against environmental sound contamination. This approach could be adapted to anode

blocks and the analysis of the signals be further studied in order to take advantage of the AE method which include better reliability, disturbance to the object, and quick analysis that makes it possible to be implemented in real time quality control like in [168].

1.7.5 Vibration analysis

The Modal Analysis (MA) approach is usually used for material characterization, numerical models updating, and quality control of different products. This technique consists of analyzing mechanical oscillations of any material around a reference position [169]. These oscillations result from external forces transmitted to the material by mean of a hammer, loudspeaker, or shaker. After acquisition of the spatial variation signals using accelerometers, microphones or laser vibro-meters, the MA decomposes these signals to that we call vibration modes. Some frequency/time indicators can be easily extracted to inform about the existence of defects. Figure 1-11 presents the principles of vibration analysis testing.

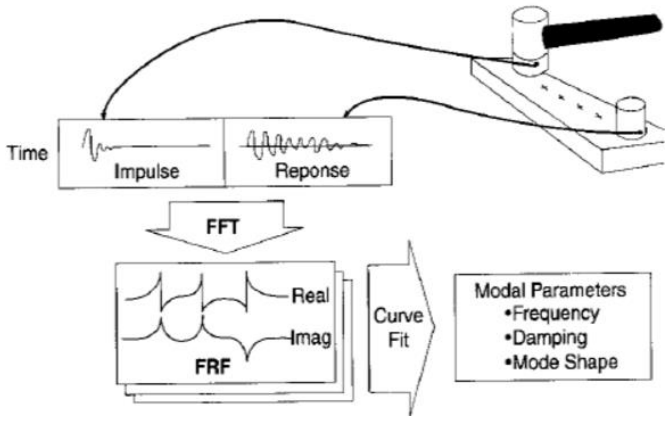

Figure 1-11 Typical vibration analysis set up with impact hammer [58].

Material vibration testing and analysis contributes to the progress in many aspects, including quality control, diagnosis prediction, and process monitoring [170-171]. The most common application is the identification of unwanted vibration modes to improve product quality. Vibration-based techniques have been successfully applied for health monitoring and quality control of orthotropic materials such as concrete and composite [172-174]. For example, it was shown that the identification of defects could be performed by measurements at specific locations since damage indexes are affected by the distance between such locations and the defects. In addition, an attempt to evaluate the effect of defects in graphitized composite on modal dynamic characteristics was carried out by

Campanelli and Engblom [175]. In the latter, an efficient computer model was successfully developed but the experimental results were difficult to analyze due to the presence of spurious modes in the frequency response data. Recently, MA has been used in order to replace some traditional methods such as visual classifications and static tests of woods [176-177]. The good correlation between physical properties of woods and their dynamic properties resulting from vibration analysis were confirmed in these works.

In general, there are a lot of advantages but also some drawbacks in the experimental vibration analysis. The most important advantage is its versatility to identify both displacement and strain with one type of sensor, which allows an effective analysis with a minimum number of sensors. In addition, it can be used to test different object sizes, allows fast tests, delivers immediate answers, and needs low cost investment in experimental as well as numerical tools. However, it does not provide information on the location and the size of defects when the block size is very large versus that of defects. The user thus can just be informed about the existence of defects and if a further control on the material is necessary. In addition, instrumentation can be a very critical issue and thus some skills would be required in bonding strain gauges or other strain sensors since they can easily degrade the quality of the measured signal. Finally, vibration analysis seems to be easily implemented in industrial process monitoring.

1.7.6 Radiography

Recently, several studies focused on the development of the radiography technique. This method is presented in Figure 1-12. The radiography principle is relatively simple: X or Γ (gamma) rays, respectively in the frequency range of 3.10^{16} Hz - 3.10^{19} Hz and > 3.10^{19} Hz, are projected by a radioactive source to analyze the structure. The resulting electromagnetic waves (possess very short wavelength: 10^{-12}-10^{-8}m for X-rays and less than 10^{-12}m for Γ-rays) cross the material where the energy beam is differently absorbed by the material contents. A photographic film captures the emitted rays where the more captured energy in some location give the information about the existence of defect. Finally, a visual examination of the photography film is to be performed by the experts [178].

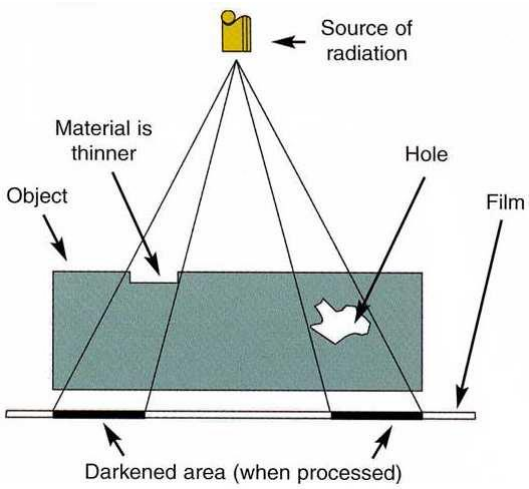

Figure 1-12 Radiography testing procedure [59].

Radiography is a method, which is often used to inspect welds for detecting external and internal defects. This method is able to check out the integrity of all types of materials (even through several centimeters of steel) and complex geometry parts. The application of X-ray radiography to detect several kinds of defects and to characterize porous materials such as ceramic, concrete and composites, have been reported since a long time [179-182]. For safety reasons, it is necessary to use this method with great caution. Indeed, the room must be surrounded by lead to confine the radiation. Unfortunately, for the productivity, time consuming and sample size, the potential of application of this technique for quality control of anodes is somewhat limited.

1.7.7 X-rays tomography

Tomography or CT scan is a recent 3D analytical technique, which provides bulk distribution images of the X-rays absorption coefficients. When the sample is considered a multi-material whose constituents absorb X-rays at various percentages, it is possible to extract a 3D image of the microstructure by segmentation. Figure 1-13 presents the tools and the principle of the technique. Tomography allows density measurements, size estimations, detecting abnormalities inside objects, and monitoring materials under stress [183-184]. Schell [185] was able to get a 3D mapping of fibrous composite material network by the application of this method. These works, as well as those of Zermatten [72], explain how to obtain porosities present in composite material using a 3D mapping. The calculation of the volume percentage of voids and their sizes, which is one of common problems in porous materials, can thus be achieved accurately (if the resolution is good and consequently the porosity is bigger than pixel size). Nevertheless, this technique is relatively

expensive and its application is limited to relatively small objects because of the available tools as well as the huge quantity of the generated data.

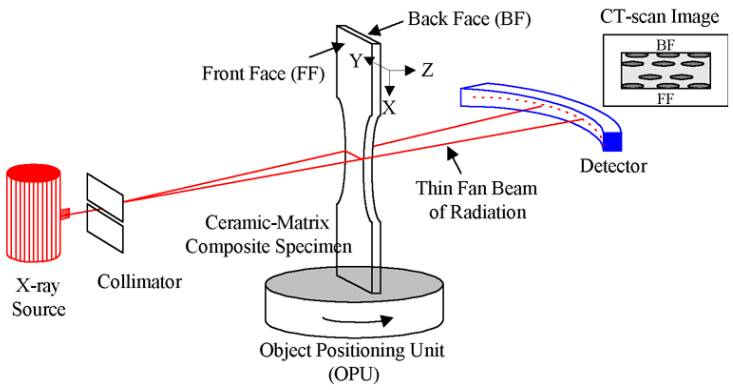

Figure 1-13 The experimental set-up for obtaining a CT-scan image [70].

In the primary aluminium production field, X-ray CT scan has been used by Adams et al. [76] in the non-destructive 3-D characterization of pre-baked carbon anodes. The method enables reconstruction of the internal morphology of carbon samples. In other works [77, 79, 80], Picard et al. have demonstrated the use of CT scanning to determine apparent density and to estimate the porosity of anode core samples. As a result, a linear relation between the anode apparent density and the X-ray attenuation coefficients (CT numbers) has been successfully developed. The anode porosity estimation has also been performed using a best-fit relationship. In addition, an automated crack detection method was successfully applied on the CT-scan images of baked carbon anode slices [80]. This crack detection based method, combining accuracy and low computation time, was previously developed by Yamaguchi [86, 91] to detect cracks in concrete. Comparing to conventional X-radiography, CT scanning is relatively long and high-cost in porosity estimation [92] but it is better in other applications that require defects identification since it gives a good 3D representation of the material. In addition to the high cost, finding an apparatus that can accommodate objects as large as the anode blocks considered in this research is an issue.

1.7.8 Thermography

The NDT infrared thermography (IR) method uses a scanning infrared camera for temperature sensing and an illumination system, most often, for transmitting the heat to the material (Figure 1-14) and this method is called active thermography. Contrariwise to that is called passive thermography, where the material is already hot and consequently doesn't need an external temperature gradient to be heated [101]. The presence of defects can be

visualized by a change in the surface temperature of the material as shown in the below mentioned Figure 1-14 right (thermal contrast). This technique also reveals the thermo-physical properties of materials such as thermal diffusivity and thermal conductivity [104]. Some works on thermographic testing of composite materials [123, 267] and especially sandwiched material [287] have been reported. In particular, when the entire thermal field of the sample can be obtained, the defects in thin objects, metallic or composite, can be detected in this thermal field by mean of suitable software. However, the detection and the characterization of small defects concentrated within the center of thick object are very difficult.

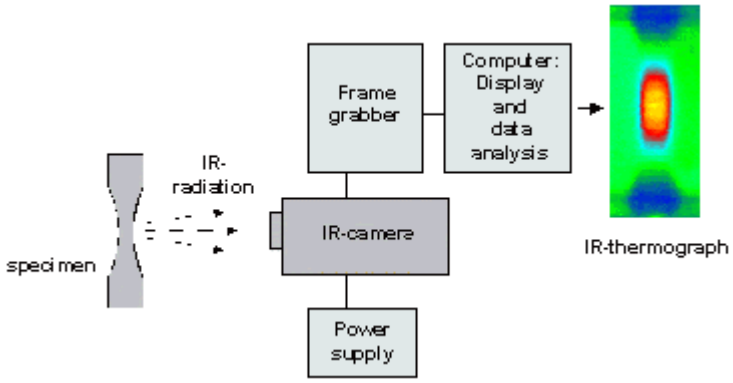

Figure 1-14 Experimental set-up used for IR thermography [71].

1.7.9 Synthesis and method selection

Each NDT method has its own set of advantages and drawbacks. Some are better suited than others in a particular application. Table 1-3 shows the characteristics of the NDT methods used in the industry. These characteristics were evaluated by Kuhn [293] based on the following criteria:

- Material: Is this method appropriate for metals and/or composite materials?
- Geometry: Is it possible to apply this method directly on the real product? Should the object size be limited or can be unlimited? The object may have a complex geometry?
- Measurements: The excitation and detection can be easily performed? What kind of configuration is possible (i.e. transmission, reflection or both of them)?
- Defect size and location: Is the technique adapted to detect surface defects, sub-surface or located in the center?

- The method impact: What type of contact is required between the material and the tools used in the technique? Does the method risk the creation of further damage? Does the nature of the technique cause negative environmental impacts?
- Rapidity of the method: is the time required to perform the tests and interpreting the results sufficiently quick to allow control in real time?
- Industrialization: Is the method easy to implement and/or automate? What is the overall cost of the method?

Table 1-3 Main features of the widely used non-destructive testing methods used in the industry (Modified from [293] and [294]).

	Visual inspection	(C) Eddy current	Ultrasonic	Acoustic emission	Vibration analysis	Radiography	Tomography	Thermography
Applicable to composite materials	++	--	++	++	++	++	++	++
Material tested directly	++	++	--	+	++	--	--	++
Large blocks sizes	++	++	++	++	++	-	-	++
Complex geometry	-	-	+	+	++	++	++	+
Subsurface volumetric defects	--	+	++	++	+	++	++	+
Respect of the block integrity	++	++	+	++	++	+	+	+
Environmental compliance	++	++	+	++	++	--	--	++
Method implementation	++	++	+	++	++	--	--	+
Price of standard equipment	++	++	-	++	++	--	--	+
Rapidity	++	-	++	++	++	-	-	++
Possibility of automation	++	-	++	+	++	--	-	++
	(C) Conductive materials only							
	(--) not suited or not possible			**(-) not well suited**		**(+)Fairly well suited**		**(++)Ideal application**

This literature review lead to a detailed overview of non-destructive techniques that can be applied for porous materials quality control where each technique has its own advantages and disadvantages under certain circumstances. Among these NDT methods, modal analysis is more appropriate for quickly evaluating the anode block quality and is

easily applicable in industry. It can also provide automated contactless tests with a minimum number of experiments. In addition, modal analysis needs a low excitation frequency, using a mild material such as rubber in order to avoid the deterioration of the fragile carbon anode.

On the other hand, acoustic emission (AE) and ultrasonic-based techniques are considered to be promising for deeper real-time control of microstructural changes and defects evolution in various porous materials. However, in many practical situations, the application of acoustic emission techniques in the anode plant is not the best choice since the fragile baked anodes must be subjected to an acute mechanical loading in order to create sounds emission, and such loading can result in permanent damage to the carbon block. Although conventional ultrasonic techniques can detect defects such as voids and cracks, they are not very sensitive to succession of defects mainly those having random orientations in several directions or being emerged in large quantity of pores. The combination of acoustic and ultrasonic emissions, named acousto-ultrasonic (AU) technique [298], provides an alternative approach that gathers the advantages of both acoustic emission and ultrasonic methods to give a detailed inspection. For this reasons, vibration analysis could be applied first to inspect the totality of manufactured anodes and check if a more detailed tests are required. Then, if necessary, acousto-ultrasonic testing would be applied to deeply analyze the defected anodes and ultimately create a coupled method.

Finally, CT-Scan can be used in order to validate acousto-ultrasonic and/or vibration results since it approximately (depend on the CT image resolution) reveals the internal structure and provides the calculation of the volume percentage of the voids (i.e. pores and cracks) and their sizes inside porous materials, especially that of baked anodes, using a 3D mapping.

1.8 Objectives

This work has been undertaken with the general aim of increasing the effectiveness of aluminium production by means of developing an inspection system to assess the quality of anodes and the presence of defects (cracks, pores, heterogeneities, etc.) before baking them or using them in the electrolysis process. This would allow manufacturers to observe in real-time the performance of the anode production process and to reduce the adverse effects of defect anodes on the performance of the electrolysis. It could also allow making timely feedback control adjustments to the anode production process. In addition, the new

inspection system should be sensitive to cracks and pores as well as their localization, and should also be selective to discriminate between these common defects.

The strategy involves two quick, non-destructive and complementary techniques for inspecting anodes directly after the baking process as shown in Figure 1-15, which represents the final inspection concept that we propose for the future. This thesis focuses on demonstrating the potential of modal analysis and acousto-ultrasonic for baked anode inspection. To the author's knowledge, this thesis presents the first application of these non-destructive techniques to the inspection of full-size individual baked carbon anode blocks. The two methods would be combined as follows. All baked anodes would be first inspected by the vibration method and then if a defect is detected, the flagged anodes would undergo a detailed inspection by acousto-ultrasonic to identify and locate the defects (i.e., diagnostic phase). The latter will allow sorting of the anodes having critical defects, which will be removed from the line and sent to recycling. The proposed inspection scheme may also provide relevant information for applying feedback corrective actions on the anode production process. For example, heterogeneities may be caused by poor mixing of the anode paste and therefore requiring an adjustment of mixing parameters such as temperature or duration. In regards to cracks, the worst defects, depending on their orientations and size, the process in which they are initiated may be also identified and consequently corrective actions to the appropriate process parameters could be implemented.

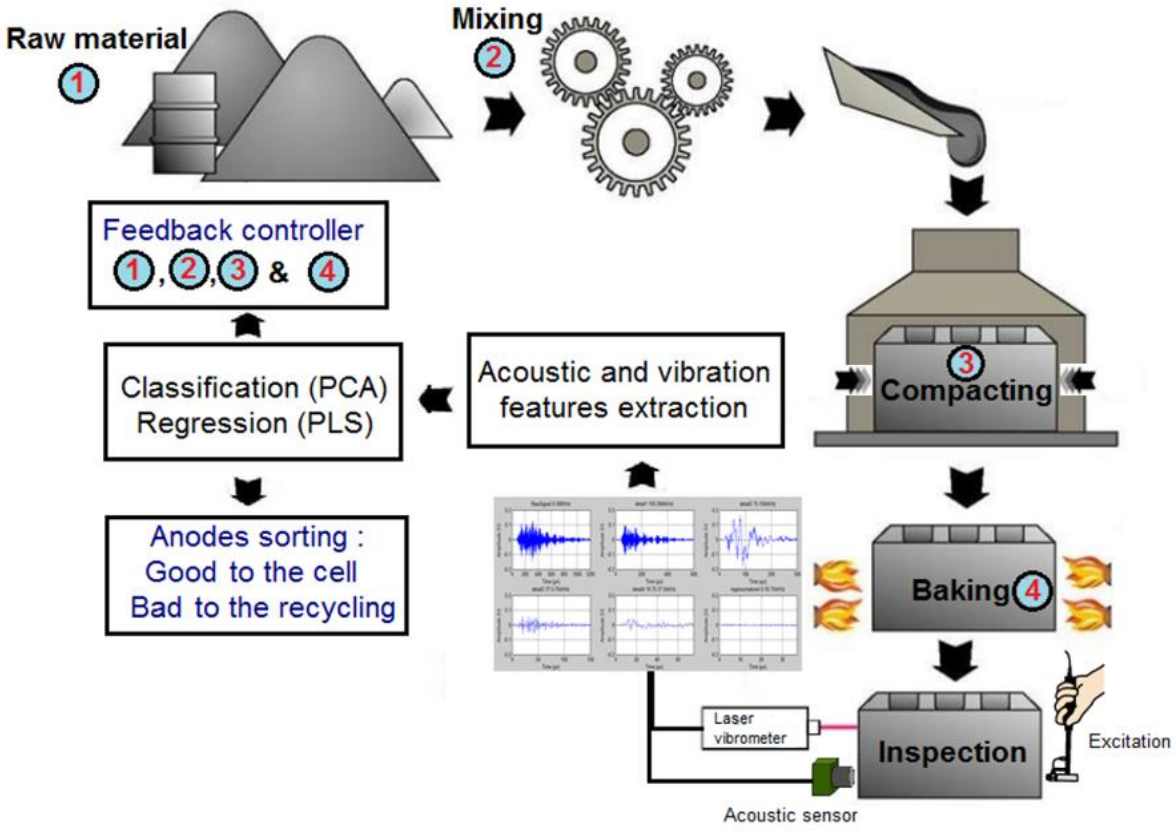

Figure 1-15 Schematic of the quality control methodology for baked anodes.

This PhD thesis then aims at demonstrating the potential of modal analysis (MA) and acousto-ultrasonic (AU) methods for the inspection of pre-baked carbon anodes. The following specific objectives were pursued in this work.

The first specific objective is to develop the experimental set-ups for investigating the selected non-destructive techniques. In particular, it is necessary to determine how to excite the anodes and to collect the corresponding response signals for both MA and AU approaches. Depending on the nature of the technique and the available tools, the investigations can be conducted either directly on the full size industrial anodes or on some samples in the beginning, and then have to be extended on full-scale industrial anodes.

The second specific objective is to develop an algorithm for each inspection technique in order to process and analyze the collected data and then calculate and select the best relevant features. These features have thus to be used in only one classification model based on multivariate statistical methods in order to allow the classification of the tested parts based on their vibration and acousto-ultrasonic signatures and make the

corresponding interpretations. Demonstrating the sensitivity of MA and UA to the most common defects in baked carbon anodes (cracks and pores) is the ultimate outcome.

The third specific objective is the validation of the obtained results by the CT-Scan technique. Since this technique is already investigated in the case of anode material, it just remains to be adapted according to our needs. Developing the new corresponding algorithms that allow the relevant analysis of the images is then required.

Finally, it is necessary to optimize both testing and analysis methods for reducing the control time consuming and demonstrate the robustness of the testing strategy on several full-scale industrial anodes in order to pave the way for the online control.

Chapter 2 Materials and methods

2.1 Introduction

As discussed in Chapter 1, modal analysis (MA) has been used extensively in evaluating the structures integrity, investigating the properties of materials and detecting defects. Acoustic emission and ultrasound are quantitative techniques and tend to be more versatile. These techniques, which give individually good results, are even more interesting when combined together. Such combination, named acousto-ultrasonic, makes it possible to mutually fill the gaps between acoustic emissions and ultrasound. As the name implies it is closely linked to the acoustic emission technique since it is equivalent to the simulation of the acoustic emission with ultrasonic sources. The acousto-ultrasonic technique is increasingly used because in many cases it complements other non-destructive methods.

Vibration analysis and acousto-ultrasonic techniques both need mechanical excitation, but consist of different acquisition technologies and their outcomes of completely different natures. Both of them use an electromechanical transducer, which generally consists of a single piezoelectric ceramic plate that converts an electrical signal into mechanical vibration and vice versa. From this point forward, these transducers will be called vibration sensor and acoustic sensor, respectively. The vibration sensor gives an electrical output proportional to the motion energy (i.e., acceleration, velocity or displacement) to which it is subjected. This electrical output usually has a wide dynamic range and frequency bandwidth. However, an acoustic sensor detects sound waves that originate from mechanical excitation and travel through the material. Acoustic sensors convert the selected sound waves to a proportional electrical signal. They typically provides clearer signals than does a vibration sensor at the cost of having a significantly narrower useful frequency range. Sound waves are created at the vibrating surface with the same frequency and proportional amplitude as the original vibration. Note that in order to avoid unnecessary repetition, the detailed description of the various equipment used in vibration and acousto-ultrasonic is not presented in this section since it is provided in sections 3.2.1, 3.2.3, 5.2 and 6.2.3.

In addition, the volumetric X-ray CT-scan technique was found to be effective for measuring anode density/porosity and was used to validate the different results. Finally, the high number of the resulting data (vibration, acousto-ultrasonic and CT) were analyzed using multivariate statistical methods, such as Principal Component Analysis (PCA) and Partial

Least Square (PLS) regression. To achieve these investigations, several industrial anode parts as well as many full size anodes were tested.

2.2 Modal analysis

2.2.1 Principles of modal analysis

Modal analysis is a dynamic method to test a material or a structure by studying its vibrational behavior under mechanical excitation. The modal characteristics are highly correlated with the vibration behavior of the object that is determined by the properties, size and geometry of the material. For a given material, any defect is able to change its characteristics and consequently its dynamic behavior. When this method is implemented, the object is subjected to a mechanical excitation in order to solicit the material. The concept includes three main phases: excitation of the object, measurement of the modal responses, and extracting specific features from these responses. However, a relevant choice of excitation and measurement tools is required since the results can be affected by these elements.

2.2.2 Types of excitation systems

The excitation of the object is critical in modal analysis because the resulting measurements depend directly on the excitation technique. The excitation tool must be able to stimulate the block with sufficient amplitude over a wide frequency band in order to allow easier acquisition, mainly when intermediate sensitivity sensors are implemented. As it was reported by Matter [289], the most common excitation methods, [186-188], are:

- Excitation with hammer;
- Excitation with shaker;
- Excitation with loudspeaker.

The hammer performs an impact excitation. It requires the object to be fixed so as not to be sensitive to the rigid modes, except when the tested object is quite heavy or the measurement sensors are installed directly on it (i.e., accelerometers). This type of excitation provides enough vibration amplitudes, but on a limited and variable frequency strip, always depending on both object and hammer materials. Impacts resulting from hammer are generally difficult to reproduce. In addition, it is very likely to introduce some parasite signals due to the lack of precision as well as the possibility of bouncing that can

be caused by the operator's hands. That is why a pre-treatment is necessary using averaging, windowing, and overlapping to perform good quality measurements [186]. A rubber hammer seems to be suitable for the current work where the anode block is quite heavy and the fundamental natural frequencies are low (under 500 Hz).

The excitations produced with a shaker are quite flexible. A random noise over a long period of time to cover a wide frequency band with constant amplitude is often selected [187]. This kind of excitation tool requires a mechanical linkage with the object. In general, a small-diameter rod is used to transmit the excitation force of the vibrator to a point on the object. The advantage of the shaker is the ease of measuring the force transmitted to the specimen and hence the amplitude, phase, and position of the excitation can be determined accurately. It is further possible to transmit high forces and to excite the specimen over a reasonably wide frequency range, between 10 Hz and a few kHz for high excitation forces (around many kN) or up to 20 kHz for low excitation force (about 20N). The drawback of this excitation technique comes from the mechanical link connecting a non-fixed object to the shaker. This problem appears just in the case of light objects, since this bond influences the modal behavior of the structure and must therefore be taken into account during data analysis. For heavier blocks such as the carbon anodes, this problem does not take place. This solution could be considered to automate and industrialize the final concept.

The speaker has the most elegant solution at first sight since it provides a contactless excitation and good results have been obtained previously [188]. The excitation is transmitted through air and sometimes the amplification of the excitation sound is required, depending on the application. In addition, by using adequate measurement systems, this excitation method allows achieving a modal analysis of the object very similar to a free (not fixed) configuration. The major disadvantage of this technique is the difficulty of measuring the excitation force transmitted to the structure. Since the excitation is transmitted through sound waves, it will be spread in the air (not punctual) and consequently will provide a weak excitation. Therefore, the precise evaluation requires measuring the features (amplitude and phase) of the pressure field exerted on the entire surface of the tested object, which is very difficult. Otherwise, it is possible to measure the excitation using a microphone, fixed as close as possible to the specimen surface and directly in front of the speaker where the excitation is maximal. An approximation of the ratio of both microphone spectra and specimen displacement can be obtained. Furthermore, due to the airborne transmission of

the excitation the speaker cannot generate sufficient vibration amplitude within the material, mainly when the corresponding object is large and dense.

A comparative study of the previous techniques has been highlighted by Lafleur et al. [189]. The results show a great similarity between the resonance frequencies and their respective dynamic properties produced by means of a hammer or a speaker. However, there is a slight difference between the results obtained by shaker and those obtained by the two other excitation techniques. The measurement errors have been attributed to the mechanical connection required by the shaker technique that acts as a preload and changes the object weight and stiffness to a certain extent. This phenomenon causes a shift in the corresponding natural modes. Hammer excitation is the least expensive and the easiest to implement, this explains why this approach was selected in this thesis project. Table 2-1 summarizes the main characteristics of each type of excitation and provides supporting arguments for our choice.

Table 2-1 Comparison of excitation methods (modified from [189]).

Features	METHOD		
	SHAKER	HAMMER	ACOUSTIC
Experimental preparation of the analysis	long	short	short
Mechanical connection with the study object	yes	no	no
Adjustment of the frequency range	easy (depending on the signal generator)	difficult (depends on the impact hammer head)	easy (depending on the signal generator)
Frequency shift	yes	Depends on the weight of the hammer	no
Change of the excitation point	long	short	defining the excitation point
Reproducibility of measurements	good	pretty good	good
Adaptation to any type of object	yes	yes	Mainly shaped structures of plates and shells

2.2.3 Measurement tools

Studying the dynamic response of materials under different conditions is very delicate for several reasons. First, such analysis requires a high degree of reliability since a repetition

of many tests is necessary. It follows that the experimental tools and procedures have to be carefully chosen in order to be not intrusive, easily repeatable, and able to provide a reliable characterization of the object dynamic behavior, as it was reported in [200]. Basically, three types of vibration measurement techniques are available for performing modal analysis. These are presented below and comments are made about their suitability for anode inspection:

- Accelerometers: these are widely used in modal analysis, partly due to their wide dynamic range and wide frequency bandwidth [190-193]. They are electro-mechanical transducers that give an electrical output proportional to the acceleration to which they are subjected. The spectral analysis of the temporal signals measured at various points on the object, leads to identification of the natural frequencies of the object and mode shapes. The measurements have to be taken when the maximum of fundamental (global) modes can be detected (i.e., it should not be limited to local or particular modes). The locations, likely to be nodes (where displacement is zero), have to be avoided and those likely to be bellies (where the displacement is maximum) have to be favored. In practice, since it is rather difficult to coincide exactly with a node, the positioning of accelerometers is not too restrictive. The interest behind searching the global modes is to identify the global deformation of the whole anode, but do not to miss detecting of some local defects. An accelerometer is a small device and is relatively low cost but it needs to be attached to the vibrating surface. This is sometimes difficult to achieve especially when the tested structure is small because the attached accelerometer itself may change the modal response of the object. It is also time consuming to place the devices and it is laborious to measure vibrations at several different locations, which is essential in the case of large objects. This is the main drawback for using accelerometers in industrial applications when short cycle times are required. Nevertheless, this technology was selected in this thesis for modal analysis of carbon anodes due to their simplicity and low cost.
- Laser vibrometer: this measurement technique, for evaluating vibrations and performing modal analysis, has a widespread application. The measurement principle is based on an optical method by means of Doppler effect [194]. The specimen is usually fitted with reflective patches to improve the laser reflection and consequently the measurements quality. The evaluation of the difference between

the incident laser beam and the reflected one allows determining the vibration intensity. The analysis of the signal acquired at each instrumented point provides a good visualization of the object deformation [195]. However, it is better to use three laser sources to obtain a three-dimensional representation of the dynamic responses. Such technology is rather expensive but allows accurate contactless measurements. It can also be easily implemented in real time control of carbon anodes since it provides quick measurements. In spite of being more expensive, laser vibrometers are preferred over accelerometers for industrial high-speed inspection.

- Microphone method: This is a rather convenient measurement method because it also allows a contactless identification of frequency responses. The measurement is multiple since the acoustic pressure is generated from the entire opposite object surface. Some studies [189] have shown that it is actually possible to achieve the modal analysis of the object using only one microphone installed near the structure. This method of modal analysis with a single reference constitutes an innovation in the field of the modal analysis. The possibility to consider only one input is argued by Bendat [196-197]. This acoustic modal analysis method is thus similar to an operating deflection shape [198-199], which would use as reference sound pressure instead of vibration intensity. The quality of frequency measurements using this configuration is perfect, and it is fully consistent with the typical frequency characteristics. However, the acoustic disturbance generated by vehicles and machines in industrial environments is the main drawback. The implementation of this method for an industrial application ideally needs a soundproofing, which adds high costs.

This study aims at developing a non-destructive inspection system that will be subsequently implemented in the anode manufacturing plants. Consequently, it is not obvious to use the microphones to measure the material response since it requires an environment without background noise, which is not the case in the anode production plants. Implementation of microphones requires using a sound isolation chamber that will likely lead to a more expensive set-up in comparison with the two former methods. Otherwise, accelerometers and laser vibrometers are widely accepted as valid tools for dynamic measurements. Their limitations rarely prevent the accurate measurement of the phenomena of interest. Several works have made a comparison between both laser vibrometer and accelerometer technologies [200-202]. It has been shown that the laser

vibrometer and accelerometer are well-correlated methods in modal analysis. However, the laser-based method can provide better quality of measurements. This is due to their immunity to electrical noise since there are no weak electrical signals transmitted by cables, and also due to the independency to the vibration frequency as well. Meanwhile, it is preferred to isolate the laser head from environmental vibrations. These reasons encourage the implementation of vibrometers for inspecting quickly and easily the anodes, and for using the results for a better process control. The accelerometer technique is worth investigating for proof of concept since it has a low cost although it is more time consuming. Accelerometers were used in this study, but this is not the best choice for the final industrial application because it needs to be adapted to high production rate.

2.2.4 Numerical modal analysis

A finite elements model was built for anode in order to support the establishing of the experimental set-up. The purpose of the model was to simulate the vibration response of the anode block obtained for different combinations of excitation points and different ways of supporting the anode. The objective was to select the combination that allows the global and coupled modes discrimination and thus facilitating the analysis. Indeed, the set-up configuration should excite the global deformation modes to be able to capture all possible types of defects of different severities (sizes). The finite element method (FEM) [203-204] seems to be the best method for the numerical modal analysis of the anode, especially in the reproduction of non-linear behavior (i.e., orthotropic material), which is very complicated. Moreover, FEM allows computing the natural frequencies and mode shapes of the object directly via a conventional calculation of the simulated vibration response to a given excitation.

The FEM model has been implemented in ABAQUS/CAE 6.14-1. The choice of this software has been conditioned by the work of Bui et al [206] who highlight the possibility of using ABAQUS for harmonic analysis with non-homogeneous materials. To minimize the resolution time of the numerical model, modeling the small details of anode, as the flutes of the stub holes, was avoided. This solution would indeed have required a significant number of elements in order to obtain a correct modeling of a complex and fine geometry relative to the dimensions of the model and would need more partitions to make a valid meshing. An elegant solution to limit the best model size without compromising on accuracy is the use of an average value at the slightly sloping sides. The boundary conditions are applied at the contact anode/supports. The anode is supported on bars using type of constraints "tie" and

"hard contact" as type of interactions that allow good modeling of degrees of freedom associated with the anode supports.

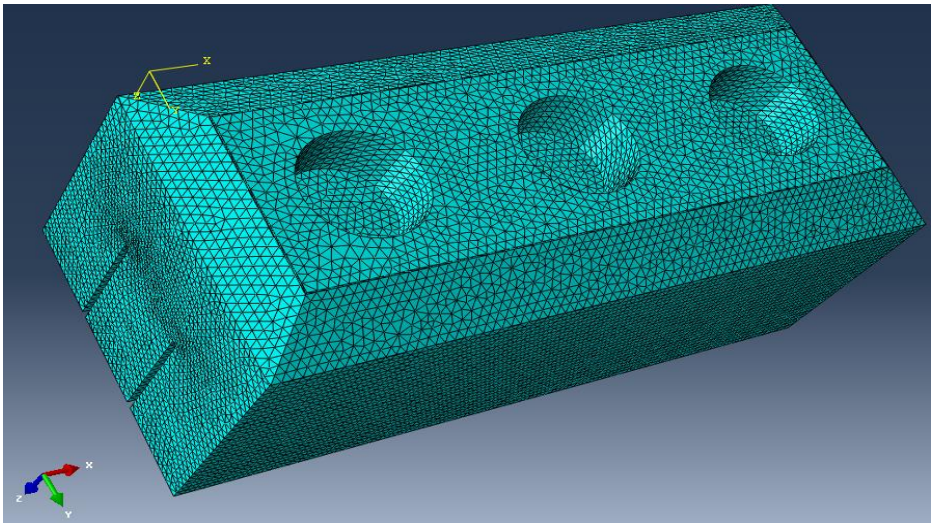

Figure 2-1 Meshing of the anode.

In order to predict the vibration responses of the full size anode, a simple three-dimensional model is constructed. It is worth mentioning that distributed irregularities, such as pores and cracks, generally cause mass and stiffness variation. Accordingly, the anode model was divided in seven different volumes, as reported in Figure 2-2 (Area #1…#7), and thus the corresponding mechanical properties were assigned to each area. The values of densities were calculated from some reference anodes using computed tomography. Contrariwise, the Young's modulus and Poisson ratio values were taken from the work of Eliassen [20] and Allaire [301], respectively, while the bars are always modeled with the standard steel properties. Table 2-2 presents the range of value used for these mechanical properties, including its designation and the respective units. The finite element model of the anode was developed using Abaqus/CAE 6.14-1 software and the anode was modelled with more than 100000 quadratic solid elements as shown in Figure 2-1. Some mode shapes of the relevant calculated modes are portrayed in Figure 2-3. Lastly, is important to mention that the selection of the equipment, accelerometer locations and excitation points as well as the best way to support the anode are detailed in Chapter 6. More details on the numerical model as well as a comparison between experimental and numerical results are available in Appendix 4.

Figure 2-2 Areas distribution for the allocation of suitable properties.

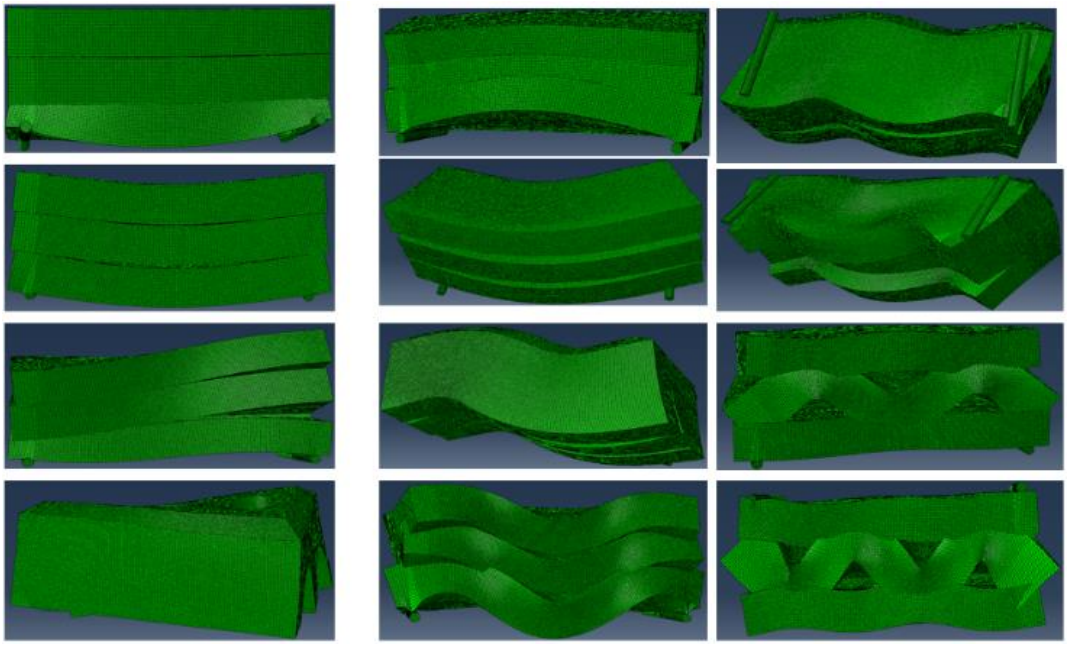

Figure 2-3 Example of the anode mode shapes.

Table 2-2 Mechanical properties of different areas.

Area	Density ($kg.m^{-3}$)	Young's Modulus (MPa)	Poisson's Ratio
1	1590	10000	0.18
2	1610	11000	0.18
3	1610	11000	0.18
4	1590	10000	0.18
5	1580	9000	0.18
6	1570	8000	0.18
7	1560	7000	0.18

2.3 Acousto-ultrasonic

2.3.1 Principles of the method

In this section, the acousto-ultrasonic (AU) technique is discussed in more details to provide the reader with a better understanding of the physical phenomena behind the AU signal propagation, and thus facilitating their analysis and interpretation. The AU is the second method that is proposed to use since it meets the final requirements of the research problem, which can be summarized as developing a non-destructive inspection method that will not only identify the defects, but will also locate and diagnose them. This technique was developed in the late 80s as a non-destructive tool for the evaluation of the mechanical properties of composite materials [207-209]. This method uses the propagation of mechanical waves to detect and quantify flaws in objects. It has received considerable attention [210] and it is especially useful to provide measurable quantitative parameters that correlate well with physical properties of various composite and porous materials [211-223].

AU combines ultrasonic characterization and acoustic-emission signal processing. The last term can result either from an acoustic generator excitation or from a sudden energy release caused by local environmental changes such as micro-cracking, grain boundary sliding, dislocation motion, etc. The generator excitation or the spontaneous event generates a mechanical wave in the material. This wave is detected at the surface by a piezoelectric transducer, which converts it into an electric signal. This same phenomenon occurs when using the acousto-ultrasonic method: an ultrasonic transducer converts a series of electrical pulses into ultrasound mechanical waves that are injected into the material. During propagation between both excitation and acquisition sensors, these waves interact with the internal morphology of the material.

Consequently, the received acousto-ultrasonic signal is information-rich about the structural features of the material. Thus, AU differs from conventional ultrasonic methods especially in the nature of the received signal. The response is actually a superposition of several waves resulting from the interaction of the original excitation signal with the microstructure of the material [212-215]. The morphological factors such as porosity, heterogeneity of composition and various defects (e.g., cracks), taken separately or together, influence the propagation of the waves and correlate at the same time to changes in the material’s mechanical properties.

2.3.2 Theory of mechanical wave propagation

Contrary to electromagnetic waves that can propagate even in vacuum, elastic waves need a material medium, fluid or solid, to be able to propagate. The elastic wave is generated by a mechanical disturbance propagation such as expansion, compression, shearing and vibration inside materials. This disturbance has some temporal shapes. If it is sinusoidal with unique duration, the phenomenon is then called harmonic or monochromatic since it has a single frequency. It can also comprise several harmonics; it is then periodic but with several superposed frequencies. In all cases, there are three frequency ranges:

- $f \leq 20$ Hz – Low-frequency waves – **Infrasound** field
- $20 \text{ Hz} \leq f \leq 20$ kHz – Audible frequency – **Audible** field
- $f \geq 20$ kHz - High-frequency waves – **Ultrasonic** field

In order to have a more detailed idea on different frequency bands, which are associated with real applications, each of the following ranges is assigned to a practical field of application [344]:

- 1µHz-1Hz : Geophysics, seismology
- 10Hz-100Hz : Geological, Seismic
- 10-100kHz : Ultrasonic cleaning systems (fronts, gear, ...)
- 1-30kHz : Generation of ultrasound by means of microwave
- 10-100kHz : Submarine acoustics
- 50-500kHz : Non-destructive testing with air-coupled ultrasonic
- 20kHz-20MHz : Non-destructive testing with contact or immersion, Acousto-ultrosonic, Medical, Ultrasound
- 20-100MHz : Acoustic microscopy (thin imaging)
- 100MHz-1GHz : Acousto-optic, acousto-electronic
- 1GHz-1 THz : Study of matter (microscopic)

From a wave propagation point of view, any material medium can be considered as a linear sequence of N spherical particles, each of mass Mi, connected by springs having stiffness Ki, which results in a discrete medium with N degrees of freedom, as illustrated in Figure 2-4. When the first spring k1 is placed into motion by means of an external force F_{ext}, oscillation will take place at the natural frequency fn which is among the properties of the system. This spring tends to return to its equilibrium state, and it does so by launching the

mass M1 to the right. The latter compresses the second spring K2, which is connected to the corresponding mass M2. Thus, side by side, the masses displace to the right, while the springs are successively compressed and so on until return to the equilibrium position. Such a phenomenon is actually the disturbance propagation in a material medium.

Figure 2-4 Explanatory diagram of propagation [224].

It is then possible to define a spatial dimension of the interference that is the wavelength λ calculated by ratio of the speed (c) and the frequency of the wave (f): λ = c / f. For an effective inspection, the distance between adjacent masses of the sequence have to be smaller than the wavelength λ in order to decrease the effect of the signal dispersion in interfaces between the particles. In addition, the wavelength should be two times smaller than the size of the sought defect.

2.3.3 Propagation modes

There are two basic types of wave motions (propagation modes) for mechanical waves: longitudinal and transversal waves. In longitudinal waves the displacement of the medium is parallel to the propagation direction of such wave (compressional waves: Figure 2-5 a). This type of wave can propagate in all material medium. In transversal wave, the displacement of the medium is perpendicular to the propagation direction of the wave (shear wave: Figure 2-5 b). Since there is no mechanism for driving motion perpendicular to the propagation of the wave in fluid medium, the transversal waves cannot propagate in liquids and gases.

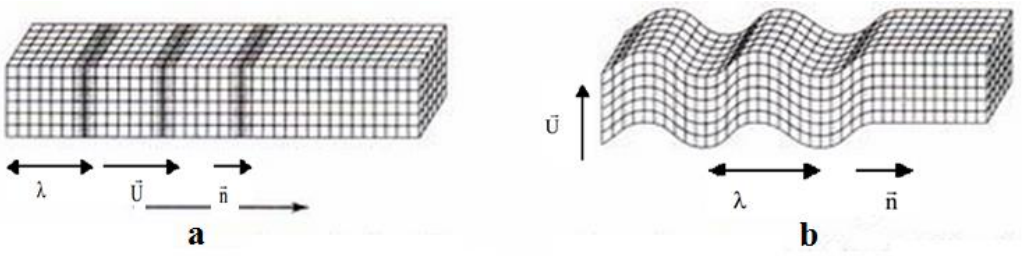

Figure 2-5 a) Longitudinal mode, b) Transversal mode, λ: Wavelength. $\vec{U}$: Displacement vector. $\vec{n}$: Direction of wave vector, [225].

2.3.4 Wave propagation velocity

Mechanical waves can propagate through any material medium at a particular speed, which depends on the elastic and inertial properties of the material. Some equations are used to establish the link between the speed of the longitudinal wave V_L and that of transversal wave V_T by means of elastic modulus E and shear modulus G in an isotropic and infinite medium (a given material can be considered as a finite medium when the wavelength is much shorter than the object dimensions):

$$V_L = \sqrt{\frac{E}{\rho}.\frac{(1-\mu)}{(1+\mu).(1-2\mu)}} \quad \text{and} \quad V_T = \sqrt{\frac{G}{\rho}} \tag{2.1}$$

where ρ is the density of the propagation medium and μ is its Poisson ratio.

The elastic modulus E and shear modulus G of a solid material medium are related to each other by the Poisson's ratio:

$$\frac{E}{G} = 2.(1+\mu) \quad \text{and} \quad \mu = \frac{\frac{1}{2}.\left(\frac{V_L}{V_T}\right)^2 - 1}{\left(\frac{V_L}{V_T}\right)^2 - 1} \tag{2.2}$$

Physical characteristics of a material, especially the elasticity and the density clearly affect the wave velocities. Some examples of propagation velocities in three different materials are shown in Figure 2-6. It is worth mentioning that the more flexible the medium is, the lower the propagation speed is and vice versa.

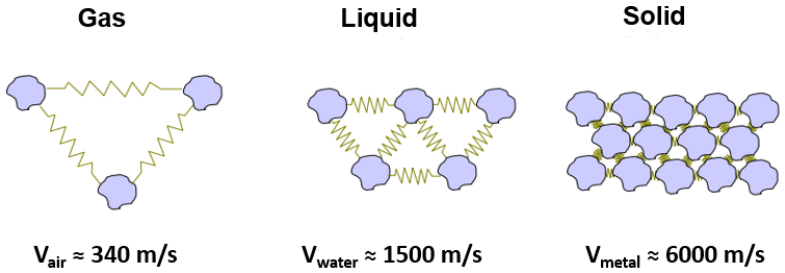

Figure 2-6 Propagation velocity rates of the compression waves for the three basic matter phases [303].

The anode is a porous material made of a solid part (skeleton) and a fluid part (air). Generally, when an acoustic wave propagates in a porous material, the thousands of irregularities around pore as well as cracks cause the dispersion and the diffusion of the

acoustic wave. Consequently the incident wave can be divided to back scattered, absorbed and transmitted component. When applying the acousto-ultrasonic approach, the waves propagating in the material are assumed to be large compared with the size of the volume of homogenization (scale at which porosities and cracks are large enough to be considered as defects). This condition allows to neglect the effects of spatial diffusion and dispersion, and to consider only the attenuation effect which can be evaluated by measuring the transmitted component of the signal. In the case of micro- and macro-cracks, the latter will slow down the wave propagation to a greater extent for the same excitation signal, and thus it will attenuate more the measured signal. This lies in the fact that the macro-pores have more opened surfaces, called crack lips, which dissipate the wave through their mechanical vibration. Moreover, it is difficult to say which affect more the signals between micro-cracks or any type of pores, because this always depends on the quantity of open surfaces (free edges). The velocity of sound waves in solids is proportional to the elastic properties of the medium in which they propagate. In Table 2-2, it was mentioned that the Young modulus of the anode material varies between 7000-11000 MPa, and the anode density varies between 1560-1610 $Kg.m^{-3}$, and the Poisson ratio is about 0.18. The acoustic wave propagation velocity in the anode material calculated using equation 2.1 gives a range of 2100-2800 $m.s^{-1}$.

2.3.5 Excitation and acquisition

In general, the possibility to have several sensor placement configurations (Figure 2-7) is one of the points that make this method versatile. Indeed, the measurements can be performed in three different ways: 1) direct, where the sensors are applied to both sides of the specimen, 2) indirect, where the transmitter is held at a fixed point, the receiver is moved successively at predetermined distances, 3) semi-direct, where the sensors are applied to the perpendicular surfaces. On other hand, the transmitter and receiver must have sufficient bandwidth to excite all the frequencies necessary to examine the material. According to Vary [208], a transducer of 1MHz bandwidth would be adequate to characterize composite and other orthotropic materials. However, in the porous materials the maximum frequency is much less than other orthotropic materials because the high frequency components of the signal, usually above 300 kHz, are completely attenuated in the material. Consequently, the bandwidth is limited on one side by the minimum excitation frequency, which is limited by the wave generator output, and on the other side by the material attenuation. After

preliminary test we limited our frequency bandwidth between 100-300 KHz, which result in wavelength varying between 7-28 mm.

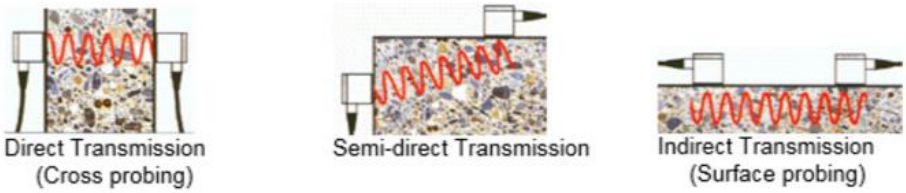

Figure 2-7 Sensors configurations [226].

The sensors must be attached to the specimen using a thin film of a coupling fluid such as a gel, silicone grease or hot glue. It is necessary to apply sufficient pressure against both of sensors to remove the reverberation problems in the coupling as well as the surface roughness problems. The coupling fluid features are very important because they have a significant effect on the amplitude of the detected signal. Hashemi [227] showed the effects of pressure, type of coupling fluid, and film thickness on the wave amplitude changes. The results indicate that, for a given testing frequency, there is an optimal pressure and thickness for a coupling liquid. In addition, the amplitude of the received signal generally increases with an increase in the pressure at the transducer/specimen interface and a decrease in the coupling film thickness. This is certainly due to the fact that the uniformity of the coupling is enhanced, and the air trapped in the coupling is released when pressure is applied. To avoid all these problems, an alternative technique based on solid couplant (i.e., hot glue) was used to test anode parts and blocks.

2.4 Signal analysis

In the case of porous structures, known by their very complex behavior, the selected features calculated from the time series signals must be sensitive and specific to the defects in order to result in high-level identification. These methods must therefore be robust in terms of signal discrimination. Each feature belongs to one of the following three main approaches: temporal, frequency and hybrid (time/frequency) approach. Each of these approaches have its advantages and its limitations, as will be detailed in the following sub-sections.

2.4.1 Temporal approaches

A first analysis of the signals using the temporal method is always desired. According to several studies (mentioned below) that aimed to choose the appropriate treatment for different applications, interesting results can be found through this kind of analysis. These

methods are most often based on waveform recognition techniques that are correlated to some characteristics of the material. Their main advantage lies in the ease of implementation in terms of calculation algorithms.

- **The peak value of the amplitude**

It is an effective and simple tool for extraction of the attenuation characteristics for temporal signals due to propagation distance and interfaces. A real application for homogeneous material was introduced by Wang et al. [153] in analysis of time signals propagated through metal turbine blade with multiple interfaces. It was shown that it is possible to manage the compressed signals via the crest values, which justifies the effectiveness of these descriptors and the interest in its implementation. Another study by Valentin and Pachaud [228], showed how the amplitudes of the temporal signals reflect the nature of the physical mechanisms involved in the degradation of the composite material (epoxy reinforced with carbon fibers). They also established a relation between signal attenuation and cracks parallel to the fibers.

- **Arithmetic mean and standard deviation**

The arithmetic mean of the signal is the sum of numerical values (the sampling points of the signal) divided by their total number:

$$\langle x \rangle = \frac{1}{N} \sum_{1}^{N} x_i \tag{2.3}$$

The mean value of the signal may help detect changes in the wave form symmetry caused by irregularities in the material. As longitudinal waves propagate, the material undergo a series of compression and depression, and as soon as these waves meet the irregularities, their harmonics become asymmetric. In other words, the irregularities such as pores and cracks impose a faster decay of the amplitude (linked either to the compression or the depression) and the harmonics will not remain symmetrical. The addition of the differences between all the harmonics of the same signal results in a mean value that may be different from zero.

Alternatively, weighted averages can also be used as a temporal feature to represent a temporal series (x_i) (vibration or acousto-ultrasonic signals). It is computed as the weighted sum of all the numbers in the time series divided by the sum of their weights:

$$\bar{x} = \frac{\sum_{i=1}^{n} w_i x_i}{\sum_{i=1}^{n} w_i} \tag{2.4}$$

where w_i are the weight of x_i and N is the total number the sampling point s in the signal (i=1…N).

The standard deviation of 1D-signal is defined as follows:

$$\sigma = \sqrt{\frac{1}{N}\sum_{i=1}^{N}(x_i - \bar{x})^2} \tag{2.5}$$

where $\bar{x}$ is the arithmetic mean and N is the total number of time sample points.

In general, combinations of indicators are used instead of individual; i.e., the "crest factor" is the ratio of standard deviation to arithmetic mean. In addition to the defects detection, such combinations can provide additional guidance. For example, Boulenger et al. [229] were able to implement this indicator in real time monitoring of bearings. Indeed, a low value of the crest factor was associated to the existence of a specific damage. Therefore, these combinations of features may be used to characterize the signals gathered from anode blocks.

- **Energy**

This descriptor is frequently used in temporal signals analysis. It represents a whole signal characterization, which minimizes the individual and local effects that are usually not important. The energy of the signal to be analyzed (x_i) is expressed as:

$$E = \sum_{i=1}^{N} \left| x_i \right|^2 \tag{2.6}$$

At first, when analyzing the attenuation characteristics of the signals due to interfaces in synthetic and acrylic bones, Qi [230] found that the energy attenuation is more sensitive than other factors such as the amplitude. Secondly, it has been shown that the energy level of a decomposed signal provides good defect localization in composite materials [231]. The concept of energy reveals different modes of potential failure in the material by discriminating the amount of energy in different frequency bands. In light of this, the implementation of this indicator for capturing internal defects in a porous material seems to

be promising. Furthermore, Wang et al. [153] showed that the energy is an effective tool for evaluating the attenuation due to propagation distance and interfaces through the steel turbine blades by the decomposition of the acoustic signals in different frequency bands. Thus, it was concluded that the energy extraction could have a good chance for giving appropriate results in the case of anode materials.

- **Root mean squares**

The root mean squares (RMS) of temporal series can be written in the following discrete form:

$$RMS = \sqrt{\frac{1}{N}\sum_{i=1}^{N}[x_i]^2} \tag{2.7}$$

According to its mathematical equation the whole energy of the signal is contained in the RMS. It should have at least some, but not all, of energy advantages because there is the possibility to increase the undesirable noise effect. Usually, noise in signal may come from sensors, electrical connections, amplifiers, interfaces or external effects such as machines in industrial environments. The noise caused by the latter is usually difficult to get rid of it, since it is located at low frequency. Other kind of noise can be easily removed using thresholding or filtering methods, since most often the noise is localized at high frequencies. Therefore, in some applications, RMS is not the most effective indicator, but it has retained its place since it is very easy to understand its behavior. In a series of tests, Jokinen and Jantunen [232-233], made a comparison between the RMS and some of the previously presented descriptors during the control of steel drilling tools. Their results showed that the RMS was not always the best descriptor, but still is among the most four effective indicators. It is then highly recommended to investigate the implementation of this feature in carbon anodes inspection.

- **Skewness and Kurtosis**

Skewness and Kurtosis are two dimensionless descriptors. They are expressed in terms of third order and fourth order moments of the signal density distribution, S and K respectively:

$$S = \frac{\frac{1}{N}\sum_{i=1}^{N}(x_i - \bar{x})^3}{\sigma^3} \tag{2.8}$$

$$K = \frac{\frac{1}{N}\sum_{i=1}^{N}(x_i - \bar{x})^4}{\sigma^4} \quad (2.9)$$

where x_i is a measurement provided by the sensor and N is the total number of data points in the time series for this variable.

The success of these parameters is relatively limited in industrial applications. However, they were used by researchers as a baseline for the evaluation of new indicators and typical works [234-235]. Finally, the use of these indicators in active inspection of heterogeneous materials have to be investigated. In addition, simultaneous implementation of several indicators could be more interesting.

2.4.2 Frequency approaches

In order to unveil the properties of a given signal, one alternative is to use a mathematical transformation that allows moving into frequency domain. The majority of the frequency techniques, detailed below, provide an easy detection of defects, but it is not possible to give an indication about the location of these defects in the object. In special cases, such as rotating machines and periodic defects indications that have specific frequency signatures, these techniques offer the possibility of making an effective diagnosis. The different existing frequency descriptors will be presented in the following sub-sections.

- **Fast Fourier Transform**

Fast Fourier Transform (FFT) is a commonly used tool to transform signals and then to detect variations in a frequency domain. By this transformation, it is possible to decompose any temporal function into a sum of sinusoidal basic functions where each of them is defined as a complex exponential of different frequency. This transformation therefore gives a unique way to see any function as the sum of simple sinusoidals. Although the FFT is a simple mathematical tool, its widespread popularity is due to its practical application in a number of fields of science and engineering. The mathematical formulation of FFT is associated with any temporal signal x(t) that produce a function depending on the frequency (f) as follow:

$$X(f) = \int_{-\infty}^{+\infty} x(t)e^{(-j2\pi ft)}dt \quad (2.10)$$

where the Fourier spectrum X(f) is a complex-valued function of frequency, which absolute value |X(f)| represents the amount of that frequency present in the original function, and its complex argument is the phase offset Φ(f) of the basic sinusoid in that frequency:

$$|X(f)| = \sqrt{Re(X(f))^2 + Im(X(f))^2} \quad \text{and} \quad \Phi(f) = -\arctan\left(\frac{Im(X(f))}{Re(X(f))}\right) \tag{2.11}$$

At this point it is important to mention that x(t) and X(f) have the same physical meaning but in different representations. More details for these transformations are available in [236].

The Fourier transform preserves the energy contained in the basic timing signal. Meanwhile we can define the spectra of energy and the spectra of the density of the energy. The latter is commonly used in temporal signal characterization during real applications. This is contrary to the energy spectra, which is used in the case of transient signals. Furthermore, we can define the Discrete Fourier Transform (DFT) that converts a finite sequence of equally-spaced samples of a function into an equivalent-length sequence of equally-spaced samples:

$$X_n = \sum_{i=0}^{N-1} x_i \, e^{-j2\pi \frac{in}{N}} \tag{2.12}$$

where $n \in [0, N-1]$ and X_n represents the sequence of the sampled signal.

The Fourier approach is specifically used to differentiate the signals from each other through their frequency content [237]. In addition, other interesting quantitative analyses were developed in [238-239]. These works were the subject, respectively, of cracks and intergranular cracks detection within steel. They have resulted in some relationships between the event source in the frequency function and crack severities. The major advantage of this transformation is the fast calculation method using specific algorithms. Among others, this transformation introduced a compromise between temporal observation window and frequency resolution. However, it requires dealing with complex mathematical calculations, even for the simplest structures, which needs relatively advanced numerical tools.

- **Frequency Response Functions**

The calculation of frequency response functions (FRF) and other spectral variables involves more specialized notions of signal processing which will not be detailed here. Nevertheless, an overview of different FRF forms will be reported. Considering an input signal x(t) and an output signal y(t) which are corresponding respectively to the excitation force and the response of the structure given by the sensor. We then define:

- The auto-spectra: $S_{XX}=X(f)*X(f)$ and $S_{YY}=Y(f)*Y(f)$, where f is the frequency.
- The cross spectra or inter-spectra : $S_{XY}=X(f)*Y(f)$ and $S_{YX}=Y(f)*X(f)$

The FRF can then be calculated by three different evaluations. Table 2-3 shows the relative definitions and respective benefits:

Table 2-3 The different evaluations of FRFs [336].

Evaluation H1	$\frac{Y(f)}{X(f)} = \frac{S_{yx}}{S_{xx}}$	Minimizes input error
Evaluation H2	$\frac{Y(f)}{X(f)} = \frac{S_{yy}}{S_{yx}}$	Minimizes output error
Evaluation Hv	Eigenvector associated with the smallest eigenvalue of the matrix: $\begin{bmatrix} S_{xx} & S_{xy} \\ S_{yx} & S_{yy} \end{bmatrix}$	Minimizes the overall error in the least squares sense

The most frequently used evaluation is H1. A different choice should be based on considerations related to noise on the inputs and outputs. Although the Hv evaluation is more time consuming, it is much more accurate, which may compromise the real time calculation of FRF calculated on the given signals. However, these techniques are not effective for defects characterization of some porous materials such as concrete [240]. It is more pronounced when the defects dimensions are very small compared to the object size since these defects cause minor variations in FRFs. Furthermore, the temporal information is completely lost. In addition, this indicator needs an instrumented measurement tool as well as an instrumented excitation tool to measure both of input and output signals.

- **Resonant frequencies**

The resonant frequency determination technique has been applied in the field of heterogeneous materials such as refractory products [241]. Most applications for this analysis are related to shock excitation rather than continuous vibration. Usually, the energy of the waves dissipates in the form of a vibratory phenomenon through the object. This phenomenon has variable complexity depending on the nature of the impact force and the vibrating body characteristics: i.e., elasticity modulus, weight, shape coefficient and Poisson's ratio. An application of elastic modulus calculation using the resonant frequency was highlighted in [242]. The sample was vibrated at several (n) frequencies and the fundamental resonant frequency N was associated to the natural frequency of the maximum amplitude. The dynamic modulus E_d of elasticity can be obtained from the following formula:

$$E_d = \frac{10^{-7}}{981}.4.L^2.N^2.\rho \qquad (2.13)$$

where E_d is the modulus measured in GPa, L is path length travelled by the wave in cm, N is the frequency in Hz, and ρ is the density in g/cm^3. It is important to notice that, in the case of longitudinal vibrations (i.e., what we measure by our acousto-ultrasonic sensors), the cross-section of the specimen (circular, rectangular, thin or thick) has no influence on the modulus value. However, in other cases such as that of transversal and torsional vibrations the above formula would include information about the shape of the sample [347]. Two methods exist for determining the resonant frequency N of an object:

- ✓ Detecting the maximum amplitude of vibration by continuous change of the excitation frequency.
- ✓ Measuring the natural frequency of the sample after several excitation pulses.

Such a method may not effective enough in the inspection of carbon electrodes since it aims at characterizing the whole object at one time.

- **Fine strip analysis**

The frequency resolution is related with the temporal observation window. The proximity of the dynamic signatures of flaws in some applications requires considerable precision in frequency, which is not feasible with conventional analysis methods. However, to solve such a problem we refer to what is called "zoom method", known as Fourier Transform narrowband. This method consists of concentrating the calculation on a small

window. This technique was applied in bearings condition monitoring by Tebec [243]. The whole analysis was conducted through the following steps:

- Multiplying the signal by a complex exponential to translate the signal spectrum around a well-defined frequency.
- Filtering the signal at the band of interest to delete the background noise.
- Resampling of the signal with new durations equal to the width of the band divided by the frequency resolution.
- Interpretation of the new spectrum.

- **Cepstral analysis**

The logarithm of the spectrum of a signal is called the cepstrum. What differs the spectrum of a time signal from its cepstrum is the current variable that represents the quefrency (time) of the latter while it represents the frequency for the spectrum. El-Wardany et al. [244] applied the cepstral method to analysis temporal signals acquired during drilling tool inspection. In this work, the peak of quefrency indicates the presence of defect in the tool.

2.4.3 Time-frequency approaches

The time/frequency methods are increasingly used in the NDT field, especially in time signal processing. These methods have the benefits of the methods mentioned earlier and provide additional advantages.

- **Wavelet transform**

A wavelet is a finite length wave that represents any temporal function or signal by a weighted sum of translated and dilated wavelets. This transformation is similar to time-frequency domain filter, which is defined by some parameters such as translation, dilation and scaling. Indeed, the local extraction of singularities is possible by locally analyzing the signal, as it has been applied to the identification of cracks in the elastic plates in [245]. The wavelet transform allows the evaluation of defect severity and its location since it is possible to decompose a signal into multiple sub-signals. Among these indicators, changes in the spatial response determines the location of defects and changes in values of the wavelet coefficients reflects defects quantity and sizes. The major advantage of these transforms is

that they perform not only the frequency decomposition, like FFT and DFT, but also the time domain decomposition. Three main wavelet families exist: the Continuous Wavelet Transform (CWT) [250, 251], the Discrete Wavelet Transform (DWT) [246-247], and the Wavelet Packet Transform (WPT) [248, 249]. Each of these transforms offers a different advantage. The CWT and WPT perform complete decomposition, level by level, of a signal but DWT focuses mainly on relatively low frequency bands. The choice of any transform depends on the application. Generally, DWT is recommended for detecting large defects while the other two transforms are recommended for rigorous inspections. For this reason, this type of wavelet (DWT) is exploited in the coming chapters to analyze the signals acquired through the anodes. This will have a very good asset, especially, with the presence of highly attenuated signals that are containing a significant level of noise caused by the scattered waves. These wavelets will thus serve to filter the signals while keeping the essential temporal variable.

Then, in this work, the representative frequency band is obtained by decomposing the acousto-ultrasonic signal into different wavelet levels. Each wavelet level corresponds to a certain frequency band.

The WT of the function X(t) is defined as follows [150]:

$$X_w(a,b) = \frac{1}{\sqrt{a}} \int_{-\infty}^{\infty} h^*\left(\frac{t-b}{a}\right) x(t)dt \qquad (2.14)$$

where h(t) is the mother wavelet, $h^*(t)$ its complex conjugate, a is the first scale parameter that is controlling the dilatation and contraction, and b is the second parameter for translation control. For large value of a, the wavelet becomes a stretched version of the mother wavelet that is a low frequency function while for small a, it becomes a contracted wavelet, that is a short high frequency function. There are several good mother wavelet for the purpose of engineering applications. However, three representative WTs, Daubechies, symlet and coiflet were investigated, and better results were obtained with the Daubechies wavelet. This wavelet is based on the Haar function.

$$f(t) = 1 \qquad 0 < t < 1 \qquad (2.15)$$

A weighted sum of Eq. (2.15), called the scaling function of the wavelet, is given by

$$f_j(t) = \sum_{k=0}^{N-1} c_k f_{j-1}(2t - k) \tag{2.16}$$

This equation defines an iterative procedure to determine the scaling functions of the Daubechies wavelets.

The time-frequency duality is always limited. Therefore, the simultaneous optimization of the frequency resolution and the time resolution is impossible since they are negatively correlated. Finally, to apply these analytical approaches, it is therefore obvious to have multi-frequency signals. For this reason, it is important to excite the material under a wide frequency band.

2.5 Computed tomography method

2.5.1 Principle of the method

Computed tomography (CT), or the well-known CT-Scan technique, is a recent 3D analytical technique, which provides sophisticated images based on X-ray absorption coefficients of any material [79, 188]. It can provide a powerful non-destructive evaluation (NDE) by means of producing 2-D and 3-D cross-sectional images of an object from flat X-ray images where the resolution is linearly proportional to the object size. When the sample is considered a multi-material whose constituents absorb X-rays at various percentages, the object images can be extracted by segmentation. The resolution of the images is however limited by the apparatus technology. The object have to be placed between an imaging system and radiation source where one of them have to be turntable. Like a film radiograph, 2-dimensional shadowgraph images can be produced by the imaging system and a software produces cross-sectional images of the object.

2.5.2 X-Ray computed tomography data acquisition

X-ray images were obtained using a Somatom Sensation 64 located at INRS-ETE research Centre in Quebec City (Figure 2-8). The CT method has one main advantage that overcomes some limitations; it does not damage or destruct the object and thus it preserves the internal structure of the material, which is mandatory when further tests have to be carried out. On the other hand, the Siemens Somatom Sensation 64 was designed for the human body and consequently was too small for industrial anodes. For this reason, it was necessary to slice the anode block. In order to obtain good contrast between defects and background (carbon), image resolution had to be adapted to the object size [151]. The final

resolution was 0.7 × 0.6 × 0.7 mm^3 where the thickness of voxels (volumetric pixels) was 0.7 mm.

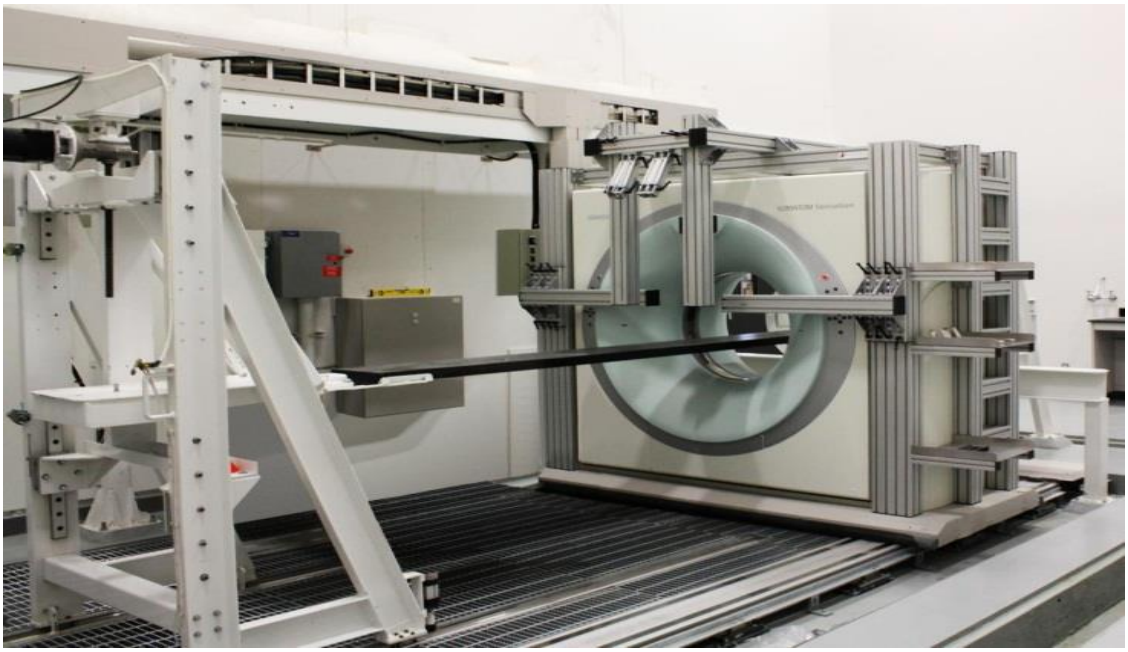

Figure 2-8 INRS-ETE Siemens Somatom Sensation 64 (Courtesy of INRS-ETE).

The CT-scan apparatus provides a 3D matrix of pixels with attenuation coefficients, varying between 1024 and 3071 HU. The attenuation coefficients are converted to grayscale images since they are correlated to the local density of the sample, as we can see in Figure 2-9 left [188, 252]. The voids (i.e., cracks and pores) inside the anode sample correspond to groups of dark pixels surrounded by lighter background (Figure 2-9 right). The dense impurities (e.g. cast iron contamination) correspond to the few brighter pixels.

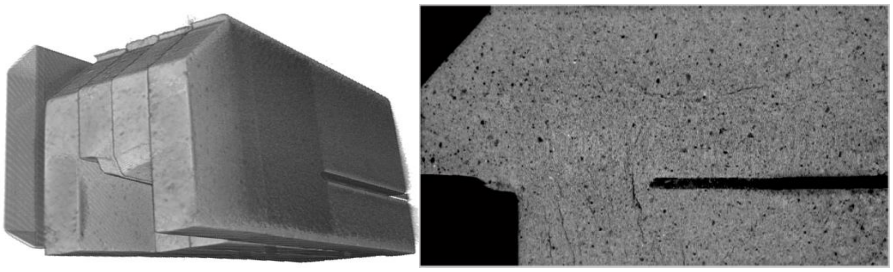

Figure 2-9 The appearance of the obtained images: left, 3D-image of four different slices. Right, 2D-cross sectional image.

2.6 Image texture analysis

Several image processing techniques are available for defects detection and have been summarized in a review paper [99]. Three tools are widely employed for variability

detection in images. a) Fourier transform, which breaks up a signal into an alternant representation, characterized by sine and cosine. b) Gabor transform which is a type of short-time Fourier transform that uses a window function to determine the sinusoidal frequency and the phase content of local sections of signal. c) Wavelet transform, which breaks up a signal into multi-resolution bands in form of shifted and scaled versions of the original (or mother) wavelet.

The wavelet transform method is preferred over the Fourier transform, since it provides better spatial localization, and over the Gabor transform since it can maintain good space and frequency localization [253]. In addition, wavelet textural analysis has shown a better performance than the above mentioned methods in several applications [254-256]. Such advanced signal processing method is now considered as state of the art in the literature. However, it requires a deeper understanding of the designer parameters such as mother wavelets and their order, decomposition level, and wavelet shapes. It will help selecting the most suitable parameters since they vary from one application to others [257-261]. These works have shown that the selection of the design parameters is critical in the case of detecting local characteristics but is less important when just an overall textural characteristic of the entire image is required. Wavelet coefficients can be considered as correlation coefficients between raw images and a wavelet filter. Consequently, the good design of these coefficients can improve the textural analysis performances [256, 262].

The 2D-wavelet transform performs an image decomposition into multiresolution bands. At each decomposition level, the resulted image is decomposed into four sub-band images: horizontal detail, vertical detail, diagonal detail, and approximation that will be decomposed in the next level and so on. The raw image is considered as the approximation at the first scale. The wavelet coefficients resulting from this decomposition consists of sets of so-called detail coefficients obtained in three directions (horizontal, vertical and diagonal) at each decomposition level, and a final set of approximation coefficients containing low frequency information. As for 1D signals, there are three main wavelet transform methods; DWT, WPT, and CWT. All of these three wavelet transforms have been implemented in various applications, and for each application one of them seems more effective than others. CWT, like other rational wavelet analysis methods, does not favor any spatial range and this can induce a lack of consistency in some image characterization approaches. DWT can overcome this drawback since it privileges the low frequency components. Consequently, for the case of the carbon anode material where cracks identification is required, the discrete

wavelet can be directly pointed out. However, some numerical algorithms can improve the performance of WPT over that of DWT [231]. After some preliminary analysis, the DWT based approach was selected to extract the textural features of the CT-Scan images in this work (chapter 4).

This approach needs first to select a wavelet function (i.e., mother wavelet), several of which are introduced in the literature [263-265]. The selection of specified functions is highly dependent on the application, where their pixel-to-pixel characteristics and similarity in a given direction are the main selection parameters. Daubechies and Symlet wavelets are two numerical functions usually noted as Db and Sym, respectively. These functions were chosen for their orthonormality (no overlap in frequency bands), their resemblance to CT-scan images, and the fact that they overcome the problem of discontinuities with continuous derivatives. At this point, it can be said that the wavelet function has the capability to expand for capturing coarse textures at low frequency or to shrink for capturing fine textures at high frequency. For this reason, wavelet transform is often referred into a high-pass or low-pass filtering approach. Consequently, the 2D-signal is separated to vertical, horizontal, and diagonal textural variations when it is convoluted with Db or Sym that are represented by three detail sub-images named D_j^v, D_j^h and D_j^d, respectively, at j^{th} decomposition level. Several statistical indicators can be calculated through the sub-images e.g., energy, variance, entropy, and mean [254, 266]. In this work, energy was found to be sufficient to effectively quantify the majority of image textures for the three directions and all decomposition levels. The sub-image energy is defined as follows:

$$E_j^k = \frac{\sum_{x=1}^{x}\sum_{y=1}^{y}\left|D_j^k(x,y)\right|^2}{xy} \tag{2.17}$$

where D is the detail component image that includes x*y pixels, obtained in k directions (v, h and d) and at the j^{th} decomposition level. In the framework of normalization, each energy component is divided by the original image size (x*y). At this point, it is important to mention that for each anode slice, inspected by CT-scan, 100 successive images were collected. The sum of the energy values for the three directions for each image was calculated.

2.7 Latent variable methods

Latent variable methods (LVMs) consist of a family of multivariate statistical approaches used for analyzing large datasets. They are widely used in the chemometrics

literature for data clustering and classification [269-270]. The most commonly used LVMs are Principal Component Analysis (PCA) and Projection to Latent Structure (PLS) [271-272]. Briefly, PCA and PLS project a multivariate dataset from a high dimensional space to a lower dimensional space, allowing to visualize and interpret the information contained in Big Data. These methods have been used in materials inspection based on acoustic features [282-283] as well as on vibration features [284-286] and very interesting results have been obtained. In addition, some authors [273-274, 282] have combined wavelet analysis with PCA, called Wavelet-PCA, to improve the results of control. In this thesis, a large number of features were computed from the acousto-ultrasonic and vibrational responses of the various materials in order to describe them. It was found that these features were highly collinear. Instead of performing feature selection, it was decided to use all of them together to maximize the chances of detecting and discriminating anode defects. To cope with collinearity, PCA was used to cluster anode parts or anode blocks based on their acousto-ultrasonic and modal responses. Projection to Latent Structures (PLS) regression was also used to correlate acousto-ultrasonic features and textural descriptors collected from corresponding X-ray CT-Scan images. This regression method is known as a strong multivariate statistical method that works better than traditional multiple linear regression (MLR) [275] on highly collinear datasets as is the case in this thesis. Although multivariate and wavelet methods have generally been used to explore data for non-destructive evaluation, there has been little or even no attempt to consider their applications for the intricate cases highlighted in this project.

2.7.1 Principal Component Analysis (PCA)

PCA is a widely used multivariate statistical method for the analysis of large datasets containing noisy and highly collinear data. Assume a data matrix **X** (I×J) containing J measurements collected from I samples. Furthermore, assume that both systematic variations and noise are present in this data. PCA decomposes the variance structure of **X** by finding a small number of orthogonal latent variables A <<< J capturing most of the systematic variations in **X**, but leaving noise or irrelevant information as residuals. These latent variables (also called components) are defined as linear combinations of the J original measurements and together define a lower dimensional subspace allowing easy visualization and interpretation of the information contained in large datasets.

The PCA decomposition is expressed mathematically as shown below [276].

$$\mathbf{X} = \sum_{a=1}^{A} \mathbf{t}_a \mathbf{p}_a^T + \mathbf{E} \tag{2.18}$$

where the orthogonal vectors $\mathbf{t_a}$ (I×1) are those latent variables (called scores) providing the coordinates of each sample in the low dimensional subspace (plane or hyperplane) after projection. The subspace itself is defined by A orthonormal loading vectors $\mathbf{p_a}$ (J×1), which are defined as a linear combination of the original variables (i.e., $\mathbf{t_a} = \mathbf{X}\ \mathbf{p_a}$). The projection residuals are collected in the residual matrix **E** (I×J). The loading vectors are calculated in such a way that $\mathbf{t_1}$ explains the greatest amount of variance in **X**, $\mathbf{t_2}$ the second greatest amount of variance that not explained by the first component, and so on. The cross-validation procedure is typically used to select the sufficient number of principal components.

2.7.2 Projection to latent structures (PLS)

PLS is one of the powerful multivariate statistical methods that can correlate the signal features of the anode samples gathered in matrix **X** with corresponding image textural features collected in a second matrix **Y** consisting of H variables and I observations. This regression method has the advantage to overcome the strong correlation between the columns of both **X** and **Y** while building linear relationships between them. The model based on PLS is used to explore the relationships existing within and in between both datasets, **X** and **Y**. It can be seen as an extension of PCA, but for two sets of data.

As for PCA, the set of constraints ensure that the weight vectors **W** are orthonormal and that latent variables (**t**'s) are orthogonal to each other. The objective for using PLS in this thesis is to relate the acoustic response of anode samples to their microstructural characteristics obtained after applying wavelet texture analysis to X-ray CT-Scan images [272, 277]. The model equations are presented below:

$$\mathbf{X} = \mathbf{T}\mathbf{P}^T + \mathbf{E} \tag{2.19}$$

$$\mathbf{Y} = \mathbf{T}\mathbf{Q}^T + \mathbf{F} \tag{2.20}$$

$$\mathbf{T} = \mathbf{X}\mathbf{W}^* \tag{2.21}$$

$$\mathbf{W}^* = \mathbf{W}(\mathbf{P}^T\mathbf{W})^{-1} \tag{2.22}$$

The common latent variable space of both **X** and **Y** is represented by the scores **T** (I×A). The latter corresponds to the combinations of the **X** variables that are highly correlated

with the **Y** data. The weights of each variable in each component are collected in the weight matrix **W*** (J×A). The **P** (J×A) and **Q** (H×A) matrices contain the loading vectors defining the latent variable spaces of **X** and **Y**, respectively. **E** (I×J) and **F** (I×H) are the PLS model residuals.

2.7.3 Model interpretation tools

PCA and PLS offer many diagnostic tools for helping model interpretation and learning from data. The first two are the scatter plots of the scores (**t**'s) and the loading plot (**p**'s) that are used to visualize respectively relationships between the observations and the variables, and their clustering patterns. Usually, a combination of two latent variables is visualized simultaneously through these tools using 2D scatter plots.

A complementary information to the score space is given by the square prediction errors (SPE) that represent the sum of squares of the residuals (**e**) for any observation [278, 331]. SPE is used to verify how well the model fits each observation and whether outlier data are present. The residual errors for the i^{th} observation is computed by [279]:

$$SPE_i = \sum_{k=1}^{K} e_{ik}^2 \tag{2.23}$$

where K is the number of columns of **X** (N×K).

Contribution metrics are used to diagnose a shift or important change in the data [279]. This parameter is usually calculated between two clusters of observations in a score plot to see how much each variable contributed in the variation. The mathematical formula for the contribution of variable X_k (C_k) to a shift in the score space from group 1 to group 2 is the following:

$$C_k = (X_{k,2} - X_{k,1}) \sqrt{\sum_{a=1}^{A} \left(\frac{t_{a,2} - t_{a,1}}{S_{ta}}\right)^2 p_{k,a}{}^2} \tag{2.24}$$

where $t_{a,1}$ and $t_{a,2}$ represent the average of the score values for group 1 and 2 along the a^{th} component. The variables $X_{k,1}$ and $X_{k,2}$ are the mean values of the k^{th} x-variable calculated for the first and second group of data, respectively. Index *a* identifies the component number, S_{ta} is the standard deviation of the a^{th} score, and p_{ka} is the loading value for the k^{th} x-variable in the a^{th} component. In general, a higher contribution for one variable means that this variable has an important contribution in the change according to the given direction.

The Hotelling's T^2 represents how far an observation is from the origin of a score plot. It can also be used for detecting outliers in the LV space. It is calculated as follows [280]:

$$T_i^2 = \sum_{a=1}^{A} \frac{t_{ia}^2}{S_{ta}^2} \tag{2.25}$$

where S_a^2 is the variance of $\mathbf{t}_a$ in the PCA model, A is the total number of latent variables, and t_{ia} is the score value of observation i for a^{th} latent variable. The T^2 can be used to define a control region in a latent variable space where the outliers are found outside the confidence interval that is usually drawn at 95% of the variation.

Another parameter, which can summarize the importance of the variables in a PLS model, for **X** and **Y** simultaneously, is named variable importance on the projection (VIP) [281] and is defined as:

$$VIP_{j,A} = \sqrt{\frac{J\sum_{a=1}^{A} W_{j,a}^2 \; SS_Y(a)}{SS_Y(A)}} \tag{2.26}$$

where $W_{j,a}$ is the weight of the j^{th} X-variable in the a^{th} PLS latent variable, $SS_Y(a)$ is the sum of squares of **Y** explained by the a^{th} LV of the PLS model and $SS_Y(A)$ is the total sum of squares of **Y** explained by the model. Otherwise, the VIP is a weighted sum of squares of the PLS weights where the variables having a VIP larger than 1 are the most influential in the model [278, 331]. Finally, the ProMV software version 15.08 (ProSensus, Ancaster, ON, Canada) was used to build PCA and PLS models.

2.8 Anode parts and blocks

A full size baked anode, manufactured at the Alcoa Deschambault smelter located in Quebec - Canada (ADQ), was used for investigating the acousto-ultrasonic technique. The anode was first sliced and scanned using computed X-ray tomography (CT-scan) to reveal its internal structure. The anode block was carefully sliced since the scanning area of the X-ray apparatus (Siemens Somatom Sensation 64) was designed for the human body and consequently was too small for the anode (Figure 2-8). It was first cut into 26 slices of equal thickness along its length and then each slice was cut further in half along the height of the anode. A total of 52 half slices were finally obtained as we presented in Figure 2-10. It is known that spatial distribution of anode density, mainly due to the random distribution of

pores and cracks, within the block is non-uniform. In addition, the internal structure at both ends of the anodes as well as below and between the stub holes are expected to be systematically different. The top and the bottom of each slice were also cut prior to collecting the acousto-ultasonic measurements in order to keep a unique height and standardize the geometry of all slices to be selected (Figure 2-11).

Several slices were selected in different positions according to the special needs of different tests. Finally, each of them was divided into 6 corridors along the sample height, as shown again in Figure 2-11. These corridors of equal width were marked using a white chalk. They were numbered from 1 to 6 where corridor 1 corresponds to the anode center and the last corridor is close to the outer surface.

Figure 2-10 Baked anode after slicing.

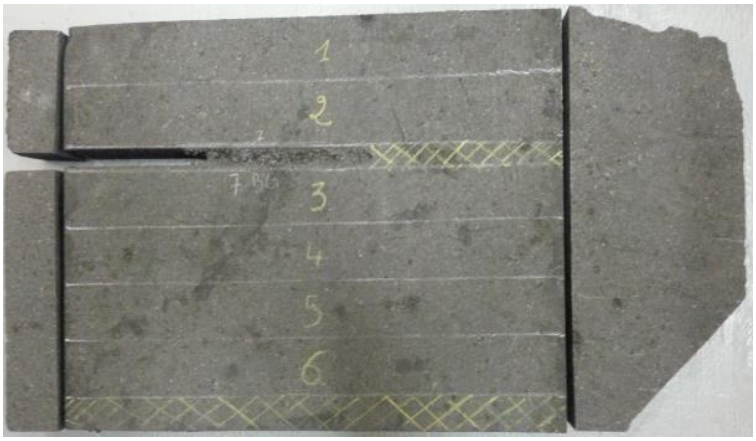

Figure 2-11 Preparation of six corridors after removing top and bottom.

An additional set of 27 full size baked anodes manufactured at ADQ smelter were selected in order to validate the robustness of the proposed approaches and paving the way

for the online control. Defect-free anodes as well as anodes holding different types of defects are required for this demonstration. Since it is difficult to assess non-destructively whether an anode contains internal defects or not, it was decided to select the anodes according to the following plan:

- Anodes produced under different conditions: some under normal operation and some others during paste plant start-up;
- Anodes containing open (visible from the surface) transversal and longitudinal cracks;
- Anodes holding surface defects due either to intensive baking or to handling.

The majority of the selected anodes had no externally visible defects. These anodes were numbered from A1 to A27. Table 2-4 shows which anodes were assigned to each of the previously mentioned categories.

Table 2-4 Anode numbers and description.

Anode numbers	Description
1, 4, 5, 6, 10, 11, 16, 17, 18, 19, 20, 21, 22, 23, 24, 25, 26, 27	Free of external defects
2, 3, 7	Cracks visible externally
8, 12, 13	Surface defects
14, 15	Start-up anodes

Some examples of these anodes are shown in Figure 2-12. Anode A1 had no externally visible defects, A2, A3 and A7 had large cracks visible on the surface, and A8, A12 and A13 had different types of surface defects.

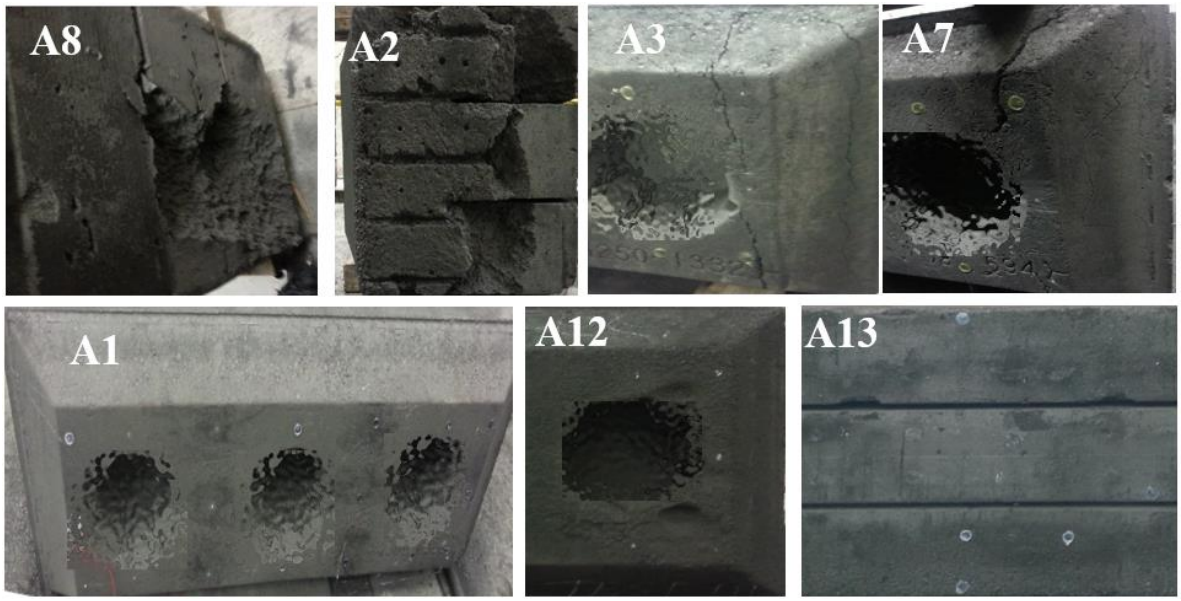

Figure 2-12 Some examples of the selected anodes with various defects.

Chapter 3 The potential of acousto-ultrasonic techniques for inspection of baked carbon anodes

Résumé

Les anodes de carbone cuites contribuent à la performance optimale des cellules de réduction en aluminium. Cependant, la qualité actuellement décroissante et la variabilité croissante des matières premières anodiques (coke et brai) rendent difficile la fabrication des anodes avec une qualité globale constante. L'interception d'anodes défectueuses (comportant beaucoup de fissures et de pores) avant leur installation dans des cellules de réduction dont ils risquent de détériorer la performance est donc importante. C'est une tâche difficile, même dans des usines modernes d'anodes et bien instrumentées, car les essais en laboratoire utilisant des échantillons (carottes) ne peuvent caractériser qu'une faible proportion des anodes produites en raison du coût, du temps et de la nature destructive des méthodes analytiques. De plus, ces résultats ne sont pas nécessairement représentatifs du bloc d'anode entier. L'objectif de ce travail est de développer une méthode rapide et non destructive pour le contrôle de la qualité des anodes cuites en utilisant des techniques acousto-ultrasoniques (AU). Les réponses acoustiques des échantillons d'anodes (tranches) ont été analysées à l'aide d'une combinaison des indicateurs temporels calculés à partir des signaux AU et de l'analyse des composantes principales (PCA). Les signaux AU ont été trouvés sensibles aux pores et aux fissures et ont été capables de discriminer les deux types de défauts. Les résultats ont été validés qualitativement en soumettant les échantillons à la tomographie à rayons X.

Abstract

High quality baked carbon anodes contribute to the optimal performance of aluminium reduction cells. However, the currently decreasing quality and increasing variability of anode raw materials (coke and pitch) make it challenging to manufacture the anodes with consistent overall quality. Intercepting faulty anodes (e.g., presence of cracks and pores) before they are set in reduction cells and deteriorate their performance is therefore important. This is a difficult task, even in modern and well-instrumented anode plants, because lab testing using core samples can only characterize a small proportion of the anode production due to the costly, time-consuming, and destructive nature of the analytical methods. In addition, these results are not necessarily representative of the whole anode block. The objective of this work is to develop a rapid and non-destructive method for quality control of baked anodes using acousto-ultrasonic (AU) techniques. The acoustic responses of anode samples (sliced sections) were analyzed using a combination of temporal features computed from AU signals and principal component analysis (PCA). The AU signals were found sensitive to pores and cracks and were able to discriminate the two types of defects. The results were validated qualitatively by submitting the samples to X-ray Computed Tomography (CT scan).

Keywords: baked carbon anode; non-destructive testing; acousto-ultrasonics; principal component analysis (PCA); primary aluminium smelting

M. Ben Boubaker, D. Picard, J. Tessier, H. Alamdari, M. Fafard and C. Duchesne , The Potential of Acousto-Ultrasonic Techniques for Inspection of Baked Carbon Anodes, Metals, Vol. 6 (7), 151, (2016), pp. 1-13.

3.1 Introduction

The currently decreasing quality and increasing variability of anode raw materials (coke and pitch) make it challenging to manufacture the anodes with consistent overall quality. Intercepting faulty anodes before they are set in reduction cells and deteriorate their performance (i.e., energy consumption and efficiency) requires testing all or the majority of the manufactured anodes. However, even in modern and well-instrumented anode manufacturing plants, the traditional lab inspection strategy based on core sampling can, at best, evaluate the properties of about 1% of the manufactured anodes due to the costly, time-consuming, and destructive nature of the analytical methods. In addition, the core sample properties are typically available after the anode is set in the reduction cells due to the long lab delays. For economical and logistics reasons, it is generally not possible to improve the rate of anode testing by increasing the lab workload. Furthermore, the properties obtained from core samples are not necessarily representative of the whole anode block, as reported by Sinclair and Sadler [69,74], who provide a complete list of issues related to the use of core samples for quality control and decision-making. Indeed, anode blocks are heterogeneous materials that may contain different types of internal defects (i.e., coke particles not penetrated by pitch, regions of high/low pitch concentration, pores and cracks) which can lead to the anisotropic distribution of properties within the block. The current strategy may completely miss these defects if the core is not sampled where the defects are located. Hence, the mechanical properties and electrical resistivity obtained from core samples may only reflect localized properties. Therefore, rapid and non-destructive techniques to inspect anode blocks should be investigated in order to provide a better picture of the anode quality in a timely fashion. This would allow anode sorting strategies to be put in place and feedback-corrective adjustments to be implemented on the paste plant and baking furnace operation parameters.

Recent research efforts were focused on developing systems for measuring the anode resistivity distribution online based on the work of Seger [112,113] and/or Haldemann and Fawzi [116]. For example, a device called MIREA (*Mesure Instantanée de la Résistivité Électrique Anodique*) was proposed to measure the anodic electrical resistance [114,115]. Basically, an electrical current entering by the stub holes is passed through the anode in a similar way to if the anode was rodded while several voltage drop measurements are collected at different locations on the anode surface. A numerical model of the anode is then used together with the voltage drop measurements to estimate the anode resistivity

distribution. Alternatively, the resistivity distribution can be measured using an array of electrical contact points placed at the top and bottom of the anode and by measuring the voltage drop at each of these points [119,295]. In addition to providing resistivity measurements, these systems should allow detecting the presence of defects within the anodes since damage within the carbon block should, in principle, disturb the electrical current distribution. However, their ability to discriminate between different types of defects (e.g., pores vs. cracks) has not been demonstrated.

Alternatively, the internal structure of the anodes could be inspected by acousto-ultrasonic (AU) techniques. These non-destructive methods have been widely used in the inspection of composite materials, such as concrete and refractories [296-298]. However, applications of AU for testing complex porous materials naturally containing pores and cracks, such as baked carbon anodes, are not as common as for denser materials such as parts made of metal alloys or highly graphitized carbon materials, which are expected to be free of internal voids. The main issue with the anodes is separating defects affecting their performance in the reduction cells from the internal porosity, which is always present, when both types of voids attenuate the acoustic waves propagating through the materials. The only publicly available reports on the application of acoustic methods on carbon electrodes appear to be those of Allaire [299] and Allaire et al. [300] using the SonicByte™ system [301]. Their work mainly focused on measuring the elastic properties of refractory and carbonaceous materials as a means of detecting defects. Although this technique may help identify faulty anodes, it only provides an estimate of the overall material properties. Inspecting the anode block at different positions should provide more information about the distribution of pores and cracks within the volume, and provide a clearer diagnostic. This is essential for taking appropriate corrective actions on the anode manufacturing plant operations. In addition to detecting and discriminating the internal anode defects, the AU signals could provide measurements of the anode density distribution, which is complementary information to electrical resistivity measurements.

The objective of this work is to investigate the sensitivity of the acousto-ultrasonic techniques to defects within the internal structure of carbon anode materials. It focuses especially on the detection and identification of two types of internal voids, namely pores and cracks, using the attenuated acoustic signal propagating through the material. To prove the concept, a baked anode was sliced along its length and analyzed by X-ray Computed Tomography (CT scan) to reveal its internal structure [80]. Acoustic excitation waves at

different frequencies were sent through the materials and the attenuated signals were measured at different positions on a certain number of slices. Several features were computed from the AU signals and collected in a data matrix, which was then analyzed using principal component analysis (PCA) [277]. The clustering patterns obtained in the PCA score space suggest that the proposed approach is sensitive to the concentration of pores and the presence of cracks, and that both types of voids can be distinguished. The results were validated qualitatively using CT scan images.

The paper is organized as follows. The experimental details about the acoustic inspection set-up as well as the baked anode samples are presented first. The methods used for processing and analyzing the acoustic signals are then described. The results obtained with the proposed approach are presented and discussed. Finally, some conclusions are drawn.

3.2 Experimental

3.2.1 Acoustic Inspection System

An overview of the AU signal measurement system is shown in Figure 3-1. Signal conditioning was performed by pre-amplifiers. The conditioned signal (with an amplification gain of 40 dB) was sent to the main data-acquisition board in which the AU waveforms and parameters were stored.

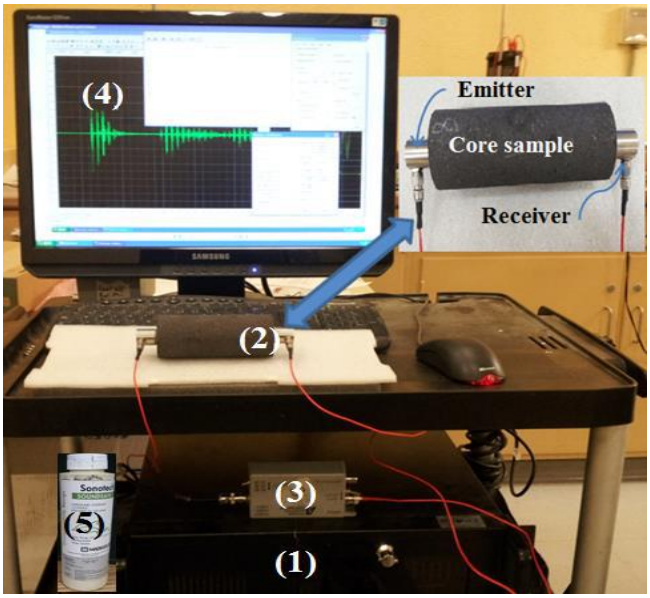

Figure 3-1 The acoustic inspection system. (1) multi-channel acoustic emission system, (2) acoustic sensors, (3) pre-amplifier, (4) AEwin™ software, (5) coupling gel.

The system is composed of four Physical Acoustics™ (PAC) hardware components (MISTRAS Group Inc.: Princeton Jct., New-Jersey, USA). The components are identified directly within Figure 3-1 and are also listed below:

(1) PAC SAMOS™ multi-channel acoustic inspection system consisting of four 16-bit PCI-8 boards, including a 1-MHz analog-digital converter on each channel.

(2) PAC R6-α resonant transducers (bandwidth 10 kHz–1 MHz, resonant frequency at 55 kHz, 15 mm Ø).

(3) PAC model 2/4/6 pre-amplifier (10 kHz–2 MHz).

(4) PAC application software AEwin™ (Physical Acoustics, version E3.41, Princeton Jct., New-Jersey, USA , 2008) for SAMOS™.

Acoustic coupling (gel type) was also used to ensure a good contact between the acoustic sensors and the baked anode samples (number 5 in Figure 3-1). Note that an anode core sample is shown in this figure (Figure 3-1) for illustration purpose only.

3.2.2 Baked Anode Samples

A full-scale baked anode manufactured at the Alcoa Deschambault smelter located in Quebec, Canada (ADQ), was used in this work. The anode was first scanned using computed X-ray tomography (CT scan) to reveal its internal structure [80]. This imaging technique is non-destructive in nature, but it is expensive to purchase and operate, and the data analysis is too time-consuming to be used for routine anode inspection at the plant. Hence, the CT scan images were used to qualitatively validate that the variations observed in the attenuated acoustic signals were associated with pores and cracks. The baked anode was sliced prior to imaging because the available instrument could not take samples as large as an anode. It was first cut into 26 slices of equal thickness along it length as shown in Figure 3-2a, and then each slice was cut further in halves along the height of the anode (see Figure 3-2b). A total of eight slices were selected for collecting the acoustic signals. These correspond to slices numbered 2, 3, 5, 7, 11, 15, 24, and 25 identified in red in Figure 3-2a. They were selected in such a way to obtain a representative sampling of the internal structure of the anode. The slices were selected at both ends of the anode as well as below and between the stub holes. It is well known in the field that spatial distribution of anode density, pore and crack concentration within the block is non-uniform, and that the internal structure at both ends of the anodes, below and between the stub-holes are expected to be systematically different. Note that the top and bottom of each half slice were also cut prior

to collecting the acoustic measurements to obtain samples of even height and to standardize the sample geometry for all the selected slices (see Figure 3-2b). Finally, each sample was divided (virtually) into six corridors along the sample height as shown again in Figure 3-2b. These corridors of equal width were delimited using a white chalk. They were numbered 1 to 6 from the center of the anode toward its outer surface.

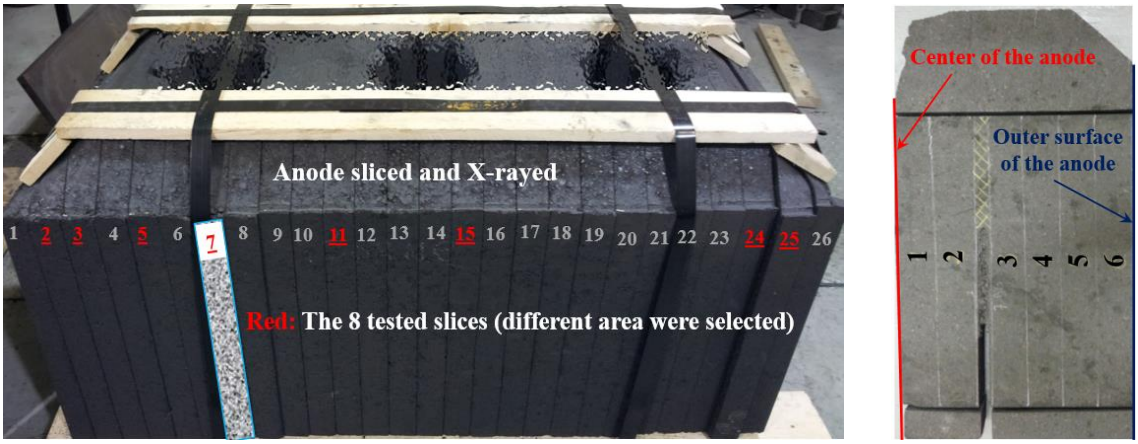

(**a**) (**b**)

Figure 3-2 The sliced baked anode. (**a**): The selected eight slices are identified in red; (**b**): Example of the seventh slice used for acoustic testing.

An example CT scan image is shown in Figure 3-3 for slice number 7. The numbers within the image identify the six corridors drawn on the slices, in the same order as discussed previously (1 is at the center of the anode and 6 is close to the outer surface). The image clearly shows the pores and cracks, and regions of different densities (proportional to gray level intensities).

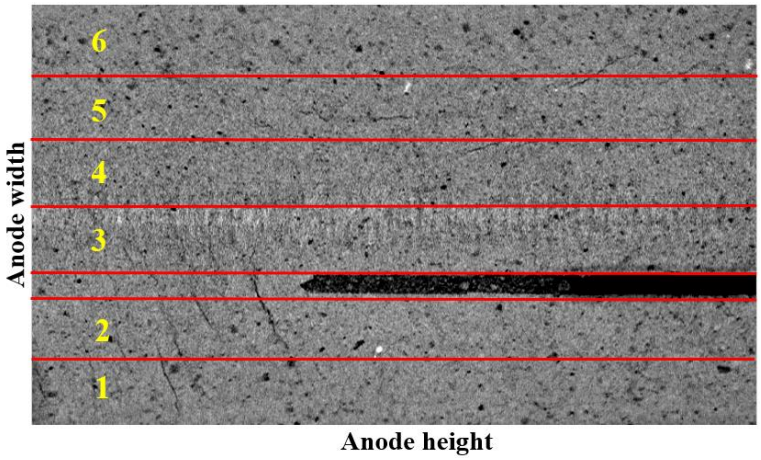

Figure 3-3 Example X-ray Computed Tomography (CT scan) image obtained for slice number 7. The 6 corridors within the slice are virtually divided by red lines and are identified by numbers 1-6. The black region correspond to one of the anode slot.

3.2.3 Acoustic Inspection Data Collection

The acoustic sensors were mounted and put into close contact with the samples as shown in Figure 3-4. Both sensors (emitter and receiver) were positioned at both ends of a given corridor within a slice. They were maintained into position using a clamping device. The interfaces between the sensors and the material were filled with coupling gel in order to maintain appropriate signal transmission. The material in each corridor was then submitted sequentially to seven different excitation frequencies (100, 130, 150, 170, 200, 230, and 250 kHz) while recording the attenuated acoustic signals. This procedure was repeated for each of the 6 corridors and for the 8 anode slices. In addition, preliminary work (not shown) has established that 250 kHz is the maximum excitation frequency for this material because the acoustic signal was found to be completely attenuated at higher frequencies. The data collection strategy was found to be repeatable and it was not necessary to average several raw signals to reduce measurement errors. The sample surface quality was similar for most samples. It is therefore considered that the signal attenuation is mainly due to the material properties and voids (pores, cracks) and the effect of surface quality is negligible.

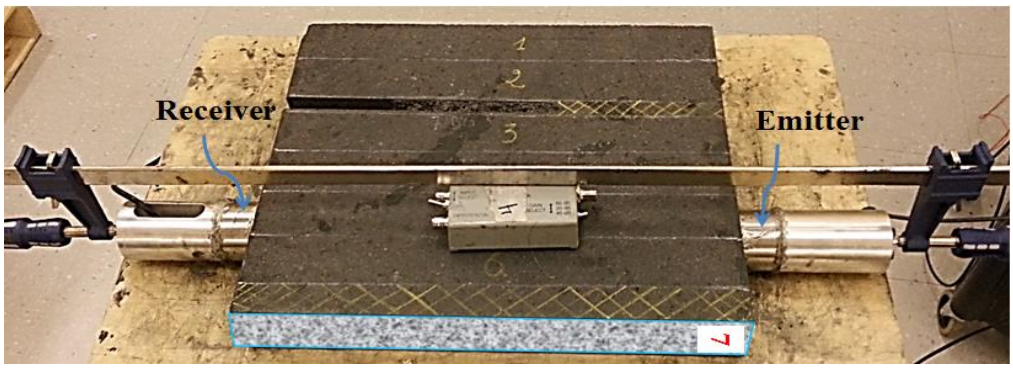

Figure 3-4 Acoustic data acquisition set up through different corridors of an anode slice. The corridors are identified by numbers in the figure.

Some of the acoustic signals acquired at different frequencies on a particular corridor are shown in Figure 3-5 for illustration purpose. The signal attenuation pattern clearly changes as a function of the excitation frequency. According to mechanical wave propagation theory [303-305], there is a relationship between the attenuation at a given frequency and the size of the voids inside a material. Higher frequency waves are attenuated by smaller voids compared to lower frequency waves. Hence, exciting the material at different frequencies should help detect variations in void sizes within the material.

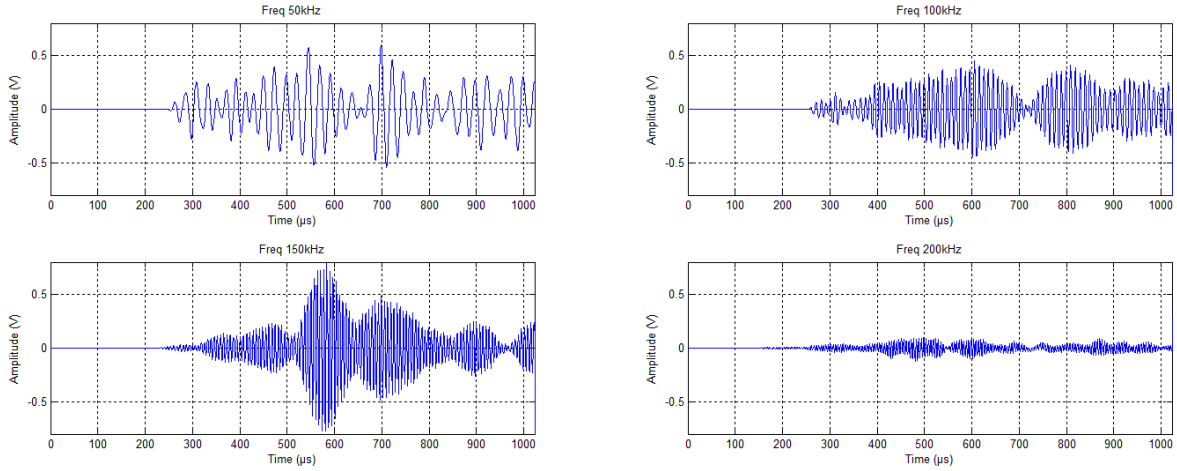

Figure 3-5 Examples of raw acoustic signals acquired at different excitation frequencies.

3.3 Acoustic Signal Processing and Analysis

3.3.1 Acoustic Features Extraction

Waveform processing of acoustic signals has routinely been used for detecting defects in materials. The acoustic wave propagating through the material attenuates at defects and discontinuities such as voids, cracks and inclusions. Hence, efficient techniques for acoustic signal analysis should allow distinguishing materials with and without defects. Although direct analysis of all the raw signals could be performed using, for example, unsupervised clustering techniques such as principal component analysis (PCA) [282], it was instead decided to compute a small number of commonly used temporal features from each attenuated acoustic signal in order to reduce the size of the dataset to be analyzed and facilitate interpretation of the results. Indeed, a total of seven signals were collected from the material contained in each corridor (one for each excitation frequency), and one such raw signal is formed by several thousands of data points. The following commonly used time domain scalar attenuation features were therefore computed from each raw attenuated acoustic signal [307]: the maximum (MAX), mean, standard deviation (STD), energy (E), root mean square (RMS), skewness (S) and kurtosis (K) of the signal time series *x*(i), i = 1, 2, …N:

$$MAX = \max_{i=1}^{N} x(i) \tag{3.1}$$

$$\text{Mean} = \bar{x} = \frac{1}{N}\sum_{i=1}^{N} x(i) \tag{3.2}$$

$$\text{STD} = \sqrt{\frac{1}{N}\sum_{i=1}^{N} (x(i) - \bar{x})^2} \tag{3.3}$$

$$E = \sum_{i=1}^{N} \left| x(i) \right|^2 \tag{3.4}$$

$$\text{RMS} = \sqrt{\frac{1}{N}\sum_{i=1}^{N} [x(i)]^2} \tag{3.5}$$

$$S = \frac{\frac{1}{N}\sum_{i=1}^{N} (x(i) - \bar{x})^3}{\text{STD}^3} \tag{3.6}$$

$$K = \frac{\frac{1}{N}\sum_{i=1}^{N} (x(i) - \bar{x})^4}{\text{STD}^4} \tag{3.7}$$

where *N* is the total number of data points in the signal time series (same for all signals collected in this work). Signal processing was performed using Matlab version R2014a (MathWorks, Natick, MA, USA).

The data was stored in a (48 × 49) dimensional matrix **X**. The 49 columns correspond to the seven temporal features computed from the seven attenuated acoustic signals collected from each of the 48 samples (six corridors × eight anode slices). Principal component analysis (PCA) was then used to analyze the information contained in the feature matrix ***X***.

3.3.2 Principal Component Analysis (PCA)

PCA is a widely used multivariate statistical method for the analysis of large datasets containing noisy and highly collinear data, as is the case in this study. Assume a data matrix **X** (I × J) containing J measurements collected from I samples. Further, assume that both systematic variations and noise are present in this dataset. PCA decomposes the variance-covariance structure of **X** by finding a small number of orthogonal latent variables A << J capturing most of the systematic variations in **X**, but leaving noise or irrelevant information as residuals. These latent variables (also called components) are defined as linear combinations of the J original measurements and together define a lower dimensional

subspace allowing easy visualization and interpretation of the information contained in large datasets. The PCA decomposition is expressed mathematically as shown below:

$$\mathbf{X} = \sum_{a=1}^{A} \mathbf{t_a} \mathbf{p_a}^{T} + \mathbf{E} \tag{3.8}$$

where the orthogonal score vectors $\mathbf{t_a}$ (I × 1), a=1,2,…,A, are those latent variables providing the coordinates of each sample in the low dimensional subspace (plane or hyperplane) after projection. The subspace itself is defined by the A orthonormal loading vectors $\mathbf{p_a}$ (J × 1), which are linear combinations of the original variables (i.e., $\mathbf{t_a} = \mathbf{X} \times \mathbf{p_a}$). The projection residuals are collected in the residual matrix **E** (I × J). The loading vectors are calculated in such a way that $\mathbf{t_1}$ explains the greatest amount of variance in **X**, $\mathbf{t_2}$ the second greatest amount of variance left unexplained by the first component, and so on.

PCA effectively performs unsupervised clustering of the I samples in the latent variable subspace, which can be visualized using scatter plots of the scores (**t**'s). The differences between the clusters can be interpreted using the loading vectors (**p**'s). The reader is referred to Wold et al. [277] for more details about PCA. The ProMV software version 15.08 (ProSensus, Ancaster, ON, Canada) was used to build the PCA models.

3.4 Results and Discussion

The mechanical wave exciting a porous material, such as carbon anode materials, usually has complex propagation characteristics. PCA was applied to the attenuated acoustic signal feature matrix **X** to assess whether the anode samples (corridors) located at different positions within the block could be distinguished based on their attenuation behavior (quantified by temporal features at different frequencies).

A total of 15 principal components (i.e., latent variables) were found statistically significant by a cross-validation procedure [308]. The cumulative sum of squares explained (R^2) and predicted (Q^2) by the first two PCA components are provided in Table 3-1. Only those two components are discussed since they were found sufficient to discriminate the samples. They explain 65% of the variance of the attenuation features (**X**) and maintained a relatively good performance in prediction by cross-validation (Q^2 = 56%).

Table 3-1 Percent cumulative sum of squares explained (R^2) and predicted (Q^2) by the principal component analysis (PCA) model built on attenuation features collected from anode slices.

Component	R^2 (%)	Q^2 (%)
1	56.5	49.3
2	65.2	56.0

Figure 3-6 presents the latent variable score space (t_1 vs. t_2) for the first two components of the PCA model. Each marker corresponds to the attenuation behavior of one particular corridor (one row in **X**). Those were labeled in the plot using the slice and corridor numbers (slice#_corridor#) presented in Figure 3-2. The clustering pattern in the t_1-t_2 score space reveals that corridors 1–2, 3–5, and 6 of any slice roughly cluster in three groups (black, orange and blue markers, respectively). At this point, it is important to make a note that the corridors labeled #1 are located at the center of the anode and #6 at the outer surface. It can also be observed that the attenuation features of corridors 1–2 and 6 seem more variable than those of corridors 3–5 (the orange cluster is tighter than the black and blue clusters).

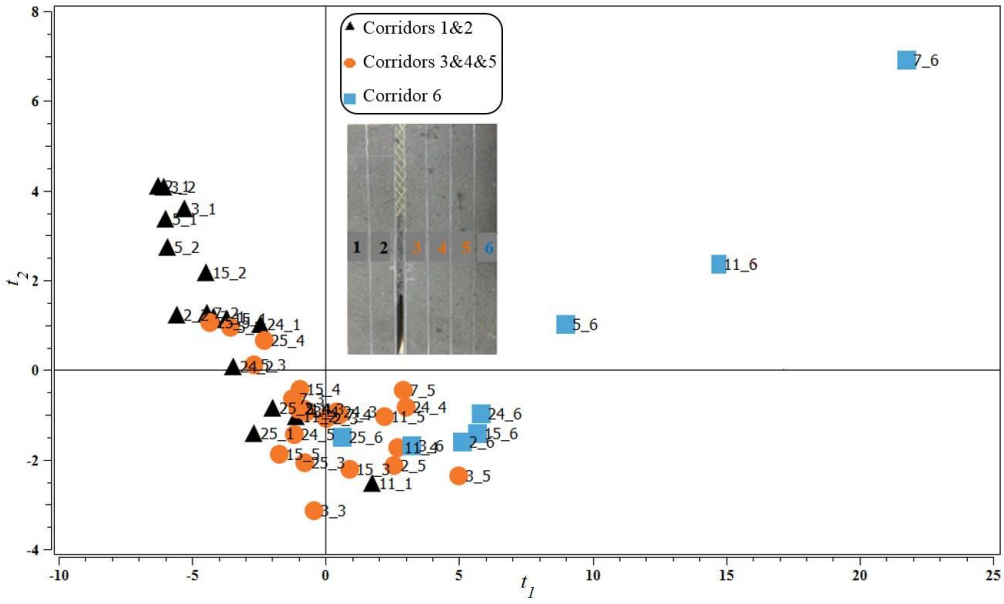

Figure 3-6 The t_1-t_2 score plot of the principal component analysis (PCA) model built on acousto-ultrasonic (AU) signal attenuation features.

In order to interpret the differences between the three clusters based on the internal structure of the corridors, the CT scan images of the eight slices were examined first. To support the discussion, the images of four of these slices are provided in Figure 3-7. In general, it was found that the central/upper regions of corridors 1–2 in most slices were

showing several cracks, whereas the lower part of these corridors had a high density of pores. Corridors 3–5 were much denser with a few cracks, sometimes extending from corridors 1–2 in the transverse direction. Finally, corridor 6 rarely showed cracks but had a variable density of pores. Therefore, the clustering pattern shown in the score plot (Figure 3-6) suggests that the first component (t_1) is sensitive to the presence of cracks because, from right to left in the score plot (along the t_1 direction), the corridors cluster according to the increasing presence of cracks. The second component (t_2), on the other hand, seems to distinguish dense from porous regions. Corridors 3–5 (orange markers) are denser and cluster in the negative t_2 region as opposed to those corridors characterized by a high pore density (most of the corridors 1–2 and some 6) fall in the positive t_2 region.

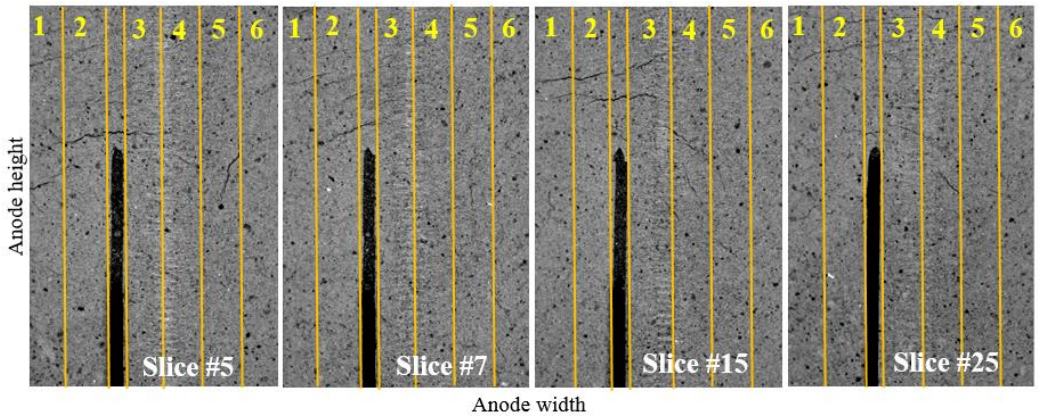

Figure 3-7 X-ray images showing the distribution of cracks and pores through different corridors for selected anode slices.

These results are also in agreement with carbon plant knowledge. The region below the stub holes corresponding to corridors 1–2 in slices #5, #7, #11, and #15 are generally expected to show a higher concentration of cracks, as shown in Figure 3-8. Most of these corridors fall in the cluster formed by the black markers. Corridors 1–2 in slices #24 and #25 (edges) project closer to the denser region (orange markers), which is normally expected unless cracks extend in the longitudinal direction from the center of the anode towards its surface, as seems to be the case for the other edge of the anode (slices #2 and #3). Finally, it is important to understand that the overlap between the clusters should not be interpreted as a misclassification as it was not attempted to do so. Although cracks and pores are expected to concentrate in certain regions within the anode block, they may very well be found in locations where they are less or not expected (hence the overlap between clusters) but still need to be detected by the inspection system. The color code used to distinguish the corridors and slices in Figure 3-6 was selected for illustration purposes only.

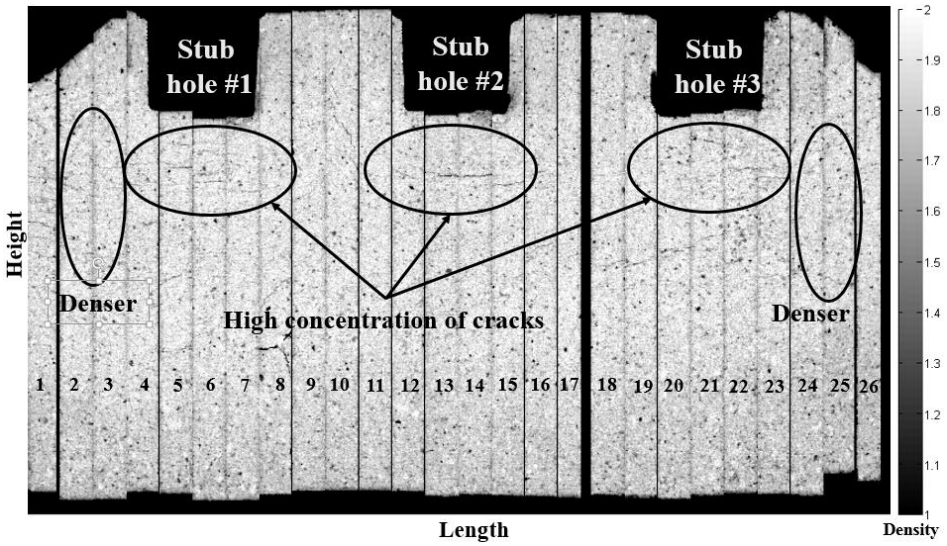

Figure 3-8 X-ray images showing a transversal section of the sliced anode.

The relationships between the clusters in the score space (Figure 3-6) and the attenuation features are now interpreted using the p_1-p_2 loading plot shown in Figure 3-9. As discussed previously, each score vector $\mathbf{t_a}$ is defined as a linear combination of the attenuation features (i.e., $\mathbf{t_a} = \mathbf{X} \times \mathbf{p_a}$), and the loading vector $\mathbf{p_a}$ contains the weights of each feature in that linear combination. The weights of each feature in both components are presented in the form of a scatter plot (Figure 3-9). Each point in this graph corresponds to one feature calculated at one excitation frequency (i.e., one column of **X**). The label of each point identifies the feature name followed by the excitation frequency.

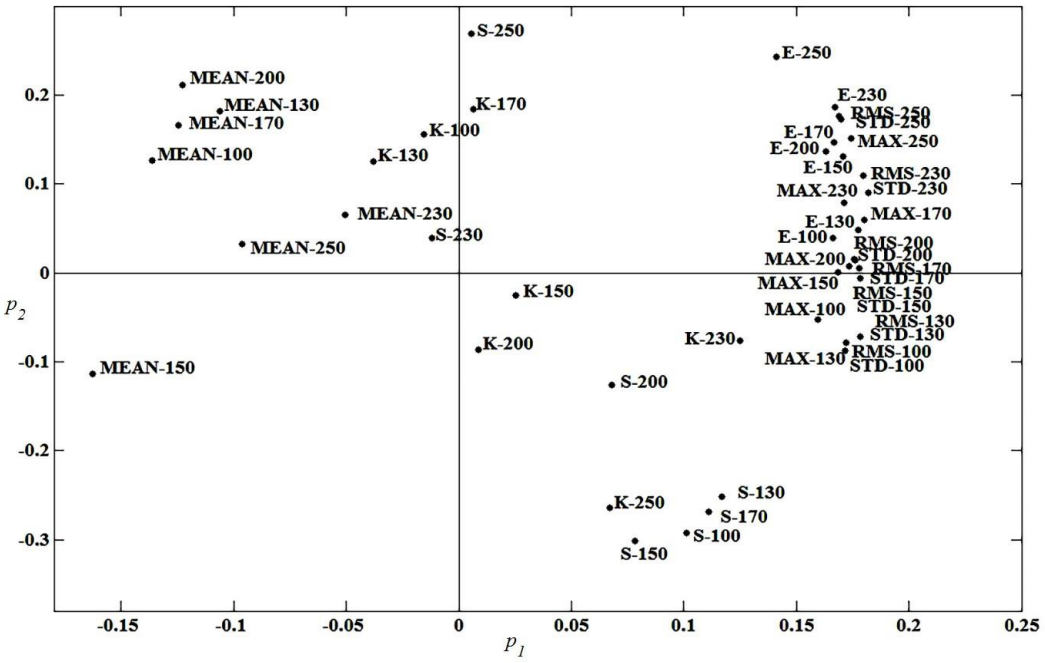

Figure 3-9 The p_1-p_2 loading plot of the PCA model built on AU signal attenuation features. MAX: maximum, STD: standard deviation, E: energy, RMS: root mean square, S: skewness, K: kurtosis. Numbers next to the feature names indicate the excitation frequency (kHz).

The loading plot is interpreted as follows. The absolute value of the loading weights indicates the importance of the feature in a given component, whereas the sign of the weights informs about the sign of the correlation between pairs of features. Those features with loading values of the same sign are positively correlated while those with opposite signs are negatively correlated. Figure 3-9 reveals that the first component is mainly driven by the mean and the variance-related features (MAX, E, RMS and STD). In addition, the mean features have an opposite sign compared to the others, indicating that they are negatively correlated with MAX, E, RMS, and STD. This means that moving from the positive t_1 region (a low concentration of cracks) towards negative t_1 values (a high concentration of cracks) involves lower values of the variance-related features (MAX, E, RMS and STD) and higher values of the mean of the signal. This is consistent with AU signal attenuation by an increasing concentration of cracks. The second component (orthogonal to the first) involves most features except for the kurtosis and skewness (K and S) in particular, which were not as important in the first component. These features are negatively correlated at all frequencies, except for at 200 kHz. In addition, their loading values switch signs around that frequency. This suggests that the presence of pores modifies the shape of the distribution of the AU signal (as opposed to simple attenuation of the signal by cracks). Furthermore,

the fact that the loading values for K and S are frequency-dependent may indicate that t_2 is not only sensitive to pore concentration, but also to their size. For example, corridor #6 of slice 7 (see Figure 3-3) has a high concentration of large pores, corridors #1–2 are also characterized by large pores but they are fewer in number compared to corridor #6, and corridors #3–5 have smaller pores. In the score plot (Figure 3-6), corridor #6 has the highest t_2 value, corridors #1–2 have intermediate values, and corridors #3–5 have the lowest values for this slice. Hence, the larger the pore size, the higher the t_2 values. The relationship between pore size and the shape of the AU signals at different frequencies is currently being investigated further.

3.5 Conclusion

Defective baked carbon anodes decrease the performance of primary aluminium reduction processes by increasing energy and carbon consumption in the electrolysis cells. It is therefore important to detect them before they are set in reduction cells. However, the current quality control schemes used by most anode manufacturers based on core sampling and lab characterization are inadequate to cope with the currently decreasing quality and increasing variability of the anode raw materials. They can, at most, assess the quality of a small percent of the anode production. In addition, the time delay introduced by lab characterization is too long to allow timely feedback-corrective actions to be applied on the anode manufacturing process when deviations of anode properties from their target occur, and/or to reject and recycle the defect anodes. Hence, new rapid and non-destructive techniques are required for inspecting every individual baked anode before they are rodded and set in reduction cells.

The objective of this work was to investigate the potential of acousto-ultrasonic (AU) techniques to detect the presence of defects affecting the performance of baked anodes in the cells, such as pores and cracks, and to discriminate both types of defects. To achieve this goal, a full-scale anode was sliced in both longitudinal and transversal directions and imaged using X-ray Computed Tomography (CT-Scan) to reveal its internal structure. Each half slice was further virtually divided into six corridors along the anode height, from the center of the anode to its external surface. At one end, the anode samples (corridors) were submitted to an acoustic excitation signal at seven different frequencies ranging from 100 to 250 kHz, while at the other end, the attenuated acoustic signals were recorded. A vector of temporal attenuation features was calculated from the attenuated signal of each anode sample. Principal component analysis (PCA) was then applied to the attenuation feature matrix in order to

perform an unsupervised clustering of the acoustic response of each anode sample (i.e., the corridor in each tested slice).

The results have shown that the temporal features calculated from the AU signals are sensitive to the presence of cracks within the anode samples (measured by overall signal attenuation) and to the density of pores distributed throughout the material. It was also found that both types of defects have a different signature in the AU signals and could be discriminated in the PCA score space. Furthermore, it appears that some combinations of temporal AU features computed at various frequencies are correlated with pore size, although further work is required to confirm this. These results were validated qualitatively by using the CT scan images of the samples and they were also found in good agreement with anode manufacturing process knowledge.

The proposed approach appears very promising for full-scale anode inspection. In addition to detecting and discriminating important defects, the AU system could also provide measurements of the anode density distribution, a complement to the electrical resistivity measurements currently being developed in the field. Future work will concentrate on the scale-up of the approach to industrial-scale baked anodes and to investigate its robustness. Regarding the acoustic inspection set-up, minimizing the acquisition time of the acoustic signals at multiple points, coping with variations in anode surface quality (i.e., roughness) and a more complex geometry are the main challenges to be addressed for application at full scale. The analysis of the acoustic signals will also need to discriminate the variations in the signals caused by changes in raw material properties, anode formulation and process operations from internal defects.

Acknowledgments: The authors would like to acknowledge the financial support of the Natural Sciences and Engineering Research Council of Canada (NSERC), Fonds de Recherche du Québec—Nature et Technologies (FRQNT), Alcoa and the Aluminium Research Centre—REGAL. The assistance provided by REGAL personnel, Hugues Ferland and Guillaume Gauvin from Université Laval, in preparing the experimental set up is also greatly acknowledged.

Chapter 4 Inspection of Prebaked Carbon Anodes using Multi-Spectral Acousto-Ultrasonic signals, Wavelet Analysis and Multivariate Statistical Methods

Résumé

L’efficacité des cellules de réduction dans la production d'aluminium primaire est fortement influencée par les propriétés des anodes cuites. La production des anodes de qualité constante est plus difficile aujourd'hui en raison de la variabilité croissante des matières premières. La prise de mesures correctives instantanées pour atténuer l'impact des fluctuations des matières premières sur la qualité de l'anode est également difficile compte tenu de la stratégie d'échantillonnage et de caractérisation actuellement utilisée par la plupart des fabricants d'anodes. En effet, selon cette stratégie, en termes de capacité les laboratoires ne peuvent supporter qu’une très faible proportion (environ 1%) des analyses de la totalité des anodes produites à cause de la capacité limitée des ressources et du coût élevé. À ce problème de capacité s’ajoute aussi le retard causé par le long délai nécessaire pour les analyses de laboratoire. L'objectif de ce travail est donc de développer des méthodes rapides et non destructives pour l'inspection des anodes cuites. Dans un précédent travail, il a été démontré que les signaux acousto-ultrasoniques, collectés à partir des tranches d’anode à différentes fréquences, sont sensibles aux défauts de l’anode (pores et fissures) ce qui a été validé qualitativement par la tomographie à rayons X. Pour améliorer cette approche, ce présent travail fait plutôt appelle à l'utilisation des signaux d’excitation multi-spectrales ainsi que la corrélation quantitative entre les signaux acousto-ultrasoniques et les défauts extraits des images de tomographie. Pour ce faire, les transformées en ondelettes et la méthode des moindres carrés partiels ont été mises en œuvre, respectivement, pour l’analyse des signaux et la régression. Il en résulte un temps d’acquisition plus court et un modèle plus spécifique et robuste pour l'inspection des anodes. La performance de cette approche a été mise en évidence à l'aide d’échantillons d’anodes industrielles.

Abstract

Reduction cell operation in primary aluminium production is strongly influenced by the properties of baked anodes. Producing consistent anode quality is more challenging nowadays due to the increasing variability of raw materials. Taking timely corrective actions to attenuate the impact of raw material fluctuations on anode quality is also difficult based on the core sampling and characterization scheme currently used by most anode manufacturers because it is applied on a very small proportion of the anode production (about 1%), and long-time delays are required for lab characterization. The objective of this work is to develop rapid and non-destructive methods for inspection of baked anodes. In past work, it was shown that acousto-ultrasonic signals collected from anode parts at different frequencies were sensitive to anode defects (pores and cracks) and this was validated qualitatively using X-ray computed tomography. This work attempts to improve the method by using multi-spectral excitation signals and by establishing quantitative relationships between the acousto-ultrasonic signals and defects extracted from tomography images using Wavelet Transforms and Partial Least Squares (PLS) regression. This results in shorter acquisition time and a more specific and robust model for anode inspection. The method performance is illustrated using samples collected from industrial scale anodes.

Keywords: Non-destructive testing; acousto-ultrasonic signals; CT-Scan images; PCA; PLS.

M. Ben Boubaker, D. Picard, J. Tessier, H. Alamdari, M. Fafard and C. Duchesne, Inspection of Prebaked Carbon Anodes using Multi-Spectral Acousto-Ultrasonic signals, Wavelet Analysis and Multivariate Statistical Methods, ICSOBA, Québec, Canada, 2016 (it will be submitted to Metals soon).

4.1 Introduction

Most modern primary aluminium smelters use the Hall-Héroult (H-H) electrochemical process to reduce alumina powder to metal aluminium. To carry out the reaction, prebaked carbon anodes are utilized in order to distribute the electrical current in the reduction cells, and to supply the carbon required by the reaction. Hence, the anodes are consumed and need to be replaced according to a predefined set cycle. The overall performance of the H-H process is strongly influenced by the quality of the anodes blocks. For instance, a low electrical resistivity is important to maximize the energy efficiency. A high mechanical strength and density and low reactivity to air and CO2 are desired to minimize carbon consumption, and to reduce the environmental footprint and greenhouse gas (GHG) emissions. Any physical defects within the anode blocks, such as pores, cracks or compositional heterogeneities, may adversely affect the anode performance, and consequently, that of the reduction cells. Producing high quality anodes consistently is therefore a major concern for the manufacturers who are currently facing degrading quality, increasing variability and cost of the anode raw materials (petroleum coke and coal tar pitch).

The traditional anode quality control scheme used by the industry and consisting of collecting core samples from the baked anodes and characterizing them in the laboratory is inadequate to address the current needs. Indeed, core samples are gathered from a very small proportion of the anode production (often less than 1%) because of the destructive and time/resource consuming nature of the procedures. Furthermore, the samples themselves represent only 0.1-0.2% of the anode block volume which properties are known to be anisotropic. Finally, the core sample properties are typically available after a long time delay, which limits the implementation of feedback corrective adjustments to the anode manufacturing process when deemed necessary. Therefore, alternative rapid and non-destructive techniques are required for assessing the quality of individual baked anodes before they are set in the H-H reduction cells.

Recent research efforts focused on developing devices for measuring the electrical resistivity of the individual green [119, 295, 327] and baked [114, 115] anode blocks using different technologies. These sensors allow measuring a very important anode property related with energy efficiency, but their capacity to detect, locate and diagnose physical defects within the anode blocks has yet to be established. Alternatively, the performance of acousto-ultrasonic (AU) techniques for detection of various defects in carbon anodes has

been demonstrated in previous work [309] using sequential acoustic excitation at different frequencies. Sliced anode samples were tested using this approach and their acoustic responses was analyzed using Principal Component Analysis (PCA). The relationship between the attenuation of the acoustic signals and the presence of different defects was validated qualitatively using X-ray images collected from the slices. However, sequential excitation at multiple points on the material is a lengthy process, and shortening the cycle time of the acoustic inspection scheme is highly desirable for industrial implementation.

The aim of this work is to demonstrate that exciting the anode materials using a single frequency modulated acoustic wave (multi-frequency signal) can lead to similar or better results compared to sequential excitation, while significantly reducing cycle time. For instance, the sequential excitation scheme used in previous work to obtain good inspection results consisted of testing the materials at seven excitation frequencies in the 100-250 kHz range for each measurement point [309]. A single frequency modulated wave in the same range would reduce cycle time by 7 to 1 for the same number of data points. A side objective of this work is to validate the proposed approach more quantitatively, by building empirical regression models between the acoustic response of the materials and the corresponding CT-scan images. These images are used for the sole purpose of confirming the inspection results as they would not be available in an industrial implementation.

Under frequency-modulated excitation, the material response signal is more complex as it also contains multiple frequencies. To quantify the acoustic attenuation at different frequencies, the signal needs to be first decomposed. One approach consists of using the Fast-Fourier transform (FFT) [310-313]. However, it only performs frequency domain decomposition and does not capture variations in the signal frequency content through time, which may limit the performance in defect detection and identification. An alternative approach is to perform time-frequency decomposition of the signals using the Wavelet Transforms (WT) [314-316, 345], which were shown to be a powerful tool in all areas dealing with transient signals [317-319]. Qi et al. [231-320] showed the effectiveness of the Discrete Wavelet Transform (DWT) to process the acousto-ultrasonic signals from composite materials. A similar approach is used in this work.

To quantify defects in tomographic images, texture analysis techniques are used since the defects introduce local variations in grey level intensity in the images according to some relatively well defined patterns (e.g., round spots for pores and streak lines for cracks). Again

here, one could extract textural features from tomographic images using the two-dimensional Fast Fourier Transform (2D-FFT) [321]. The frequency decomposition of the images could be used determine the severity of the defects. However, variations in frequency content within the images (i.e., spatial information) cannot be extracted using this approach. On the other hand, the 2D Discrete Wavelet Transform (2D-DWT) is effective for extracting both frequency and spatial information [322]. Wavelet texture analysis has proved a useful tool in several areas dealing with noise and low variation in images.

After applying the WT to both sets of data (acoustic signals and images), wavelet features were extracted and analyzed using PCA in order to explore the clustering pattern of the various anodes slides. A regression model was then built between both data sets. The results show that the attenuated acoustic response of the materials obtained after frequency-modulated excitation are sensitive to the presence of cracks within anode samples, and to the density of pores distributed throughout the anode samples (slices). The performance of this approach was found to be similar to that obtained using sequential excitation [6], but with a significant reduction in cycle time.

4.2 Materials and experimental data acquisition

4.2.1 Baked anode samples and X-Ray CT-Scan imaging

A full-size industrial baked carbon anode was scanned using a Siemens Somatom Sensation 64 tomograph. The scanning area of the X-ray apparatus was limited to objects of less than 40 × 40 mm^2 cross-section. Since the anode was too large to fit in the scanning area in one piece, it was cut in several slices as shown in Figure 4-1. The cutting was performed with care to avoid altering any anode defects. Furthermore, a higher image resolution at each scan is obtained when the samples are smaller in size, which increases the contrast between defects and the background [252]. The anode was first cut into 26 slices (Figure 4-1 a), and then each of them were cut further in halves along their heights (Figure 4-1 b). The top and bottom of each half slice was also cut to obtain samples of uniform geometry before collecting the acoustic response of the material. Note that the following eight slices were selected for further AU analysis: 2, 3, 5, 7, 11, 15, 24, and 25 (indicated using red numbers in Figure 4-1 a). These slices span a range of internal structures, and were selected from areas which are expected to contain different types of defects (see [309] for more details).

The CT-scan measured the attenuation coefficients of the material for a set of 512×512 3D voxel (volumetric pixel) per scan, which correspond to the tomograph resolution. Given the slice dimensions, the voxels had a resolution of 0.7×0.6×0.7 mm. The X-ray attenuation coefficients of the voxels (also called CT numbers) were converted to grayscale images showing spatial variations correlated with the materials density [77, 252]. Cracks and pores appear as groups of dark pixels surrounded by lighter background (carbon anode). The high-density impurities appear as bright pixels inside a darker background. Figure 4-2 shows an example X-ray CT-Scan image for one slices.

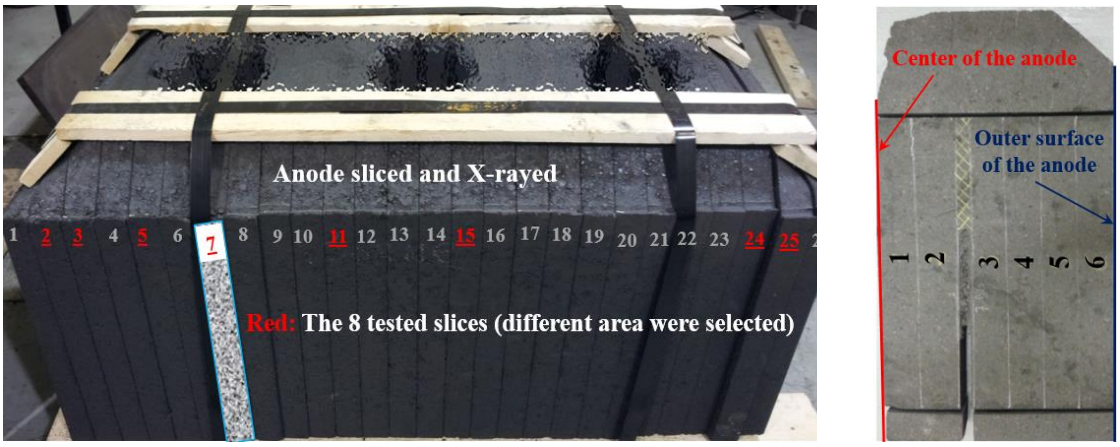

(**a**) (**b**)

Figure 4-1 The sliced baked anode. (a): the selected 8 slices are identified in red; (b): Example of a slices used for acousto-ultrasonic testing [309].

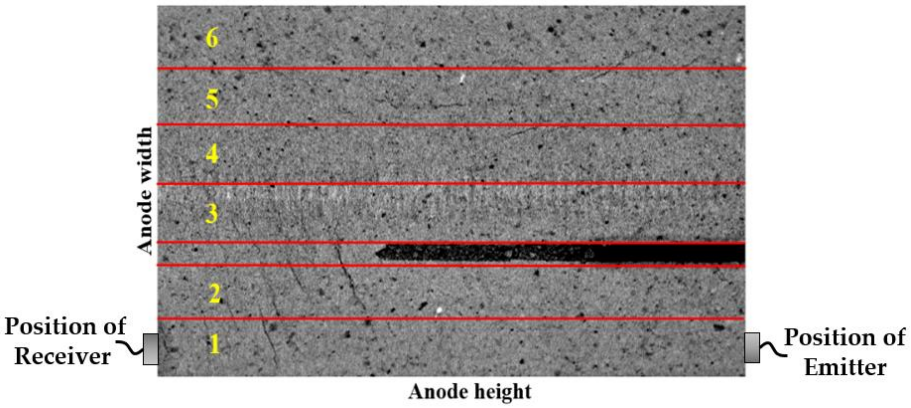

Figure 4-2 Example X-ray Computed Tomography (CT Scan) image obtained for slice 7. The corridors are identified by the red lines and numbered from 1-6. The black region corresponds to one of the anode slots [309].

4.2.2 Acousto-ultrasonic signal acquisition

The acousto-ultrasonic inspection system used in this work was described in details in [6]. It consists of a multi-channel acousto-ultrasonic apparatus using two acoustic sensors

(an emitter and a receiver), a pre-amplifier, and a software for controlling the excitation and recording the emission signals. The sensors were mounted on both ends of the anode slices (one on top and the other on the bottom surface) using mechanical clamps. Couplant gel was applied on the anode surfaces before the sensors were put into contact with the materials. This was made to ensure good contact between the sensors and the anode samples which typically have rough surfaces. The sensors were placed *vis-à-vis* each other and moved together along the anode width so as to measure the AU response of the materials included in the 6 so-called corridors identified by a white chalk in Figure 4-1 b), and by red lines in Figure 4-2. The material structure clearly changes from the center of the anodes to the external surface (corridor 1 and 6 in Figure 4-2, respectively), as shown by variations in material density (i.e., gray level) and the presence of pores and cracks. As mentioned in the previous section, such variations in the material structure are also expected along the length of the anode (i.e., various slices).

The excitation signal was specified as a modulated frequency signal between 100 and 300 kHz as shown in Figure 4-3. This range was selected based on previous work [309]. The AU measurements were made using a pre-amplification gain of 40dB, and sampling rate of 1000 kHz. This procedure was repeated for all 6 corridors (Figure 4-1 b) in each of the selected anode slices.

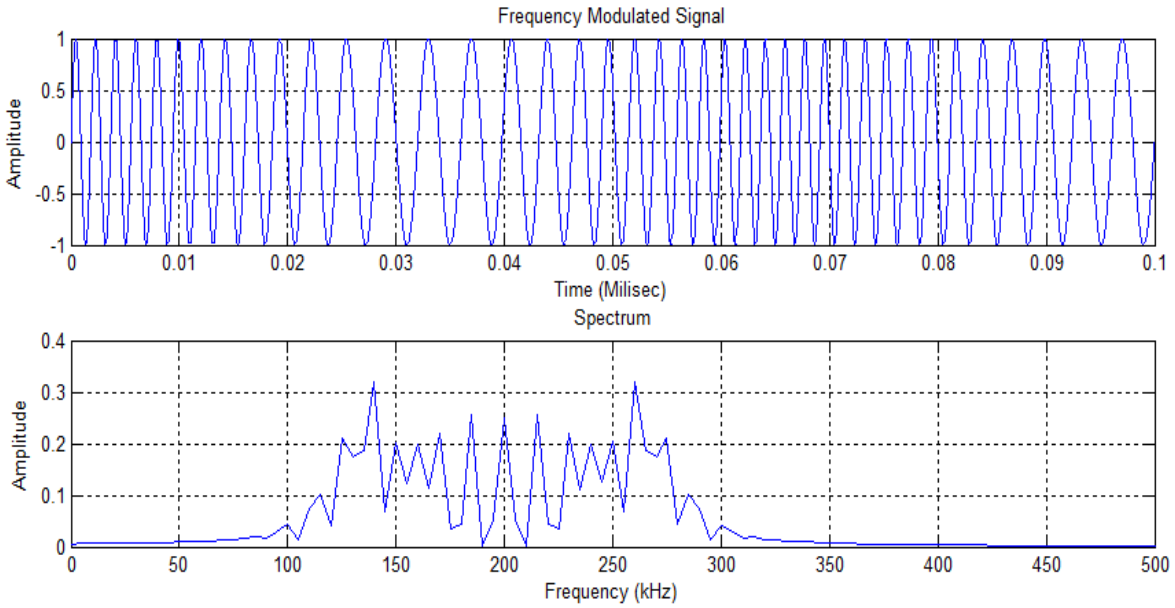

Figure 4-3 The frequency modulated waveform used as the excitation signal. Both the time series (top) and the frequency content (bottom) of the signal are shown.

4.3 Extraction of features from acoustic signals and X-ray images

4.3.1 Acousto-ultrasonic signals

The majority of the acousto-ultrasonic signals propagating through the porous anode materials are in the frequency range of 10-300 kHz. Dividing this range into a set of consecutive frequency bands may help relate different time-frequency features of AU signals to various anodes defects. The wavelet transforms were used to decompose the signals and extract meaningful time-frequency domain features from them.

The decomposition of a continuous 1D signal x(t) using a specific scaled or dilated mother wavelet ψ (t,a,b) is obtained by the convolution of both the signal and the wavelet function as follows [324]:

$$d_{a,b} = \frac{1}{\sqrt{a}} \int_{-\infty}^{+\infty} x(t)\, \psi\left(\frac{t-b}{a}\right) dt \qquad (4.1)$$

In the above equation, ψ (t) is the mother wavelet function which corresponds to a wave of finite length and having a particular shape. Several types of mother wavelet exist (e.g., Haar, Daubechies, Coiflet, Symlet, Mexican Hat, etc.), and they mainly differ by their shape (frequency content). The type of mother wavelet is typically selected so as to match the shape of the signal x(t) the best possible. The Daubechies wavelet (Db5) was selected in this work. This choice came after selecting the best results from trying several different mother wavelets. Parameters a and b are called the scaling and the translation parameters, respectively. The former stretches the mother wavelet and changes its frequency content while the latter performs a translation of the wavelet over time. The results of the convolution is a scalar quantity $d_{a,b}$, called the wavelet detail coefficient, and represents how well the signal x(t) matches the dilated mother wavelet at scale a and time point b. Changing the scaling coefficient a from a small to a large value progressively dilates the wavelet and therefore allows extracting information about signal x(t) from high to low frequency. Translating the wavelet using parameter b from the beginning to the end of the x(t) signal allows capturing information at different time points. Hence, changing a and b in a nested fashion performs a spatial-frequency decomposition of signal x(t) and how well the signal matches at wavelet at scale a and time point b is quantified by the detail coefficient $d_{a,b}$. Note that the acoustic signals analyzed in this work are discrete (i.e., sampled at a given

frequency). A discrete version of equation 4.1 exist for sampled signals as well. This leads to the so-called Discrete Wavelet Transform (DWT), which is numerically implemented as a filter bank, involving sets of low and high-pass filters, instead of a convolution integral (equation 4.1). Instead of changing the scale by contracting or dilating the mother wavelet, the latter is kept at a fixed length but the signal itself is progressively decimated according to a dyadic sampling selected for computing efficiency and to avoid signal aliasing. Hence, at the first scale, the wavelet extracts high frequency information, and subsequent scales extracts lower frequency components. The mother wavelet to use as well as the number of scales (integer number) are set by the user. For more details on the DWT, the reader is referred to [322].

After performing the wavelet decomposition of discrete signal x(i), a set of vectors of detail coefficients $d_a(i)$ is obtained, one for each scale a. Each vector contains the detail coefficient at a given scale but for all time points. In other words, the original signal x(i) is decomposed into a set of detail signals $d_a(i)$, each containing information about a certain frequency band. Three time domain features were then calculated from each time series $d_a(i)$, i=1,2,…N, N being the number of samples in the time series. These features are the maximum (MAX), the root mean square (RMS) and the time of flight, or arrival time (AT). These features are calculated as follows:

$$MAX_a = \max_{i=1}^{N} d_a(i) \tag{4.2}$$

$$RMS_a = \sqrt{\frac{1}{N}\sum_{i=1}^{N}\left[d_a(i)\right]^2} \tag{4.3}$$

$$AT_a = i \quad \text{when} \quad d_a(i) \geq 0.15 \times \max(d_a(i)) \tag{4.4}$$

The acoustic response of the materials x(i) was decomposed up to level 4 (four different discrete values of a) and the MAX and RMS features were calculated from each of them as well as the arrival time. Figure 4-4 provide an example of a raw acoustic signal decomposed into 4 frequency bands (details 1-4), and also shows the residual signal after four decomposition levels (called approximation).

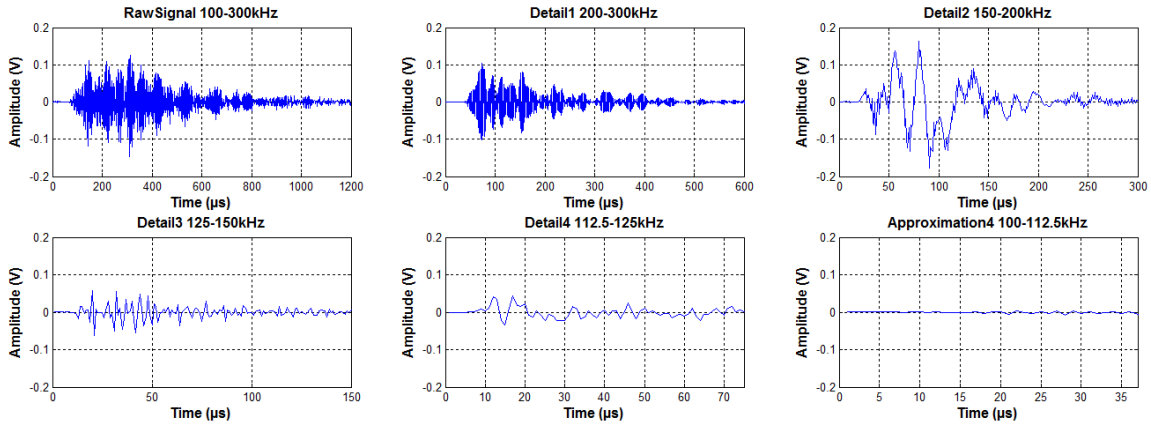

Figure 4-4 Example wavelet decomposition of an acoustic signal using 4 decomposition levels. The raw signal, the 4 wavelet detail signals as well as the residuals (approximation) are presented.

The data were then collected in a (48×15) dimensional matrix **X**. The 15 columns correspond to the three features computed from the 4 wavelet detail signals as well as the approximation for all of the 48 samples (6 corridors × 8 anode slices). Signal and image processing were performed using Matlab version R2014a (MathWorks, Natick, MA, USA).

4.3.2 X-ray image texture analysis

The texture of X-ray images was analyzed using a very similar approach as for the acoustic signals. The tomography data were first converted to grayscale images. The Discrete Wavelet Transform was then applied to the images to extract textural information. The choice of using texture analysis on X-ray images is motivated by the fact that it allows to detect and quantify anode defects in an automated fashion without having to segment the images (a more tedious operation). The main difference in the application of wavelets to images and acoustic signals is that images are 2D signals. An image is a matrix of data $I(n_X,n_Y)$ where n_X and n_Y are the number of pixels in the horizontal and vertical directions in the images and the elements of that matrix correspond to the X-ray attenuation coefficients converted to grayscale values. The convolution between a mother wavelet and the image signals (i.e., discretized version of equation 4.1) is performed along each row and each column of the image (horizontally and vertically) as well as diagonally. Wavelet detail coefficients are obtained for each pixel of the images at each scale and for each of the three directions. These are collected into matrices D_j^k where j correspond to the scale, k to each direction (h,v,d), and each element of these matrices to the detail coefficient at a certain pixel location (n_X, n_Y). These matrices can also be shown as images for visual interpretation, and are typically called wavelet detail sub-images (D_j^h, D_j^v, D_j^d). At the first scale, high

frequency information is captured from the images in all three directions and these are associated with small objects or patterns in the image. As the scale increases, lower frequency information introduced by larger objects or patterns are extracted. The 5th order Daubechies wavelet (Db5) wavelet was selected for extracting textural information from the X-ray images.

Several scalar textural descriptors or textural features can be calculated from the wavelet detail sub-images, the most popular being the energy, variance, entropy, and the mean [254, 266]. Our results showed that the energy is sufficient to extract information related with anode defects (pores and cracks) within the X-ray images. The energy is calculated as follows from the wavelet detail sub-images at each scale and for the three directions:

$$E_j^k = \frac{\sum_{m=1}^{n_X}\sum_{n=1}^{n_Y}\left|D_j^k(m,n)\right|^2}{n_X n_Y} \tag{4.5}$$

where d_j^k is the detail coefficient for pixel located at the (n_X, n_Y) position within an image in the kth direction (k = h, v, d) and at the jth scale. The total number of pixel within the images ($n_X \times n_Y$) is used to normalize the energy values. The X-ray images were decomposed up to scale 4. This yields 12 energy values per anode corridor (4 scales $\times$ 3 directions). These values were collected for the 48 corridors and stored in matrix **Y** of dimensions (48$\times$12).

The application of wavelet decomposition to one such X-ray image is shown in Figure 4-5. It displays the original image as well as the detail sub-images for each of the 4 scales and directions. The sub-images are identified by the direction first (h,v,d) and then by the scale number (1,2,3,4). For instance, sub-images v3 displays the information extracted from the image by the wavelet in the vertical direction at scale 3. The vertical and diagonal sub-images at scales 2-4 clearly capture the profile line of the vertical and diagonal cracks in the image. This information will be regressed against the acoustic signals in order to link the acoustic attenuation to anode defects quantitatively.

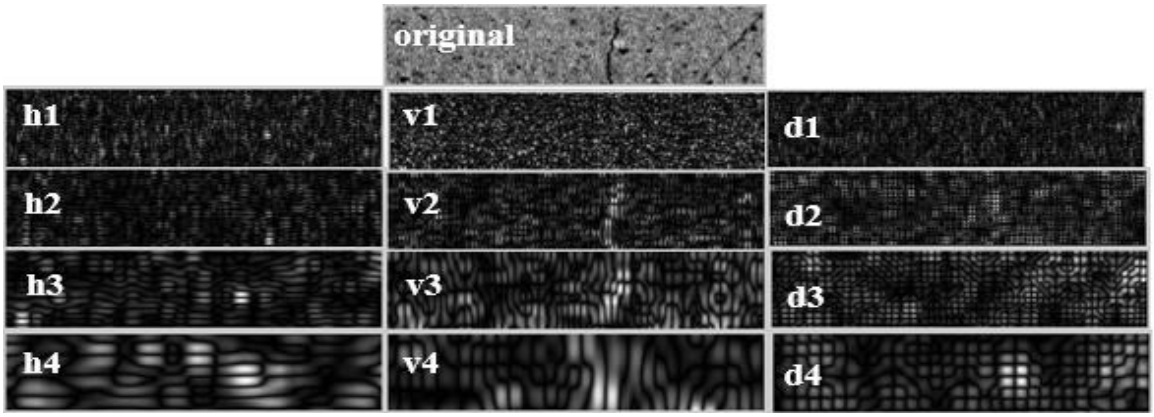

Figure 4-5 2D discrete wavelet decomposition of an X-ray image at 4 scales and in 3 directions. The wavelet sub-images are identified by the direction of analysis (h,v,d) followed by the scale number (1-4).

4.4 Multivariate statistical methods for analysis of the AU signal and image features

Multivariate statistical methods are used to analyze the large data matrices obtained in this study. First, Principal Component Analysis (PCA) is used to cluster the X-ray images based on their texture (**Y** data). Then, Partial Least Squares (PLS) regression is used to build relationships between the acoustic attenuation data (**X**) and then image textural features (**Y**). These methods are briefly described below.

4.4.1 Principal Component Analysis (PCA)

Data clustering in the latent variable space using methods such as PCA is widely used for the analysis of large datasets containing noisy and highly collinear data. PCA summarizes the variations contained in a large set of J variables $\mathbf{X}=[\mathbf{x}_1, \mathbf{x}_2,\ldots, \mathbf{x}_J]$ by a much smaller number of orthogonal latent variables (or scores) $\mathbf{T}=[\mathbf{t}_1, \mathbf{t}_2,.., \mathbf{t}_A]$ (A<<J) together capturing the dominant sources of variations in the data. The scores are obtained by an eigenvector-eigenvalue bilinear decomposition of the **X** matrix and is mathematically expressed as follows [277, 346]:

$$\mathbf{X} = \sum_{a=1}^{A} \mathbf{t}_a \mathbf{p}_a^T + \mathbf{E} = \mathbf{T}\mathbf{P}^T + \mathbf{E} \tag{4.6}$$

where the orthogonal vectors $\mathbf{t}_a$ are the latent variables (called scores) providing the coordinates of each sample in the low dimensional subspace (plane or hyperplane) after projection. The subspace itself is defined by the A orthonormal loading vectors $\mathbf{p}_a$, which are linear combinations of the original variables (i.e., $\mathbf{t}_a = \mathbf{X}\,\mathbf{p}_a$). The projection residuals are

collected in the residual matrix **E**. The loading vectors are calculated in such a way that $\mathbf{t_1}$ explains the greatest amount of variance in **X**, $\mathbf{t_2}$ the second greatest amount of variance not explained by the first component, and so on. Plots of the score values are used to visualize the clustering pattern of the data while the loadings allow interpretation of the patterns by the changes in the variables. The reader is referred to [277] for more details on PCA.

4.4.2 Partial Least Squares (PLS) regression

The PLS regression method is used here to correlate the acousto-ultrasonic features of the anode corridors gathered in **X** matrix with corresponding image textural features collected in **Y**. Similar as for PCA, this regression method has an advantage of overcoming the strong correlation between features in both data blocks. Each PLS latent variable is calculated in such as was to maximize the covariance in both data matrices and the following model structure is obtained [271, 272]:

$$\mathbf{X} = \mathbf{T}\mathbf{P}^{\mathrm{T}} + \mathbf{E} \tag{4.7}$$

$$\mathbf{Y} = \mathbf{T}\mathbf{C}^{\mathrm{T}} + \mathbf{F} \tag{4.8}$$

$$\mathbf{T} = \mathbf{X}\mathbf{W}^{*} = \mathbf{X}\mathbf{W}(\mathbf{P}^{\mathrm{T}}\mathbf{W})^{-1} \tag{4.9}$$

where the latent variable space of both **X** and **Y** correspond to the scores **T** (orthogonal PLS components) which relate **X** to **Y**. The sub-spaces of **X** and **Y** are modelled by the loading matrices **P** and **C**, respectively, while the corresponding residuals are stored in **E** and **F**. Finally, the so-called weight vectors **W*** contains the linear combinations that expresses **T** in terms of **X** and allow to make predictions of **Y**.

The PLS method also performs clustering of samples vector in the latent variable subspace according to the **Y** data. The clustering patterns can be visualized using scatter plots of the scores (**t**'s). The differences between the clusters can be interpreted using the loading weight vectors (**w***'s). The reader is referred to Wold et al. [272] for more details about these methods. The ProMV software version 15.08 (ProSensus, Ancaster, ON, Canada) was used to build PCA and PLS models.

4.5 Results and discussion

The X-ray image textural features (**Y** data) are analyzed first using PCA in order to associate them with anode defects (voids such as pores and cracks). A PLS regression

model is then built using both the acoustic and image textural features in order to correlate them. This provides a quantitative validation of the impact of anode defects on the acousto-ultrasonic features.

4.5.1 Texture analysis of X-ray images

Using the cross-validation procedure [308], two PCA components (or latent variables) were found significant and together explain most of the variations in the image textural features. The cumulative sum of squares explained (R^2) and predicted (Q^2) by the first two PCA components are provided in Table 4-1. The first two components were found sufficient to discriminate the corridors based on their textural features since they explain over 83% of variance of the textural features stored in **Y** (Q^2=83.21% in Table 4-1).

Table 4-1 Percent cumulative sum of squares explained (R^2) and predicted (Q^2) by the PCA model built on textural features collected from anode slices X-ray images.

Component	R^2 (%)	Q^2 (%)
1	60,3	58,7
2	84	83.21

The main variability directions in the image dataset captured by the two PCA components are presented in the t_1-t_2 score plot shown in Figure 4-6. Each marker in this plot represents a summary of the textural features of one particular corridor. These are identified by the slice number followed by the corridor number. Corridors having similar textural features cluster close to each other while those having different features cluster in different locations in the latent variable space. It is observed that the corridors located in the same position within the slices cluster together (see markers of the same color in Figure 4-6). Furthermore, each group is discriminated from the others along both PCA components except those of slice number 25. This slice is located close to the corner of the anode block, and contains larger pores and cracks which makes them look like either corridors #1-2, typically containing several cracks, or to corridors #6 that contain lots of pores. This explain why the corridors of slice #25 cluster close to corridors #1-2 or #6.

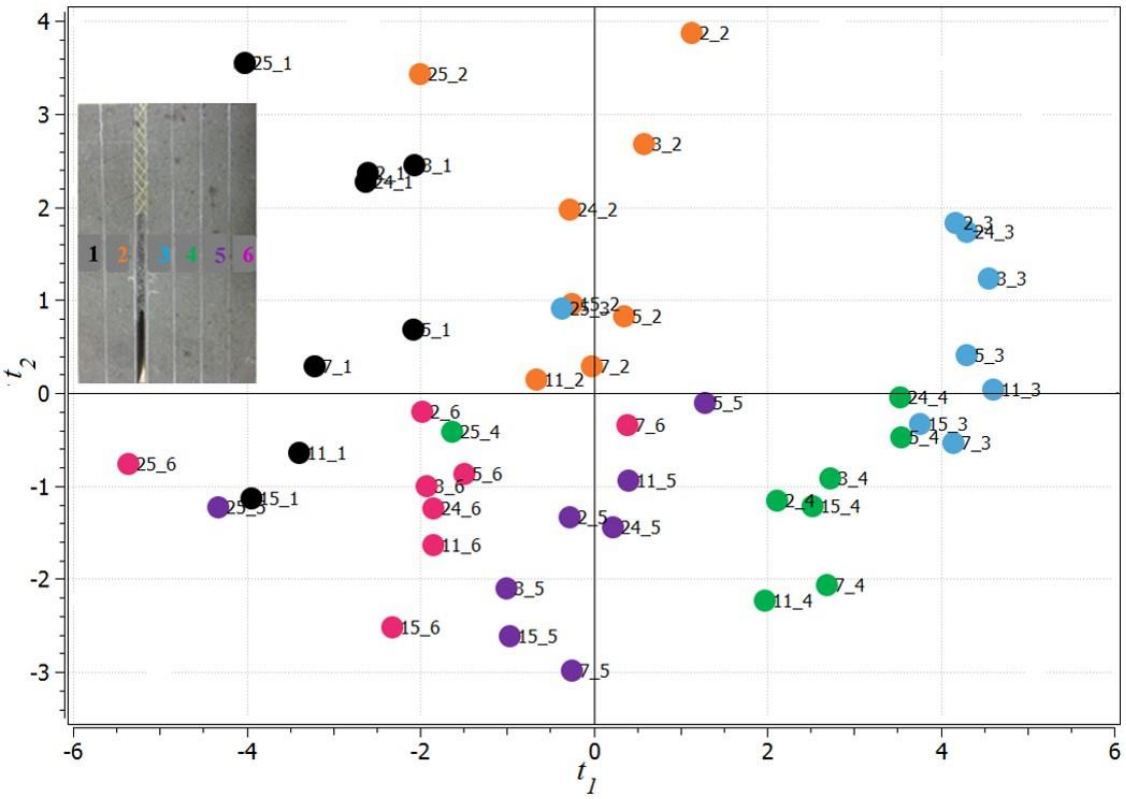

Figure 4-6 Score plot of the PCA model (t_1-t_2) showing the clustering pattern of the corridors in each slice based on their textural features extracted from X-ray images. Observations are identified by the slice number (red numbers in Fig. 1) followed by the corridor number (1-6). Different colors are used to distinguish the different corridors as shown in the anode slice image included in the figure.

The clustering pattern in the score space can be interpreted based on changes in the textural features by examining the p_1-p_2 loading plot shown in Figure 4-7. Each point in the loading plot corresponds to one textural feature calculated from the image of each corridor. They are labeled according to the feature name followed by the wavelet decomposition level. The loading values define the weight of each textural features in each component. The higher the absolute value of the loadings the more important the features are in a given component. The signs of the loadings indicates the sign of their correlation. Features having loading values of the same sign are positively correlated and those having opposite signs are negatively correlated. The loading plot reveals that the first component is driven by most wavelet decomposition levels, and all of them have loading values of the same sign (i.e., vary all together in the same direction). This component seems to explain variations in density and/or the total volume of voids (i.e., defect severity) across the X-ray images. A denser region is characterized by higher CT numbers and hence by higher grey levels in the image. This typically leads to higher energy values as calculated from the wavelet texture

analysis. Since corridors 3-4 (and 5 to some extent) are known to be denser, it is expected that these corridors would fall in the positive t_1 region (see Figure 4-6) because the energies at all scales and directions would be higher. On the contrary, corridors 1-2 and 6 typically contain more defects (cracks and pores) and therefore are less dense. Hence, lower CT numbers, grey level intensities and energies. Thus, it is expected that these would fall in the negative t_1 region of the score plot.

The second component, however, is driven by a contrast between the energies at scales 1-2 vs 3-4 since these two groups have loading values of opposite signs. This component seems to capture textural variation that corresponds to defects sizes. Corridors containing larger defects (e.g., cracks) should be characterized by higher energies at lower frequencies (scales 3-4) and lower energy at higher frequencies (scales 1-2) since the lower frequency bands are associated with larger objects or patterns. Since corridors 1-2 typically contain more cracks they fall in the positive t_2 region (higher energies at scales 3-4 and lower at scales 1-2). The situation is opposite with corridor 6 typically containing pores (clusters in negative t_2 region). Hence, the proposed wavelet texture analysis of X-ray images seems to capture variations in density and to discriminate between small and large defects in the anode samples (i.e., pores vs cracks).

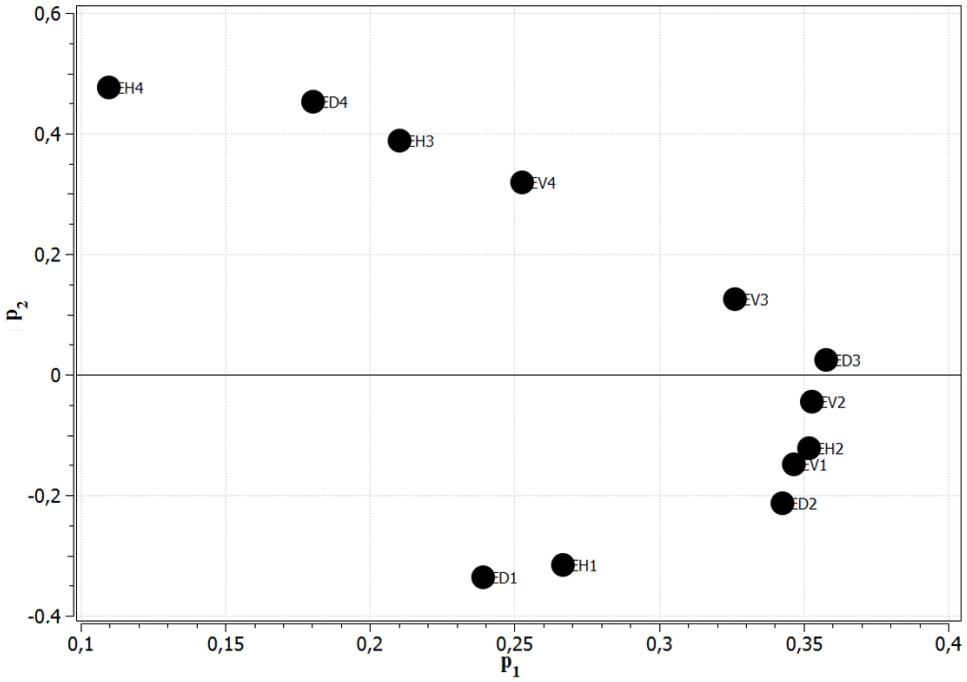

Figure 4-7 Loading plot of the PCA model (p_1-p_2) built on image textural features (**Y** data). The energy features are identified by letter "E" followed by the wavelet direction (H, V, or D), and scale number.

4.5.2 Regression of X-ray image textural features on acousto-ultrasonic features

Five PLS components were found statistically significant by a standard cross-validation procedure, and together explain about 40% of the variance of the image features (Y data). However, the first two were found sufficient in number to discriminate samples based on their acousto-ultrasonic features.

The latent variable score space for the first two components of the PLS model is displayed in Figure 4-8. Each marker in the plot corresponds to the acousto-ultrasonic response of one corridor, which are identified as described in the previous section. The clustering pattern in the t_1-t_2 score space reveals that corridors 1-2, 3-5 and 6 of any slice cluster in 3 groups (black, orange and blue markers, respectively). At this point, it is important to remind that corridors #1 are located at the center of the anode and corridors #6 at the outer surface. It can also be observed that the attenuation features of corridors 1-2 and 6 seem more variable than the majority features of corridors 3-5 (orange cluster tighter than black and blue).

The first component (t_1) in Figure 4-8 seems to capture the types of defects in the materials since the corridors where most of the cracks were found (1-2) are located in the negative t_1 region, those characterized by high concentration of pores (corridor 6) are located in the positive t_1 region, and corridors 3-5 containing a mixture of both fall in between the two. The w_1^*-c_1 – w_2^*-c_2 loadings bi-plot presented in Figure 4-9 confirms this interpretation. The sign of X-loadings and Y-loadings (w*'s and c's or black and red markers in Figure 4-9) indicate the sign of the correlation between pairs of features whereas their absolute values is proportional to their importance in a given component. Note that comparing the black or the red loading values allows interpreting the correlation between the acoustic or the image textural features, whereas comparing the black against the red loadings provide information about the cross-correlation between the acoustic and the textural features, and the relationship between both the X and Y datasets. Clearly, the first PLS component captures a similar contrast in the energies at scales 3-4 vs 1-2 as the second PCA component discussed in the previous section. The variations in the acoustic features (black markers in Figure 4-9) are also consistent with those in the X-ray image textural features (red markers in Figure 4-9). When the materials mainly contains cracks, especially when these are oriented perpendicular to the wave propagation direction, arrival times should be longer, the signals more attenuated (lower MAX and RMS features), and

the energies in lower frequency range (scales 3-4) should be higher compared to scales 1-2. Hence, those corridors containing more cracks should fall in the negative t_1 region, and those having a higher concentration of pores (and less cracks) should fall in the positive region. This is consistent with the clustering pattern shown in Figure 4-8. The X-ray images of selected corridors are also shown in Figure 4-10. Slices 5_1 and 7_1 both have similar t_2 values but extremely different t_1 scores compared to corridors 5_6 and 7_6. Their X-ray images clearly show that the former two corridors contain several transversal cracks and some pores whereas the latter two mostly contains pores, which are also larger.

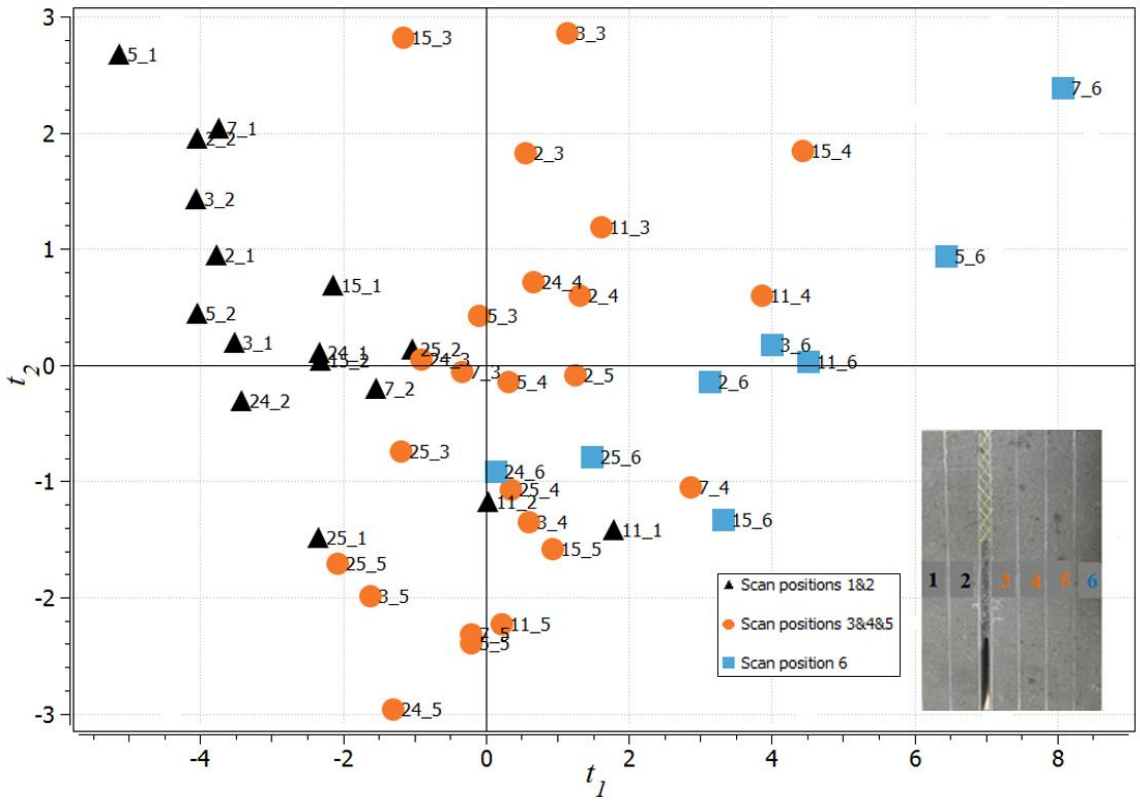

Figure 4-8 Score plot of the PLS model (t_1-t_2) between acoustic attenuation and X-ray image textural features. Observations are identified by the slice number (red numbers in Fig. 1) followed by the corridor number (1-6). Different colors are used to distinguish the different corridors as shown in the anode slice image included in the figure.

The second component does not segregate the corridors as much as t_1 does, as most of them span the t_2 range. Since it is orthogonal to the first component, the second captures a different source of covariation between the acoustic and textural features. The loading plot (Figure 4-9) shows that all features have the same sign in the t_2 component (all positive), although the energies in scales 1-2 and most of the MAX and RMS features (except RMSD4) contribute less in this component. The same sign for the loadings means that they all vary

together in the same direction. This is consistent with the first component of the PCA model presented in the previous section, which was associated with variations in material density and/or total volume of voids. Indeed, corridors containing more and larger voids (cracks and/or pores) would lead to longer arrival times, and more energy at scales 3-4 (lower frequencies). Hence, they would project in the positive t_2 range compared with corridors containing fewer and smaller voids, which would fall in the negative t_2 area. The X-ray images for corridors 3_3 and 15_3 have similar t_1 values, but very different t_2 scores compared with corridors 5_5 and 24_5. The images in Figure 4-10 clearly show that the former two projecting in the high t_2 region contain more and larger voids (or defects) compared with the latter two falling in the lower t_2 region.

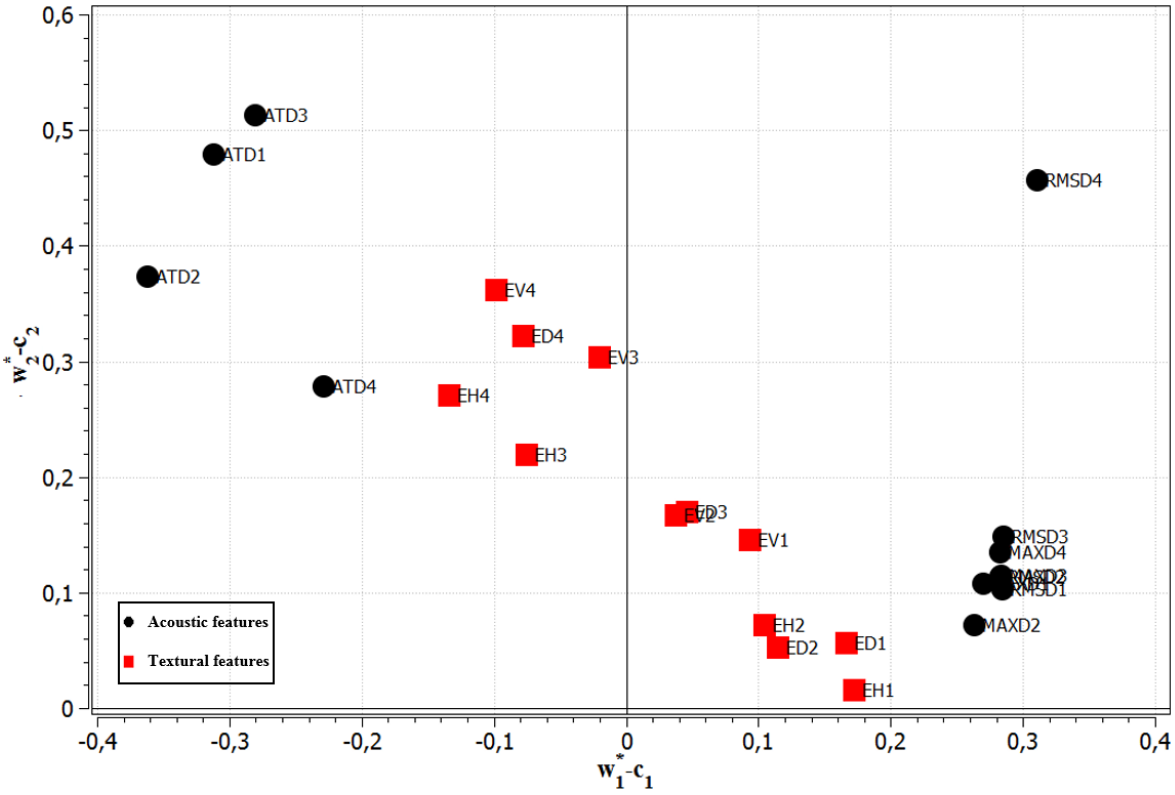

Figure 4-9 Loadings bi-plot (w_2^*-c_1 – w_2^*-c_2) of the PLS model between acoustic attenuation signals and X-ray image textural features. The features are identified by their names and by the scale at which they were calculated (1-4).

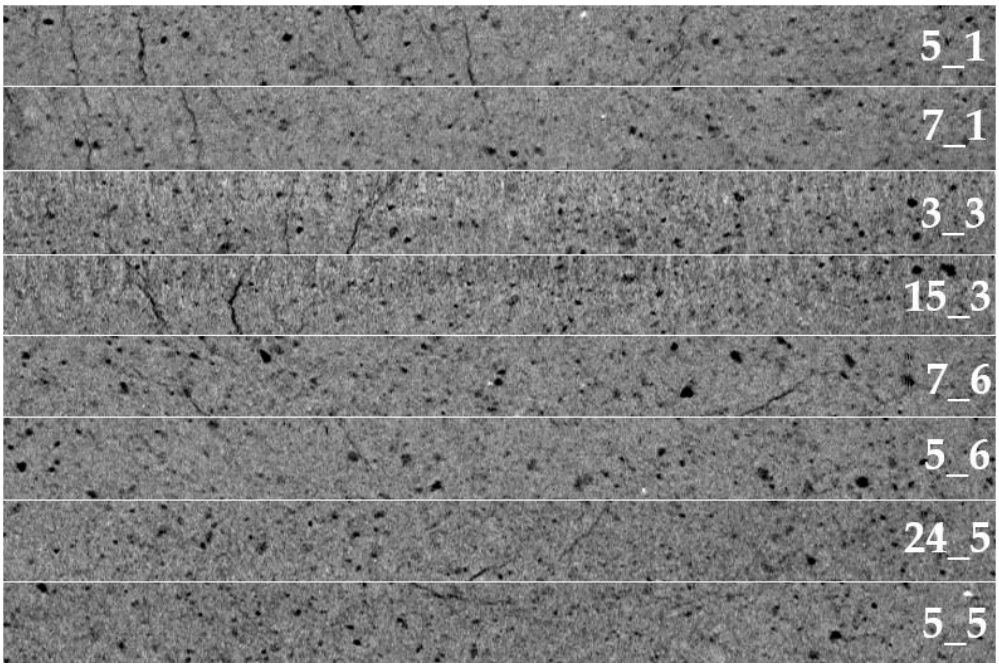

Figure 4-10 X-ray images showing the distribution of cracks and pores in selected corridors.

4.6 Conclusion

Baked carbon anodes are used in the Hall-Héroult aluminium reduction process to distribute the electrical current throughout the cells, and to provide the source of carbon required by the electrolytic reaction. However, poor quality anodes containing structural defects such as cracks and a high concentration of pores, can deteriorate the reduction cell performance by reducing energy efficiency and increasing carbon consumption. The current quality control scheme based on collecting core samples from a small proportion of the anode production and characterizing them in the laboratory is not adequate for detecting pores and cracks in a rapid and non-destructive fashion. Research efforts are currently being made to develop new sensors for inspecting individual anode blocks non-intrusively, at a speed compatible with industrial requirements.

Past work have demonstrated the potential of acousto-ultrasonic techniques (AU) to detect pores and cracks in anode samples using sequential excitation at different frequencies [309]. However, this approach require long cycle times to collect all measurements. The present work aims at reducing cycle time by using a single frequency-modulated excitation, and showing that such an approach leads to similar inspection results

as those obtained with sequential excitation. A quantitative validation of the inspection results is also proposed using X-ray images collected from each sample used in this study.

A full size baked carbon anode was cut into 26 slices of equal thickness. A total of 8 slices distributed along the anode length and showing different internal structures were selected for this work. After collecting X-ray images of the samples using a CT-Scan, they were excited by a frequency-modulated wave at 6 different points along the slice width. The AU signal received after the wave propagated through the material at each location (so-called corridors) was recorded. The Discrete Wavelet Transform (DTW) was used to decompose the AU signals into different frequency bands, and to perform texture analysis of the X-ray images. A number of scalar features were subsequently calculated from the wavelet sub-signals and images. Multivariate latent variable methods such as Principal Component Analysis (PCA) and Partial Least Squares (PLS) regression were then used to cluster the corridors in each slice according to their internal structure. A regression model was also built between the AU signals and the X-ray images in order to relate variations in the acoustic signals with the presence of defects in the material.

The results show that the textural features extracted from the X-ray images efficiently detected the voids in the anode samples, and allowed to discriminate pores from cracks, and captured the severity of those defects. The PLS regression model built between the X-ray image textural and the AU signal features for each corridor clearly showed that variations in the acoustic response of the samples also allows detecting and discriminating both types of defects, and to assess their severity. Furthermore, the inspection results obtained with the frequency-modulated excitation led to the same conclusions as those obtained with sequential excitation [6], with a significantly shorter cycle time.

The proposed non-destructive acousto-ultrasonic inspection approach appears very promising for a real-time quality control of industrial scale pre-baked carbon anodes. Future work will investigate the application of the inspection scheme to full size anodes collected from an industrial manufacturing plant.

Chapter 5 Inspection of baked carbon anodes using a combination of multi-spectral acousto-ultrasonic techniques

Résumé

Le fonctionnement optimal des cellules d'électrolyse utilisées dans la production d'aluminium primaire est fortement influencé par la qualité des anodes, notamment par la présence de défauts microstructuraux tels que les fissures et les pores. La qualité des anodes commerciales disponibles souffre d'une variabilité croissante due à celle des matières premières. Le système actuel de contrôle de la qualité des anodes précuites consiste à mesurer différentes propriétés basées sur l'échantillonnage et la caractérisation au laboratoire. Cependant, les échantillons ne sont pas représentatifs de la population, car seulement moins de 1% des anodes produites sont analysées. Il y a aussi un délai de plusieurs semaines avant d'obtenir les résultats du laboratoire, ce qui rend le contrôle du processus de rétroaction difficile. Pour faire face à ce problème, un système d'inspection non destructive pour des échantillons d'anodes utilisant des signaux acousto-ultrasoniques et des méthodes statistiques multivariées a été développé, puis amélioré pour application directement sur plusieurs blocs d'anodes industrielles fabriquées par l'usine de Alcoa à Deshambault. Les résultats montrent que les caractéristiques acousto-ultrasoniques dans différentes gammes de fréquences sont sensibles à la présence des défauts ainsi que leur localisation dans les blocs anodiques. Ce travail démontre également les effets de la cuisson sur la qualité des anodes. La validation de cette approche a été accomplie au moyen d'images recueillies après le sciage de quelques anodes parmi celles qui ont été testées.

Abstract

The operation of Hall-Héroult electrolytic cells in the production of primary aluminium is strongly influenced by the quality of baked carbon anodes, and particularly by the presence of microstructural defects such as cracks and pores. The traditional pre-baked anode quality control scheme used by most aluminium smelters consists of measuring different properties based on core sampling and laboratory characterization. However, the samples are not representative of the population, as core samples are typically collected from less than 1% of the manufactured anodes. The delay of several days to obtain the lab results also make feedback process control adjustments difficult to implement in a timely manner. Such corrective actions would greatly help coping with the increasing anode raw material variability (coke and pitch). A non-destructive testing method was previously developed and tested on anode samples using acousto-ultrasonic signals and multivariate statistical methods. This paper reports on the application of the inspection scheme to several industrial scale anode blocks. It is shown that the acousto-ultrasonic features in different frequency ranges were found sensitive to the defects severity as well as their location in the anode blocks. The proposed approach also allowed clustering the anodes according to the conditions under which they were baked. The results were validated using images collected after cutting some anodes.

Key words: Non-destructive testing, acousto-ultrasonics, wavelet analysis, PCA, baked carbon anodes, primary aluminium smelting.

M. Ben Boubaker, D. Picard, J. Tessier, H. Alamdari, M. Fafard, C. Duchesne, Inspection of baked carbon anodes using a combination of multi-spectral acousto-ultrasonic techniques, will be submitted to NDT&E international soon.

5.1 Introduction

The Hall-Héroult electrolytic cells are widely used for primary aluminium smelting. In this process, large carbon blocks acting as anodes distribute the electrical current throughout the cells. They also participate in the electrolytic reduction reaction and therefore, they need to be replaced after a set cycle of about 20-30 days. The baked anodes are often manufactured on site using petroleum coke and coal tar pitch as the main raw materials.

A major concern in the aluminium industry is the declining quality and increasing variability of the anode raw materials. The frequent supplier changes made in order to meet quality specifications while reducing purchasing costs further contributes to incoming raw material variability. Variations in raw materials properties combined with changes in the anode manufacturing process conditions may create internal flaws such as pores and cracks within the anode blocks, which, in turn, affect the performance of the aluminium reduction cells by decreasing their energy efficiency and increasing the specific carbon consumption. The anode quality control scheme widely used throughout the industry consists of collecting core samples from baked anodes according to a well-established sampling plan, followed by core characterization in the laboratory. This control strategy is applied to a small proportion of the anode production (about 1% typically), because it is costly, time consuming and destructive. In addition, the core samples themselves are not necessarily representative of the whole anode block which properties are known to be spatially anisotropic (a core sample is about 0.1-0.2% of the block volume). Furthermore, lab characterization results are often available after a delay of several days, which limits the application of feedback corrective actions to the manufacturing process in a timely fashion. Hence, there is a need for developing rapid and non-destructive techniques to assess baked anode quality before setting them in aluminium reduction cells.

Empirical models have been proposed to predict individual baked anode quality, for instance net carbon consumption [78, 325], which is considered as an overall indicator of anode performance. Raw material properties and/or process data are used as model inputs. Other authors have applied latent variable modeling techniques for predicting the baked anode properties measured from core samples [90, 93]. The models were built using routinely collected historical data, from raw material properties to process parameters and final anode core properties. Multivariate statistical methods, such as Principal Component Analysis (PCA) and Partial Least Squares (PLS) regression were used to estimate the models. Empirical models allow making predictions on anode properties as soon as the input

data is available (no need to wait for lab results). However, they do not provide direct information on the anode internal structure, and are limited by the quality of the routinely measured plant data and their sampling frequency.

Current research focuses on developing rapid and non-destructive sensors for quality assessment of individual anode blocks. Electrical resistivity measurements systems are being developed for green [119, 295, 327] and baked anodes [114,115] based on different technologies. These new devices provide measurements for the resistivity distribution within the anodes, a very important property affecting reduction cell performance. However, their capacity to detect and locate defects within them, and to identify and discriminate different types of flaws has not been demonstrated yet. The defect diagnosis phase is, however, crucial for decision making on what actions operators should implement on the anode manufacturing process and/or whether an anode should be rejected and recycled back to the manufacturing plant.

The acoustic emission technique (AE) has been considered for the inspection of various materials and processes [152, 237, 328]. Non-destructive evaluation based on acoustic signals and multivariate statistical techniques was also tested on different porous materials other than carbon anodes [282, 283, 330]. An apparatus, based on sonic wave propagation, was developed to measure the physical properties of refractory and carbonaceous materials including anode materials [299, 301]. It was primarily designed for characterizing the materials, but can also detect large flaws on small samples having simple geometries. A combination of acousto-ultrasonic techniques and PCA for data clustering was recently proposed for anode quality assessment [309, 332]. This approach was tested on smaller anode parts (slices) and its ability to detect voids and to discriminate between pores and cracks was demonstrated. The present work reports on the application of the method to a number of industrial scale anode blocks selected based on the presence (or absence) of externally visible defects, and differences of processing conditions under which they were manufactured. The method was able to detect the presence of cracks within large anode blocks and was sensitive to the damage severity (volume of voids). It was also possible to locate the cracks and provide indications on their orientation within the anodes. This paper also shows that the proposed approach may be able to discriminate the anodes based on difference in the thermal history under which they were baked, which is known to impact on their internal structure. The results obtained with the proposed approach were

validated by cutting a certain number of anodes and collecting images of the internal surfaces.

5.2 Materials and experimental set-up

A total of 27 industrial-scale baked anodes were obtained from the Alcoa Deschambault Quebec (ADQ) smelter. In order to test the proposed approach, it was necessary to select anodes of different quality including defect free anodes, and some containing defects of different types and sizes (severity). Since this task is difficult to achieve without destroying the blocks to get access to their internal structure, it was decided to sample anodes belonging to three groups, as shown in Table 5-1. The first group of anodes had defects visible from their external surfaces. For example, anodes A2, A3, and A7 contain large transversal cracks, and anodes A8, A12, and A13 show surface degradation mainly caused by burning of the material during the baking operation. The second group had no externally visible defect but were manufactured under different process conditions. Anodes A14 and A15 were produced during plant start-up whereas A16-A27 were baked in different positions within the furnace where they have been submitted to a more or less severe thermal history. The last group (anodes A1, A4, A5, A6, A9, A10 and A11) had no external defects but some of their manufacturing conditions could not be retrieved (i.e. baking positions).

Table 5-1 Anode numbers and description.

Anode description	Anode numbers
Visible external defects	
Transversal cracks	2, 3, 7
Degradation and burn	8, 12, 13
Produced under different conditions (no external defects)	
Start-up anodes	14,15
Different baking positions	16-27
No external defects but baking position unknown	1, 4, 5, 6, 9, 10, 11

The experimental set-up shown in Figure 5-1 was used to measure the propagation behavior of the mechanical waves through the tested industrial anodes. First, the blocks were flipped on their side onto two steel bars isolated from environmental vibrations using rubber parts. It was safer to turn the anodes on their side because the acoustic sensors were mounted manually on the blocks. Flipping of the anodes would not be necessary using an industrial automated set-up. A computer generated acousto-ultrasonic frequency modulated wave was sent through the material by a transmitter in order to excite the anode

block on one surface, and the attenuated response wave was recorded by the receiver located *vis-à-vis* the transmitter but on the opposite surface. Both acoustic sensors were held in place on the anode using hot glue. Alternatively, an automated mechanical clapping device could be designed to maintain the sensors in place by applying a certain pressure on them. Coupling gel could also be applied between the sensors and the anode surface to ensure good contact (if necessary). After several preliminary tests, it was determined that exciting the anodes in the 100-200 kHz frequency band was the most relevant range for detecting and discriminating anode defects [332].

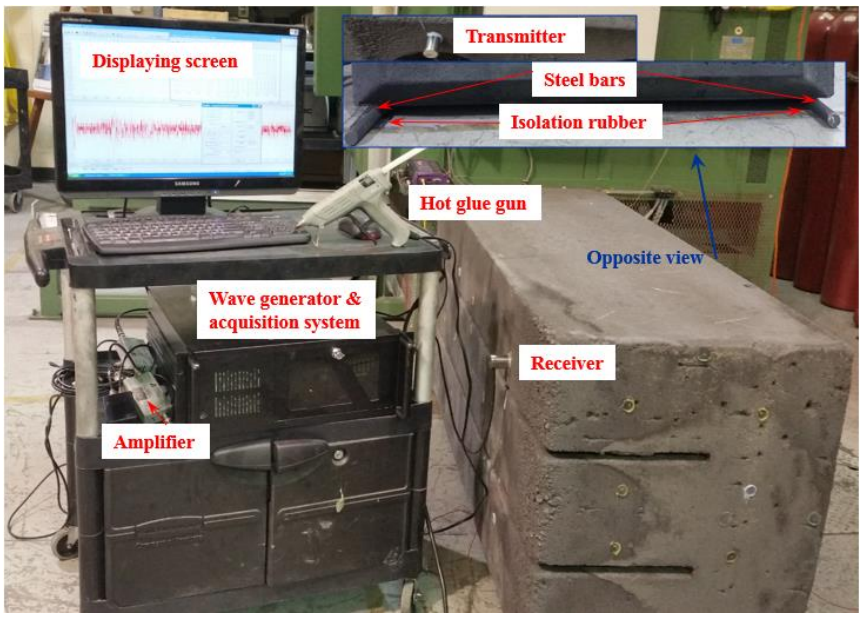

Figure 5-1 Experimental acousto-ultrasonic measurement set-up.

The measurements were collected at 29 different positions on each anode as shown in Figure 5-2. For the excitation points 1-21, the sensors were mounted on the top and bottom surfaces in order to measure the acoustic wave attenuation across the anode height. The attenuation along the length of the anode (long side) was obtained from the last 8 excitation points (22-29). The anodes were tested in both directions to assess whether it is possible to discriminate defects having different orientations in the block (e.g., cracks oriented horizontally, vertically or diagonally). Indeed, the mechanical wave should be more attenuated by cracks oriented in the perpendicular direction to the wave propagation front for a given defect size. Hence, the excitation points 1-21 should better capture defects mostly oriented horizontally while points 22-29 should capture vertically-oriented defects more clearly. Diagonal cracks are expected to affect the signal in both directions. Some excitation points could not be tested for a few anodes because of physical damage at that

location (e.g., sensors could not be mounted due to piece broken off). Two templates made of cardboards were prepared and used to ensure that the excitation and measurement points on the four surfaces were always at the same location for all tested anodes. The wave attenuation data were gathered sequentially (one position at a time) but could also be made simultaneously by using several pairs of sensors, which would make the method applicable for real time control.

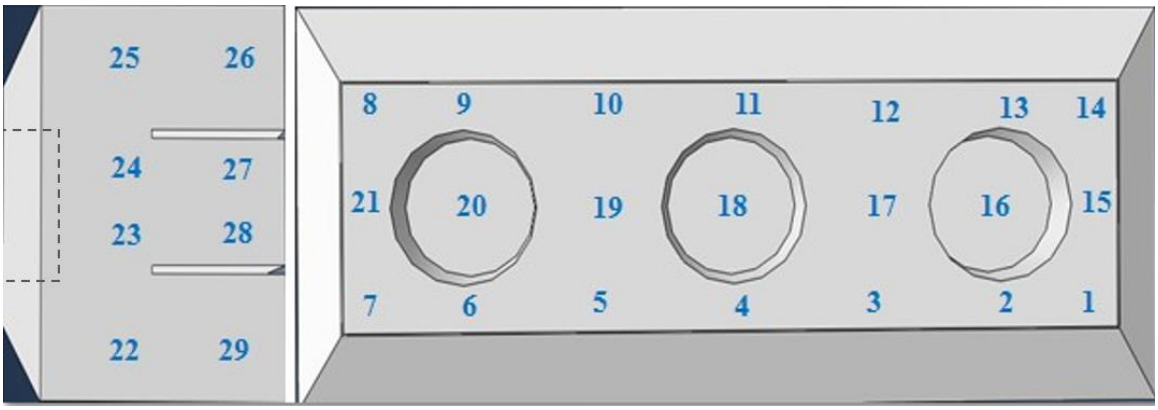

Figure 5-2 Location of the 29 excitation positions on each anode.

5.3 Processing and analysis of acousto-ultrasonic signals

The anodes are complex spatially anisotropic and porous materials. They always contain pores and sometimes defects such as cracks. Both types of voids attenuate the propagation of mechanical waves, but the main objective is to detect the signature of cracks within the blocks. This is possible to achieve using the experimental set-up detailed previously. Indeed, Figure 5-3 shows the difference between the attenuated waves (responses) collected from an anode containing cracks and porosity (highly attenuated) and another from an anode containing only porosity (slightly attenuated signal). The acoustic data clearly shows that signal of the damaged anode is more attenuated, and the time required for the wave to arrive at the receiver sensor (i.e., arrival time or AT) is longer than that of the sounder anode.

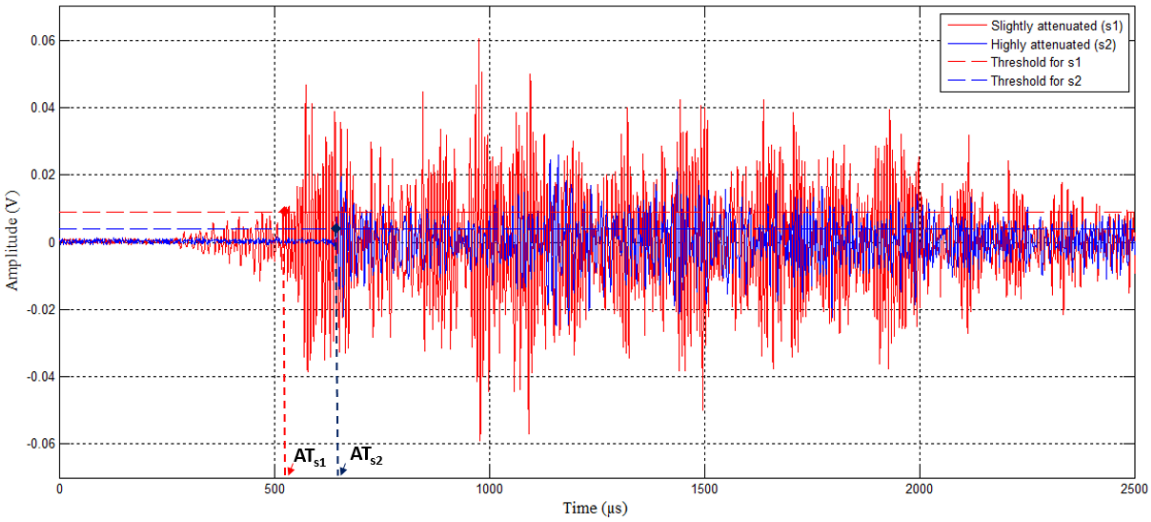

Figure 5-3 Examples of two raw acoustic signals with varying degree of attenuation.

In order to detect damaged areas and to obtain indications on the severity of the flaw from the 29 excitation points on each anode, the signal processing and analysis framework shown in Figure 5-4 was established. The signals were first pre-processed by truncating after the first 1365 points (or about 1023 µs), instead of original signal length of 4095 points. This was performed to eliminate the influence of reflections from the anode sides, and helps detecting defects and discriminating the anodes since the remaining three quarters of the signals were found very similar for all anodes. Signal truncation is not shown in Figure 5-4. Thus the truncated signal is considered as the raw input signal to the analysis framework.

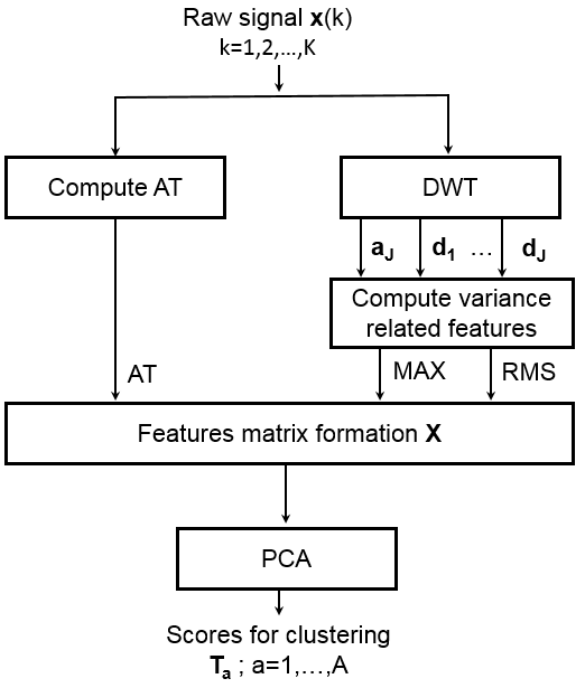

Figure 5-4 Signal processing and analysis framework.

The acoustic features calculated from each discrete raw signal **x**(k), k=1,2,…,K (i.e., attenuated wave signal at one excitation point) were obtained using the approach described in previous work [332]. Since the excitation signal is a frequency-modulated wave (multi-frequency), it was first decomposed into a certain number of frequency bands using the Discrete Wavelet Transform (DWT). The attenuation of the sub-signals in each frequency band was then quantified by two scalar features: the maximum sub-signal value (MAX) and its root mean square (RMS). In parallel, the time of flight or the arrival time (AT) of the raw signal was also calculated. The AT calculated from the raw signal and the MAX and RMS features computed at each sub-band for all excitation points and all anodes were then collected and organized into a feature matrix **X**. The data in **X** were organized in two ways in order to answer different research questions (more on this later). Principal component analysis (PCA) was then applied to the feature matrix **X** in order to cluster the anode based on their acoustic responses. More details on the various steps of the method are provided next.

5.3.1 Acoustic attenuation features

The DWT decomposes the raw signal **x**(k) into J+1 sub-band signals by means of a filter bank [322]. The user first selects a mother wavelet (finite length wave of a particular

shape) mathematically represented by two orthogonal functions, namely the scaling and wavelet functions. Both functions are expressed as filters which cutting frequency can be modulated at discrete dyadic values or so-called wavelet decomposition levels j=1, 2, …, J. High frequency information is extracted from the raw signal at the first level (j=1). Subsequent decomposition levels (j=2, 3, …, J) progressively extract lower frequency components. The convolution (or inner product) of the raw signal **x**(k) and the scaling and wavelet functions at J decomposition levels yields a set of detail coefficients vectors $\mathbf{d}_j(k)$ j=1, 2, …, J, representing the degree of similarity of the raw signal with the wavelet function at a given scale (or frequency). The convolution with the scaling function after J decomposition levels leads to the approximation signal $\mathbf{a}_J(k)$ containing the residual low frequency information of the signal after J decomposition levels. In this work, the Daubechies wavelet (Db5) [333] was selected since it matched the shape of the signal fairly well. Four decomposition levels (J=4) were found sufficient to allow good defect detection and anode discrimination performance.

As illustrated in Figure 5-4, the MAX and RMS scalar features were calculated from all detail coefficient vectors $\mathbf{d}_j(k)$ j=1, 2, …, J and the final approximation vector $\mathbf{a}_J(k)$ as shown below, where **s**(k) represents a detail or the approximation vectors:

$$MAX = \max_{k=1}^{K} \mathbf{s}(k) \tag{5.1}$$

$$RMS = \sqrt{\frac{1}{K}\sum_{k=1}^{K}[\mathbf{s}(k)]^2} \tag{5.2}$$

The velocity of the acoustic wave is also affected by the presence of any flaw in the anode. It can be evaluated by calculating the arrival time of the corresponding waves directly from the raw signal. The arrival time can be easily calculated by setting a threshold relative to the magnitude of the signal and recording the time of the first threshold crossing [247, 335]. It was found that setting a threshold amplitude at 15% of the raw signal maximum value provided adequate results. This is slightly higher than typical threshold values (e.g., 10% [247]), but was necessary due to a higher level of baseline noise. The baked anodes are porous materials containing discontinuities (i.e., pores and cracks) which generates scattered waves and consequently a higher level of noise. All calculations described in this subsection were implemented in the Matlab software version R2014a (MathWorks, Natick, MA, USA), using custom scripts.

$$AT = k \qquad \text{When} \qquad [\mathbf{x}(k) \geq 0.15 \times \max(\mathbf{x}(k))] \tag{5.3}$$

As mentioned earlier, the data were arranged in two different ways, depending on the objective of the analysis: comparing the overall acoustic response of the anodes (between anode variability) or analyzing the within anode variability. The signal processing framework shown in Figure 5-4 yields a total of 2(J+1) +1 attenuation features for each excitation point and for each anode (i.e., 11 features since J=4). In order to compare the overall anode responses, the features computed for all excitation points for each anode were stored row-wise in the $\mathbf{X_b}$ matrix which dimensions are (27×319). The number of rows correspond to the total number of anodes, and the number of columns to the product of the number of excitation points and the number of attenuation features (29×11=319). To investigate the within anode variability, the attenuation features for each excitation point for a given anode were stored row-wise in $\mathbf{X_w}$, and the data for all anodes were concatenated vertically. In this case, $\mathbf{X_w}$ is (783×11) dimensional since there are 27 anodes and 29 excitation points for each (27×29=783 rows), and 11 attenuation features (columns). Note that data for some excitation points are missing because the measurements could not be collected for some anodes, as mentioned previously. Also, these feature matrices were subsampled in the different case studies presented later in order to emphasize certain results.

5.3.2 Analysis of the acoustic features using PCA

The acoustic attenuation features matrices $\mathbf{X_b}$ and $\mathbf{X_w}$ have large dimensions and their columns are highly collinear. Principal Component Analysis (PCA) was therefore applied for dimensionality reduction and for coping with the inter-correlated features. PCA performs the following bilinear decomposition of the variance-covariance of a data matrix **X** (I×M):

$$\mathbf{X} = \sum_{a=1}^{A} \mathbf{T_a P_a}^{T} + \mathbf{E} \tag{5.4}$$

Where $\mathbf{T_a}$ (I×1) is the lower dimensional subspace formed by the A orthogonal score vectors (**T**'s), and $\mathbf{P_a}$ (J×1) contains the corresponding orthonormal loading vectors which are linear combinations of the original variables (i.e. $\mathbf{T_a} = \mathbf{X}\ \mathbf{P_a}$). The model residuals are gathered in the residual matrix **E** (I×M). The components (pairs of **T**'s and **P**'s) are ordered in such a way that the first component ($\mathbf{t_1}$) captures the greatest amount of variations in the data, whereas the second component captures the greatest amount of variance orthogonal to the first, and so on. In this application, PCA clusters the anodes as a function of their

acoustic attenuation features. The clustering pattern can be observed in scatter plots of scores ($\mathbf{T_a}$'s). Loading plots ($\mathbf{P_a}$'s) are used to interpret the clustering patterns based on changes in the attenuation features. For more details on PCA the reader is referred to Wold et al. [277]. The PCA models were built using the ProMV software version 15.08 (ProSensus, Ancaster, ON, Canada). The data matrices were all mean-centered and scaled to unit variance (auto-scaling) prior to applying PCA.

5.4 Results and discussion

The potential of the proposed acousto-ultrasonic technique for baked anode inspection is demonstrated using three case studies. The first two focus on showing the capacity of the method to detect defects and assess their severity by comparing the overall acoustic responses of the anodes (i.e., between anode variability). Indeed, the primary objective of the system is to determine whether an anode is sound enough to be set in the reduction cells or should be sorted out of the production line and recycled because it is damaged too severely. The first case study concentrates on the acoustic responses measured through the stub holes because cracks are known to develop underneath them due to the anode forming process. In the second, all measurement points are used to show that the overall anode responses can be discriminated based on the thermal history under which they were baked. Finally, the third case study illustrates how to assess the within anode variability in order to locate the defects and obtain more detailed information about the anode blocks. These pieces of information would help diagnose the source of the flaw and determine if feedback corrective adjustments should be implemented on the manufacturing process.

5.4.1 Defect severity underneath stub holes

The dataset used for the first study was formed by extracting the attenuation features obtained from excitation points 16, 18 and 20 (see Figure 5-2) from the $\mathbf{X_b}$ feature matrix. The resulting $\mathbf{X_{b,stub}}$ dataset of dimensions (27×33) was subsequently modeled by Principal Component Analysis. A total of 6 principal components (PC's) were found to be statistically significant by a standard cross-validation (CV) procedure. The cumulative percentage of the variance of the features explained (R^2_{cum}) and predicted (Q^2_{cum}) by the PCA model after 6 PC's were 94.89% and 87.76%, respectively. However, only the first two components are investigated in this case study because they were found sufficient to cluster the anodes

according to defect severity. The variance explained and predicted by the first two PC's are provided in Table 5-2.

Table 5-2 Cumulative percent of the variance of $X_{b,stub}$ explained and predicted by PCA.

Components	R^2_{cum} (%)	Q^2_{cum} (%)
1	70.26	64.56
2	80.84	71.75

A scatter plot of the scores ($\mathbf{t_1}$-$\mathbf{t_2}$) is presented in Figure 5-5. The clustering pattern shows four different anode groups spread along the $\mathbf{t_1}$ direction and identified by dots of different colors (blue, orange, black, and green). The second component, however, does not discriminate the groups as much as the first PC. The variability along this direction seems to affect all the groups. The anodes identified by black dots are more spread than others in the $\mathbf{t_2}$ direction.

In order to interpret the clustering pattern in the score space based on changes in the attenuation features, the loading plot of the first two PC's ($\mathbf{p_1}$-$\mathbf{p_2}$) presented in Figure 5-6 is examined. In this plot, each point corresponds to one attenuation feature. These were labelled by their names (MAX or RMS), followed by the wavelet sub-signal and decomposition level (details or approximation), and the excitation point number. For instance, label MAXD3_18 refers to the maximum value calculated from the vector of detail coefficients at the 3rd decomposition level ($\mathbf{d_3}$) of the raw signal measured at excitation point #18. The arrival times were simply identified by AT followed by the excitation point number. To interpret the plot, it is important to understand that the sign of the loadings indicates whether the correlation between the features is positive (same signs) or negative (opposite signs), and their absolute value is proportional to the importance of the corresponding features in a given component. In the first PC, the variance-related features (MAX and RMS) are all positively correlated to each other because their loadings have the same sign, but are negatively correlated with arrival times. Hence, the anodes clustering in the negative $\mathbf{t_1}$ region have higher arrival times and lower MAX and RMS values, and those projecting in the positive $\mathbf{t_1}$ region have the opposite combination of features. This means that the defect severity increases from right to left in the score plot (along the $\mathbf{t_1}$ axis). Indeed, a more damaged material slows down the wave propagation and attenuates the signal more significantly.

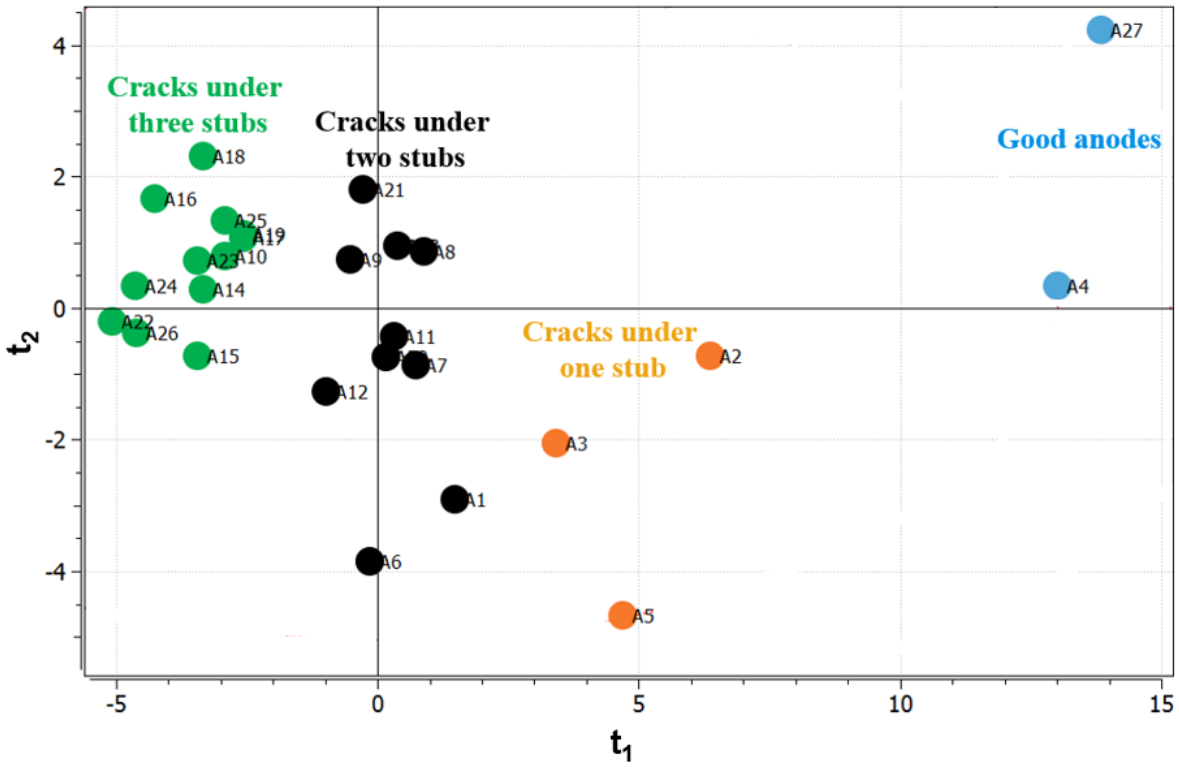

Figure 5-5 PCA score plot (t_1-t_2) of the anode responses underneath the stub holes.

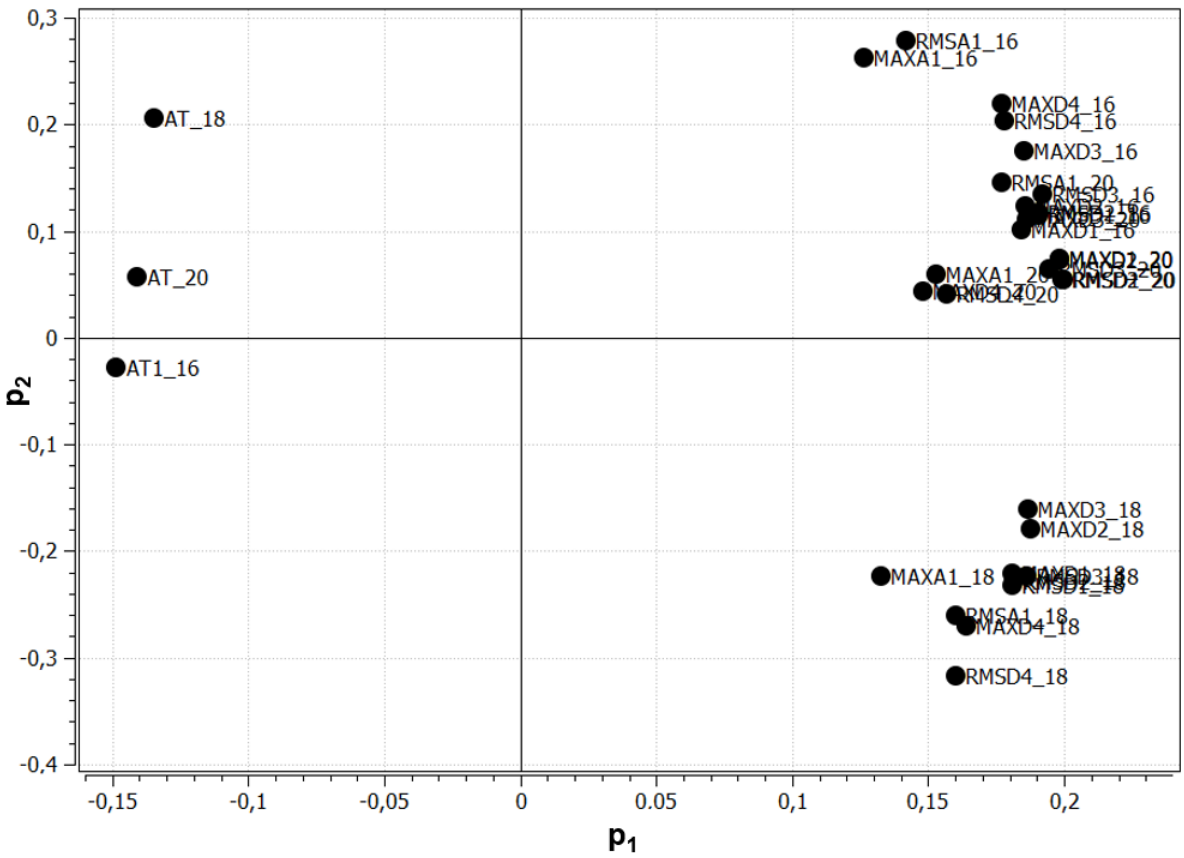

Figure 5-6 PCA loadings plot ($\mathbf{p_1}$-$\mathbf{p_2}$) for the anode responses underneath the stub holes.

To validate the information captured by the first component, a certain number of anodes were cut after collecting the acousto-ultrasonic measurements, and images of their internal surfaces were collected. Examples of those images are shown in Figure 5-7. These images support the observations made on the four clusters identified in Figure 5-5. Note that the size of the cracks in these images has been manually enlarged for a clearer visual appreciation. The images of anodes A4 and A27, belonging to the blue group in Figure 5-5, clearly show the absence of cracks underneath the stub holes. The cut of anode A5 (orange group) shows a long horizontal crack extending from the right edge to the region below one stub hole. Cracks under two stub holes are observed in the images of anodes A11 and A20 (black group). Finally, all the other anodes shown in Figure 5-7 (A14, A17-A19, A23, A24, A26) belong to the green clusters and all of them contain cracks underneath the three stub holes. Therefore, the first component seems to capture variations in the features related with the presence of cracks and their severity (total void volume associated with cracks).

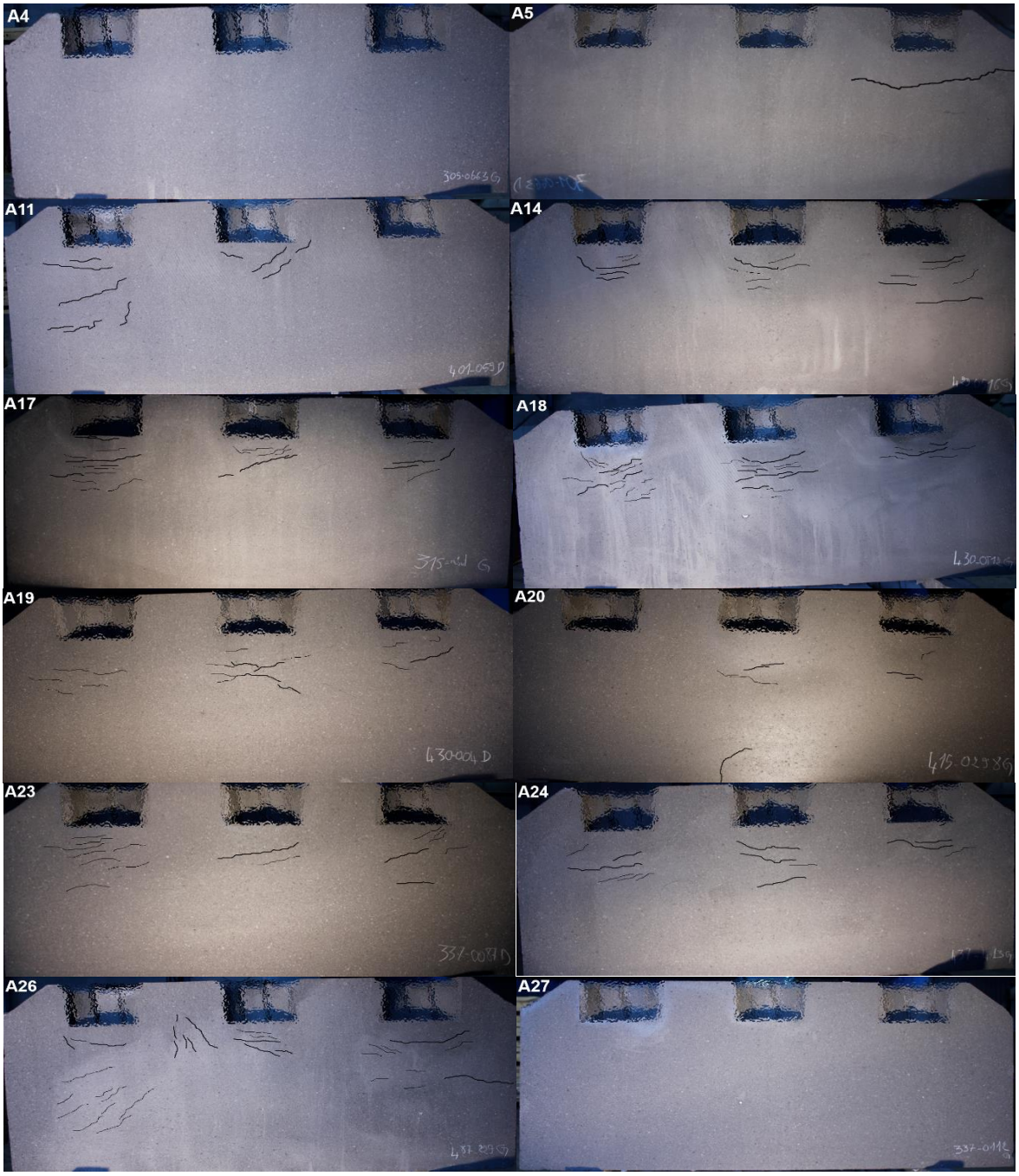

Figure 5-7 Images of cuts made on some tested baked anodes. The anode number is indicated in the top left corner of each image.

The second component, however, captures a different source of variation since the PC's are orthogonal to each other. The loading plot (Figure 5-6) reveals that the features computed for excitation point #18 vary in opposite direction to those of points #16 and #20 in the PC2 direction. Based on the signs of the $\mathbf{p_2}$ loading values, it can be said that the anodes falling in the negative $\mathbf{t_2}$ region show less attenuation at the center (point 18) than at

both ends of the anodes (points 16 and 20). The anodes projecting in the positive $\mathbf{t_2}$ region of the score plot (Figure 5-5) show the opposite behavior. The variations captured by the second component seems related with an uneven distribution of the anode properties along its length. Fluctuations in the anode formulation and/or in the processing conditions during the anode paste mixing and forming operations may explain spatial variations of the properties within the anodes. However, this could not be verified at the time the experiments were conducted. Nevertheless, this result shows the potential of the approach for detecting changes in the anode homogeneity.

5.4.2 Effect of baking position

This section investigates the sensitivity of the acousto-ultrasonic signal features to the thermal history of the anodes during baking. It is well known in the field that anodes baked in different positions within open-top ring furnaces are submitted to slightly different temperature profiles, and this may affect their internal structures as well as the development of their mechanical properties. Indeed, Figure 5-8 shows how the anodes are organized and stacked in the pits of one section in a typical furnace. Pit #1 is adjacent to the external wall whereas pit #6 is located close to the center of the furnace. The thermal history of the anodes vary according to where they were positioned in the furnace as shown in Figure 5-8. The position of the anodes is identified by the pit number, followed by the row and column number in which they were placed. A total of 12 anodes baked in warmest, intermediate and coldest regions of the furnace (positions 111, 222 and 333 or red, green and blue colors in Figure 5-8) were sampled (4 anodes/position). The baking position of the rest of the anodes (27-12=15) were unknown. The aim here was to verify whether the inspection scheme could cluster the anodes based on those baking positions. The complete $\mathbf{X_b}$ (27×319) data matrix including all 29 excitation points was decomposed by PCA. Although 9 principal components were found significant by cross-validation (R^2_{cum}=86.87% and Q^2_{cum}=56.98%), only the statistics for the first two components are presented in Table 5-3. These two components were found sufficient to cluster the anodes according to their baking position.

Table 5-3 Cumulative percent of the variance of $\mathbf{X_b}$ explained and predicted by PCA.

Components	R^2 (%)	Q^2 (%)
1	47.33	37.98
2	56.38	41.29

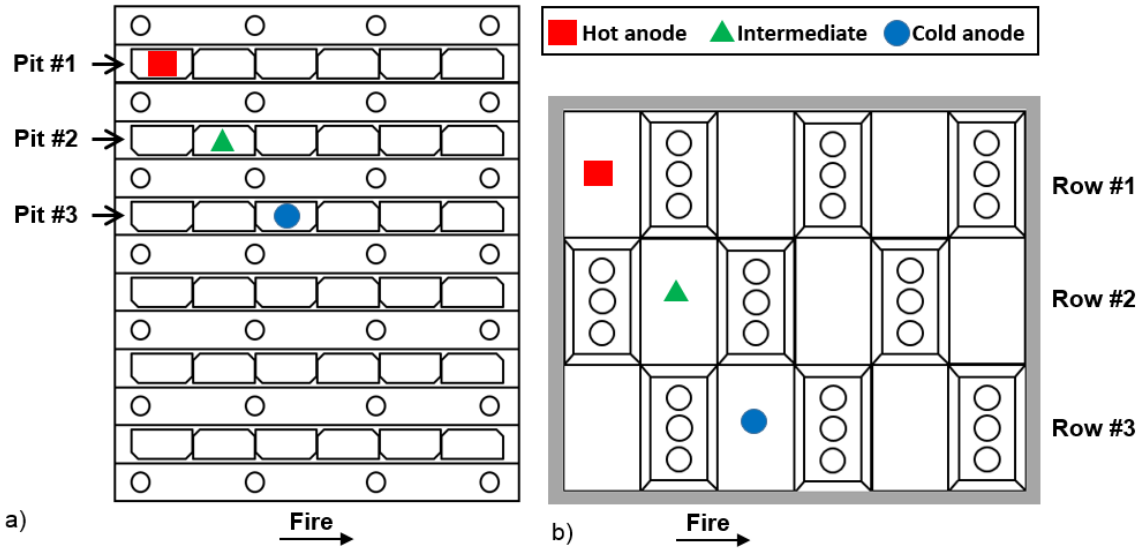

Figure 5-8 Different baking positions; a) Top view of one furnace section, b) Side view of one pit. Positions 111, 222 and 333 correspond to the warmest (red), the intermediate (green), and the coldest (blue) regions in the furnace.

The score plot ($\mathbf{t_1}$-$\mathbf{t_2}$) of the PCA model is presented in Figure 5-9. The anode baking positions are identified using the same colors as in Figure 5-8. In general, a trend seems to exist between damage severity and the baking positions, since the anodes cluster roughly according to them. The loading plot ($\mathbf{p_1}$-$\mathbf{p_2}$) shown in Figure 5-10a) leads to a similar interpretation for the first component as in the previous case study, that is damage severity increases from right to left in the score plot. Most of the anodes baked in the warmest position (111) fall in the more damage region (negative $\mathbf{t_1}$ values) whereas those baked in the coldest position (333) cluster in region where the anodes are less damaged (positive $\mathbf{t_1}$ values). The anodes baked in position 222 fall in between the two extremes. A possible explanation for this clustering pattern is that the anodes baked under warmer conditions may have been submitted to a higher heating rate which could have led to a faster degassing of pitch volatile components, and an increasing the number and/or size of the cracks within the material. However, this could not be confirmed. Anode A26 project in the damaged region although it was baked in the coldest position. Such confounding between classes is expected since baking position is not the only factor affecting the development of cracks. Figure 5-7 indeed confirms that anode A26 contains several cracks. The anodes identified by black dots (baking positions unknown) span the entire score space, but no link can be made between damage severity and thermal history during baking for those.

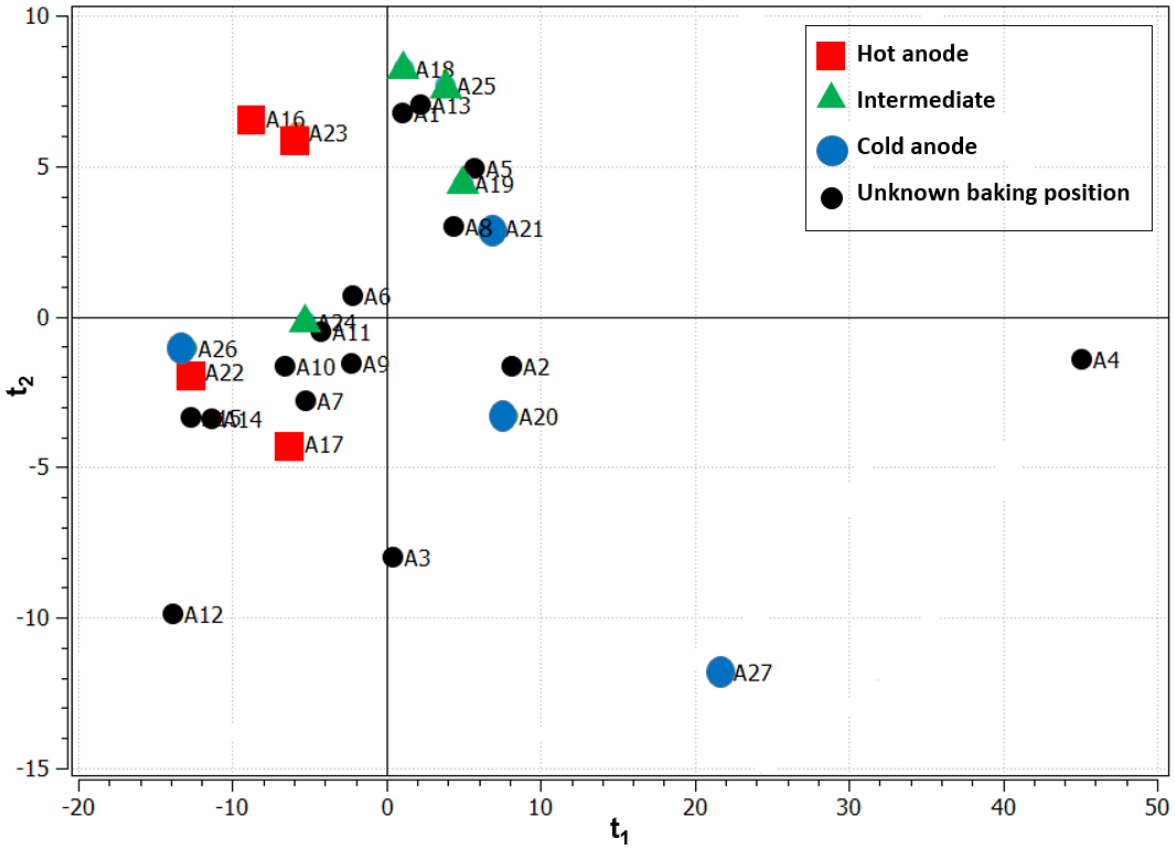

Figure 5-9 PCA score plot (t_1-t_2) obtained using the data collected for all excitation positions. The colors indicate the anode baking positions in the furnace (red: 111; green: 222; blue: 333; black: position unknown).

The loadings of the second component (PC2) are difficult to interpret based on Figure 5-10a) only because of the larger number of features (the figure is cluttered) and the absence of spatial mapping of the loadings on the anodes (i.e., the 29 excitation points in Figure 5-2). To clarify the interpretation of the second component, the signs of the PC2 loading values for the MAX feature were indicated next to the excitation point numbers on the anodes as shown in Figure 5-10b). Negative and positive loading values were identified using blue and red colors, respectively. Again in this case, the second component seems to capture spatial variations in anode properties within its volume, as the MAX features for the region in red vary in a negatively correlated fashion relative to those of the region in blue. The reasons for this behavior are similar as those invoked in the first case study (i.e., changes in anode paste formulation and process conditions). Note that overlying the signs of the loadings for the RMS features would lead the same conclusions since RMS is very highly collinear with MAX. Plotting the AT loadings would only change the signs of the loadings since AT is negatively correlated with MAX and RMS, but this would not change

the interpretation. Finally, the conclusion regarding excitation points 16, 18, and 20 seems different than the one reached in the first case study (i.e., they vary together instead of 18 against 16 and 20). This is explained by the fact the data used in this case include all the features and more variability compared to the first case. Hence, the PCA model captures more dominant source of variations than that of the center versus the edges. Additional components (PC's) may capture the more subtle variations related with the stub hole regions.

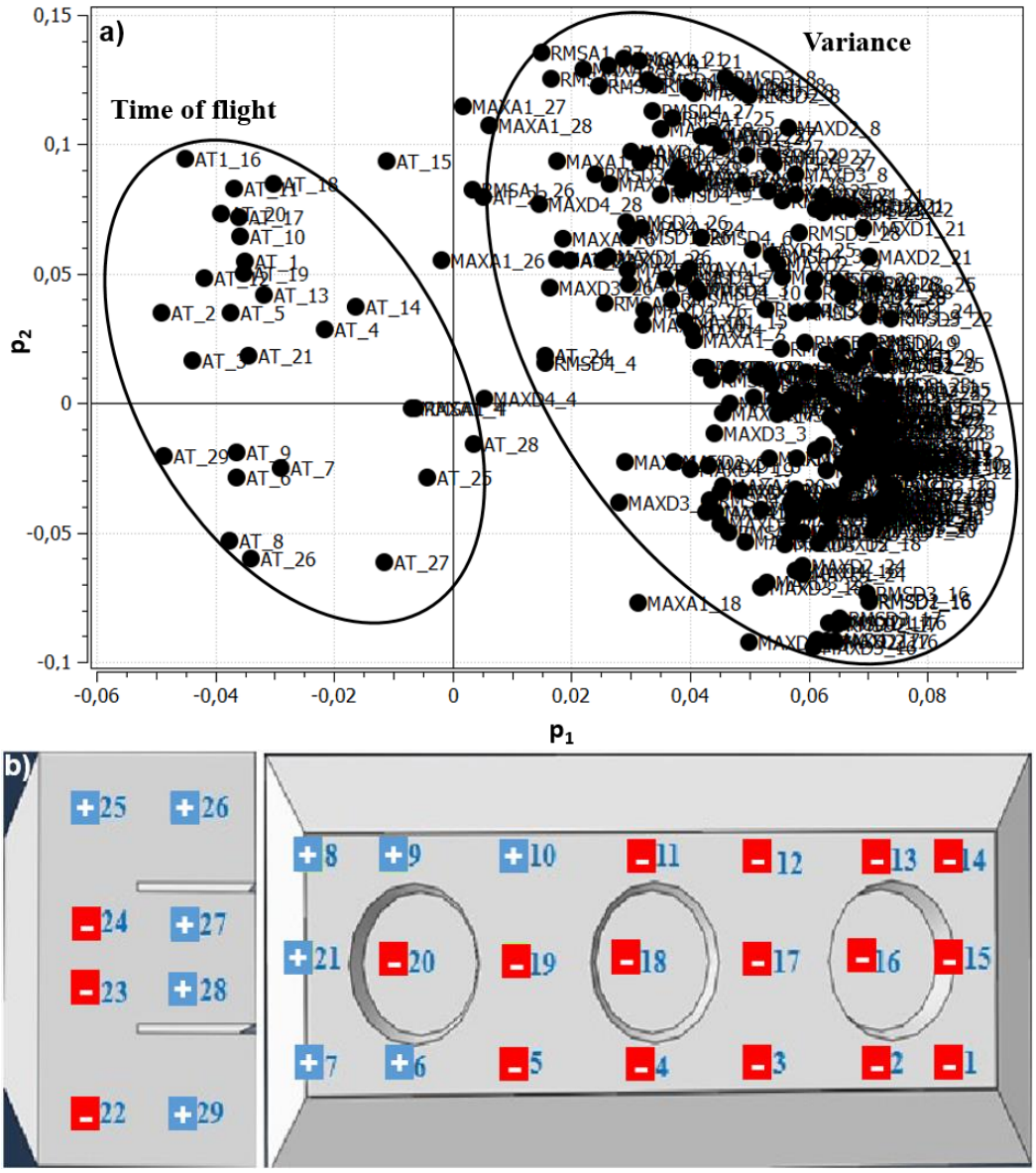

Figure 5-10 PCA model built using all excitation points. a) Plot of the loadings ($\mathbf{p_1}$-$\mathbf{p_2}$), b) map of signs of the $\mathbf{p_2}$ loadings on the anodes.

5.4.3 Assessment of the within anode variability

The intra anode variability is investigated separately for the signals collected across the anode height (points 1-21) and its long side (points 22-29), because the material thickness in between the sensors is significantly different in these two cases. Furthermore, the excitation points collected in the stub holes (points 16, 18, and 20) are also analyzed separately from points 1-21 for the same reason (i.e., the stub holes are a few inches deep). Systematic differences between the three sets of signals are expected because thicker materials attenuate the signal to greater extent, but these variations are irrelevant in the inspection problem. Hence, separate PCA models were built on each set of excitation points. The following two subsections examine the anode responses in the longitudinal direction first. Then, a signal attenuation map using the first component of all three PCA models is proposed to illustrate a potential anode inspection scheme.

5.4.3.1 Excitation along the longitudinal direction (points 22-29)

The data obtained from the 8 excitation points (22 to 29) on each of the 27 anodes were extracted from $\mathbf{X}_w$, resulting in a (216×11) dataset. However, for illustration purposes, it was decided to concentrate on 4 anodes spanning the score space of the PCA model built using all the anodes. The selected materials include a sound anode (A4), one containing a crack extending in the horizontal direction along the anode length (A5), and two anodes containing cracks in the vertical direction along the anode height (A3 and A7). The internal structure of anodes A4 and A5 can be visualized in Figure 5-7. The cracks in anode A3 and A7 are shown in Figure 5-11. These two anodes were not cut because the cracks were visible from the surface.

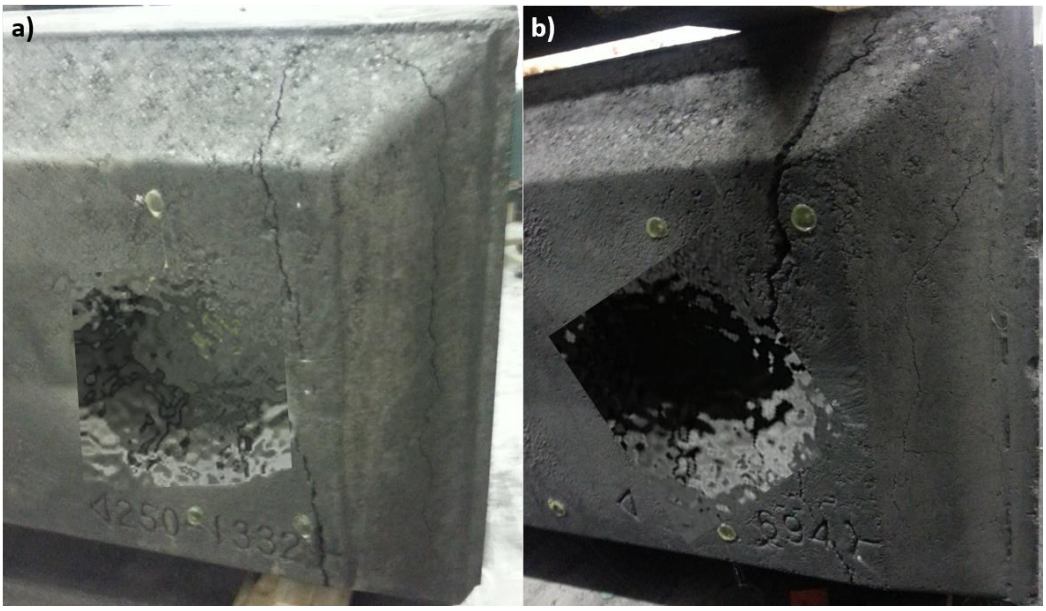

Figure 5-11 Pictures of the most severely damaged anodes, a) A3 and b) A7.

PCA was applied to the reduced dataset $\mathbf{X}_{w,L}$ (32×11). Four principal components were found statistically significant by cross-validation. The model statistics are presented in Table 5-4.

Table 5-4 Cumulative percent of the variance of $\mathbf{X}_{w,L}$ explained and predicted by the PCA model built on anodes A3, A4, A5 and A7.

Components	R^2_{cum} (%)	Q^2_{cum} (%)
1	74.20	72.21
2	86.04	82.88
3	93.30	91.77
4	96.96	95.66

The PCA score and loading plots for the first two components are shown in Figure 5-12 and Figure 5-13, respectively. Different colors are used in the score plot to identify the measurements collected from each anode (A4: black; A5: red-orange; A3: green; A7: blue). The scores clearly show that the measurements collected on the sound anode (A4) cluster in the right hand side of the plot, whereas the most severely damaged anodes (A3 and A7) project in the left hand side. This separation along $\mathbf{t}_1$ is again explained by the overall attenuation of the acoustic signals as shown by the PC1 loadings (Figure 5-13). A shift towards the left is also observed for those excitation positions where defects were detected (see dashed areas on the anodes in Figure 5-12). In the case of anode A5, the measurement points 26-29 all cluster in the sound material region close to anode A4, but those collected for positions 22-25 are significantly shifted towards the left (more damaged region). The

image of anode A5 in Figure 5-7clearly shows the presence of a horizontal crack extending in the region below the stub holes and above the sluts. A similar behavior is also observed for anode A7, but this material globally attenuates the signals to greater extent, as all measurement points are located further to the left compared to A5. Anode A3 also attenuates the signals more significantly. However, all the excitation points shift towards negative $\mathbf{t_1}$ values, except for position 29. This indicates that the region where the crack is present covers a larger area in the anode compared to A5 and A7. Finally, the relative position in the score plot of anodes A3 and A7 with respect to A5 seems consistent, because the cracks in the former two anodes are oriented in the perpendicular direction to the wave propagation front, and thus attenuates the wave more significantly compared to A5 in which the crack is parallel to the wave.

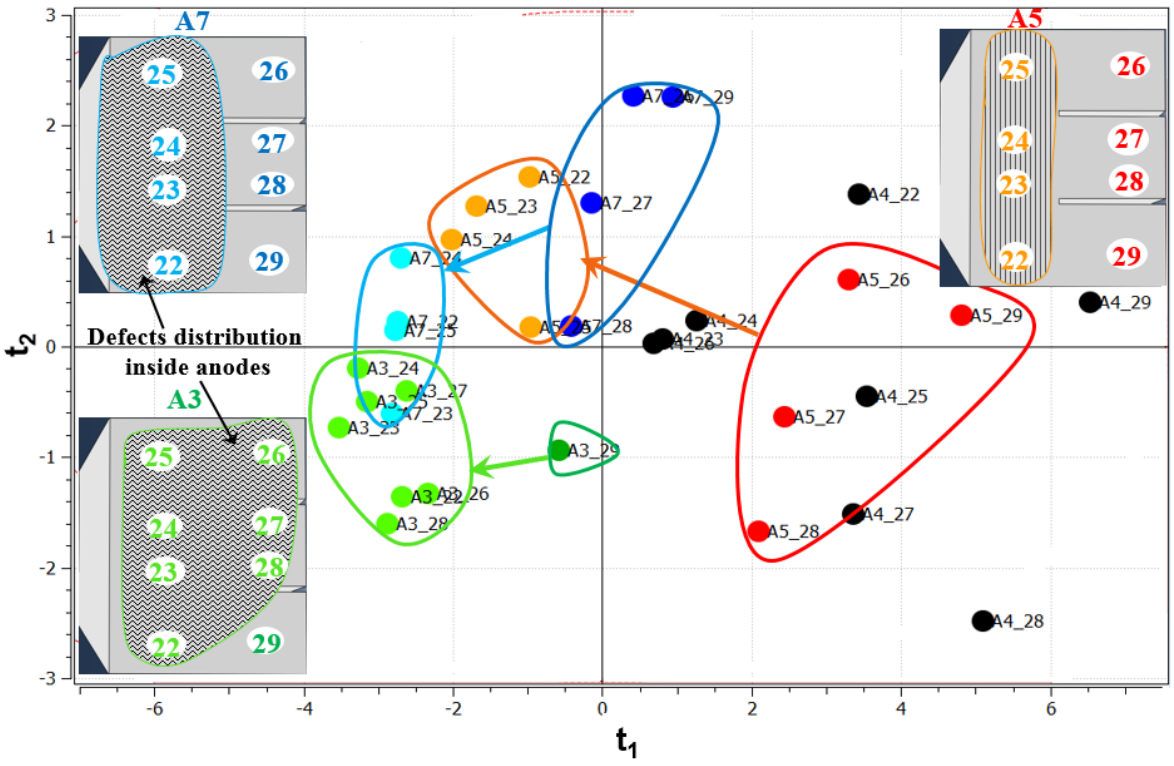

Figure 5-12 PCA score plot ($\mathbf{t_1}$-$\mathbf{t_2}$) showing the intra anode variability in the longitudinal direction (excitation points 22-29).

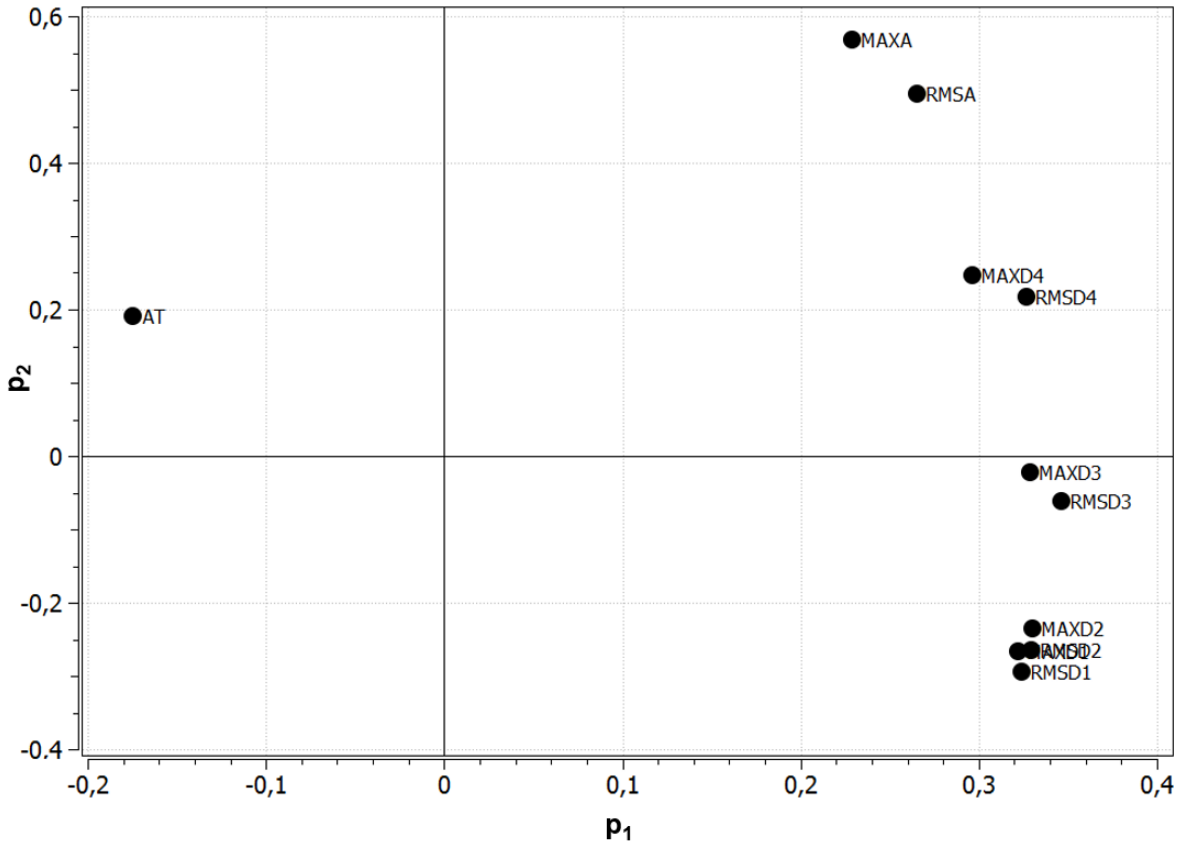

Figure 5-13 PCA loadings ($\mathbf{p_1}$-$\mathbf{p_2}$) capturing the intra anode variability in the longitudinal direction (excitation points 22-29).

The second component captures a contrast in the acoustic attenuation features in different frequency ranges. Indeed, the low frequency components of the signal (wavelet approximation and d_4 sub-signals) have the same sign in PC2, but opposite signs compared to the higher frequency sub-signals (d_1-d_3). This PC is, however, more difficult to interpret because the material may be more or less sensitive to different frequencies for several reasons. The lower region of the anodes (excitation points 26-29) is known to be less dense and more homogenous compared with the upper region (points 22-25) which is typically denser and more heterogeneous (observations specific to vibro-compacted anodes). Significant density gradients exist in this area, which often contains cracks [79, 292]. The geometry of the material through which the wave propagates is also different in these two regions. The wave propagation path is more complex around points 22-25 because of the presence of the stub holes (indicated by the dashed line in Figure 5-2) and the upper end of the sluts, whereas the excitation wave at points 22-29 propagates into a simpler geometry (rectangular shape). Further experimental studies are necessary to clarify the interpretation of PC2.

5.4.3.2 Attenuation maps

To illustrate how the measurements collected at all excitation points could be used in an anode inspection scheme, acoustic signal attenuation maps were prepared, as shown in Figure 5-14. In this figure, the values of the scores of the first component ($\mathbf{t_1}$) of the three PCA models are displayed using a color map. PC1 explains 78.9%, 85.1%, and 68.6% of the variance of the datasets collecting excitation points 1-21 (excluding stub holes), 16-18-20, and 22-29, respectively. It was previously shown that less attenuated materials fall in the positive $\mathbf{t_1}$ region, and the most attenuated ones fall in the negative quadrants (see Figure 5-12). This observation is also consistent for all three PCA models (i.e. loading plots are similar). Hence, the score values were scaled from 0 to 1 using the maximum and minimum values in such a way that 0 and 1 are assigned to the least and the most attenuated signals in the dataset, respectively. A color map ranging from dark blue to dark red was then applied on each excitation point shown in the anode drawings (Figure 5-2) to indicate progressively higher attenuation of the signals. Note that the score values obtained with different PCA models cannot be compared, since the scaling of the data matrices for each set of excitation points is different. Therefore, it was decided to adjust the color map based on the minimum and maximum score values obtained by each PCA model separately. This implies that one can compare the colors for those excitation points within the same set, but not between the sets.

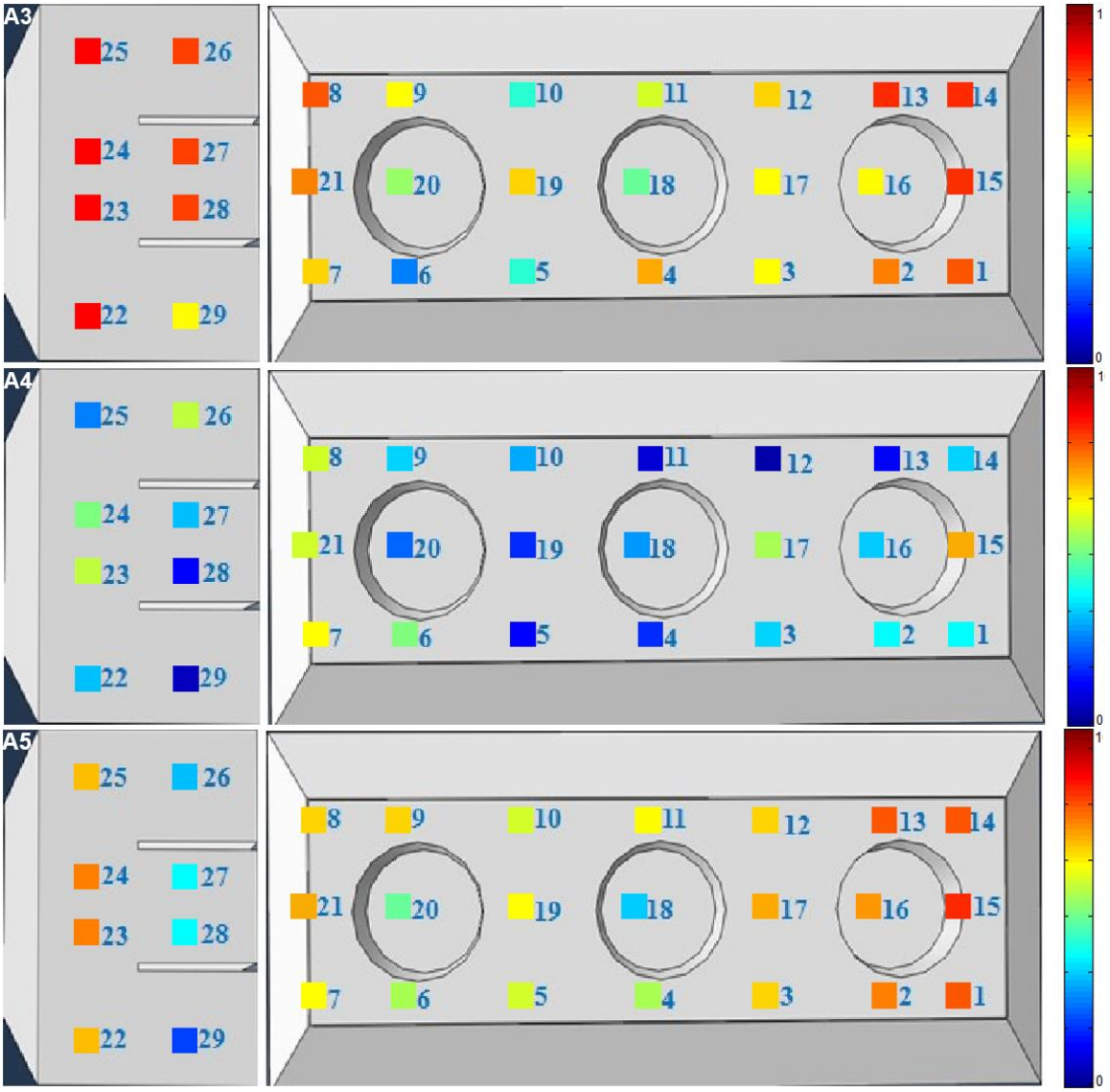

Figure 5-14 Maps of the $\mathbf{t_1}$ score values associated with signal attenuation for anodes A3, A4, and A5. The color bar indicates the level of attenuation on relative scale, from low (dark blue) to high attenuation (dark red).

Although attenuation maps can be obtained for all 27 anodes, as shown in Appendix 3, only those for anode A3, A4, and A5 are presented in Figure 5-14 for sake of conciseness. These three anodes were investigated in section 4.3.1 (Figure 5-12) and illustrate different defect severity and orientation within the block. The map for anode A3 clearly shows a greater signal attenuation on the right hand side of the anode block (points 1-2 and 13-15) and for most excitation points in the transversal direction (all points except 29). The cracks in this anode are visible from the surface as shown in Figure 5-11 a). The cracks are clearly detected and correctly located in the attenuation map. The sound anode A4 is overall less attenuated compared with the other two anodes (most points are blue). The map shows no

indication of cracks, which is consistent with the image of the anode cut in Figure 5-7. Finally, the map of anode A5 provide evidence of a defect in the right hand side of the anode (points 1-2, 14-16), and in between the stub holes and the upper end of the sluts (points 22-25). The longitudinal crack invisible from the surface (see Figure 5-7) was again correctly identified and located. The maps clearly demonstrate the capacity of the proposed inspection scheme to detect and locate the defects in the anodes. Indeed, detailed information about the defects could lead to a more precise diagnostic and help find an assignable root cause. This is essential to determine the corrective actions to implement on the manufacturing process.

5.5 Conclusion

This paper presents a practical application of non-destructive testing techniques for the inspection of the carbon anodes used in the Hall-Héroult aluminium reduction cells. The proposed approach would be useful to develop a quality control scheme for individual anode blocks, which currently lacks in the field. The method is based on the combination of multi-spectral acousto-ultrasonic signals and Principal Component Analysis (PCA), allowing to detect and locate defects, and discriminate different anodes based on their acousto-ultrasonic signatures. A set of full-scale baked anodes were selected from the Alcoa Deschambault Quebec (ADQ) smelter, including anodes containing a variety of defects and/or produced under different manufacturing conditions. The anodes were scanned along both transversal and longitudinal directions using acousto-ultrasonic sensors at multiple locations. The acousto-ultrasonic signatures of each anode were obtained from their response recorded in the 100-200 KHz frequency range. The large set of features was analyzed using PCA in order to cluster the tested anodes based on their acousto-ultrasonic signature. Numerical images collected after cutting some of the tested anodes were also used to support the results interpretation.

The acoustic attenuation features obtained for 29 excitation points on the anodes were organized in two different data matrices in order to analyze both the between and within anode variability. The sensitivity of the acoustic signals to defect severity was demonstrated by using the attenuation features obtained from the stub-hole regions. The proposed approach was able to clearly distinguish anodes have no cracks underneath the stub holes from those having cracks under one, two and all three of them. Using the data collected from all 29 excitation points, it was possible to show that the anodes baked in different positions within the open pit ring furnaces, which were submitted to a slightly different thermal history,

could also be distinguished to some extent. This analysis also showed that the first component of the PCA model captured the overall attenuation of the acoustic signals while the second could be related to heterogeneities within the blocks. Finally, after investigating the anodes intra-variability, it was possible to show the ability of the proposed approach to detect and locate defects within the anode blocks, and assess their severity. Attenuation maps were used to illustrate a potential way to implement the inspection scheme in practice. This framework could be used for industrial real time inspection of carbon anodes to improve the efficiency of the electrolysis by means of intercepting defect anodes before they are set in reduction cells and/or by allowing feedback corrective actions to be implemented on the manufacturing process.

Future work will look at paving the way for the final industrial application by demonstrating the performance and robustness of the inspection scheme on a wider range of anodes with more variability. The link between the results of the inspection technique and the anode performance in the cells will be explored by means of tracking the tested anodes in the pot-room. Finally, the tolerable defects interval and how to use the information about those defects for designing automatic feedback control schemes will also be investigated as part of this continued research effort.

Chapter 6 Non-destructive testing of baked anodes based on modal analysis and principal component analysis

Résumé

Le contrôle de la qualité des anodes cuite est encore essentiellement basé sur l'échantillonnage et la caractérisation des carottes. Seule une faible proportion de la production peut être testée par cette méthode en raison du coût, du temps et de la nature destructive des techniques analytiques. En outre, les propriétés des carottes ne sont pas nécessairement représentatives de celles du bloc entier. Une méthode rapide et non destructive pour le contrôle de la qualité de l'anode basée sur l'analyse modale est donc proposée. Un certain nombre d'anodes cuites fabriquées dans des conditions différentes à la fonderie d'Alcoa Deschambault a été retenu pour la validation de la méthode. Les anodes ainsi sélectionnées ont été excitées mécaniquement à différents endroits et donc les signaux de vibration des blocs ont été mesurés par des accéléromètres. L'analyse en composantes principales (PCA) a été utilisée pour regrouper les modes de vibration des anodes. Les résultats montrent que l'approche proposée permet de détecter et de distinguer différents types de défauts internes au sein des anodes. Certaines anodes testées ont été coupées et imagées afin de confirmer visuellement ces résultats.

Abstract

Baked anodes quality control is still mostly based on core sampling and characterization. Only a small proportion of the production can be tested by this method due to the costly, time consuming, and destructive nature of the analytical techniques. Furthermore, the core properties are not necessarily representative of those of the whole block. A rapid and non-destructive method for anode quality control based on vibration modal analysis is proposed. A number of baked anodes produced under different conditions at the Alcoa Deschambault smelter were selected. These were excited mechanically at different locations and the vibration signals of the blocks were measured by accelerometers. Principal Component Analysis (PCA) was used to cluster the vibration modes of the anodes. It is shown that the proposed approach allows detecting and distinguishing different types of anode internal defects. Some of the tested anodes were cut and imaged in order to confirm the results visually.

Keywords: Aluminium smelting, baked carbon anode, NDT, vibration, modal analysis; PCA

M. Ben Boubaker, D. Picard, J. Tessier, H. Alamdari, M. Fafard, C. Duchesne, Non-destructive testing of baked anodes based on modal analysis and principle component analysis, TMS, Light Metals, 2017, 1289-1298.

6.1 Introduction

The decreasing quality and increasing variability of the anode raw materials [337,338], combined with the frequent supplier changes made to reduce purchasing costs and meet specifications, make it increasingly difficult for carbon plant operators to manufacture anodes with consistent quality. Since fluctuations in anode properties may affect the performance of reduction cells, it is important that sudden drifts in anode quality be detected, and that corrective actions be implemented in a timely fashion. This is difficult to achieve using the quality control scheme based on core sampling and lab characterization currently used in most modern primary aluminium smelters. Only a small proportion of the production can be tested by this method due to the costly, time consuming, and destructive nature of the analytical techniques. In addition, it is known that the core properties are not necessarily representative of those of the whole block. Hence, developing rapid and non-destructive methods for quality control of individual baked anode blocks are highly desirable.

New devices for measuring the electrical resistivity distribution in carbon anodes were recently proposed as an indicator of anode quality [114, 115]. These systems target one of the most important anode properties (electrical resistivity) and should enable feedback corrective actions to be implemented on the anode manufacturing process (e.g. paste formulation). Although these instruments have been shown to detect changes in resistivity distribution, it is not clear at this point if these measurements could be used to diagnose the cause of these changes and discriminate between the various types of anode defects occurring in practice (e.g., cracks, poorly mixed paste, etc.).

This work investigates an alternative and perhaps complementary approach based on vibrational excitation of the baked anodes and modal analysis. This non-destructive testing method can potentially be a more direct approach for sensing the anode internal structure because physical defects modify the material vibration response. It should provide overall information about the quality of an anode block, and enable defect diagnosis if these have a different impact on the anode vibration response. Modal techniques are also easy to implement for online defect detection and quality control. A similar approach has been applied for various porous materials [340,341].

Modal analysis can be implemented in different ways depending on the application. Most of them use the lower natural frequencies obtained experimentally from the power spectrum of the material vibration response signals [342,343]. Alternative approaches

include empirical modelling of the mode shapes estimated from vibration response data [290, 302, 306], as well as numerical model updating methods [326, 329, 334]. The first approach based on natural vibration frequencies was selected in this work since it is simple and allowed discriminating the anode defects of interest.

In order to test the proposed approach, a set of full scale baked anodes were selected from the Alcoa Deschambault Quebec (ADQ) smelter. Some anodes had known defects visible from the surface and others not. Anodes free of visible defects were also included in the set. The anodes were excited mechanically on different faces and positions on the block and their vibration responses were also recorded at different locations. The vibration modes of each anode were obtained from their signal power spectrum. It was decided to use only the first two fundamental natural frequencies based on numerical modelling. The large set of vibration mode data was analyzed using Principal Component Analysis (PCA) [284, 334, 339] in order to cluster the tested anodes based on their vibration response signature. It is shown that defect free anodes can be discriminated from defect anodes. In addition, the latter could be distinguished based on the type of defect present in their structure. These results were validated by visual inspection after cutting some of the anodes.

6.2 Materials and Methods

6.2.1 Selection of Industrial Anodes

A total of 27 full-scale baked anodes manufactured at the Alcoa Deschambault Quebec (ADQ) smelter were used in this work. In order to test the proposed approach, good anodes (defect free) as well as anodes including different types of defects are required. Since it is difficult to assess whether an anode contains defects or not without destroying them (unless defects are visible from the surface), it was decided to select a variety of anodes produced under different conditions (i.e., normal operation and during paste plant start-ups) as well as some anodes containing known defects, visible from the surface (i.e., cracked anodes, surface defects due either to intensive firing or to handling). Most of the selected anodes had no externally visible defects. The anodes were numbered from A1 to A27. Table 6-1 shows which anodes were assigned to each of the previously mentioned categories.

Table 6-1 Anode numbers and description.

Anode numbers	Description
1, 4, 5, 6, 10, 11, 16, 17, 18, 19, 20, 21, 22, 23, 24, 25, 26, 27	Free of external defects
2, 3, 7	Cracks visible externally
8, 12, 13	Surface defects
14, 15	Start-up anodes

Some example anodes are shown in Figure 6-1. Anode A1 has no externally visible defect, A3 and A7 had large cracks visible from the surface, and A8, A12 and A13 had different types of surface defects.

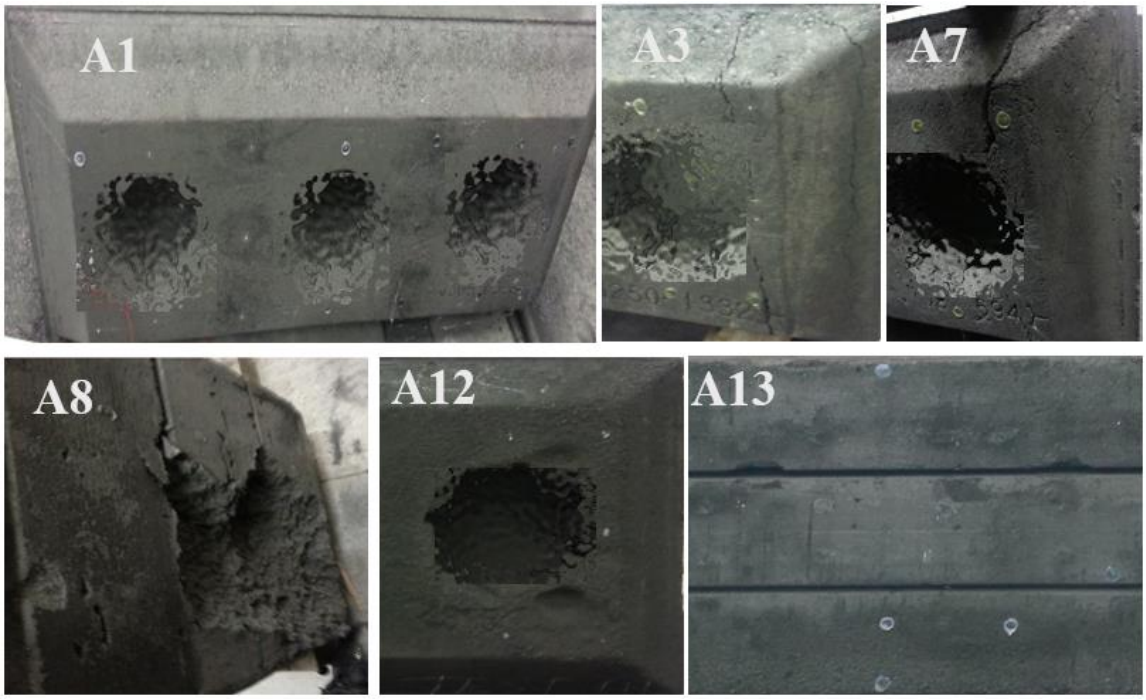

Figure 6-1 Example of anodes showing different types of defects.

6.2.2 Numerical Modeling

A finite elements model of a baked anode was built in order to guide in the development of the experimental mechanical vibration set-up. The purpose of the model was to simulate the vibration response of an anode obtained for different combinations of excitation points and type and position of the anode supports as shown in Figure 6-2. The objective was to select the combination allowing to identify the most global vibration modes with the highest signal-to-noise ratio that capture the most important defects.

Some of the small geometrical details of the anode, such as the flutes in the stub hole, were simplified in the model because they were found to have little impact on the global vibration modes. The boundary conditions were applied either at the bottom or at the side of the anode so as to leave only two translations and one rotation modes to simulate different supports as per the tested configurations shown in Figure 6-2 (plan support, three prismatic supports or bars). The interaction constraints "tie" and "hard contact" allowed good modeling of the degrees of freedom associated with the anode supports.

In order to predict the vibration responses of the full-scale anode, a simple three-dimensional model was constructed. It is worth mentioning that distributed irregularities such as pores and cracks generally cause mass and stiffness variations. Accordingly, the anode model was divided into seven zones along the anode height (numbered in yellow in Figure 6-5), and different mechanical properties were assigned to each zone. The ranges were as follows: density 1560-1610 $kg.m^{-3}$, Young's modulus 7000-11000 MPa and Poisson's ratio 0.18. The density values were obtained from X-ray computed tomography images collected in previous work [80]. The Young's modulus and Poisson ratio values were taken from the work of Eliassen [20] and the CIR Laboratory [301], respectively. The supports (bars and prisms) always had the properties of steel. The finite element model of the anode was developed using the Abaqus/CAE 6.14-1 software and the anode was modelled with more than 100000 quadratic solid elements. Some of the simulated modes are shown in Figure 6-3.

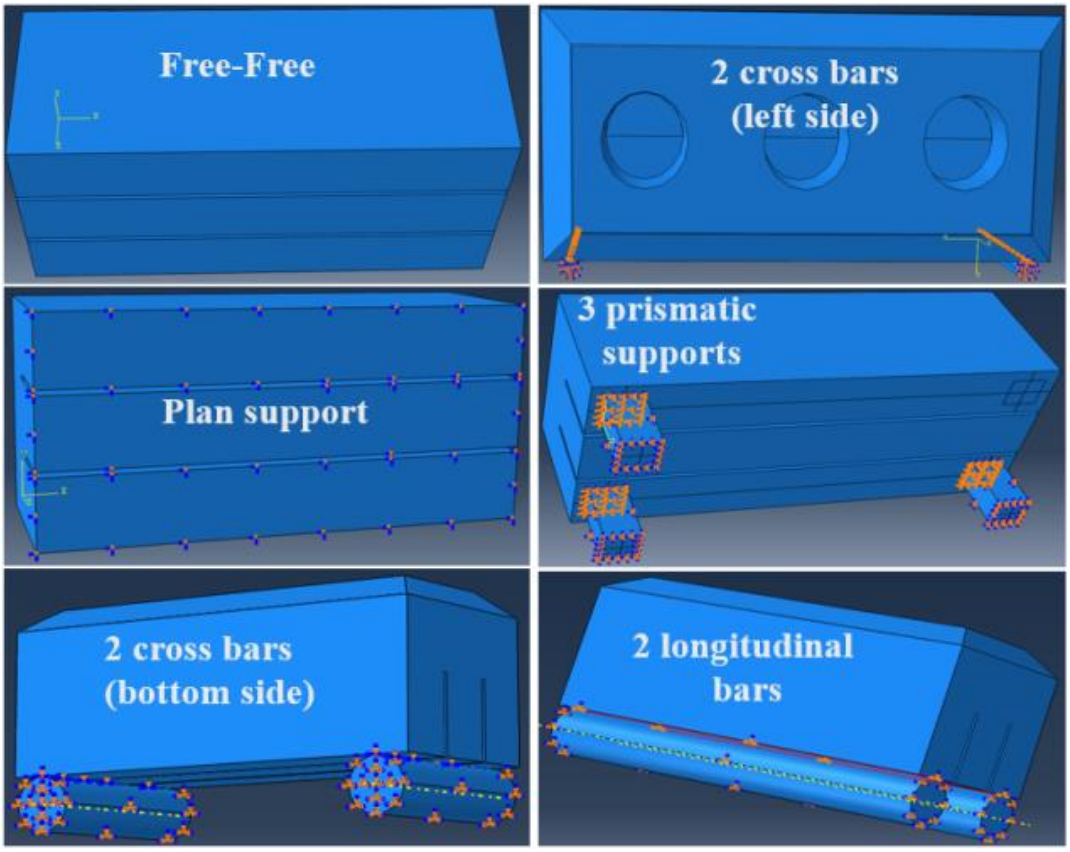

Figure 6-2 Different tested supports configurations.

After simulating the different support configurations and excitation positions shown in Figure 6-2, the one where the anode sits on its side on two cross bars was selected (top right in Figure 6-2). This configuration yielded lower frequency vibration modes, which should help distinguishing the various types of anode defects.

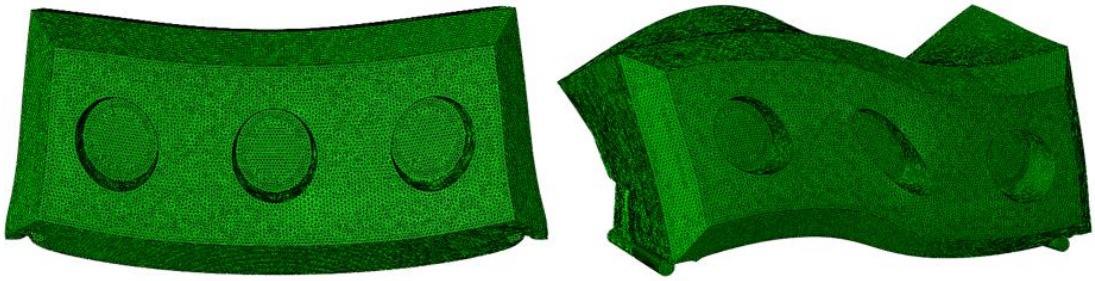

Figure 6-3 The first two simulated vibration modes of the anode for the two cross bars configuration and excitation on the top.

6.2.3 Excitation and Measurement Set-Up

The vibration set-up shown in Figure 6-4 was designed to identify the natural frequencies of the anodes after mechanically exciting them on four faces. A soft rubber

impact hammer was used for the excitation in order to reduce the induced resonance and increase the amount of energy transferred by the mechanical displacement. The anode was excited at five different places on each face as shown in Figure 6-5. The accelerometers were positioned differently when exciting on different faces as shown in Figure 6-6. The colors of the dots in these two figures identify the excitation face. Note that excitation faces E2 and E3 (blue and red dots in Figure 6-5) are the same, but the accelerometers were placed differently in these two cases. Each excitation test was repeated 8 times to average out inaccuracies caused by manual excitation.

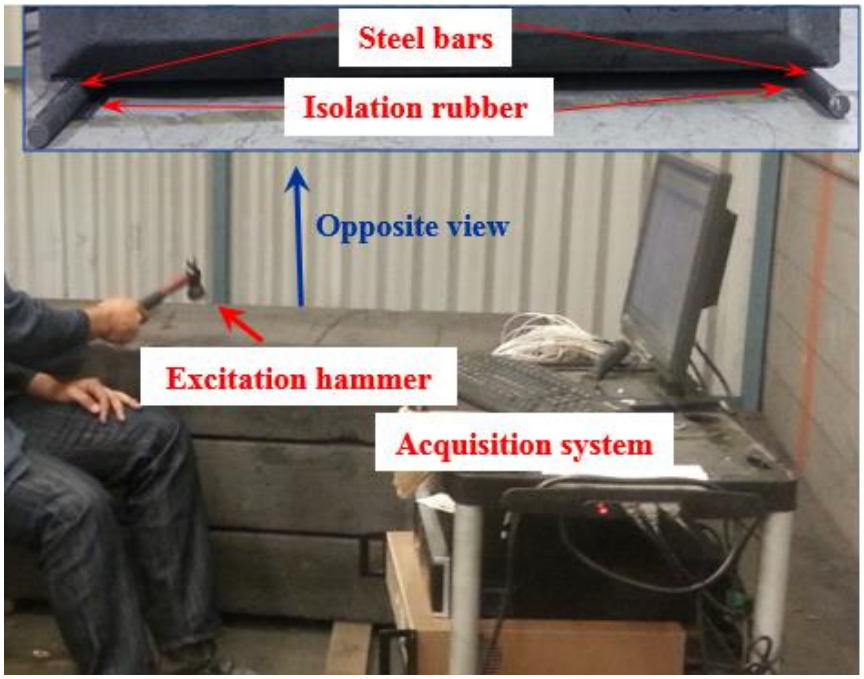

Figure 6-4 Experimental mechanical vibration set-up.

Seven accelerometers (Kristler, model 8310A25A1M11SP15M) were distributed across each face and measured the acceleration resulting from each excitation. They were held in place using hot glue to ensure good contact, especially for those mounted vertically which could fall off the anode during testing.

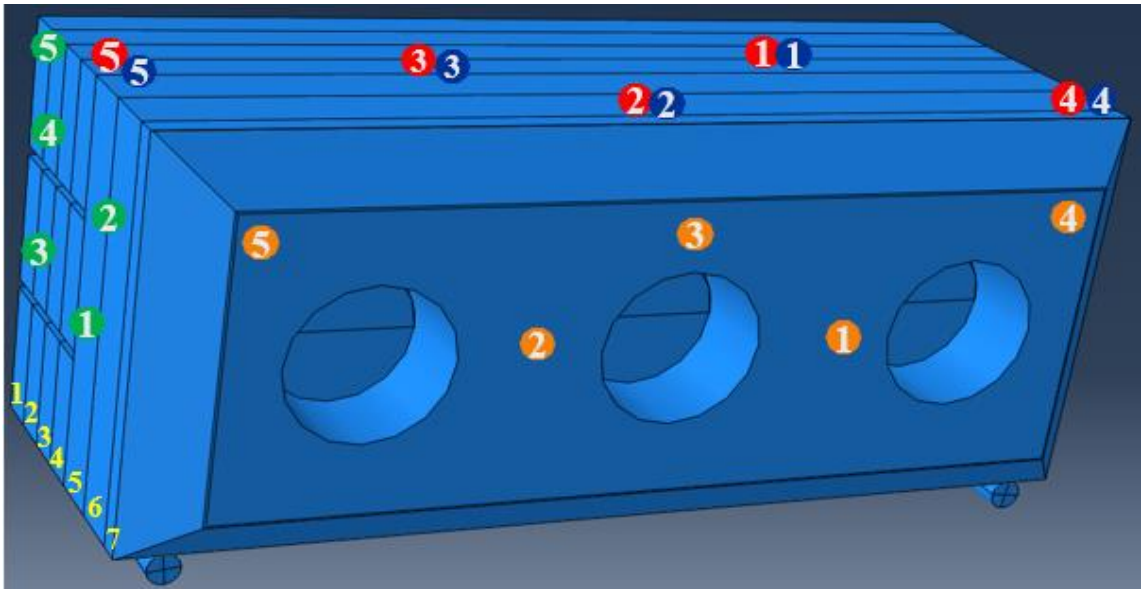

Figure 6-5 Position of the five excitation points (identified by numbers) on four different anode faces (E1-orange, E2-blue, E3-red, E4-green circles).

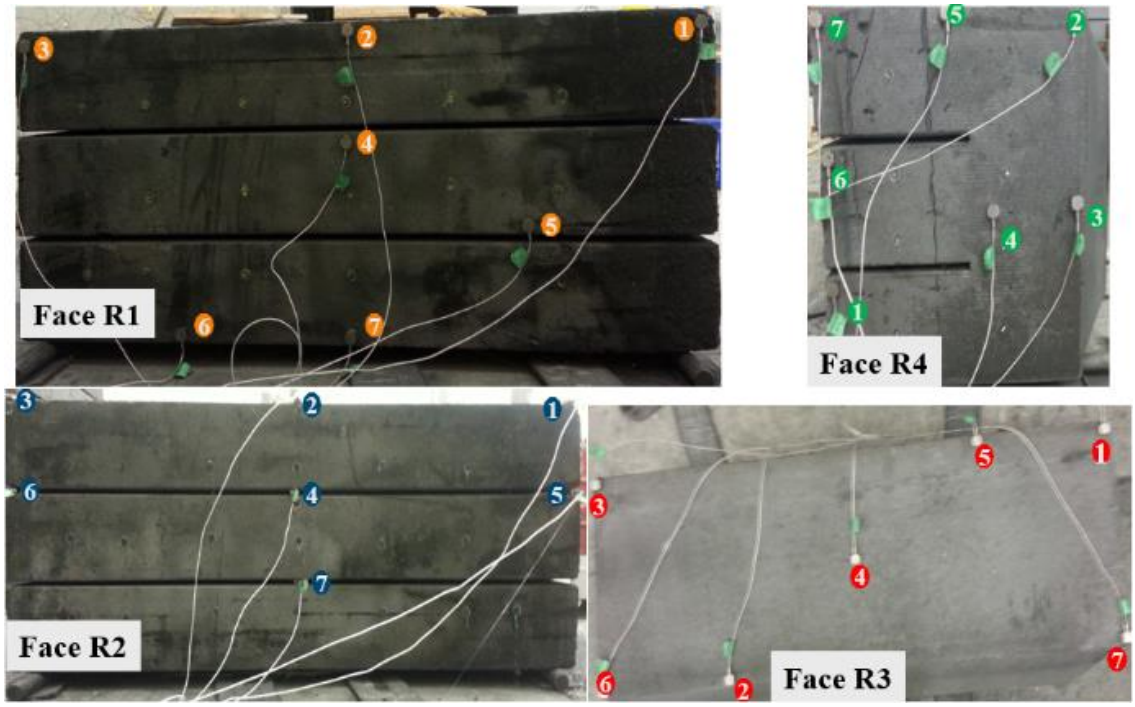

Figure 6-6 Position of the seven accelerometers (identified by numbers) for measuring the response of each corresponding excitation face (R1-orange, R2-blue, R3-red, and R4-green dots).

The acquisition system Vishay 6100 Series was used to acquire the accelerometer signals by strain gauge cards. Since high-level reading cards were unavailable, all accelerometers had to be connected with a line voltage reducer device to strain gauge reading cards. The system can acquire accurate signals at a frequency of 10,000 Hz

playback channels. In addition, the system software (Strainsmart, Vishay) can analyze the raw data of each 16384 series by mean of Fourier transform. The longest data acquisition time was 6.4 seconds, which includes the time required for excitation and reading the data of the accelerometers. The data exported from the acquisition system were the relative amplitudes on a set of frequencies for each of the accelerometers.

6.3 Modal Analysis of the Vibration Signals

6.3.1 Mode identification and features calculation

An algorithm developed in Matlab version R2014a (MathWorks, Natick, MA, USA) was used to identify the first two fundamental natural frequencies after transferring the time signal into frequency domain using Fast Fourier Transform (FFT). Figure 6-7 shows the power spectra of the vibration responses of 11 anodes measured by one accelerometer located at the same position on the top face (E1-orange dots in Figure 6-5). The power spectra show two dominant peaks at 60 Hz and 300 Hz corresponding to the first two global modes, so called fundamental modes. The presence of defects in the anode structure would cause these peaks to shift on the frequency scale. After some preliminary work, it was decided to limit the analysis to frequencies lower than 500 Hz because the modes beyond that frequency did not help discriminate the anodes. This also increases the resolution of the signals and facilitates the identification of the modes.

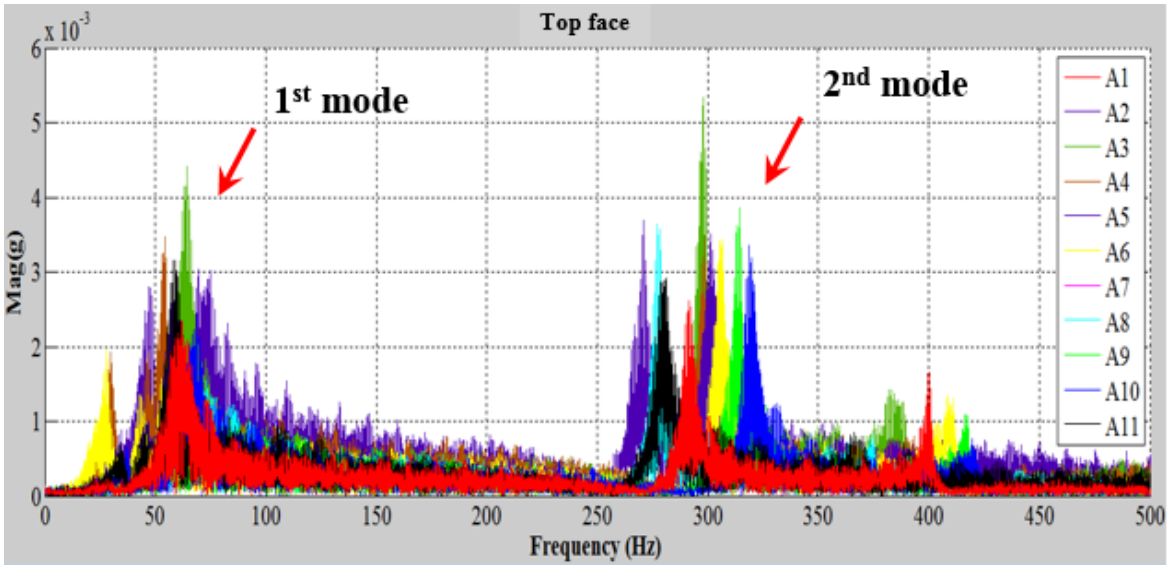

Figure 6-7 The first two peaks of the power spectrum of 11 anodes obtained from one accelerometer after excitation on the top face.

The first two peaks of each anode vibration response were selected for the analysis since they are the most accurate and were found sufficient to detect and discriminate the defects present in the anodes. Modal tests were thus conducted initially on a defect free anode to identify the first two fundamental natural frequencies as shown in Figure 6-7. Identical tests were subsequently performed on all the 27 anodes. The frequency at which the first two peaks occurred for a given anode was extracted from each vibration response collected from that anode (i.e., 5 excitation points × 4 faces × 7 accelerometers = 140 signals/anode) and these were stored in a (1×280) row vector. This vector of frequencies contains the vibration signature of one baked anode. Collecting those vectors for all the tested anodes yields a matrix **X** of dimensions (27×280). This large data matrix was then analyzed using PCA.

6.3.2 Principal Component Analysis (PCA)

PCA is a multivariate statistical method approximating a high dimensional dataset **X** (I×J) by a much lower dimensional subspace **T** (I×A), where A<<J, explaining the main variance directions in the data. It performs the following bilinear decomposition of the data matrix **X**:

$$\mathbf{X} = \sum_{a=1}^{A} \mathbf{t}_a \mathbf{p}_a^T + \mathbf{E} \tag{6.1}$$

Where the orthogonal score vectors $\mathbf{t_a}$ (I×1) represent the projection of each observation (row in **X**) into the lower dimensional subspace formed by the corresponding orthonormal loading vectors $\mathbf{p_a}$ (J×1). The latter consists of linear combinations of the original variables (i.e. $\mathbf{t_a} = \mathbf{X}\,\mathbf{p_a}$). The model residuals are gathered in the residual matrix **E** (I×J). The principal components (pairs of **t**'s and **p**'s) are ordered in such a way that the first (t_1) captures the greatest amount of variations in the data, whereas the second captures the greatest amount of variance orthogonal to the first, and so on. Scatter plots of the scores $\mathbf{t_a}$ allow to visualize the clustering patterns of the observations (i.e., tested anodes) in the lower dimensional subspace. Interpretation of the clustering patterns based on the original variables (columns of **X** or the vibration modes) is obtained by using scatter plots of the loading values $\mathbf{p_a}$. For more details on PCA the reader is referred to Wold et al. [277].

6.4 Results and Discussions

In this section, the results of the PCA model applied to the anode vibration data matrix **X** are presented first. The clustering patterns of the anode vibration response is explained and interpreted based on the vibration modes. The results are then further validated by showing images of cuts made on several of the tested anodes to unveil their internal structure. Finally, a simplified PCA model is presented based on a reduced number of accelerometers and excitation points in order to show that similar conclusions can be reached using a simpler experimental vibration set-up.

The first two PCA components were found sufficient to discriminate the anodes based on their vibration response. Only these two are discussed here. The cumulative sum of squares explained (R^2) by the PCA model using the two first components is provided in Table 6-2. About half of the variance contained in the vibration mode data matrix **X** is captured using only the first two components. The columns of **X** were mean-centered and scaled to unit variance prior to applying PCA (common practice).

Table 6-2 Percent cumulative sum of squares explained (R^2) by the PCA model built on modal features collected from anodes.

Component	R^2 (%)
1	33.2
2	53.0

The PCA results are presented in Figure 6-8 and Figure 6-9. Figure 6-10 supports the discussion by showing images of some of the anode cuts. The clustering pattern of the 27 anodes is shown in the $\mathbf{t_1}$-$\mathbf{t_2}$ score plot (Figure 6-8). Each point in the plot corresponds to the vibration response signature of one anode. They were labelled and colored according to the anode number and description presented in Table 6-1. The anodes containing known defects visible from the surface (red and blue dots) as well as the start-up anodes (green dots), which are expected to be different, fall on the left hand side of the score plot in the negative $\mathbf{t_1}$ region. All these anodes clearly distinguish themselves from most of the other anodes having no externally visible defects (black dots). At the time of vibration testing, it was unknown whether the latter group of anodes contained defects within their structure or not. This explains why cutting the anodes was necessary for validation purposes. It is also interesting to note that these anodes (black dots) divide into roughly two groups: anodes A19, A21, A23 and A27 (lower right quadrant), and all the others. It will be shown later that

the former group of anodes had no or very few internal defects after visual inspection of their cuts. The others had different types of defects.

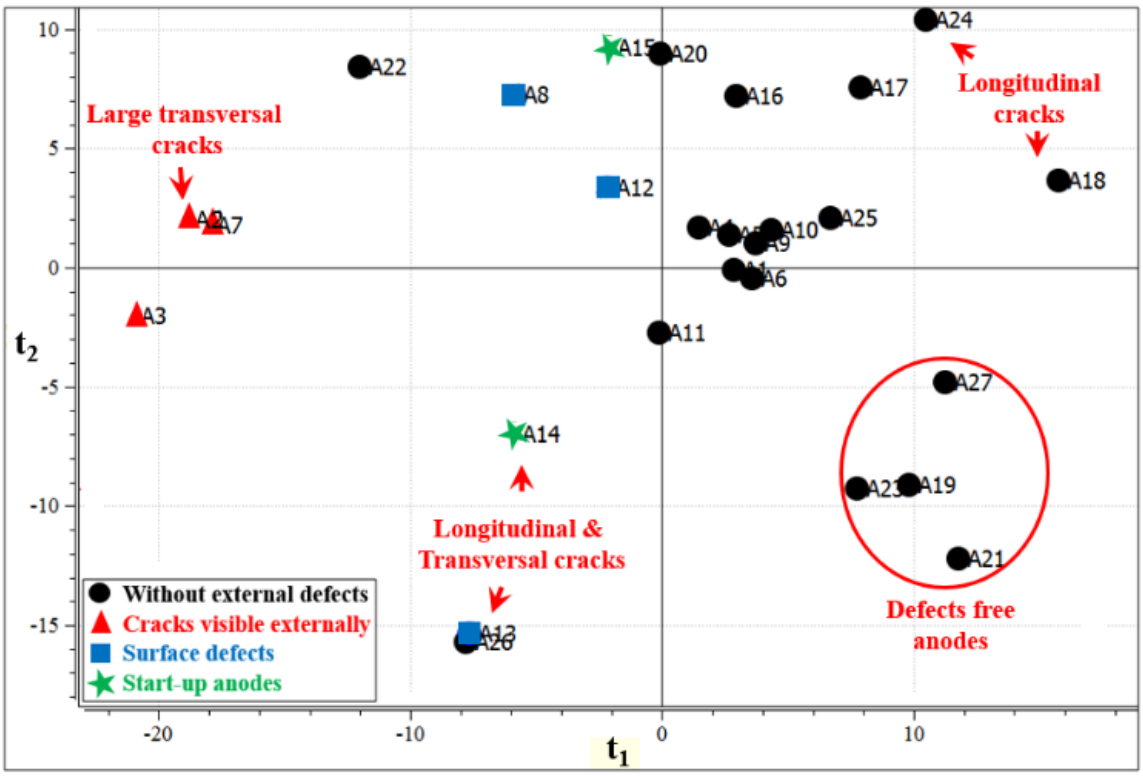

Figure 6-8 PCA score plot (t_1-t_2) of the anode vibration responses.

Images of the internal structure of some anodes are provided in Figure 6-10 in order to support the observations made on the anodes clustering pattern (Figure 6-8). Note that the size of the cracks in these images has been virtually enlarged for a clearer visual appreciation. The anodes containing cracks visible from the surface (red dots in Figure 6-8) all cluster together in the negative t_1 region. The image of anode A2 after cutting shows large transversal (vertical) cracks at one end. The anodes A18 and A24 clustering in the extreme positive t_1 region had several longitudinal (horizontal) cracks below the stub-holes. Anodes A14 and A26 (lower left quadrant) had a mixture of vertical and horizontal cracks also below the stub-hole regions. Finally, the images of anodes A19 and A27 revealed no or very few defects in their structure. These results clearly show the potential of modal analysis for detecting the presence of defects within baked anodes. It also demonstrates a good sensitivity to the types of defects. A clearer diagnosis may help selecting appropriate remedial actions to implement on the manufacturing process and/or establishing anode sorting schemes.

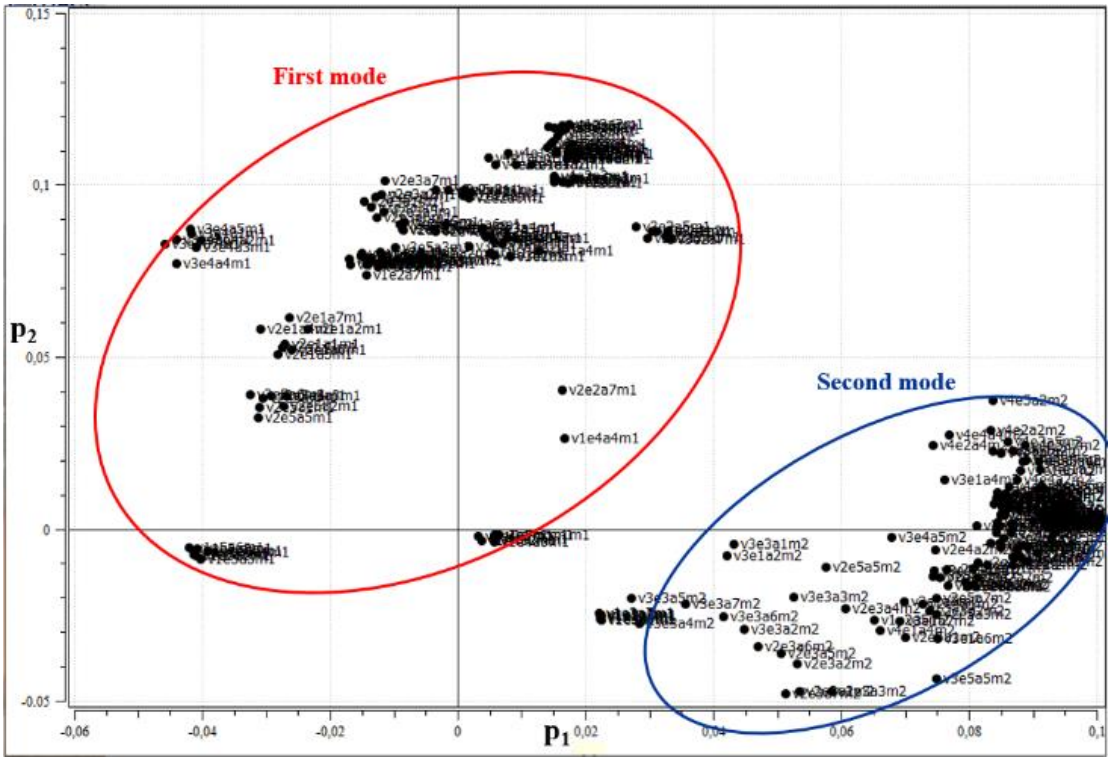

Figure 6-9 PCA loadings ($\mathbf{p_1}$-$\mathbf{p_2}$) of the anode vibration responses.

The loading plot shown in Figure 6-9 is now used to interpret the clustering pattern observed in Figure 6-8 in relation with how the presence of defects shifted the first two vibration modes. Each point on this plot is related with the frequency of its corresponding mode obtained after exciting the anode at a given position, on a given face and recorded by one of the seven accelerometers. To facilitate the reading of the plot, the vibration modes are identified by ellipses.

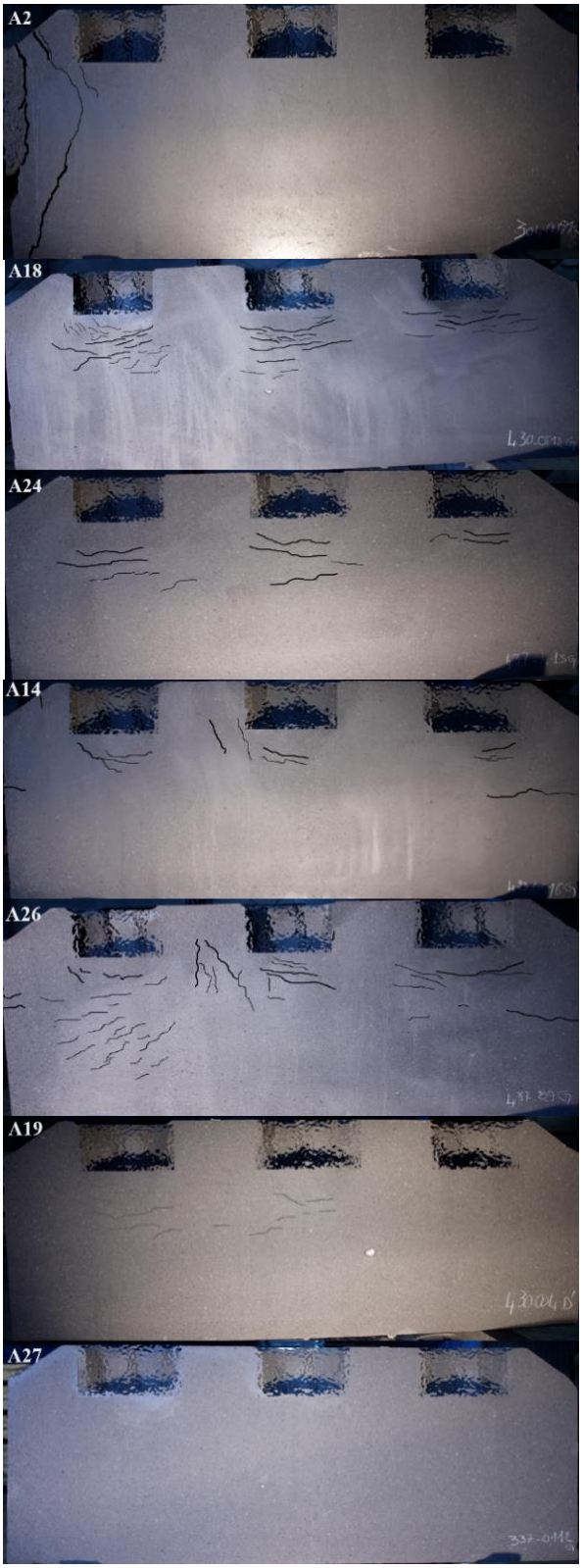

Figure 6-10 Images of cuts made on some tested baked anodes.

The loading plot should be interpreted as follows. The absolute value of a loading indicates the importance of the corresponding variable (vibration frequency for a given mode in response to an excitation at one point on one face) in a given component. The signs of the loading values are used to interpret the correlation between pairs of variables. Modal features having loading values of the same sign for one component are positively correlated and they are negatively correlated when they have opposite signs. The loading values can be interpreted independently for each PCA component since they are orthogonal to each other. Figure 6-9 shows that most of the first mode features have strong loadings along the second component ($\mathbf{p_2}$) and weak values along the first ($\mathbf{p_1}$). The opposite can be said about the loading values of the second mode. This suggests that the separation of the anodes along the first PCA component ($\mathbf{t_1}$) is determined by the second vibration mode and the separation along t_2 by the first vibration mode. Hence, the second vibration mode for the anodes having positive t_1 score values shifted towards higher frequencies compared to the average of the 27 anodes, and vice-versa for the anodes having negative $\mathbf{t_1}$ values. Similarly, the first mode of the anodes clustering in the positive t_2 score region shifted towards higher frequencies and in the opposite direction for those anodes clustering in the negative $\mathbf{t_2}$ region.

Therefore, it seems that the direction of the shifts in the second vibration mode indicates the orientation of the cracks. A shift towards lower frequencies is associated with anodes containing cracks mostly oriented vertically (cluster in the left hand side of the score plot). A shift towards higher frequencies suggests that the cracks are mostly oriented horizontally (anodes in the right hand side of the plot). Those clustering around the $\mathbf{t_1}$ origin (frequency around average value) contain a mixture of crack orientations. The first mode separates anodes A13, A14, A26 and A19, A21, A23, A27 from all the other anodes along the t_2 axis. It is speculated that the shifts in the first mode related with this clustering pattern may be due to differences in the physical and/or mechanical properties of the anodes affecting their dynamic vibrational response. This will be clarified in future work.

6.5 Pruning of the PCA model

Although the proposed approach seems promising, it uses many excitation points and accelerometers which can become cumbersome and time consuming for an industrial implementation. It addition, the loading plot (Figure 6-9) has shown that several of the

responses obtained for different excitation points and accelerometers were redundant (i.e., very similar loading values). Pruning of the PCA model was therefore investigated.

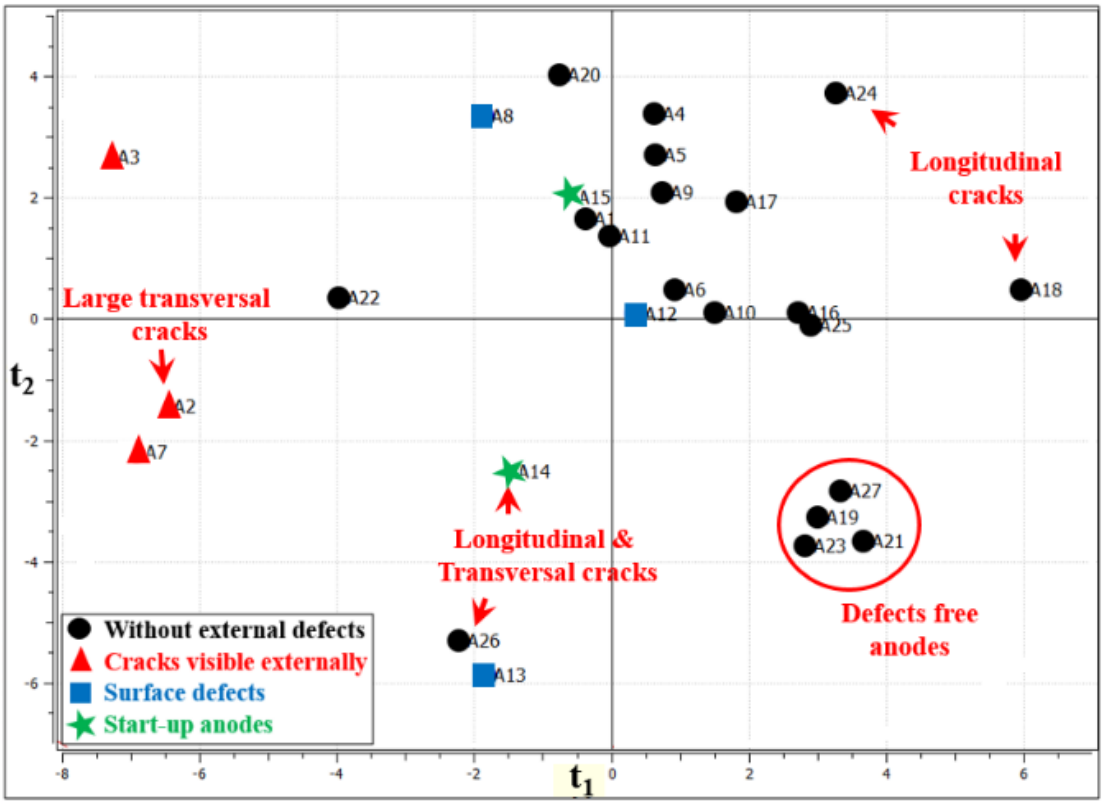

Figure 6-11 PCA score plot (t_1-t_2) after model pruning.

The results shown in Figure 6-11 were obtained for a pruned model based on one single excitation point (instead of 5) on the four anode faces and vibrations recorded by 4 accelerometers (instead of 7). Hence, the dimensions of the vibration data matrix **X** were significantly reduced to (27×32). Comparing Figure 6-8 and Figure 6-11 reveals only minor differences in the clustering pattern of the anodes, and do not change the conclusions obtained using the original model. It is therefore clear that the experimental set-up for modal analysis can be optimized to reduce cycle time while providing useful information for baked anode quality control.

6.6 Conclusion

Modal analysis was investigated for rapid and non-destructive testing of individual baked carbon anodes. A set of full scale baked anodes were selected from the Alcoa Deschambault Quebec (ADQ) smelter, including some high quality anodes and defect anodes (visible from the surface and not). The anodes were excited mechanically on

different faces and positions on the block and their vibration response was also recorded by accelerometers at different locations. The vibration modes of each anode were obtained from their signal power spectrum in the 0-450 Hz range. Numerical modelling of the anode was used to support the experimental set-up design. The large set of vibration mode data was analyzed using Principal Component Analysis (PCA) in order to cluster the tested anodes based on their vibration response signature.

It was shown that defect free anodes can be discriminated from defect anodes. In addition, the latter could be distinguished based on the type of defect present in their structure. The second vibration modes were found to be sensitive to the presence and orientation of cracks within the anode block while the first might be related to changes in the physical and mechanical properties of the anodes. These conclusions were supported by images of the internal structure of the anodes collected after cutting some of them. Based on these promising results, the modal analysis set-up will be further refined and optimized in future work.

Acknowledgement

The authors would like to acknowledge the financial support of the Natural Sciences and Engineering Research Council of Canada (NSERC), Fonds de Recherche du Québec – Nature et Technologies (FRQNT), Alcoa and the Aluminium Research Centre – REGAL. The assistance provided by REGAL personnel (Hugues Ferland and Guillaume Gauvin), and by the Alcoa Deschambault anode plant technical staff is also greatly acknowledged.

Chapter 7 Conclusion and recommendations

7.1 Conclusion

Current competition between aluminium producers and environmental constraints deepen the necessity of reducing the energy consumption of the manufacturing process as well as carbon consumption through a superior process control. The highly recommended optimization of manufacturing parameters consists of ensuring a consistent production of high-quality anodes, due to the fact that the anode raw materials are becoming highly variable. This variability leads, in several cases, to faulty anodes containing internal cracks and voids. As a result, intercepting of the afore-mentioned faulty anodes prior to their installation in reduction cells and deterioration of their performance is important. On the other hand, the current inefficient quality control strategy practiced by the majority of anode plants is based on anodes core sampling and measurements of static properties such as mechanical and physical properties, chemical composition and air/CO_2 reactivity. Hence, based on the fact that the above-mentioned strategy does not allow the immediate detection of defect anodes, instantaneous corrective actions are not possible to adjust the production process.

To sum up, it becomes a priority to find effective methods to maintain consistent anode quality and consequently compensate the variability originating from raw materials.

The aim of the current project was to elaborate the design and implementation of an inspection system to perform an effective quality control of baked carbon anodes. This would allow manufacturers to monitor the performance of the anode production process in real-time as well as to reduce the adverse effects of defective anodes on the overall performance of the electrolysis process. This novel system would not only allow feedback corrective actions to be implemented on the anode production process, but also make it possible to detect, locate and evaluate the severity of the internal defects of anode blocks.

By applying a combination of modal analysis, acousto-ultrasonic techniques, and signal analysis techniques, it has been shown that various defects within the anode blocks can be detected, discriminated and localized. Several multivariate models have been developed in order to cluster the anodes. These models would help establish an effective anode sorting strategy. The proposed models also help further understanding the variability in the anodes introduced by some variations in manufacturing conditions. It is hoped that

such information will eventually enable the implementation of feedback corrective actions on process operation. In addition, a third non-destructive technique based on X-ray image analysis was implemented to validate the investigation results. Finally, the totality of demonstration results on industrial anodes have been successfully validated by a numerical images taken after cutting many tested anodes.

7.2 Original contributions

As the first step in this project, the potential of acousto-ultrasonic (AU) technique to detect defects affecting performance of baked anodes in electrolysis, such as pores and cracks, and also to discriminate between both types of defects was investigated. First, a full-scale anode was sliced in both longitudinal and transversal directions and imaged using X-ray Computed Tomography (CT-Scan) to reveal its internal structure. Each half slice was further virtually divided into six corridors along the anode height, from the center of the anode to its external surface. In this case, seven AU waves having different frequencies ranging from 100 to 250 kHz were propagated and measured through the anode samples (corridors). The wave attenuation behavior was quantified by many temporal features which values are calculated from the recorded signals. An attenuation feature matrix containing the acoustic responses of the anode samples (i.e., all corridor of all tested slices) was then used in a Principal component analysis (PCA) model, which performed an unsupervised clustering of such corridors. The results showed that the temporal features calculated from the AU signals are not only sensitive to the presence of cracks within the anode samples (measured by overall signal attenuation) but also to the density of pores distributed throughout the material. It was also found that each defect has a unique signature in the AU signals, as they could be discriminated in the PCA score space. Furthermore, it appears that some combinations of temporal AU features computed at various frequencies are correlated with pore size. These results were validated qualitatively by using the CT scan images of the samples, and they were also found to be in good agreement with anode manufacturing process knowledge. In addition to detecting and discriminating significant defects, the AU system could also provide measurements of the anode density distribution.

For the second part of this project, in order to optimize both testing and analysis times, multispectral acousto-ultrasonic techniques, combined with multivariate statistical methods, were used in an attempt to quickly assess the presence of defects in the internal anode structure. The same full size anode (utilized in the previous part) was used, which was sliced

in both longitudinal and transversal directions. First, the 1D wavelet transforms were used to decompose each raw signal and calculate the corresponding multispectral sub-signals features. Second, the 2D wavelet transform was utilized to decompose CT-scan images and extract the sub-images textural features for quantitative validation of the observations made from the acousto-ultrasonic signal features and correlating them with internal morphology of the anode. After applying Partial Least Square (PLS) regression on both images texture and acousto-ultrasonic signatures, it was demonstrated that multispectral signals features are not only sensitive to the presence of cracks within anode samples, but also to the density of pores distributed throughout the block. The other advantages of this technique are its non-destructive nature and rapidity. From the afore-mentioned advantages and the obtained results, it can be concluded that the proposed approach appears to be very promising for a real-time quality control of industrial scale prebaked anodes.

As the third part of this project, the already-developed and optimized approach, which resulted in the combination of multispectral acousto-ultrasonic signals and PCA modelling, was implemented to inspect several industrial anodes. These anodes have been intentionally selected with different kinds of defects, while some of them were visible on the surface. These anodes were produced at Alcoa Deschambault Quebec (ADQ) smelter. The proposed inspection method consists of clustering the various anodes based on their acousto-ultrasonic signature. The results have shown that such combination gives a good discrimination of anodes that are holding different kinds of defects. Such method can also provide information about the effect of changes in thermal history during baking, as one cause of defects, particularly the cracks. However, the use of all scan positions, instead of only using some of them (e.g., the three scan positions underneath the stub holes), was found to be the most appropriate for such baking effect study. It was shown that the number of defects inside the anodes, being baked in hotter position, increases. This success is due to the strong frequency dependency of the implemented waves propagation.

In order to further optimize inspection time and prepare the system for online control, the modal analysis technique was investigated for general quality evaluation of individual anodes. Modal testing were conducted on the same set of 27 industrial baked anodes that were used to investigate the previous technique. The anodes were thus conventionally excited using a rubber hammer at different locations and the corresponding vibration responses were recorded by seven accelerometers. After coding the corresponding algorithms, the vibration modes of each anode were calculated from their power spectrum

signal. In addition, a numerical modelling of the anode was used to support the experimental set-up design. The large set of data, natural frequencies in this case, were analyzed by Principal Component Analysis (PCA) in order to cluster the tested anodes based on their vibration response signature, and hence defect-free anodes could be discriminated from the defect anodes. Another important result is that the anodes containing flaws could be distinguished from each other, based on the type of defect present in their structure. Furthermore, the second vibration modes were found to be sensitive to the presence and the orientation of cracks within the anode block while it is postulated that the first mode might be related to changes in the physical and mechanical properties of the anodes. Most of these conclusions were supported by images of the internal structure of the anodes, collected after cutting some of them.

It is worth mentioning that since real-time process monitoring is adopted in many industries and the real-time quality control of different products is becoming a key element for the industrial competition, several industries have attempted to develop reliable techniques for continuous measurements. Consequently, non-destructive testing methods for inspecting homogenous and non-porous materials have been developed and well documented. Some methods also address the quick control and even in real time. However, they can generally not be easy applied to extremely heterogeneous and porous materials (i.e., carbon anodes material) because of the non-linear effects and the high attenuation caused by such material.

Compared to existing characterization and control methods, the originality of the inspection system developed in this work, is that it combines a non-destructive and real-time (fast) measurement with a possibility to use the data interpretation to establish a predictive modeling for feedback corrective actions. In this way, it is possible to circumvent the constraints imposed by the high rate of anode production and to satisfy specific criteria in anodes sorting requested by aluminium producers including:

- Investment in measurement time and data processing should be minimal.
- Reliability of the whole control system.
- Fast delivery of test results to enable anode sorting at the right time.
- Adjustment of the corresponding process steps progressively.

Finally, the capacity of this type of control system to inspect extremely heterogeneous materials, such as those with a high degree of porosity, can extend its use to different

industry sectors. Taking the case of steel plants for example, they are using graphitized carbon anodes, which make the developed control system effective. The inspection methods can also be applied in civil engineering fields where several new materials are being added to improve the quality of concrete, which complicates the material morphology. The developed system can also be applied to the control and characterization of all porous materials such as ceramics, refractories, composites, woods, etc.

The contributions of the research project in the already-developed control systems and implementing detailed analyzes are listed below:

- Optimize the process control using the combination of two different approaches that will minimize the number of parts (i.e., anodes) that will be tested by the second phase in which detailed analysis is used.

- Reduce the cost invested in the equipment and operation time of detailed method (acousto-ultrasonic) by testing all the parts using a global testing (modal analysis) first.

- Reduce the failure risk by combining two different techniques (modal and acousto-ultrasonic analyses) in this control strategy.

7.3 Recommendations for future work

The testing and analyzing methods developed in this project demonstrated to be effective for evaluating the severity, location and type of defects inside the anodes, and in general to assess the anode quality. They may also provide useful information to apply feedback corrective actions on the anode manufacturing process in order to reduce the inconsistency in the baked anode. However, the proposed approach needs to be adapted to the industrial applications. To achieve that, four main steps need to be accomplished:

- Establishing the sorting limits, which is defined in terms of critical defects (based on their kinds, severities and localizations). In this context, the real effect of the defects have to be evaluated under the electrolysis operation. The effects evaluation can be performed by the establishment of a correlation between control data and the anode performance. This performance has to be measured for industrial anodes that will be tracked during full operation.

- It is also suggested to employ other tools to provide on-line quality control. This requires novel tools that allow quick testing in both vibration and acousto-ultrasonic techniques. Modal analysis can thus be improved using an automatic hammer (pneumatic or electric) for the excitation and contact-less measurement tools such as laser-vibrometer or microphone. Regarding the acousto-ultrasonic technique, both excitation and measurements can be performed simultaneously by multiplying number of emitters and the corresponding receivers.
- The classification models, built in sorting strategy, provide a preliminary database. This database of defect and good anodes have to be extended by testing more industrial anodes. This is mainly important in the start-up of the control system. Also, models may need to be adapted when a different anode morphology or new defects are observed, from example because of a raw material supplier change. In addition, the database has to be adjusted continuously with the anode quality improvement by the effective feedback process control.

References

[1] Office of energetic efficiency. Natural Resources Canada [on-line]. http://oee.nrcan.gc.ca/organisme/statistiques/bnce/apd/guide_tableaux.cfm?attr=00 [access Nov. 2014].

[2] Metal Prices. Metal Prices & News on the Internet [on-line]. http://www.metalprices.com/# [access Nov. 2014].

[3] U.S Geological Survey. Aluminium Statistics and Information. http://minerals.usgs.gov /minerals/pubs/commodity/aluminium/ [access Dec.2013].

[4] International Energy Agency. Energy Prices and Taxes [on-line]. http://www.oecd-ilibrary.org/fr/energy/energy-prices-and-taxes_16096835 [access Dec 2013].

[5] U.S Geological Survey. Aluminium Statistics and Information [on-line]. http://minerals.usgs.gov/minerals/pubs/commodity/aluminium/mcs-2012-alumi.pdf [access Dec. 2013].

[6] Aluminium Association of Canada. Canadian primary aluminium production. The Aluminium Association [on-line]. http://www.aluminium.org/Content/Navigation Menu/News Statistics/StatisticsReports/PrimaryProduction/CanadianPrimary201202.pdf [access Dec. 2013].

[7] E.L. Bray, Aluminium Statistics and Information [on-line]. http://minerals.usgs.gov /minerals/pubs/commodity/aluminum/mcs-2012-alumi.pdf [access Dec. 2013].

[8] V. Dassylva-Raymond, Prédiction de l'efficacité de courant du procédé Hall-Héroult. Memoire de maitrise, Université du Québec à Chicoutimi, Canada, 2009.

[9] P. Voisin, Extractive metallurgy of aluminium (Documentary background paper: TIP554DUO ref. paper: M2340), Engineering Techniques, 1992.

[10] K. Grjotheim, H. Kvande, Introduction to aluminium electrolysis, understanding the Hall-Héroult process, 2nd edition, Aluminium-Verlag, Dusseldorf, Germany, 1993.

[11] Aluminium association of Canada, in E & B Data [on-line]: http://fr.ebdata.com /wpcontent/uploads/2012/04/Association-de-laluminium-duCanada1.pdf [access Nov. 2016].

[12] F. Habashi, Extractive metallurgy of aluminium, in Handbook of Aluminium: Alloy production and materials manufacturing, vol. 2, G. E. Totten and D. S. MacKenzie, Eds., first edition, New York, Marcel Dekker, 2003, 1-45.

[13] K. Grjotheim, C. Krohn, Aluminium electrolysis: The chemistry of the Hall-Heroult process, first edition, Aluminium-Verlag GmbH, 1977.

[14] Aluminium Industry Technology Roadmap, 2003, The Aluminium Association, Available [on-line]: http://www1.eere.energy.gov/manufacturing/resources/aluminium/pdfs/al_ roadmap.pdf [access Oct. 2016].

[15] Y. Safa, Simulation numérique des phénomènes thermiques et magnétohydrodynamiques dans une cellule de Hall-Héroult, Thèse de doctorat, École Polytechnique Fédérale de Lausanne, Lausanne, Suisse, 2005.

[16] M.D. Gadd, B.J. Welch, A. D. Ackland, The effect of process operations on smelter cell top heat losses. Light Metals 2000, 231-238.

[17] Z. Kuang, Metallurgical and Materials Transactions, B, vol. 27, 1996, 177-183.

[18] K.L. Hulse, Anode manufacture: raw materials, formulation and processing parameters, Sierre, Switzerland: R&D Carbon Ltd., 2000.

[19] W.K. Fischer, Anodes for the aluminium industry, R&D Carbon Ltd., 1995.

[20] L. Eliassen, Characterisation of mechanical properties of carbon anode materials. Master thesis, department of Structural Engineering, Norwegian University of Science and Technology NTNU, 2007.

[21] K. Khaji, H. Abbas, Baked anode density improvement through optimization anode green dry aggregate composition, Light Metals 2010, 1027-1030.

[22] M. Lustenberger, Heat treatment of carbon anodes for the aluminium industry, PhD thesis, Lausanne, 2004, 13-53.

[23] B. Hohl, Y. L. Wang, Experience report – Aostar aluminium co ltd, China anode paste preparation by means of a continuously operated intensive mixing cascade (IMC), Light Metals 2006, 583-587.

[24] W.K. Fischer, F. Keller, U. Mannweiler, The changing world of anode raw materials: Can today's carbon technology tope with it, R&D Carbon Ltd., 1999, 2-12.

[25] O.E. Frosta, T. Foosnæs, H.A. Øye, H. Linga, Modelling of anode thermal cracking behaviour, Light Metals 2008, 923-927.

[26] M.W. Meier, Cracking behaviour of anode, R&D Carbon Ltd., Chapter 4, 1996, 251-268.

[27] R. C. Perruchoud, Survey on worldwide-prebaked anode quality, Light Metals 2004, 573-578.

[28] F. Durand, D. Rouby, G. Fantozzi, B. Allard, D. Dumas , Characterization of the high-temperature mechanical behaviour of carbon materials, Carbon, vol. 32 (5), 1994, 857-865.

[29] M. Tkac, Porosity development in composite carbon materials during heat treatment, Thesis for the degree of philosophiae doctor, Norwegian University of Science and Technology, 2007, 27-37.

[30] F. Keller, P.O. Sulger, Anode baking - baking of anodes for the aluminium industry. R&D carbon Ltd., 2008.

[31] L. Edwards, N. Backhouse, H. Darmstadt, M-J Dion, Evolution of anode grade coke quality, Light Metals 2012, 1207-1212.

[32] W.K. Fischer, R.C. Perruchoud, Influence of coke calcining parameters on petroleum coke quality, Light Metals 1985, 811-826.

[33] B. Vitchus, F. Cannova, H. Childs, Calcined coke from crude oil to customer silo. Light Metals 2013, 1-10.

[34] A. Radenovic, Properties of carbon anode components for aluminium production, Professional Paper, NAFTA, vol. 63 (3-4), 2012, 111-114.

[35] R.J. Tosta M, E.M. Inzunza, Structural evaluation of coke of petroleum and coal tar pitch for the elaboration of anodes in the industry of the aluminium, Light Metals 2008, 887-892.

[36] R.H. Wombles, J.T. Baron, Laboratory anode comparison of Chinese modified pitch and vacuum distilled pitch, Light Metals 2006, 535-540.

[37] A. Alscher, R. Wildforster, Performance of binder pitch with decreased QI-content in anode making - Formation, nature, properties and substitution of quinoline insolubles, Light Metals 1990, 583-589.

[38] B.E. Hansen, The effect of heat treatment on pitch quality, Ph.D. Thesis, Department of chemical engineering, Technical University of Denmark, 2001, 21-240.

[39] D. Auguie, Formation of thin mesophase layers at the interface between filler and binder in prebaked anodes. Effect of mixing on mesophase, Carbon, vol. 19, 1981, 277-284.

[40] D. Belitskus, Effect of carbon recycle materials on properties of bench scale prebaked anodes for aluminium smelting, Metallurgical and Materials Transactions B, vol. 12, 1981, 135-139.

[41] T.L. Weng, V.M. Vera, Effects of butt particle size and butt fraction on prebake anode properties, Light Metals 1984, 1005-1013.

[42] W.K. Fischer, R.C. Perruchoud, Interdependence between properties of anode butts and quality of prebaked anodes, Light Metals 1991, 721-724.

[43] K. Azari Dorcheh, Investigation of the materials and paste relationships to improve forming process and anode quality. Ph.D. Thesis, Laval University, 2013.

[44] S.S. Jones, J.D. Bacha, J.W. Newman, J.L. White, Anode-Carbon Usage in the Aluminium Industry, In Petroleum-Derived Carbons. Washington, DC: American Chemical Society, 1986, 234-250.

[45] P. Stokka, Green paste porosity as an indicator of mixing efficiency, Light Metals 1997, 565-568.

[46] S.P. Perez, Quality improvement for anode paste used in electrolytic production of aluminium, IAS Annual Meeting, Kowloon, Hong Kong, China, 2005, 523-528.

[47] M. Tkac, T. Foosnaes, H.A. Oye, Effect of vacuum vibroforming on porosity development during anode baking, Light Metals 2007, 885-890.

[48] B. Hohl, A. Pinoncely, J.C. Thomas, Anode paste preparation by means of a continuously operated intensive mixing cascade at Aostar Qimingxin Aluminium China, Light Metals 2004, 511-515.

[49] D. Belitskus, Effects of mixing variables and mold temperature on prebaked anode quality, Light Metals 1985, 915-924.

[50] M.W. Meier, Cracking behavior of prebaked carbon anodes used for the aluminium production [on-line], http://e-collection.library.ethz.ch/eserv/eth:40099/eth-40099-01.pdf [access Nov. 2016].

[51] S.S. Zhuchkov, S. A. Khramenko, Effect of pitch quality on properties of baked anodes. The second international congress Non Ferrous Metals, Aluminium Reduction Technology, Part VI, 2010, 333-335.

[52] The merrick group, inc., Eddy current testing [on-line], http://www.merrickgroupinc.com/2015/08/what-is-eddy-current-testing/ [access Nov. 2016].

[53] Y. Xie, D. Kocaefe, Y. Kocaefe, L. Wei, S. Zou, A. Wu, Correlation between anode recipe and anode properties, International Journal of Engineering and Innovative Technology (IJEIT) Vol. 2, Issue 8, 2013, 23-27.

[54] J. Lauzon-Gauthier, C. Duchesne, J. Tessier, Texture analysis of anode paste images, Light Metals 2014, 1123-1128.

[55] O. E. Frosta, A. P. Ratvik, H. A. Øye, Properties and production conditions affecting crack formation and propagation in carbon anodes, Light Metals 2012, 1293-1298.

[56] Energy workforce, Ultrasonic testing [on-line], http://www.energyworkforce.net/?p=126 [access Nov. 2016].

[57] Euro physical acoustics SA, Acoustic emission products [on-line], http://www.epandt.com/us/produits_ea_us.html [access Nov. 2016].

[58] Crystal Instruments, Modal testing [on-line], http://www.crystalinstruments.com/modal-testing/ [access Nov. 2016].

[59] Radiographic testing [on-line], https://www.nde-ed.org/GeneralResources/Method Summary/RT1.jpg [access Nov. 2016].

[60] U. Mannweiler, F. Keller, The design of a new anode technology for the aluminium industry, JOM, vol. 46, 1994, 15-21.

[61] A. J. Rolf, Measures to improve carbon baking, Light Metals 1992, 739-745.

[62] F. Keller, Importance of baking technology on anode quality, R&D Carbon Ltd., Anode, Anode for the aluminium industry, 2nd edition, 2006, 223-242.

[63] P. Mahieu, P. Sedmak, Improving fuel gas injection in anode baking furnace, Light Metals, 2014, 1165-1169.

[64] F. Keller, P.O. Sulger, M.W. Meier, D.S. Severo, V. Gusberti, Specific energy consumption in anode bake furnaces, R&D Carbon Ltd., 2013, 13-53.

[65] D.S. Severo, V. Gusberti, P.O. Sulger, F. Keller, M.W. Meier, Recent developments in anode baking furnace design, Light Metals 2011, 853-858.

[66] G.A. Bain, J.P. Pruneau, J. Williams, The effect of prebaked anode baking temperature in potroom performance, Light Metals 1971, 444-449.

[67] T. Liu, Les C. Edwards, C.P. Hughes, B.J. Mason, Thermal shock crack initiation and propagation behavior of carbon anodes, Light Metals 1995, 733-740.

[68] W.K. Fischer, M.W. Meier, M.W. Lustenberger, Cooling of green anodes after forming, Light Metals 1999, 351-357.

[69] K.A. Sinclair, B.A. Sadler, Improving carbon plant operations through the better use of data, Light Metals 2006, 577-582.

[70] J. Kim, P.K. Liaw, The non- destructive evaluation of advanced ceramics and cermic-matrix composites [on-line], http://www.tms.org/pubs/journals/JOM/9811/Kim/Kim-9811.html [access Nov. 2016].

[71] S.U. Fassbender, W. Karpen, A. Sourkov, NDE of fatigue on metals thermography, acoustic microscopy and positron annihilation method [on-line], http://www.ndt.net/article /wcndt00/papers/idn319/idn319.htm [access Nov. 2016].

[72] E. Zermatten, Tomography-based characterization of porous media applied to snow, bone scaffolds and reticulated ceramics, PhD thesis, École Polytechnique Fédérale de Lausanne, Lausanne, Suisse, 2013.

[73] F. Keller and W.K. Fischer, Development of anode quality criteria by statistical evaluation of operational results in the electrolysis, Light Metals 1982, 729-740.

[74] K.A. Sinclair, B.A. Sadler, Which strategy to use when sampling anodes for coring and analysis? Start with how the data will be used, Light Metals 2009, 1037-1041.

[75] Y. Safa, Simulation numérique des phénomènes thermiques et magnétohydro-dynamiques dans une cellule de Hall-Héroult, PhD thesis, École Polytechnique Fédérale de Lausanne, Lausanne, Suisse, 2005.

[76] A.N. Adams, O. Karacan, A. Grader, J.P. Mathews, P.M. Halleck, H.H. Schobert, The non-destructive 3-D characterization of pre-baked carbon anodes using X-ray computerized tomography. Light Metals 2002, 535-539.

[77] D. Picard, H. Alamdari, D. Ziegler, B. Dumas, M. Fafard, Characterization of a full-scale prebaked carbon anode using X-ray computerized tomography, Light Metals 2011, 973-978..

[78] M. McClung, J.A. Ross, A Method to Correlate Raw Material Properties to Baked Anode Core Performance, Light Metals 2000, 481-486.

[79] D. Picard, H. Alamdari, D. Ziegler, B. Dumas, M. Fafard, Characterization of pre-baked carbon anode samples using X-Ray computed tomography and porosity estimation, Light Metals 2012, 1283-1288.

[80] D. Picard, J. Lauzon-Gauthier, C. Duchesne, H. Alamdari, M. Fafard, D. Ziegler, Automated crack detection method applied to CT images of baked carbon anode, Light Metals 2014, 1275-1280.

[81] F. Grégoire, L. Gosselin, H. Alamdari, Sensitivity of Carbon Anode Baking Model Outputs to Kinetic Parameters Describing Pitch Pyrolysis, Industrial & Engineering Chemistry Research, vol. 52, 2013, 4465-4474.

[82] W. Leisenberg, Improving the Anode Baking Process by Estimation of the Anode Temperature, Light Metals 2001, 637-641.

[83] Y. Kocaefe, N. Oumarou, M. Baiteche, D. Kocaefe, B. Morais, M. Gagnon, Use of Mathematical Modelling to Study the Behaviour of a Horizontal Anode Baking Furnace, Light Metals 2013, 1139-1144.

[84] W.K. Fischer, U. Mannweiler, F. Kelle, R.C. Perruchoud, U. Bühler, Anodes for the aluminium industry. R & D Carbon Ltd., 1995.

[85] S.M. Hume, W.K. Fischer, R.C. Perruchoud, J.B. Metson, R.T.K. Baker, Influence of petroleum coke sulphur content on the sodium sensitivity of carbon anodes, Light Metals 1993, 535-535.

[86] T. Yamaguchi, S. Hashimoto, Fast crack detection method for large-size concrete surface images using percolation-based image processing, Machine Vision Appl., vol. 21(5), 2010, 797-809.

[87] W. K. Fischer, F. Keller, R. C. Perruchoud, S. Oderbolz, Baking parameters and the resulting anode quality, Light Metals 1993, 683-694.

[88] L. Eliassen, Characterisation of mechanical properties of carbon anode materials, Project report, department of Structural Engineering, Norwegian University of Science and Technology NTNU, Norway, 2006.

[89] H. Aesen, finit element analysis of anode cracking, Master thesis, Departement of structural Engineering, NTNU, Norway, 2007.

[90] J. Lauzon-Gauthier, C. Duchesne, J. Tessier, A Database Approach for Predicting and Monitoring Baked Anode Properties, JOM, vol. 64, 2012, 1334-1342.

[91] T. Yamaguchi, S. Hashimoto, Automated Crack Detection for Concrete Surface Image Using Percolation Model and Edge Information, IEEE Industrial Electronics, IECON 32nd Annual Conference, 2006, 3355-3360.

[92] A. Pierret, C.J. Moran, L.M. Bresson. Calibration and Visualization of Wall-Thickness and Porosity Distributions of Ceramics Using X-radiography and Image Processing. Journal of Archaeological Science, vol. 23, 1996, 419-428.

[93] A. Dufour, J. Tessier, L. Gosselin, C. Duchesne, Empirical modeling of the baking furnace to predict baked anode properties, Light Metals 2016, 953-958.

[94] K. Azari, H. Alamdari, D. Ziegler, M. Fafard, Influence of coke particle characteristics on the compaction properties of carbon anodes used in aluminium production, Powder Technology, vol. 246, 2013, 650-657.

[95]K. Azari, H. Ammar, H. Alamdari, D. Picard, M. Fafard, D. Ziegler, Effects of physical properties of anode raw materials on the paste compaction behavior, Light Metals 2011, 1161-1164.

[96] K. Azari, H. Alamdari, H. Ammar, M. Fafard, A. Adams, D. Ziegler, Influence of mixing parameters on the density and compaction behavior of carbon anodes used in aluminium productionⅡ, THERMEC, Quebec, Canada, Published in Advanced Materials Research, Vol. 409, 2011, 17-22,

[97] W. Bogoya-Forero, C. Duchesne, J. Tessier, Real-Time Measurement of Coke Aggregate Size and Vibrated Bulk Density Using Image Texture Analysis, Light Metals 2015, 1055-1060.

[98] P. Jignesh, W. Mark, R. Jeffrey, Historical and Future Challenges with the Vibrated Bulk Density Test Methods for Determining Porosity of Calcined Petroleum Coke, Light Metals 2011, 925-930.

[99] C. Duchesne, J.J. Liu, J.F. MacGregor, Multivariate Image Analysis in the Process Industries: A Review, Chemometrics and Intelligent Laboratory Systems, vol. 117, 2012, 116-128.

[100] ASTM D4292-10, Standard Test Method for Determination of Vibrated Bulk Density of Calcined Petroleum Coke, Annual Book of ASTM Standards, D02.05, 2010, 1-5.

[101] W.X. Reynolds, G.M. Wells, Video-Compatible Thermography, British Journal of non-destructive Testing, Vol.26, 1984, 40-44.

[102] J. Lauzon-Gauthier, Monitoring of a carbon anode paste manufacturing process using machine vision and latent variable methods, PhD thesis, Université Laval , Canada, 2015.

[103] J. Tessier, C. Duchesne, G.P. Tarcy, Multiblock Monitoring of Aluminium Reduction Cells Performance, Light Metals 2011, 407-412.

[104] X. Maldague, Theory and practice of infrared technology for non-destructive testing, John Wiley and Sons, New York, 2001.

[105]J.G. Webster, Electrical Impedance Tomography, Adam Hilger Series of Biomedical Engineering, Adam Hilger, New York, USA, 1990.

[106] T.C. Hou, J.P. Lynch, Electrical Impedance Tomographic methods for sensing strain fields and crack damage in cementitious structures, Journal of Intelligent Material Systems and Structures, vol. 20 (11), 2008, 1363-1379.

[107] A. Peled, J.M. Torrents, T.O. Mason, S.P. Shah, E.J. Garboczi, Electrical impedance spectra to monitor damage during tensile loading of cement composites, ACI Materials Journal, vol. 98 (4), 2001, 313-322.

[108] S. Feliu, J.C. Galvan, M. Morcillo, interpretation of electrical impedance diagram for painted galvanized steel, Prog. In Organic Coatings, vol. 17 (2), 1989, 143-153.

[109] K. Kimmo, S. Aku, L. Anssi, J.M.M. Paulo, P.K. Jari, Electrical Resistance Tomography imaging of concrete, Cement and Concrete Research, vol. 40, 2010, 137-145.

[110] W. Daily, A. Ramirez, A. Binley, S. Henry-Poulter, Electrical Resistance Tomography of Concrete Structures, Proceedings of ECAPT94: 3rd European concerted action meeting on process tomography, Lisbon (Portugal), 1994.

[111] J.F. Lataste, C. Sirieix, D. Breysse, M. Frappa, Electrical resistivity measurement applied to cracking assessment on reinforced concrete structures in civil engineering, NDT & E International, vol. 36, 2003, 383-394.

[112] E.J. Seger, Method and means for measuring electrode resistance. US patent US3735253, 1973.

[113] E.J. Seger, New method of measuring electric resistance for quality control, Light Metals, 1978, 283-290.

[114] M.J. Chollier-Brym D. Laroche, A. Alexandre, M. Landry, C. Simard, L. Simard, D. Ringuette, New method for representative measurement of anode electrical resistance, Light Metals 2012, 1299-1302.

[115] G. Léonard, S. Guérard, D. Laroche, J.C. Arnaud, S. Gourmaud, M. Gagnon, M.J. Marie-Chollier, Y. Perron, Anode Electrical Resistance Measurements : Learning and Industrial On-line Measurement Equipment Development. Light Metals 2014, 1269-1274.

[116] P.R. Haldemann, E.P. Fawzi, Methods and Apparatus for Non-destructively Detecting Flaws in a Carbon Anode, US Patent US5473248, 1995.

[117] D. Audet, L. Parent, System and method to forecast the electrical conductivity of anodes for aluminium production before baking. US Patent US7576534, International patent IPC, CA 2590482, 2005.

[118] D. Kocaefe, D. Bhattacharyay, Y. Kocaefe, Method for analyzing an anode and device thereof, Provisional patent application US 61/939768, 2014.

[119] Y. Kocaefe, D. Kocaefe, D. Bhattacharyay, Quality control via electrical resistivity measurement of industrial anodes, Light Metals 2015, 1097-1102.

[120] E. Rayer, F. Daubigney, M. Peyrot, L'utilisation de la vidéoendoscopie en remplacement de la radiographie pour les contrôles non destructifs, journées Cofrend Toulouse, 2008.

[121] S.Y. Lee, S.H Lee, D.I. Shin, Y.K. Son, C.S. Han, Development of an inspection system for cracks in a concrete tunnel lining, Canadian Journal of Civil Engineering, vol. 34 (8), 2007, 966-975.

[122] J. Dumont-Fillon, Contrôle non destructif (CND), Techniques de l'ingénieur, dossier R1400, 1996.

[123] R.J. Schliekelmann, Non-destructive Testing of Adhesive Bonded Joints, AGARD Lecture Series. Vol. 102 (8), 1979, 1-37.

[124] A. Benouis, A. Grini, Estimation of concrete's porosity by ultrasounds, Elsevier, Physics Procedia, vol. 21, 2011, 53-58.

[125] M.G. Hernandez, M.A.G. Izquierdo, A. Ibanez, J.J. Anaya, L.G. Ullate, Porosity estimation of concrete by ultrasonic NDE. Elsevier, Ultrasonics, vol. 38, 2000, 531-533.

[126] M.L. Costa, S.F. Müller de Almeida, M.C. Rezende, The influence of porosity on the ILSS of carbon/epoxy and carbon/bismaleimide fabric laminates, Composites Science and Technology, vol. 61, 2001, 2101-2108.

[127] M. Goueygou, Z. Lafhaj, F. Soltani, Assessment of porosity of mortar using ultrasonic Rayleigh waves, NDT&E International, 2009, vol. 42, 353-360.

[128] B. Mascaro, Caractérisation ultrasonore de la porosité dans les composites, Thèse de doctorat, Université Paul Sabatier, Toulouse, France, 2006.

[129] L. Liu, B. Zhang, D. Wang, Z. Wu, Effects of cure cycles on void content and mechanical properties of composite laminates, Composite Structure, vol. 73, 2006, 303-309.

[130] S. Liu, E. Guo, V.M. Levin, F. Liu, Y.S. Petronyuk, Q. Zhang, Application of acoustic microscopy technique for 3D imaging bulk microstructure of carbon fiber-reinforced composite, Ultrasonics, vol. 44, 2006, e1037-e1044.

[131] M. Gerlanc, D. Haddad, G.W. Hyatt, J.T. Langloh et P. Hilaire, Ultrasonic study of normal and fractured bone, Clinical orthopaedics and related research, vol. 111, 1975, 175-180.

[132] D. Hans, S. Srivastav, C. Singal, R. Barkmann, C. Njeh, E. Kantorovich, C. Glüer, Genant H.K., Does combining the results from multiple bone sites measured by a new quantitative ultrasound device improve discrimination of hip fracture, Journal of Bone and Mineral Research, vol. 14(4), 644-651, 1999.

[133] I. Siegel, G.T. Anast, T. Melds, The determination of fracture healing by measurement of sound velocity across the fracture site, Surgery, Gynecol, Obstetrics, vol. 107 (3), 1958, 327-332.

[134] G. Van der Perre, G. Lowet, In vivo assessment of bone mechanical properties by vibration and ultrasonic wave propagation analysis, Bone, vol. 18(1), 1996, 29-35.

[135] M. J. Grimm, J. Williams, Use of ultrasound attenuation and velocity to estimate young's modulus in trabecular bone, Bioengineering Conference, IEEE Nineteenth Annual Northeast, Newark, NJ, USA, 1993, 62-63.

[136] T. E. Matikas, P. Karpur, S. Shamasundar, Measurement of the dynamic elastic moduli of porous titanium aluminide compacts. Journal of material science, vol. 32, 1997, 1099-1103.

[137] S. Ould Naffa, M. Goueygou, B. Piwakowski, F. Buyle-Bodin, Detection of chemical damage in concrete using ultrasound, Elsevier, Ultrasonics, vol. 40, Issues 1–8, 2002, 247-251

[138] D.G. Aggelis, S. Hadjiyiangou, H.K. Chai, S. Momoki, T. Shiotani, Longitudinal waves for evaluation of large concrete blocks after repair, NDT & E International, vol. 44 (1), 2011, 61-66.

[139] A. Quiviger, C. Payan, J. Moysan, J. Salin, Caractérisation d'une fissure débouchante dans un béton par méthode ultrasonores, Chatou, France, EDF-R&D-STEP, 2011.

[140] T. Öztürk, O. Kroggel, P. Grübl, J.S. Popovics, Improved ultrasonic wave reflection technique to monitor the setting of cement-based materials. NDT&E International, vol. 39 (4), 2006, 258-263.

[141] I.O. Yaman, G. Inei, N. Yesiller, H.M. Aktan. Ultrasonic pulse velocity in concrete using direct and indirect transmission. ACI Materials Journal, Title no. 98-M48, 2001.

[142] J.H. Bungey, Standard test method for pulse velocity through concrete, ASTM International, 1989.

[143] P. Turgut, M.N. Okuyan, The pulse velocity variation around cylindrical concrete section. Harran University Civil Engineering Department, Sanliurfa, Turkey, 2007, 1-4.

[144] E.V.S. Espinosa, J.L. Domingez, M.G. Hernandez, M.A. Garcimartin, Ultrasonic Evaluation Of Different types of mortars subjected to attack by pig slurry, CIGR - International Conference of Agricultural Engineering, Madrid, Spain, 2008.

[145] H.K. Lee, K.M. Lee, Y.H. Kim, H. Yim, D.B. Bae, Ultrasonic in-situ monitoring of setting process of high-performance concrete. Cement and Concrete Research, vol. 34, 2004, 631-640.

[146] B. Christaras, F. Auger, E. Mosse, Determination of the moduli of elasticity of rocks. Comparison of the ultrasonic velocity and mechanical resonance frequency methods with direct static methods', Materials and structures, vol. 27, 1994, 222-228.

[147] V. Bucur, A. Perrin, Détermination du module d'Young du bois par une méthode dynamique sur carottes de sondage, Ann. For. Sci., vol. 38, 1981, 283-298.

[148] L. Moraru, F. Szendrei, Ultrasonic properties of ancient ceramic materials with porous structure, Journal of Science and Arts, vol.2 (13), 2010, 345-348.

[149] M. Asmani, C. Kermel, A. Leriche, M. Ourak, Influence of porosity on Young's modulus and Poisson's ratio in alumina ceramics, Journal of the European Ceramic Society, vol. 21 (8), 2001, 1081-1086.

[150] Q.Q. Ni, M. Iwamoto. Wavelet transform of acoustic emission signals in failure of model composites. Engineering Fracture Mechanics, vol. 69, 2002, 717–728.

[151] Physical acoustics corporation, ARB-1410 arbitrary waveform generator board and wavegen 1410 software [on-line], http://pacndt.com/downloads/news/ARB-1410%20PR.pdf [access Nov. 2016].

[152] B.L. Luk, K.P. Liu, F. Tong, Rapid evaluation of tile-wall bonding integrity using multiple-head impact acoustic method, NDT&E International, vol. 44, 2011, 297-304.

[153] X.H. Wang, C.M. Zhu, H.L. Mao, Z.F. Huang, Wavelet packet analysis for the propagation of acoustic emission signals across turbine runners, NDT&E International, vol. 42, 2009, 42-46.

[154] W.M. McCabe, R.M. Koerner, A.E. Load Jr., Acoustic emission behavior of concrete laboratory specimens, Am. Concr. Inst. J. vol. 13, 1976, 367-371.

[155] Y. Niwa, S. Kobayashi, M. Ohtsu, Studies of AE in concrete structures, Proc. Jpn. Soc. Civil Eng. vol. 276, 1978, 135-147.

[156] S. Lovejoy, Acoustic emission testing of beams to simulate SHM of vintage reinforced concrete deck girder highway bridges, Struct. Health Monit. vol. 7 (4) (2008) 327–346.

[157] P. Ziehl, M. Engelhardt, T. Fowler, F. Ulloa, R. Medlock, E. Schell, Design and live load evaluation of a hybrid FRP/RC bridge superstructure system, J. Bridge Eng., vol. 14 (5), 2009, 309-318.

[158] T. Shiotani, D.G. Aggelis, O. Makishima, Global monitoring of concrete bridge using acoustic emission, J. Acoust. Emission, vol. 25, 2007, 308-315.

[159] X. Luo, H. Haya, T. Inaba, T. Shiotani, Y. Nakanishi, Damage evaluation of railway structures by using train-induced AE, Constr. Build. Mater. vol. 18, 2004, 215-223.

[160] K. Tanaka, Y. Akiniwa, T. Nomura, Y. Sakaida, Bending strength of smooth and notched specimens of porous silicon carbide, Trans. Jpn. Soc. Mech. Eng., vol. A65, 1999, 2385–2392.

[161] S. Matsuda, M. Takahashi, Fracture strength distribution of porous ceramics under quasi-static load, Eng. Fract. Mech., vol. 77, 2010, 2601-2609.

[162] T. Whitlow, E. Jones, C. Przybyla, In-situ damage monitoring of a SiC/SiC ceramic matrix composite using acoustic emission and digital image correlation. vol. 158, 2016, 245-251

[163] R. Knehans, R. Steinbrech, W. Schaarwächter, Quantitative correlation of acoustic emission to the brittle fracture of porous sintered glass, Materials science and engineering, vol. 61 (1), 1983, 17-22.

[164] J.P. Li, C.B. Zhou, Experimental research on acoustic emission characteristics of rock mass. Rock and Soil Mechanics, vol. 25(3), 2004, 374-378.

[165] E.L. Zhao, E.Y. Wang. Experimental study on acoustic emission characteristics of rock and soil in the failure process. Journal of Disaster Prevention and Mitigation Engineering, vol. 26(3), 2006, 316-320.

[166] X.P. Lai, M.F. Cai. Couple analyzing the acoustic emission characters from hard composite rock fracture. Journal of University of Science and Technology Beijing, vol. 11(2), 2004, 97-101.

[167] Y.J. Sun, Z.M. Xu, Q.H. Dong, Forecasting water disaster for a coal-mine under the Xiaolangdi reservoir. Journal of China University of Mining & Technology, vol. 18(4), 2008, 516-520.

[168] J. E. Parks, T. Papulak, C. P. Pantelides, Acoustic emission monitoring of grouted splice sleeve connectors and reinforced precast concrete bridge assemblies. Construction and Building Materials, vol. 122, 2016, 537-547.

[169] J. Antoni, M. Sidahmed, Contrôle et diagnostic à partir des signaux acoustiques et vibratoires, Spécial congrès Surveillance 5, Acoustique & Techniques, vol. 38, 2004.

[170] J.M. Montalvao, E. Silva, An over view of the fundamentals of modal analysis, In Modal Analysis and Testing, Springer Netherlands, 1-34

[171] F.L.M. dos Santos, B. Peeters, J. Lau, W. Desmet, L.C.S. Goes. An overview of experimental strain-based modal analysis methods. LMS, A Siemens Business, [on-line], https://www.researchgate.net/publication/278963294_An_overview_of_experimental_strain-based_modal_analysis_methods, [accessed Oct. 2016].

[172] R. Aguilar, E. Ramírez, V.G. Haach, M.A. Pando, Vibration-based non-destructive testing as a practical tool for rapid concrete quality control. Constr. Build Mater, vol. 104(1), 2016, 181-90.

[173] T.H. Oijevaar, R. Loendersloot, L.L. Warnet, A. Boer, R. Akkerman, Vibration based structural health monitoring of a composite T-beam, Compos Struct, vol. 92 (9), 2010, 07-15.

[174] D.M. Prado, I.D.G. Araujo, V.G. Haach, R. Carrazedo, Assessment of shear damaged and NSM CFRP retrofitted reinforced concrete beams based on modal analysis, Engineering Structures, vol. 129, 2016, 54-66.

[175] R.W. Campanelli, J.J. Engblom, The effect of delaminations in graphite/PEEK composite plates on modal dynamic characteristics, Composite Structures, vol. 31 (3), 1995, 195-202.

[176] F. Bosa, S.B. Casagrande, On-line non-destructive evaluation and control of wood-based panels by vibration analysis, Journal of Sound and Vibration, vol. 268, 2003, 403-412.

[177] A. Paté, J.L. Carrou, B. Fabre, Modal parameter variability in industrial electric guitar making: Manufacturing process, wood variability, and lutherie decisions, Applied Acoustics, vol. 96, 2015, 118-131.

[178] R.J. Ditchburn, S.K. Burke, C.M. Scala, NDT of welds: state of the art, NDT&E International, vol. 29(2), 1996, 11-17.

[179] I. Berg. Looking through pots: recent advances in ceramics X-radiography. Journal of Archaeological Science, vol. 35, 2008, 1177-1188.

[180] F.C. de Beer, J.J. le Roux, E.P. Kearsley, Testing the durability of concrete with neutron radiography, Nuclear Instruments and Methods in Physics Research, vol. A542, 2005, 226-231.

[181] K.T. Tan, N. Watanabe, Y. Iwahori, X-ray radiography and micro-computed tomography examination of damage characteristics in stitched composites subjected to impact loading, Composites: Part B, vol. 42, 2011, 874-884.

[182] M. Balasko, I. Veres, Gy. Molnar, Zs. Balasko, E. Svab, Composite structure of helicopter rotor blades studied by neutron and X-ray radiography. Physica, vol. B350, 2004, 107-109.

[183] C. Kouzoubachian, Les principales méthodes utilisées en END, intérêts dans l'industrie, Contrôles – Essais - Mesures, Hors série n°1, 2006, 15-19.

[184] D.E. Bray, D. McBride, Nondestructive testing techniques, John Wiley & Sons (Ed.), 1992, 15-24.

[185] A.P Bovsunovsky, The mechanisms of energy dissipation in the non-propagating fatigue cracks in metallic materials, Engineering Fracture Mechanics, vol. 71, 2004, 2271-2281.

[186] P. Avitable, Experimental modal analysis, Sound and Vibration, vol. 35 (1), 2001, 20-31.

[187] A. Bracciali, P. Dugini, M. Pierini, A preliminary study of noise reduction in a passenger car through optimization of the engine suspension, In Proceedings of the international modal analysis conference. SEM Society for experimental mechanics inc., 1992, 858.

[188] J. Cugnoni, Identification par recalage modal et fréquentiel des propriétés constitutives de coques en matériaux composites, Thèse n° 3106, École Polytechnique Fédérale de Lauzanne, Lausanne, Suisse, 2004.

[189] F. Lafleur, M. Thomas, F. Laville, Analyse modale expérimentale des structures par excitation acoustique à référence unique, http://profs.etsmtl.ca/mthomas/Publications/Publications/Ama-acvm2.pdf [access July 2017].

[190] Y.S.P. Yong-Hwa Park, Vehicle interior noise and vibration reduction using experimental structural dynamics modification, Society of automotive engineers, inc., vol. 971915, 1997, 365-370.

[191] Kistler Corp., Accelerometer Calibration Certificate (8392A2), Kistler Instrument Corporation, USA, 2000.

[192] A.T.M. Willemsen, J.A. Van Alst, H.B.K. Boom, Real-time gait assessment utilizing a new way of accelerometery, J. Biomechan., vol. 23, 1990, 859-863.

[193] N.M.M. Maia, J.M.M. Silva, Theoretical and Instrumental Modal Analysis, Tauton, Somerset, England: Research Study Press LTD, 1998.

[194] M.D. Camden, L.W. Simmons, Using a Laser Vibrometer for Monitoring Dynamic Strain, Modal Analysis, and Calculating Damping, Proceedings of the SPIE, The International Society for Optical Engineering, vol. 34, (37), 1998, 311-318.

[195] P. Sriram, S. Hanagud, J. Craig, Mode Shape Measurement Using a Scanning Laser Doppler Vibrometer, Journal of Analytical and Experimental Modal Analysis, vol. 7, 1992, 169-178.

[196] J. Bendat, A.G. Piersol, Random Data, John Wiley & Sons, 1986.

[197] J. Bendat, A.G. Piersol, Engineering application of correlation and spectral analysis, John Wiley & Sons, New York, USA ,1993, 315.

[198] M. Batel, Operational Modal Analysis - Another way of Doing Modal Testing, Sound & Vibration, vol. 36 (8), 2002, 22-27.

[199] H. Vold, B. Schwarz, M. H. Richardson, Display Operating Deflection Shape from Non Stationary Data, Sound & Vibration, vol. 34 (6), 2000, 14-18.

[200] G. Rossi, R. Marsili, V. Gusella, M. Gioffre. Comparison between accelerometer and laser vibrometer to measure traffic excited vibrations on bridges. Shock and Vibration, vol. 9 (1-2), 2002, 11-18.

[201] W. Christopher, N. Christopher , A. Peter, P. Pawan, Comparison of FRF measurements and mode shapes determined using optically image based, laser, and accelerometer measurements. Mechanical Systems and Signal Processing, vol. 25, 2011, 2191-2202.

[202] C. Cristalli, N. Paone, R.M. Rodriguez. Mechanical fault detection of electric motors by laser vibrometer and accelerometer measurements. Mechanical Systems and Signal Processing, vol. 20, 2006, 1350-1361.

[203] J. Murin, M. Amin-baghai, J. Hrabovsky, R. Gogola, S. Kugler, Beam finite element for modal analysis of FGM structures. Engineering Structures, vol. 121, 2016, 1-18.

[204] H.A. Tinoco, D.A. Ocampo, F.M. Peña, J.R. Sanz-Uribe, Finite element modal analysis of the fruit-peduncle of Coffea arabica L. var. Colombia estimating its geometrical and mechanical properties, Computers and Electronics in Agriculture, vol. 108, 2014, 17-27

[205] A. Munjiza, D.R.J. Owen, N. Bicanic, A combined finite-discrete element method in transient dynamics of fracturing solids, Engineering Computations, vol.12 Iss: 2, 1995145-174

[206] T.T. Bui, A. Limam, Q.B. Bui, Vibration et caractérisation du dommage de structures maçonnées : Analyse expérimentale et numérique, 31èmes Rencontres de l'AUGC, E.N.S. Cachan, France, 2013.

[207] A. Vary, K.J. Bowles, An ultrasonic-acoustic technique for non-destructive evaluation of fiber composite quality. Polym Eng Sci, vol. 19, 1979.

[208] A. Vary, The acousto–ultrasonic approach, NASA TM-89843, 1987.

[209] J.H. Hemann, K.J. Bowles, H. Kautz, P. Cavano, Transply, crack density detection by acousto-ultrasonics, NASA-TM-100224,1987.

[210] A. Vary, Acousto-ultrasonics: retrospective exhortation with bibliography, Materials Evaluation, vol. 49, 1991, 581-584.

[211] J.C. Duke, E.G. Henneke, M.T. Kiernan, P.P. Grosskopf, A study of the stress wave factor technique for evaluation of composite materials. NASA CR 4195, 1989.

[212] H.E. Kautz, B.A. Lerch. Preliminary investigation of acousto-ultrasonic evaluation of metal matrix composite specimens. Materials Evaluation, vol. 49, 1991, 607-612.

[213] B. Tang, Acousto-ultrasonic technique applied to filled-polymer damage assessment, Journal of Spacecraft and Rockets, vol. 32 (5), 1995, 866-869.

[214] A. Tiwari, E.G. Henneke. Real-time acousto-ultrasonic NDE technique to monitor damage in SiC/CAS ceramic composites subjected to dynamic loads. ASTM STP 1184, ASTM, Philadelphia, USA, 1994.

[215] P.A. Raju, Acousto-ultrasonic evaluation of carbon composites at different processing stages, Polymer Composites, vol. 17 (2), 1996, 275-287.

[216] A. Tiwari, Real time Acousto–ultrasonic NDE technique for monitoring damage in ceramic composites under dynamic loads, NASA CR 198374, 1995.

[217]Z. Su, L. Ye, Identification of Damage Using Lamb Waves: From Fundamentals to Applications, Springer-Verlag GmbH & Co, London, 2009, 15-58.

[218] C. Zhou, Z.Su, L.Cheng, Quantitative evaluation of orientation-specific damage using elastic waves and probability-based diagnostic imaging, Mech. Syst. Signal Process. vol. 25, 2011, 2135-2156.

[219] A.S. Purekar, D.J. Pines, Damage detection in thin composite laminates using piezoelectric phased sensor arrays and guided Lamb wave interrogation, J. Intelligent Mater. Syst. Struct. vol. 21, 2010, 995-1010.

[220] T.H. Loutas, V. Kostopoulos, Health monitoring of carbon/carbon, woven reinforced composites: Damage assessment by using advanced signal processing techniques, Part II: Acousto–ultrasonics monitoring of damage development, Composites Science and Technology, vol. 69, 2009, 273-283

[221] Z. Su, C. Zhou, M. Hong, L. Cheng, Q. Wang, X.l. Qing, Acousto-ultrasonics-based fatigue damage characterization: Linear versus nonlinear signal features, Mechanical Systems and Signal Processing, vol. 45 (1), 2014, 225-239.

[222] T. Liu, S. Kitipornchai, M. Veidt. Analysis of acousto-ultrasonic characteristics for contact-type transducers coupled to composite laminated plates. International Journal of Mechanical Sciences, vol. 43, 2001, 1441-1456.

[223] E. Maillet, N. Godin, M. R'Mili, P. Reynaud, G. Fantozzi, J. Lamon, Damage monitoring and identification in SiC/SiC minicomposites using combined acousto-ultrasonics and acoustic emission, Composites: Part A vol. 57, 2014, 8-15.

[224] Educational numeric resources for the physic sic license [on-line], http://numeliphy.unisciel.fr/index [access Nov. 2016].

[225] Seismic waves (longitudinal and transversal) [on-line], http://www.mathsmelisso.fr/Ondes-sismiques.html [access Dec. 2013].

[226] Construction diagnostic center pvt. Ltd., Ultrasonic pulse velocity test [on-line]. http://www.ndtconcrete.com/ultrasonic-pulse-velocity-test.html [access Nov. 2016].

[227] H. N. Hashemi, Ultrasonic Wave Propagation in Graphite Fiber Composites, Master of Science, MIT, USA, 1979.

[228] P. Bonniau, A. R.Bunsell, Failure mechanism discrimination in carbon fibre reinforced epoxy composites. Composites, vol. 14, Issue 4, 1983, 345-351.

[229] A. Boulenger, C.Pachaud, Surveillance des machines par analyse des vibrations : du dépistage au risque, AFNOR, ISBN : 2-12-309012-3, 1995.

[230] G. Qi, Attenuation of acoustic emission body waves in acrylic bone cement and synthetic bone using wavelet time-scale analysis, Journal Biomedical, Materials Research, vol. 52 (1), 2000, 148-156.

[231] G. Qi, Wavelet-based AE characterization of composite materials, NDT&E International, vol. 33, 2000, 133-144.

[232] E. Jantunen, A summary of methods applied to tool condition monitoring in drilling. International Journal of Machine Tools & Manufacture, vol. 42, 2002, 997-1010.

[233] E. Jantunen, H. Jokinen, Automated On-line Diagnosis of Cutting Tool Condition (Second version), International Journal of Flexible Automation and Integrated Manufacturing, vol. 4 (3-4), 1996, 273-287.

[234] R.B.W. Heng, M.J.M. Nor, Statistical analysis of sound and vibration signals for monitoring rolling element bearing condition, Applied Acoustics, vol. 53 (1-3), 1998, 211-226.

[235] F. Honarvar, H.R. Martin, New statistical moments for diagnostics of rolling element bearings, Journal of Manufacturing Science and Engineering, Transactions of the ASME, vol. 119 (3), 1997, 425-432.

[236] J. Max, Méthodes et techniques de traitement du signal et applications aux mesures physiques_Tome I : Principes généraux et méthodes classiques, 4ème édition, MASSON, ISBN : 2-225-80470-2, 1985.

[237] D.G. Zimcik, D. Proulx , C. Roy, A. Maslouhi, Real time monitoring of carbon–epoxy composites using acoustic emission. NDE. SAMPE Quarterly, vol. 19 (2), 1988, 5-11.

[238] R.A. Kline, R.E. Green, C.H. Palmer, Acoustic emission waveforms from cracking steel: experiment and theory. Journal of Applied Physics, vol. 52, 1981, 141-146.

[239] H.N.G. Wadley, C.B. Scruby, G. Shrimpton, Quantitative acoustic emission source characterisation during low temperature cleavage and intergranular fracture, Acta Meterialia, vol. 29, 1981, 399-414.

[240] R.O. Curadelli, J.D. Riera, D. Ambrosini, M.G. Amani, Damage detection by means of structural damping identification, Engineering structures, vol.30 (12), 2008, 3497-3504.

[241] M.G. Boiche, M. Chatre, B. Goublaire, JC. Gourlaouen, G. Poirson. Application de la détermination de la fréquence de résonance au contrôle des produits réfractaires, Hommes et Fonderie, 1981, 21-30.

[242] J.W. Lemmens, Sonic testing of refractory brick, ceramic industry, business news publishing company, 1991.

[243] J.L. Tebec, Maintenance et contrôle qualité des machines tournantes par l'analyse du comportement vibratoire, Thèse de Doctorat d'État, Université Pierre et Marie Curie, Paris, France, 1987.

[244] T.I. El-Wardany, D. Gao, M.A. Elbesta, Tool condition monitoring in drilling using vibration signature analysis, International Journal of Machine Tools and Manufacture, vol. 36 (6), 1996, 687-711.

[245] D.E. Dimla, Sensors signals for tool-wear monitoring in metal cutting operations-a review of methods, International Journal of Machine Tools and Manufacture, vol. 40 (8), 2000, 1073-1098.

[246] C. Chen, R. Kovacevic, D. Jandgric, Wavelet transform analysis of acoustic emission in monitoring friction stir welding of 6061 aluminium, International Journal of Machine Tools & Manufacture, vol. 43, 2003, 1383-1390.

[247] Y. Ding, R.L. Reuben, J.A. Steel, A new method for waveform analysis for estimating AE wave arrival times using wavelet decomposition, NDT&E International, vol. 37, 2004, 279-290.

[248] F. Hemmati, W. Orfali, M.S. Gadala, Roller bearing acoustic signature extraction by wavelet packet transform, applications in fault detection and size estimation, Applied Acoustics, vol. 104, 2016, 101-118.

[249] F. Bettayeb, S. Haciane, S. Aoudia, Improving the time resolution and signal noise ratio of ultrasonic testing of welds by the wavelet packet, Elsevier NDT & E International, vol. 38 (6), 2005, 478-484.

[250] L. Jedlinski, J. Jonak, Early fault detection in gearboxes based on support vector machines and multilayer perceptron with a continuous wavelet transform, Applied Soft Computing, vol. 30, 2015, 636-641

[251] S. Ni, Y. Yang, P. Tsai, W. Chou, Evaluation of pile defects using complex continuous wavelet transform analysis, NDT&E International, vol. 87, 2017, 50-59.

[252] X. Boespflug, Axial Tomodensitometry-Relation between the Ct Intensity and the Density of the Sample. Canadian Journal of Earth Sciences, vol. 31 (2), 1994, 426-434.

[253] M. Vetterli, J. Kovačević, Wavelets and Subband Coding, Prentice Hall PTR, Englewood Cliffs, New Jersey, 2005.

[254] M.H. Bharati, J.J. Liu, J.F. MacGregor, Image texture analysis: methods and comparisons, Chemometrics and Intelligent Laboratory Systems, vol. 72, 2004, 57-71.

[255] P. Facco, E. Tomba, M. Roso, M. Modesti, F. Bezzo, M. Barolo, Automatic characterization of nanofiber assemblies by image texture analysis, Chemometrics and Intelligent Laboratory Systems, vol. 103, 2010, 66-75.

[256] T. Randen, J.H. Husøy, Texture segmentation using filters with optimized energy separation, IEEE Transactions on Image Processing, vol. 8 (4), 1999, 571-582.

[257] M. Reis, A. Bauer, Wavelet texture analysis of on-line acquired images for paper formation assessment and monitoring, Chemometrics and Intelligent Laboratory Systems, vol. 95, 2009, 129-137.

[258] J. Zhang, X. Wang, S. Palmer, Objective grading of fabric pilling with wavelet texture analysis, Textile Research Journal, vol. 77, 2007, 871-879.

[259] H.D. Lin, Automated visual inspection of ripple defects using wavelet characteristic based multivariate statistical approach, Image and Vision Computing, vol. 25, 2007, 1785-1801.

[260] R. Gosselin, D. Rodrigue, R. González-Núñez, C. Duchesne, Potential of hyperspectral imaging for quality control of polymer blend films, Industrial and Engineering Chemistry Research, vol. 48, 2009, 3033-3042.

[261] S. García-Muñoz, A. Carmody, Multivariate wavelet texture analysis for pharmaceutical solid product characterization, International Journal of Pharmaceutics, vol. 398, 2010, 97-106.

[262] K. Delibasis, P.E. Undrill, G.G. Cameron, Designing texture filters with genetic algorithms: an application to medical images, Signal Processing, vol. 57, 1997, 19-33.

[263] S. Amat, M. Moncayo, l^{∞}-Stability for linear multiresolution algorithms: A new explicit approach. Part II: The cases of Symlets, Coiflets, biorthogonal wavelets and super compact multiwavelets, Applied Mathematics and Computation, vol. 206, 2008, 92-103.

[264] R.C. Guido, P. Addison, J. Walker, Introducing wavelets and time-frequency analysis, IEEE Engineering in Medicine and Biology Magazine, vol. 28 (5), 2009, 13.

[265] R.C. Guido, A note on a practical relationship between filter coefficients and scaling and wavelet functions of Discrete Wavelet Transforms, Applied Mathematics Letters, vol. 24, 2011, 1257-1259.

[266] S. Borah, E.L. Hines, M. Bhuyan, Wavelet Transform Based Image Texture Analysis for Size Estimation Applied to the Sorting of Tea Granules, Journal of Food Engineering, vol. 79, 2007, 629-639.

[267] M.X. Cielo, P. Ashley, P.J., Farahbakhsh, Thermographic XDT of Aluminium Laminates, C.S.X.D.T. Journal, Vol.8. , 1987, 44-50.

[268] L. Eriksson, Multi and Megavariate Data Analysis Part I Basic Principles and Applications, 2nd ed. Umetrics Academy, Umea, Sweden, 2006, 39-101.

[269] M. Cherfaoui, J. Roget, A. Lemascon, M. Jeanville, The study of acoustic emission from composites by means of multivariate data analysis. In Sixth International Conference on Composite Materials and Second European Conference on Composite Materials, Vol. I, London, UK, 1987, 424-432.

[270] M. Cherfaoui, A. Lemascon, J. Roget. Detection and evaluation of defects in acoustic emission monitoring of bending tests. In Eighth International Acoustic Emission Symposium, Vol. III, Tokyo, Japan, 1986, 586-593.

[271] A. Hoskuldsson, PLS regression methods, Journal of chemometrics, vol. 2, 1988, 211-228.

[272] S. Wold, M. Sjöström, L. Eriksson, PLS-regression: A basic tool of chemometrics, Chemometrics and Intelligent Laboratory Systems, vol. 58 (2), 2001, 109-130.

[273] M.R. Gupta, N.P. Jacobson, Wavelet Principal Component Analysis and Its Application to Hyperspectral Images, In 2006 IEEE International Conference on Image Processing, 2006, 1585-1588.

[274] K. Tong, Wavelet Transform and Principal Component Analysis Based Feature Extraction, 2010, 1-15, https://sites.math.washington.edu/~morrow/336_10/papers/kent.pdf [access July 2017].

[275] R.B. Darlington, Regression and Linear Models, McGraw-Hill, New York, 1990.

[276] P. Geladi, B.R. Kowalski, Partial least-squares regression: a tutorial, Analytica Chimica Acta, vol. 185, 1986, 1-17.

[277] S. Wold, K. Esbensen, P. Geladi, Principal Component Analysis, Chemometrics and Intelligent Laboratory Systems, vol. 2, 1987, 37-52.

[278] L. Eriksson, E. Johansson, N. Kettaneh-Wold, S. Wold, Multi- and megavariate data analysis, principles and applications, UMETRICS, Umea, Sweden, 2001.

[279] T. Kourti, Application of latent variable methods to process Control and multivariate statistical process control in industry, International journal of adaptive control and signal processing, vol. 19 (4), 2005, 213-246.

[280] T. Kourti, J.F. MacGregor, Process analysis, monitoring and diagnosis, using multivariate projection methods, Chemometrics and Intelligent Laboratory Systems, vol. 28, 1995, 3-21.

[281] I.G. Chong, C.H. Jun, Performance of some variable selection methods when multicollinearity is present, Chemometrics and Intelligent Laboratory Systems, vol. 78, 2005, 103-112.

[282] M. Johnson, Wavelet based clustering and classification of AE transients in composite laminates using principal component analysis, NDT & E International, vol. 35, 2002, 367-376.

[283] L. Calabrese, G. Campanella, E. Proverbio. Identification of corrosion mechanisms by univariate and multivariate statistical analysis during long-term acoustic emission monitoring on a pre-stressed concrete beam. Corrosion Science, vol. 73, 2013, 161-171.

[284] E.P. de Moura, C.R. Souto, A.A. Silva, M.A.S. Irmao, Evaluation of principal component analysis and neural network performance for bearing fault diagnosis from vibration signal processed by RS and DF analyses. Mechanical Systems and Signal Processing, vol. 25, 2011, 1765-1772.

[285] I. Trendafilova, M.P. Cartmell, W. Ostachowicz. Vibration-based damage detection in an aircraft wing scaled model using principal component analysis and pattern recognition. Journal of Sound and Vibration, vol. 313, 2008, 560-566.

[286] A.J. Willis, Condition monitoring of centrifuge vibrations using kernel PLS, Computers and Chemical Engineering, vol. 34, 2010, 349-353.

[287] D.J. Hagemaier, Bonded Joints and Non- destructive Testing-Bonded Honeycomb Structures- 2, Non-destructive Testing, vol.5, 1972, 28-48.

[288] R. Ambu, F. Aymerich, F. Ginesu, P. Priolo, Assessment of NDT interferometric techniques for impact damage detection in composite laminates, Composites Science and Technology, vol. 66, 2006, 199-205.

[289] M. Matter, Identification modale numérique-expérimentale des propriétés élastiques et dissipatives de matériaux composites, PhD thesis N.4215, École Polytechnique Fédérale de Lausanne, Lausanne, Suisse, 2008.

[290] Z. Ismail, Application of residuals from regression of experimental mode shapes to locate multiple crack damage in a simply supported reinforced concrete beam, Measurement, vol. 45, 2012, 1455-1461.

[291] M. W. Meier, Cracking behavior of anodes, R&D Carbon Ltd., Sierre, Switzeland, 1995.

[292] D. Picard, J. Lauzon-Gauthier, C. Duchesne, H. Alamdari, M. Fafard, D. P. Ziegler, Crack Detection Method Applied to 3D Computed Tomography Images of Baked Carbon Anodes, Metals, vol. 6 (272), 2016.

[293] E. Kuhn, Non-destructive testing of material excited by an acoustic or thermal wave. Observation by thermography, PhD thesis, Paris West University, France, 2013, 24-26.

[294] B.C. Anon, Preliminary study of an innovative Non-Destructive Testing technique concept for detection of surface cracks in non-ferromagnetic materials, Master thesis, Catalonia polytechnic university, Spain, 2013, 7-14.

[295] M.A. Andoh, Y. Kocaefe, D. Kocaefe, D. Bhattacharyay, D. Marceau, B. Morais, Mesurement of the Electric Current Distribution in An Anode. Light Metals 2016, 889-894.

[296] J.H. Kurz, C.U. Grosse, H.W. Reinhardt, Strategies for reliable automatic onset time picking of acoustic emissions and of ultrasound signals in concrete. Ultrasonics, vol. 43, 2005, 538-546.

[297] G. Briche, N. Tessier-Doyen, M. Huger, T. Chotard, Investigation of the damage behaviour of refractory model materials at high temperature by combined pulse echography and acoustic emission techniques. J. Eur. Ceram. Soc., vol. 28, 2008, 2835-2843.

[298] T.P. Philippidis, D.G. Aggelis, An acousto-ultrasonic approach for the determination of water-to-cement ratio in concrete. Cem. Concr. Res., vol. 33, 2003, 525-538.

[299] C. Allaire, Methods and Apparatus for Non-Destructive Testing of Materials Using Longitudinal Compression Waves. U.S. Patent Number 5040419 A, 1991.

[300] C. Allaire, J. Allaire, A. Carbonneau, Room and High Temperature Measurement of the Elastic Properties of Refractories Using a New Apparatus and Set-up. In Light Metals; John Wiley & Sons: Hoboken, New-Jersey, USA, 2004, 629-636.

[301] CIR laboratory inc. Industrial quality control and room and high temperature elastic properties measuremnets [on-line], http://www.d4m.com/soluss/cir/web/document/ SonicByte-Presentation.pdf, [access Sep. 2016].

[302] R. Montanini, F. Freni, Correlation between vibrational mode shapes and viscoelastic heat generation in vibrothermography, NDT & E International, vol. 58, 2013, 43-48.

[303] M. Ohtsu, Elastic wave methods for NDE in concrete based on generalized theory of acoustic emission, Construction and Building Materials, vol. 122, 2016, 845-854.

[304] J.D.G. Peter, A.M.W. Peter, B.F.J. Roger, Real-time frequency determination of acoustic emission for different fracture mechanisms in carbon/epoxy composites. Compos. Sci. Technol., vol. 55, 1995, 405-412.

[305] L. Yang, H.S. Kang, Y.C. Zhou, W. Zhu, C.Y. Cai, C. Lu, Frequency as a key parameter in discriminating the failure types of thermal barrier coatings: Cluster analysis of acoustic emission signals. Surf. Coat. Technol., vol. 264, 2015, 97-104.

[306] H. Yang, G. Yun, Y. Cao, Effects of point defect shapes on defect modes in two-dimensional magnonic crystals, Journal of Magnetism and Magnetic Materials, vol. 356, 2014, 32-36.

[307] R.K. Miller, P. McIntire, Non-destructive Testing Handbook-Acoustic Emission Testing, American Society for Non-destructive Testing: Columbus, OH, USA, 1987.

[308] S. Wold, Cross-validatory estimation of the number of components in factor and principal component models. Technometrics, vol. 20, 1978, 397-405.

[309] M. Ben Boubaker, D. Picard, J. Tessier, H. Alamdari, M. Fafard, C. Duchesne, The Potential of Acousto-Ultrasonic Techniques for Inspection of Baked Carbon Anodes, Metals, vol. 6 (7), 151, 2016, 1-13.

[310] M. Suzuki, H. Nakanishi, M. Iwamoto, Relationship between acoustic emission characteristics and structural factors of composite materials, Composites'86: Recent advances in Japan and the united states, proceedings of Japan-US CCM_III, Tokyo, 1986, pp 631-638.

[311] N. Qing-Qing, J. Eiichi, Acoustic emission and fracture of carbon fiber reinforced thermos-softening plastic (CFRTP) materials under monotonous tensile loading, Engineering Fracture Mechanics, vol. 45 (5), 1993, 611-625.

[312] N. Qing-Qing, J. Eiichi, Fracture behavior and acoustic emission of SFC, Journal of the Society of Materials Science, vol. 42, 1993, 561-567.

[313] E. Jinen, Acoustic emission technique in the single-filament-composite test. In: First International Conference on Composite Engineering (ICCE/1), August 28-31, Louisiana, New Orleans, USA, 1994, 883-884.

[314] E.P. Serrano and M.A. Fabio, Application of the wavelet transform to acoustic emission signal processing, IEEE Transactions on Signal Processing, vol. 44 (5), 1996, 1270-1275.

[315] N. Qing-Qing, Y. Misada, Analysis of AE signals by wavelet transform, Journal of the Society of Materials Science, vol. 47, 1998, 305-311.

[316] L. Cohen, Time–frequency analysis, Prentice-Hall, Englewood Cliffs, NJ, 1995.

[317] R. Kronland-Martinet, J. Morlet, A. Grossmann, Analysis of sound patterns through wavelet transforms, International Journal of Pattern Recognition and Artificial Intelligence, vol. 1 (2), 1987, 273-302.

[318] J.D. Aussel, J.P. Monchalin, Structure noise reduction and deconvolution of ultrasonic data using wavelet decomposition (ultrasonic flaw detection), Proceedings of Ultrasonics Symposium, Montreal, Canada, IEEE, 1989, 1139-1144.

[319] R.S. Loe, K. Jung , K. Anderson, A. Abatzoglou, J. Regan, H. Arnold, W. Lawton, Status report on wavelets in signal detection and identification: comparative processing and technology evaluation, Proceedings of IEEE Sixth SP Workshop on Statistical Signal and Array Processing, Susono, Japan, 1992, 46-49.

[320] G. Qi, A. Barhorst, J. Hashemi, G. Kamala, Discrete wavelet decomposition of acoustic emission signals from carbon-fiber reinforced composites, Composites Science and Technology, vol. 57 (4), 1997, 389–403.

[321] N. Sandirasegaram, R. English, Comparative analysis of feature extraction (2D FFT and wavelet) and classification (L_p metric distances, MLP NN, and HNeT) algorithms for SAR imagery, Proceedings of SPIE 5808, Algorithms for Synthetic Aperture Radar Imagery XII, Orlando, Florida, USA, March 28, 2005, 314-325.

[322] S.G. Mallat, A theory for multiresolution signal decomposition: the wavelet representation, IEEE Transactions on Pattern Analysis and Machine Intelligence, vol. 11 (7), 1989, 674-693.

[323] K. Ono, J.S. Jeng, J.M. Yang, Fracture mechanism studies of a carbon fiber-PEEK composite by acoustic emission, In: Acoustic Emission: Current Practice and Future Directions, ASTM International, Philadelphia, PA, 1991, 395-403.

[324] K. Yamaguchi, Acoustic emission waveform characteristics from FRP during tensile test, In: Progress in Acoustic Emission III, Proceedings of the 8th International Acoustic Emission Symposium (IAES 8), JSNDI, Tokyo, Japan, 1986, 594-601.

[325] W.K. Fischer, F. Keller, R. Perruchoud, Interdependence between anode net consumption and pot design, pot operating parameters and anode properties, Light Metals 1991, 681-686.

[326] Z. Zong, X. Lin, J. Niu, Finite element model validation of bridge based on structural health monitoring - Part I: Response surface-based finite element model updating, Journal of Traffic and Transportation Engineering, vol. 2, 2015, 258-278.

[327] D.P. Ziegler, J. Secasan, Methods for Determining Green Electrode Electrical Resistivity and Methods for Making Electrodes, U.S. Patent No.: 9,416,458, Issue Date: August 16, 2016..

[328] X.H. Wang, C.M. Zhu, H.L. Mao, Z.F. Huang, Wavelet packet analysis for the propagation of acoustic emission signals across turbine runners, NDT&E International, vol. 42, 2009, 42–46

[329] Z.C. Wang, Y. Xin, W.X Ren, Nonlinear structural model updating based on instantaneous frequencies and amplitudes of the decomposed dynamic responses, Engineering Structures, vol. 100, 2015, 189-200.

[330] K.B. Kim, H.Y. Kang, D.J. Yoon, and M.Y. Choi, Pattern Classification of Acoustic Emission Signals During Wood Drying by Principal Component Analysis and Artificial Neural Network, Key Engineering Materials, vols. 297-300, 2005, 1962-196.

[331] C. Palau, F. Arregui, A. Ferrer, Using multivariate principal component analysis of injected water flows to detect anomalous behaviors in a water supply system, A case study, Water Science and Technology: Water Supply, vol. 4 (3), 2004, 169-181.

[332] M.B. Boubaker, D. Picard, J. Tessier, H. Alamdari, M. Fafard, C. Duchesne, Inspection of Prebaked Carbon Anodes using Multi-Spectral Acousto-Ultrasonic signals, Wavelet Analysis and Multivariate Statistical Methods, Proceedings of 34rd International ICSOBA Conference, October 3-6, Québec City, Canada, 2016.

[333] I. Daubechies, Ten lectures on wavelets, CBMS-NSF Regional Conference Series in Applied Mathematics, SIAM Ed, 1992, ISBN: 978-0-89871-274-2.

[334] M.J. Sundaresan, A. Ghoshal, J. Li, M.J. Schulz, P.F. Pai, J.H. Chung, Experimental damage detection on a wing panel using vibration deflection shapes, Structural Health Monitoring, vol. 2, 2003, 243-256.

[335] M. Steven, S.M. Ziola, M.R. Gorman, Source location in thin plates using cross-correlation, J Acoust Soc Am, vol. 90(5), 1991, 2551-2557.

[336] E. Foltête, Experimental methods in mechanical: Mechancal vibration testing, FEMTO-ST, UMR 6174, Course of master mechanical and engineering, Besançon, France, 2010.

[337] U. Mannweiler, W.K. Fischer, R. Perruchoud, Carbon products: a major concern to aluminium smelters, Light Metals 2009, 909-911.

[338] J.T. Baron, S.A. McKinney, R.H. Wombles, Coal tar pitch – past, present, and future, Light Metals 2009, 935-939.

[339] C. Zang, M. Imregun, Structural damage detection using artificial neural networks and measured FRF data reduced via principal component projection, Journal of Sound and Vibration, vol. 242, 2001, 813-827.

[340] M.J. Whelan, M.V. Gangone, K.D. Janoyan, R. Jha, Real-time wireless vibration monitoring for operational modal analysis of an integral abutment highway bridge, Engineering Structures, vol. 31, 2009, 2224-2235.

[341] J. Martínez-Jequier, A. Gallego, E. Suárez, F.J. Juanes, A. Valea, Real-time damage mechanisms assessment in CFRP samples via acoustic emission Lamb wave modal analysis, Composites Part B: Engineering, vol. 68, 2015, 317-326.

[342] S.W. Doebling, C.R. Farrar, M.B. Prime, A summary review of vibration-based damage identification methods, The Shock and Vibration Digest, vol. 30, 1998, 91-105.

[343] I. Trendafilova, A study on vibration-based damage detection and location in an aircraft wing scaled model, Applied Mechanics and Materials, vols. 3–4, 2005, 309-314.

[344] M. Casting, Contrôle non-destructif par ultrason, Département de mécanique aéronautique et ingénieries, Parcours : Expertise et contrôle des matériaux et structures, Université de Bordeaux1, Bordeaux, France, 2012.

[345] H. Suzuki, T. Kinjo, Y. Hayashi, M. Takemoto, K. Ono. Wavelet transform of acoustic emission signals. Journal of Acoustic Emission, vol. 14, 1996, pp 69-84.

[346] P. Geladi, H. Grahn, Multivariate image analysis, John Wiley & Sons, 1996.

[347] F. Pattou, J.C. Trutt. Méthode de mesure dynamique du module d'Young, Application aux graphites nucléaires. Rapport de la Commissariat à l'Énergie Atomique (CEA) n^{o} 2243, Centre d'Études nucléaires de Saclay, Paris, France, 1963.

Appendix 1 Similarity of the acousto-ultrasonic responses of the rods to those of their corresponding corridors

In Chapter 3, the potential of sequential acousto-ultrasonic technique was investigated for non-destructive and detailed inspection of baked anodes. This section presents the work that has not been included in Chapter 3 due to the paper-format restrictions. The objective of this section is to show that the acousto-ultrasonic responses of the corridors cut from the anode slices (call rods hereafter) are similar to those of their corresponding corridors in the slice before cutting them. This will remove the doubt about the contribution of the proximity of each corridor in the attenuation of the signals. This will allow also concluding that the classification of the corridors only depends on their contents.

Indeed, eight other slices, holding the numbers 4, 10, 12, 14, 18, 19, 21 and 22, have been selected. After removing their tops as well as their bottoms, these slices were cut in form of rods, as shown in Figure A1-1, and the rods were tested individually. Each rod is labeled by the number of the slice to which it belongs followed by its location number in the corresponding slice: 1, 2, 3, 4, 5 or 6. Therefore, six rods per slice were obtained except those who were broken due to the existence of large cracks. At this point, it is important to remember that the signals acquisition were performed after some sequential excitation at seven different frequencies: 100, 130, 150, 170, 200, 230 and 250 kHz. Finally, the acousto-ultrasonic signatures were identified by calculating the different features that were systematically gathered in the same matrix.

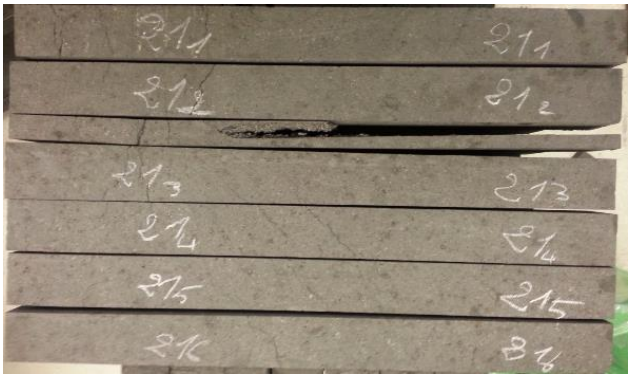

Figure A1-1 An example of 6 rods cut of slice #21.

In order to make sure that the classification contribution is mainly influenced by the propagation distance and defects interfaces and not by the location of each scan position, the tests have been carried out in a similar way as in Chapter 3. The acoustic sensors were positioned as shown in Figure A1-2. The emitter was mounted on the first end of each rod, which corresponded to the anode top, and the receiver was located on the opposite end of the sample, which corresponds to the bottom of the anode. The interfaces between the sensors and the material were filled with coupling gel in order to maintain appropriate signal transmission. Since both of top and bottom of each slice were removed, all the interfaces had low roughness. Therefore, most of the signals attenuation were considered to be caused by the internal structure of the material and not to the interface material/sensors.

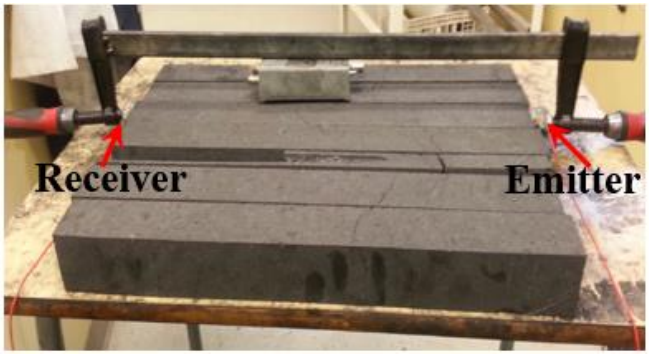

Figure A1-2 Acoustic data acquisition setup.

As a result, a total of 3 principal components were found statistically significant by cross-validation procedure. The cumulative variance of the data (acousto-ultrasonic signatures): explained part (R2) and predicted one (Q2) by the PCA model are shown in Figure A1-3. Only the first two components are kept for interpretation of the clustering pattern of the samples since they explain the majority of variation in the acoustic data.

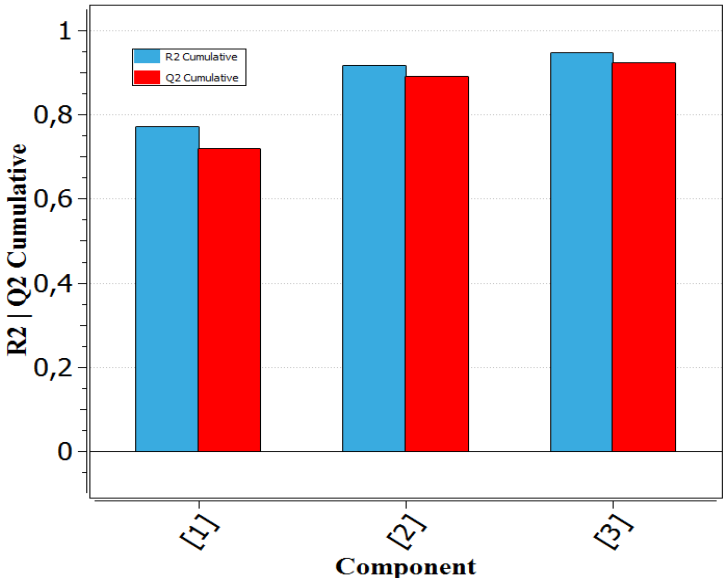

Figure A1-3 Cumulative variance explained (R^2) and predicted (Q^2) by the PCA model built on the acoustic responses of rods.

The latent variable score space for the first two components of the PCA model ($\mathbf{t_1}$-$\mathbf{t_2}$ scatter plot) is shown in Figure A1-4. This plot represents the dominant sources of variability in the AE dataset. Each marker represents a summary of the acoustic response of a given sample. These are labeled by the number of the corresponding slice followed by their position number in the same slice. Different colors were added to facilitate the visualisation of different groups. In Figure A1-4, the samples that were projected in the vicinity of each other in the score space had similar acoustic responses. It is possible to look at the clustering patterns (i.e., similarity or differences) of different samples in the latent variable score space of Figure A1-4. These clusters indicate the classification of samples according to the defects type. The CT-Scan images showed that in the first and the second corridors (black triangles), the material had many cracks with pore concentration areas whereas in corridors 3, 4 and 5 (orange circles) there was only few cracks with homogeneous pore distribution. In the 6th corridor (blue squares) there were high density of pores.

The results clearly showed that the rod samples cluster according to the following order: from the middle of the anode (first scan position) to the end of the anode (6th and last position), that is according to their contents and defects. It is important to note that the more porous and/or cracked samples were considered as the most defect samples. Therefore, it can be concluded that the first component ($\mathbf{t_1}$) corresponds to the variation of the damage caused by cracks and the second component ($\mathbf{t_2}$), to the concentration of pores. The test results revealed that the responses of the rods were similar to those of the corridors (as

presented in Figure 3-6) and consequently the acoustic responses obtained for the corridors was a function of the internal structure of this corridor and did not significantly depend on their neighbors.

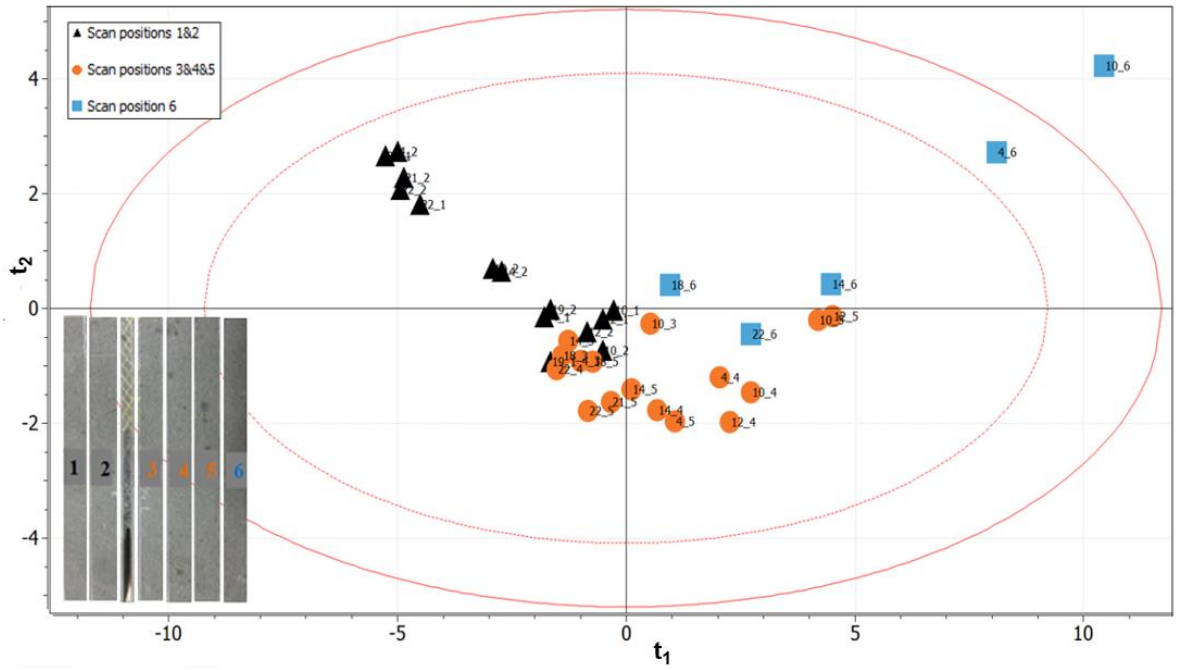

Figure A1-4 PCA scores plot of rods using sequential excitations (t_1-t_2).

Finally, the acousto-ultrasonic was applied as a control technique to detect the defects and to quantify the variations in some separated anode parts (rods). It was possible to obtain a clustering pattern similar to that of the model established using the corridor responses by cutting the corridors of each slice to an equal number of rods. This was attributed to the fact that the acousto-ultrasonic responses were not really affected by the scattering caused by the boundaries. Therefore, it was confirmed that the classification depends on the internal contents and not on the location and the surroundings of the corridors.

Appendix 2 Inspection of Prebaked Carbon Anodes using Multi-Spectral Acousto-Ultrasonic signals, Wavelet Analysis and Multivariate Statistical Methods: Additional results

As it is mentioned in the title, the implementation of different methods aimed at investigating the use of acousto-ultrasonic technique for volumetric inspection of baked carbon anodes. The study focused on mapping the morphological constituents in the carbon material in order to evaluate the spatial distribution of pores and cracks using acoustic wave attenuation. This part complement the work that has been presented in Chapter 4 by virtually dividing the slice to 7 corridors instead of 6 corridors, as shown in Figure A2-1. The depth of the new corridors corresponds to the diameter of the smallest couple of sensors available in the lab. Previously it was not possible to shrink as much the corridors because the comparison of the results of different sensors needs the depth, of each corridor, to be equal to the distance of the largest diameter (i.e., the largest couple of emitter and receiver). According to this new partition, the different region in the anode, especially the outer area, can be better characterized since the tests will be carried out in a narrower areas. To achieve and simplify the analysis, both PCA and PLS were used to provide classification and regression models. The clustering patterns obtained showed the sensitivity of the proposed approach to detect and distinguish the concentration of pores from the cracks.

As discussed in Chapter 4, Siemens Somatom Sensation 64 was used to scan a whole industrial baked carbon anode. At this point, it is important to remember that the CT-scan apparatus provides a 3D matrix (size 1000 × 1200 × 10000) full of pixels attenuation coefficients that varied between 0 and 4095, which were converted later to grayscale images as they were correlated to the carbon materials density. As shown in Figure A2-2, the cracks and the pores inside the anode correspond thus to a dark group of pixels that is surrounded by a light background. However, the bright pixels in a dark background defined the impurities in the carbon.

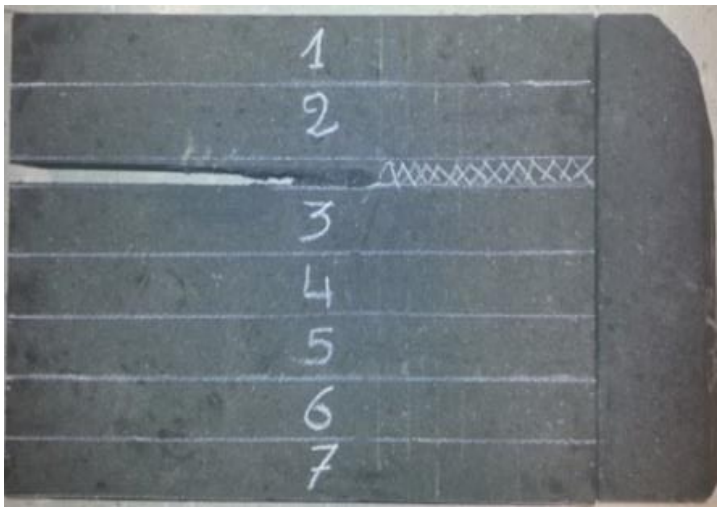

Figure A2-1 Example of a slice used for acoustic emission testing.

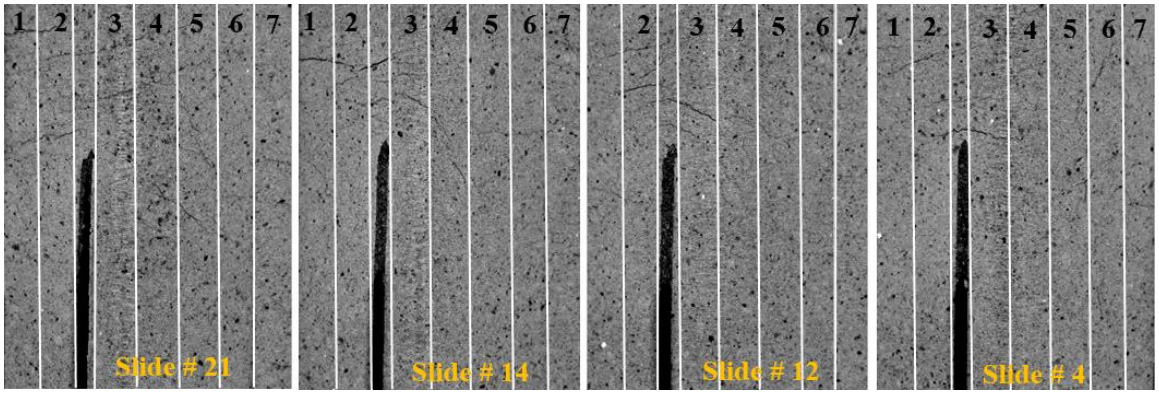

Figure A2-2 Distribution of cracks and pores through different X-ray images of some corridors.

An overview of the acoustic signal measurement system was discussed in Chapter 4. However, it is necessary to remember that one acoustic transducer was used as an emitter while the other was used as a receiver, as shown in Figure A2-3. Via the power generator, the input signals were specified as modulated frequency between 100 kHz-200 kHz. This range was found appropriate after the preliminary tests that have been conducted. The procedure was repeated for each of the seven corridors and for the eight anode slices. The waveform attenuation is mainly affected by the material through the propagation distance. Hence, the attenuation effect of the interface sensor/sample was negligible and then averaging of the repeated signals in order to reduce measurement errors was not necessary.

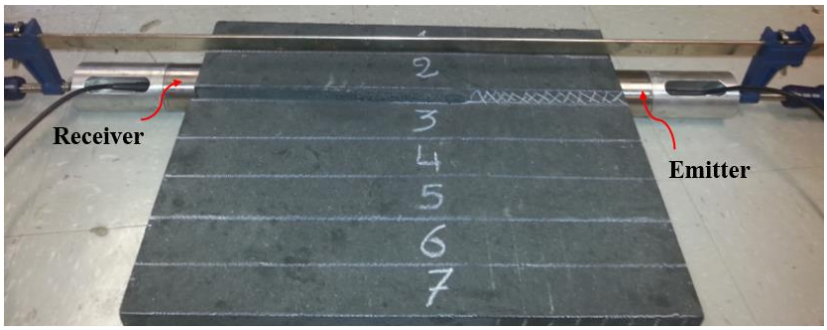

Figure A2-3 Acoustic data acquisition set-up through different corridors of an anode slice.

As results, using the cross-validation procedure [308], the PCA model needs five latent variables to explain the whole variations in textural features. The variance of the data explained (R^2) and predicted (Q^2) by the first three principal components are calculated by the model. Their values are listed in Table A2- 1. The three components are sufficient to distinguish the corridors based on their textural features when they explain over 92% of variance inside those features.

Table A2-1 Percent cumulative sum of squares explained (R^2) and predicted (Q^2) by the PCA model built on textural features collected from corridor images.

Component	R^2 (%)	Q^2 (%)
1	62,9	57,9
2	83,2	78,5
3	92,2	88,7

The main variability in the datasets is illustrated in the corresponding latent variable space for these three components of PCA model in Figure A2-4. Each marker corresponds to the fundamental textural features of one particular corridor. These were identified by the slice number followed by the corridor number. Two plots were then used for this work. The first one was assigned to the clustering pattern in $\mathbf{t_1}$-$\mathbf{t_2}$ score space. The second plot presented that of $\mathbf{t_1}$-$\mathbf{t_3}$ score space. From the plots shown in both figures, the efficiency of the classification approach can be depicted. It is noticeable that, in Figure A2-4A) and Figure A2-4B), the corridors located in the same position within the slices are clustering together with small extensions according to the second component of corridor 2-3-4-5-6 and according to both components of the remaining corridors (1 and 7). Furthermore, each group is separated from other groups according to both components except those of #1 and #7, which fall close to each other. Often, corridor #1 was mainly affected by cracks whereas corridor #7 was affected by a higher pore concentration, which were also larger in size. Since the wavelets capture variations in the image signals caused by defects (pores and cracks),

and both types of defects are large in corridors #1 and #7, the first two PCA components capture their similar effect on the wavelet energies. Consequently, the 3rd PCA component was examined (see Figure A2-4B), and this additional component was found to capture information in the energies that allowed discriminating the textural features of corridor #7 (mainly pores) from those of corridor #1 (mainly cracks).

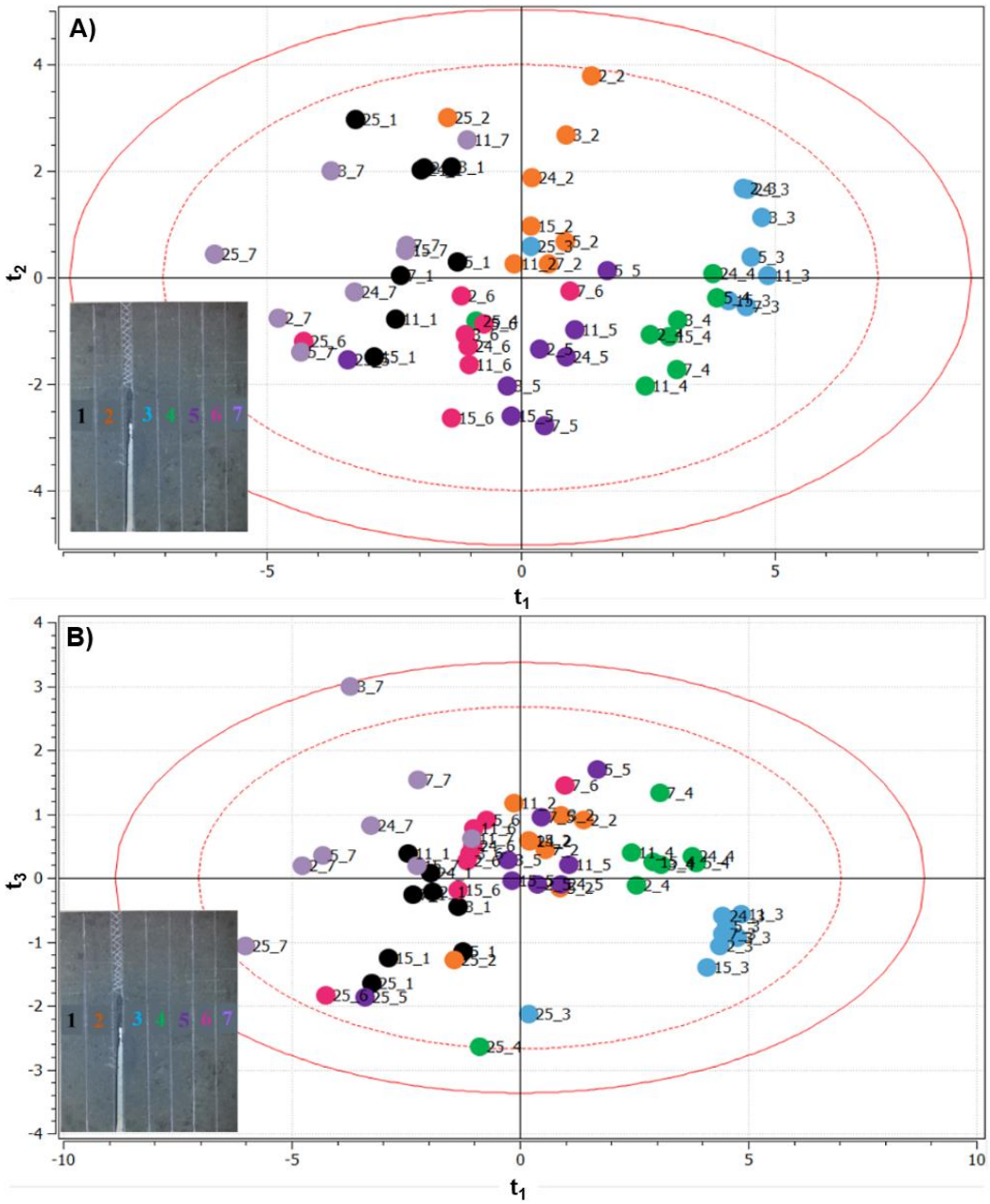

Figure A2-4 Projection of the textural images features along the plane defined by the first three principal components: (a) t_2-t_1, (b) t_3-t_1.

In this section, the link between the clusters in the score space and the textural features will be discussed using the $\mathbf{p_1}$-$\mathbf{p_2}$ and $\mathbf{p_1}$-$\mathbf{p_3}$ loading plots shown in Figure A2-5A and Figure A2-5B). These plots can be used respectively with those of Figure A2-4A) and Figure A2-4B. The direction of variations were the same in each pair of figures (the score and its loading). Each point in the graphs corresponds to one textural feature calculated from the images of one particular corridor, which were labeled with the feature name followed by the wavelet-decomposition level number. The first pair of figures (Figure A2-4A) and Figure A2-5A)) reveals that the first component was mainly driven by the frequency which implies proportionality to the size of the defects. The 4^{th} level features (EH4, EV4, and ED4) increased towards the left side of loadings plot, which means that the most damaged corridor was located in the left side of the score plot (corridor #1 and #7) and vice-versa. However, the second component was mainly driven by the direction of textural variation that corresponds to the defect types (i.e., pores or cracks). On the other hand, the fact that the loading values of horizontal and vertical directions were negatively correlated in the second pair of figures, $\mathbf{t_3}$-$\mathbf{t_1}$ and $\mathbf{p_3}$-$\mathbf{p_1}$, resolves the overlap between textural features of corridors 1 and 7 in Figure A2-4A). Furthermore, in $\mathbf{t_3}$-$\mathbf{t_1}$ it is possible to look at the divergence of the features of corridors 1 from those of corridors 7. This means that the defects in the latter corridor, which corresponds to pores, have similar effects in both directions contrary to the former corridor, which correspond to cracks. Hence, after visual observation of the contents appearance it was concluded that the central region of anode that corresponds to corridors 1-2 were showing several cracks in most slices, whereas corridor 2 had less cracks and high density of pores in its lower part. Corridors 3-4-5 were much denser with a few cracks, sometimes extending from corridors 1-2 in the transversal direction from 3 to 5. Finally, corridors 6-7 rarely showed cracks but had a variable density of pores while corridor 7 was the most porous.

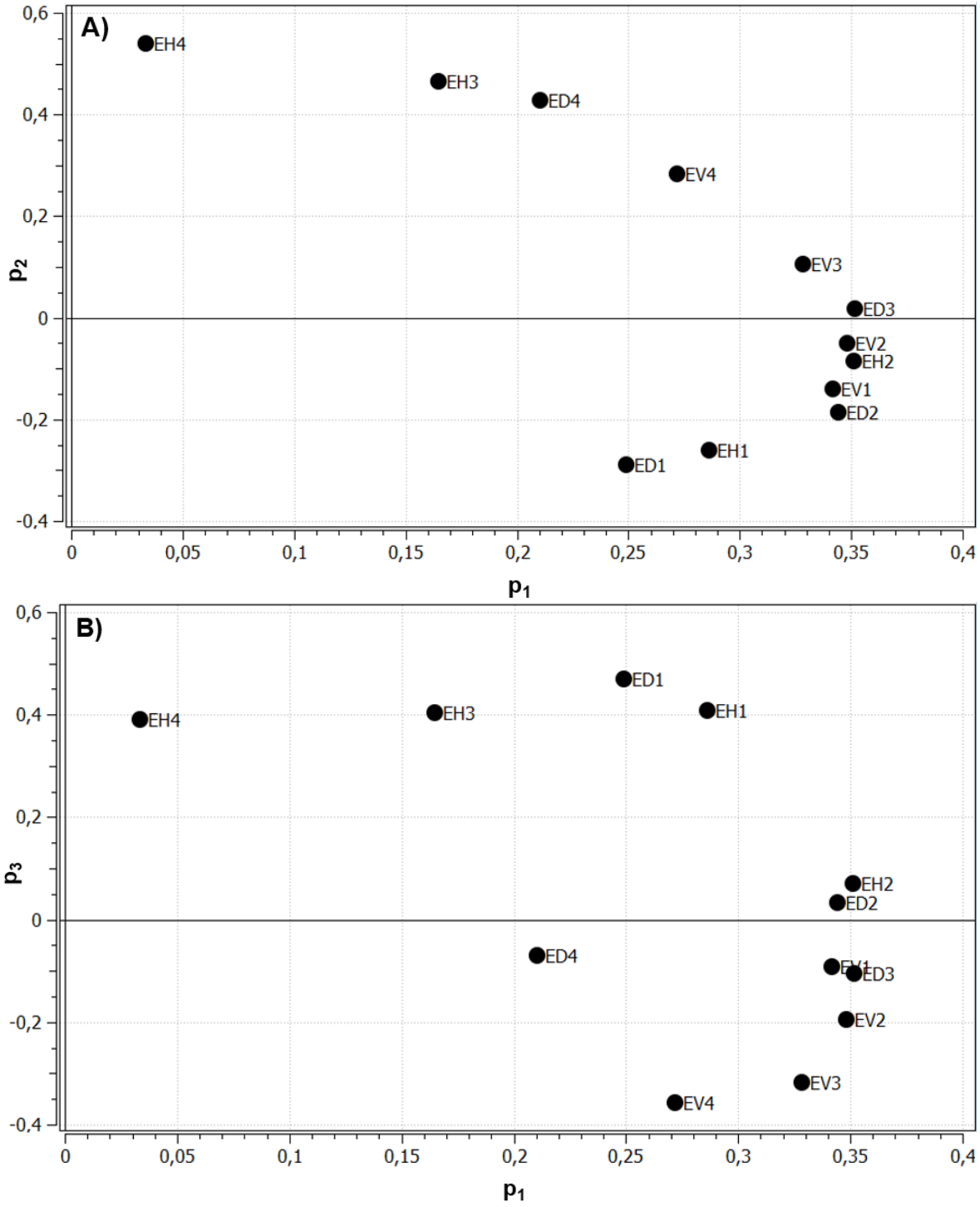

Figure A2-5 Loading plot of the PCA model built on image textural features: (A) $\mathbf{p_2}$-$\mathbf{p_1}$, (B) $\mathbf{p_3}$-$\mathbf{p_1}$.

Now, both of acoustic and textural data were analysed according to the flowchart shown in Figure A2-6.

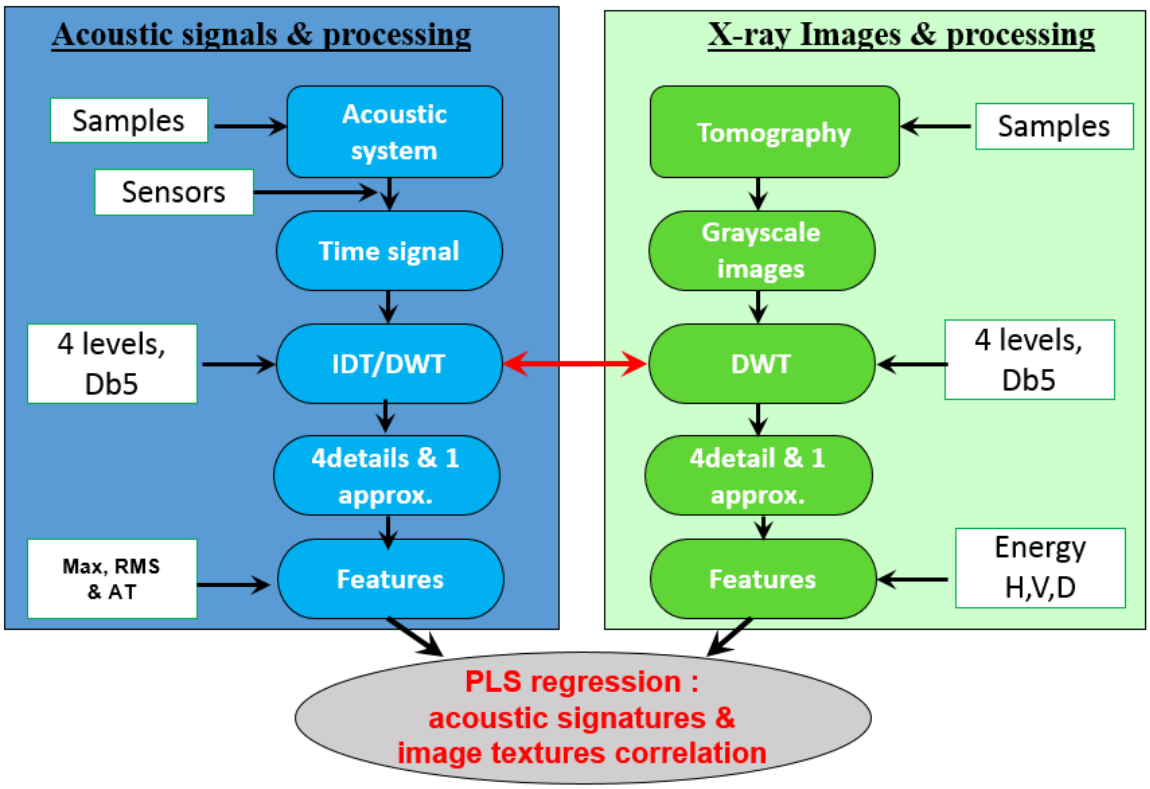

Figure A2-6 Analysis flowchart.

Only four principal components were found statistically significant by a standard cross-validation procedure. This procedure was suitable to distinguish samples based on their acousto-ultrasonic signatures. The latent variable score space for the first two components of the PLS model is displayed in Figure A2-7. Such presentation gives the dominant sources of variability in the dataset, in which each marker corresponds to the acoustic response of one corridor while keeping the previous notation (slice#_corridor#). The clustering pattern in the $\mathbf{t_1}$-$\mathbf{t_2}$ score space reveals that corridors 1-2, 3-5 and 6-7 of any slice cluster in 3 groups (black, orange and blue markers, respectively). It can also be observed that the attenuation features of corridors 1-2 and 6-7 seem more variable than the majority features of corridors 3-5 (orange cluster tighter than black and blue).

The internal structure of the corresponding samples that were previously analysed via establishing the PCA model of textural images is required to interpret the differences between the three groups. The first component indicated by the horizontal axis in Figure A2-7 captures the existence and the kind of defects (mainly cracks or pores) since the number of cracked corridors increase in the left side whereas those of porous corridors increase on the right and vice versa. The second direction, which is orthogonal to the first, is sensitive to

severity of defects (size of cracks and pores) as the denser corridors (some of corridors 3-5) are located above both of more porous corridors 1-2 and 6-7 and more cracked corridors (slice #5 and #7 as they are locating in the region under the stub holes) are located above others. Finally, it is important to note that this ascertainment is also in agreement with the carbon plant knowledge. The region below the stub holes corresponding to corridors 1-2 (black cluster) in slices #5, 7 and 15 are generally expected to show a higher concentration of cracks while obviously some others, as in slice #11, project closer to the denser region (orange markers). However, corridors 6-7 are expected to be submitted to wall friction due to a lack of lubrication in the vibro-compactor and consequently show high concentration of pores. These are projecting at the right of the score plot (blue markers) except for those of slices #24 and 25 that are more affected by the release of the compressed gas, as they are located in the anode corner.

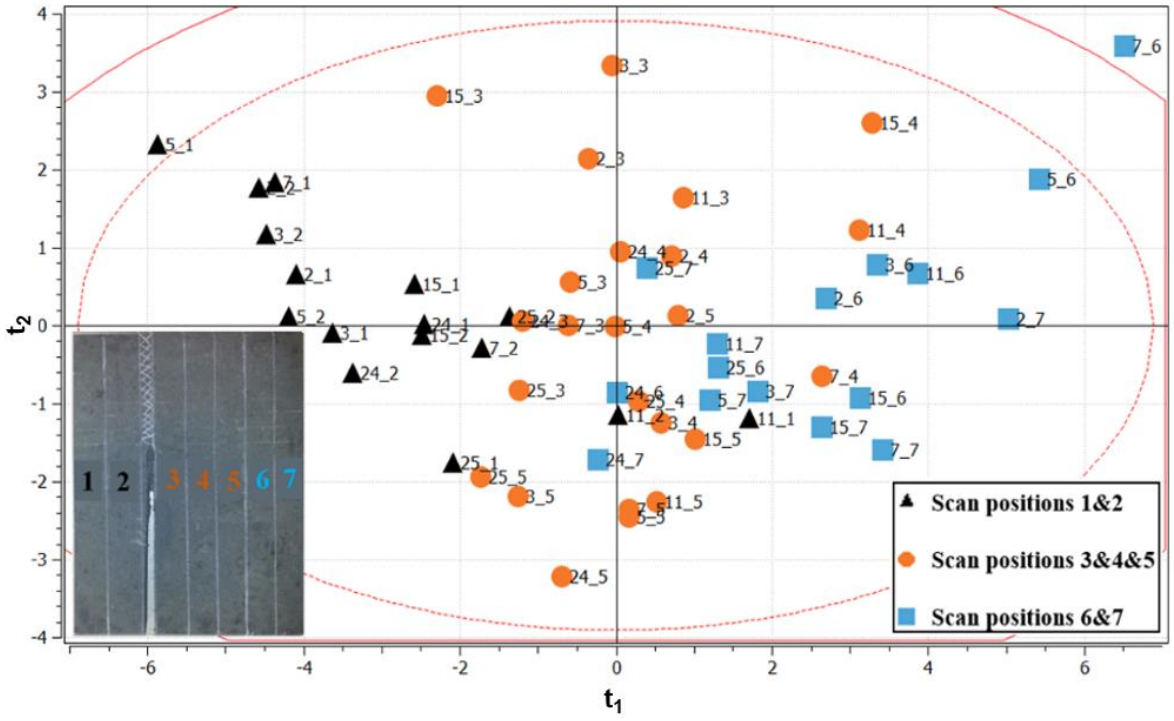

Figure A2-7 The t_1-t_2 score plot of the principal component analysis (PCA) model built on acousto-ultrasonic (AU) signal attenuation features.

It is also possible to look at the loading plot in the Figure A2-8 to explain the relationship between acoustic attenuation features and the clustering pattern in the latent variable space. The latter can be interpreted simultaneously with t_1-t_2 score plot (Figure A2-7) as follows: the sign of loadings indicates the sign of the correlation sign between pairs of features whereas their absolute values indicate the importance of the feature in a given

component. It can be concluded that the first component is mainly driven by the variance related features (MAX and RMS) and the arrival time. The former are negatively correlated to the latter since they have an opposite sign, which means that going away from the positive side towards the negative side on t_1 means an increase in the concentration of cracks and consequently an increase in the arrival time of the acoustic signal due to the wave attenuation. However, the decomposition levels control the second component when those of variance and those of arrival time (symmetrically distributed 1 to 4 and 4 to 1) are inversely proportional. This is consistent with the modification of the shape of the density distribution of the acoustic signal by pores since such decomposition levels are frequency dependent. Since these levels are frequency dependent that indicate also the size of pores, the higher the frequency attenuated the smaller are the size of the pores.

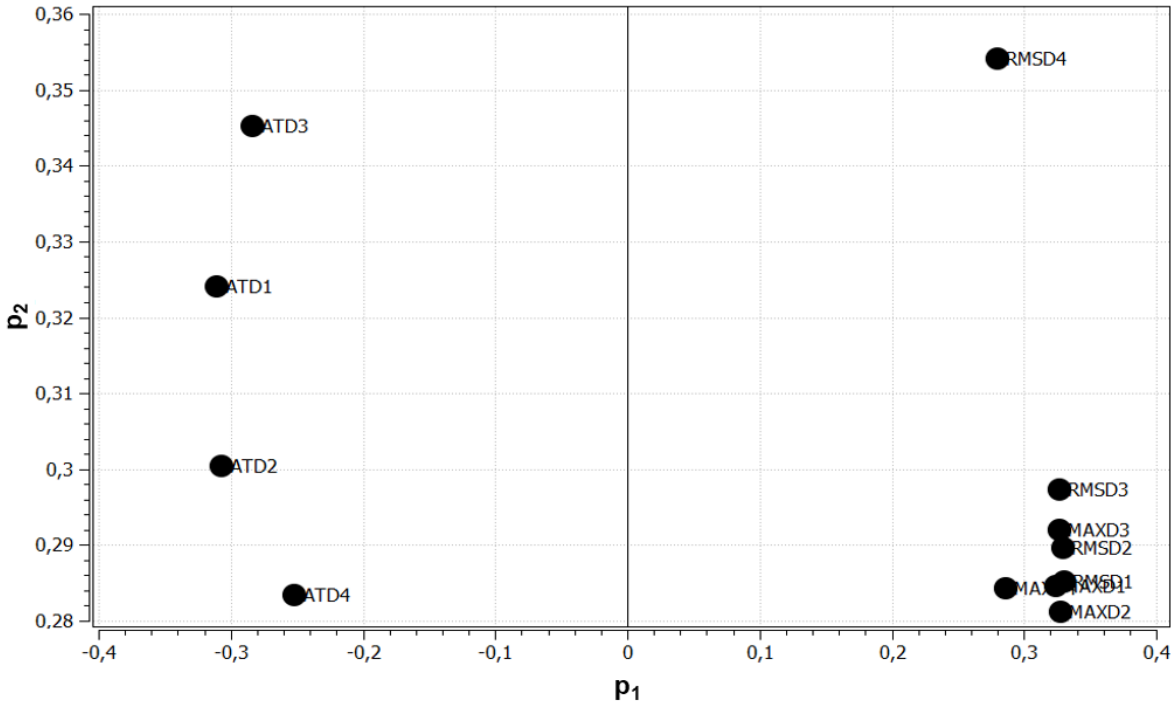

Figure A2-8 p_1-p_2 loading plot of the PLS model built on AE signal attenuation features.

The correlation between the acoustic attenuation features and the features of the textural image has been interpreted using the $\mathbf{w^*c_1}$-$\mathbf{w^*c_2}$ loadings bi-plot shown in Figure A2-9. This figure can be interpreted simultaneously with both previous scatter plots. Heading towards the left along the first component means that the significance of cracks increase, which increases the pixels intensity around these cracks and therefore increasing of energy values (red markers). This phenomenon corresponds to the acoustic signals attenuation and consequently the decreasing of the variance related features and the increasing of the arrival

time through the current component and vice versa. Contrariwise, the second component seems to be sensitive to the defects severities, since the signals are attenuated at all frequencies (high and low). This is clear in this figure where the majority of acoustic frequency is inversely proportional to those of textural features. At this point, it is important to note that the textural-feature frequencies decrease when their number markers increase.

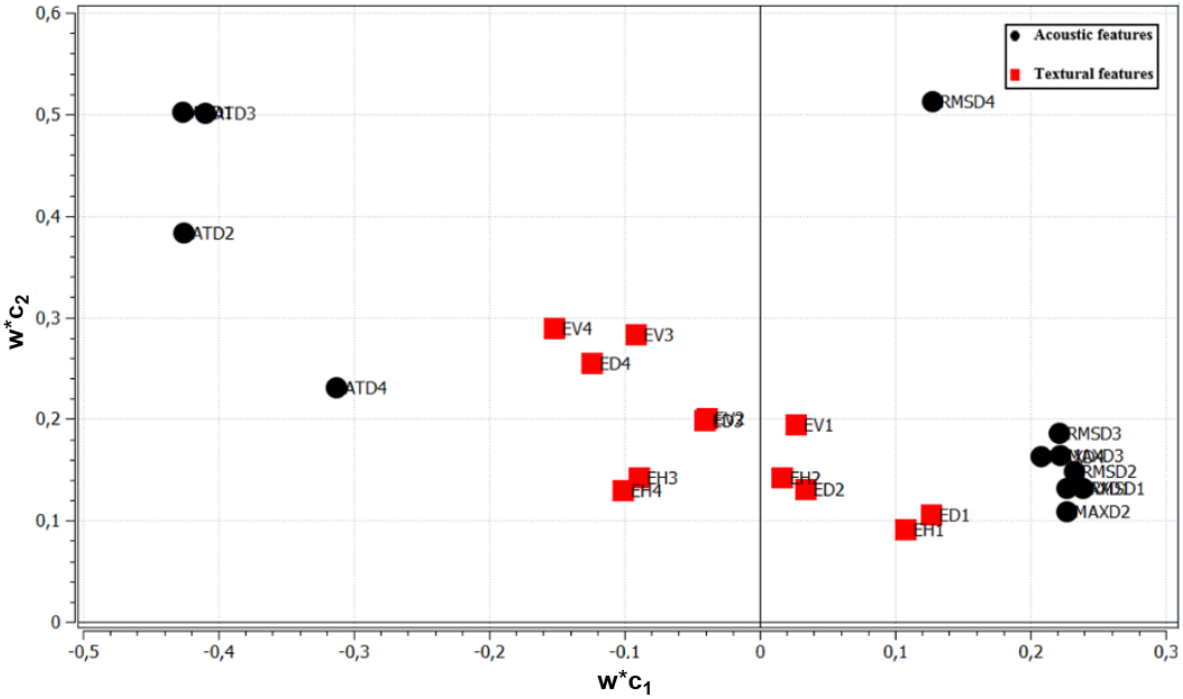

Figure A2-9 Loadings bi-plot ($\mathbf{w^*c_1}$ – $\mathbf{w^*c_2}$) of the PLS model between acoustic attenuation signals and X-ray image textural features.

Lastly, acousto-ultrasonic techniques combined with multivariate statistical methods were used in an attempt to reveal the internal physical morphology of a full-scale anode, which was sliced in both longitudinal and transversal directions. Such combination was already studied in Chapter 4 but with only 6 corridors. This part was added in order to further detail the analysis of different anode areas, especially the outer surface (7th corridor) that is holding high concentration of pores. Further, CT-scan image analysis served as a reference for quantitative validation of the observations made from the acousto-ultrasonic signatures and correlate them with the internal contains of the anode.

The results showed that it was possible to distinguish between corridors containing high density of pores and those containing different cracks. Indeed, the only overlapping was between the area most damaged by cracks (corridor #1) and the most porous one (corridor#7) in the textural image classification. However, it was possible to discriminate both

of them by means of involving the third component of the corresponding PCA model. Therefore, the acousto-ultrasonic signatures are not only sensitive to the presence of cracks and pores concentration within anode material but they are also able to discriminate both of them. Besides, the non-destructive nature and the rapidity of the procedure are extra advantages of the acoustic technique. Therefore, from these advantages and the obtained results, it can be confirmed that the proposed approach is promising for a real time quality control of prebaked anodes.

Appendix 3 Attenuation maps of all tested anodes

For sake of conciseness the attenuation maps of only A3, A4, and A5 were presented in chapter 5. Consequently we added this appendix to illustrate the attenuation maps of all anodes. At this point, is important to remember that the scores values of the first component ($\mathbf{t_1}$) of three PCA models are displayed using a color map. These three models were built on the datasets collecting excitation points 1-21 (excluding stub holes), 16-18-20, and 22-29, respectively. The score values were scaled from 0 to 1 using the maximum and minimum values in such a way that 0 and 1 are assigned to the least and the most attenuated signals in the dataset, respectively. As it is illustrated in Figure A3-1**,** the color map ranging from dark blue to dark red was then applied on each excitation point shown in the anode drawings to indicate progressively higher attenuation of the signals.

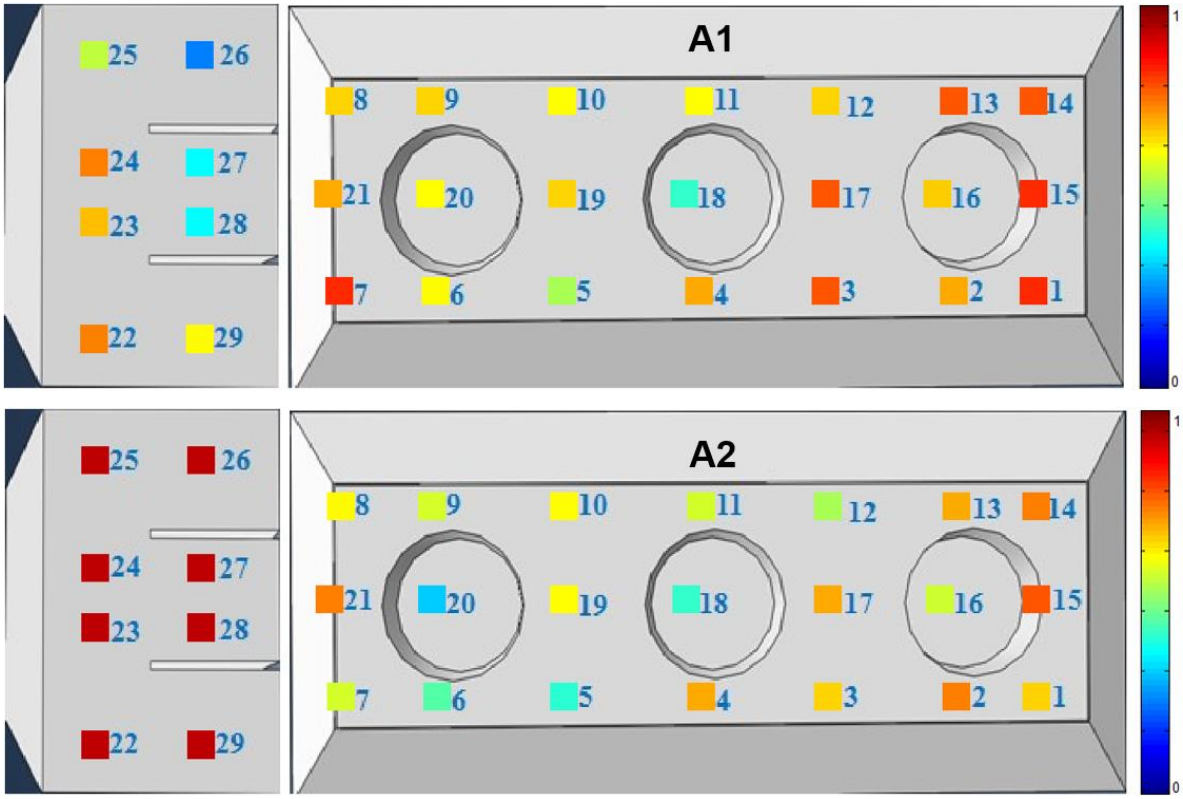

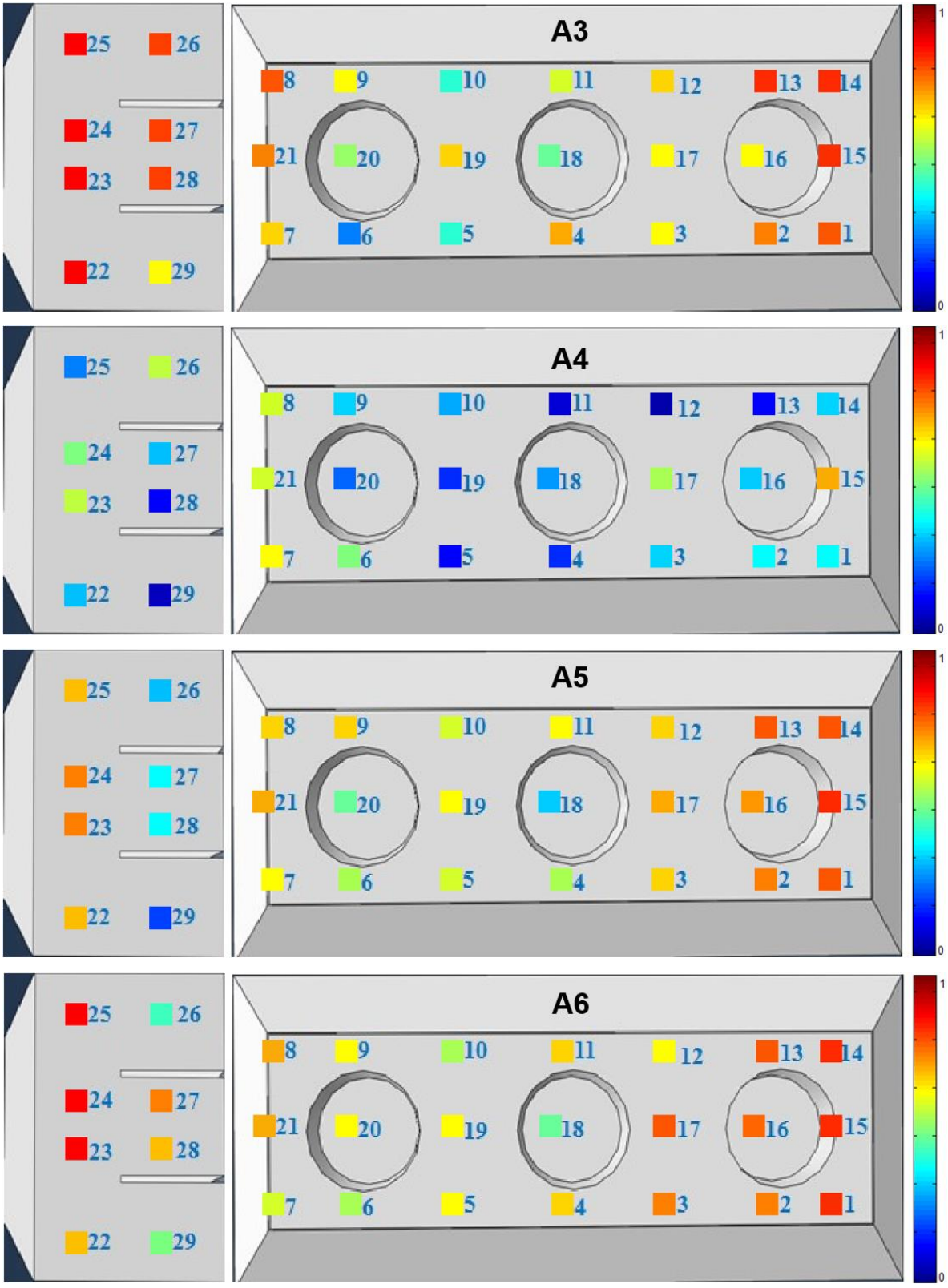
A3
A4
A5
A6
25 26
24 27
23 28
22 29
8 9 10 11 12 13 14
21 20 19 18 17 16 15
7 6 5 4 3 2 1
1
0

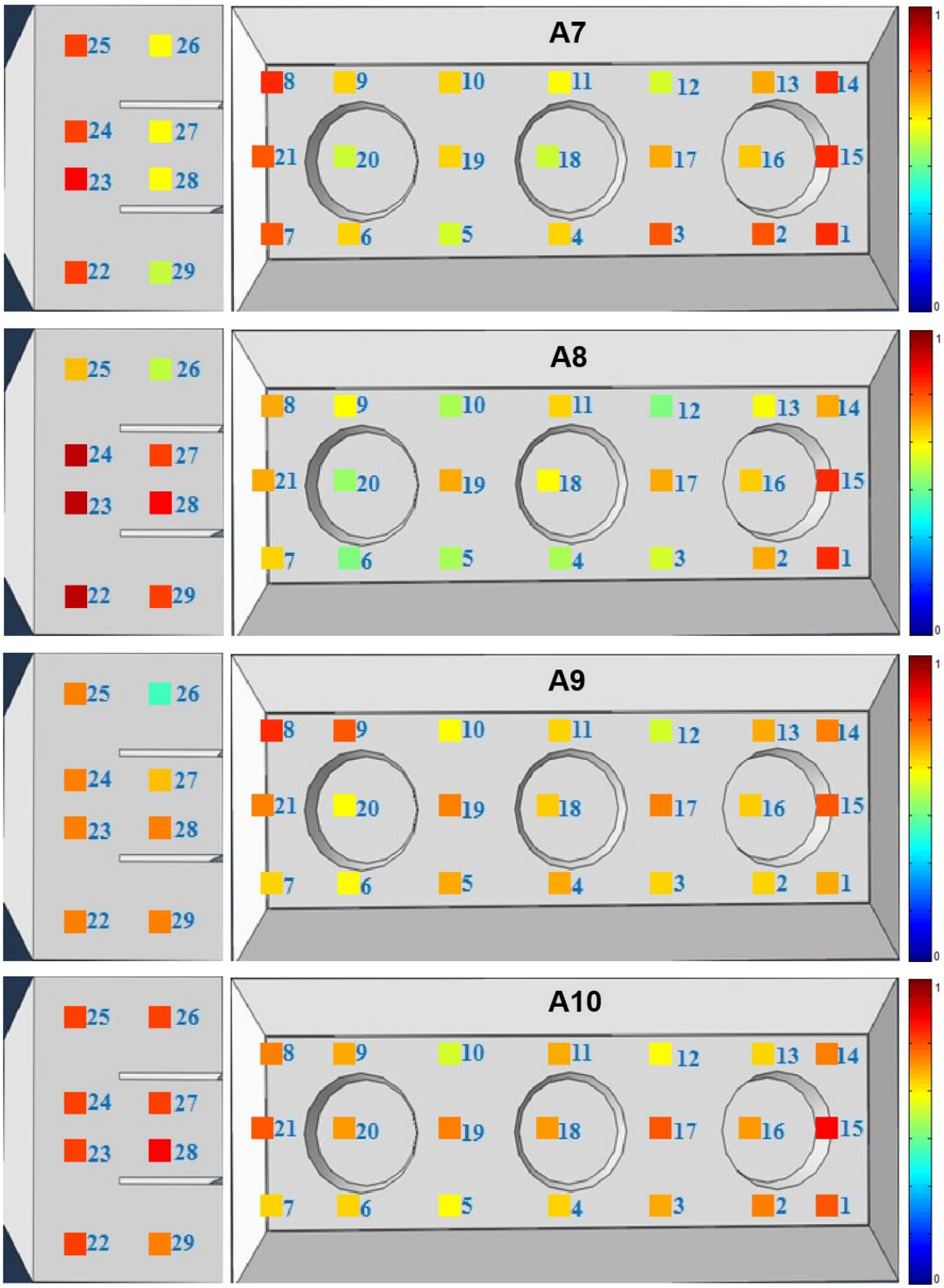
A7
A8
A9
A10
25 26
24 27
23 28
22 29
8 9 10 11 12 13 14
21 20 19 18 17 16 15
7 6 5 4 3 2 1
1
0

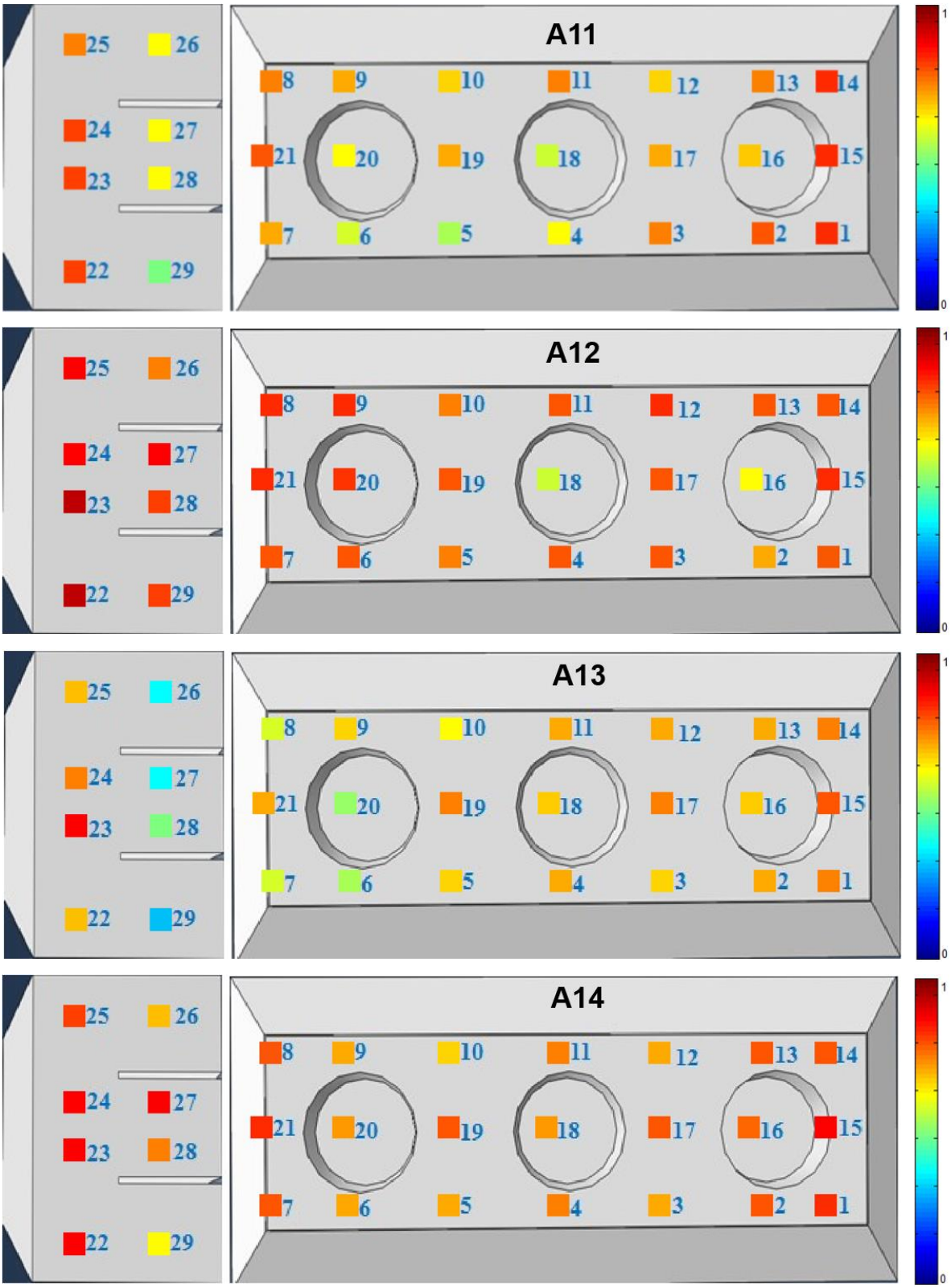
A11
A12
A13
A14
25 26
24 27
23 28
22 29
8 9 10 11 12 13 14
21 20 19 18 17 16 15
7 6 5 4 3 2 1
1
0

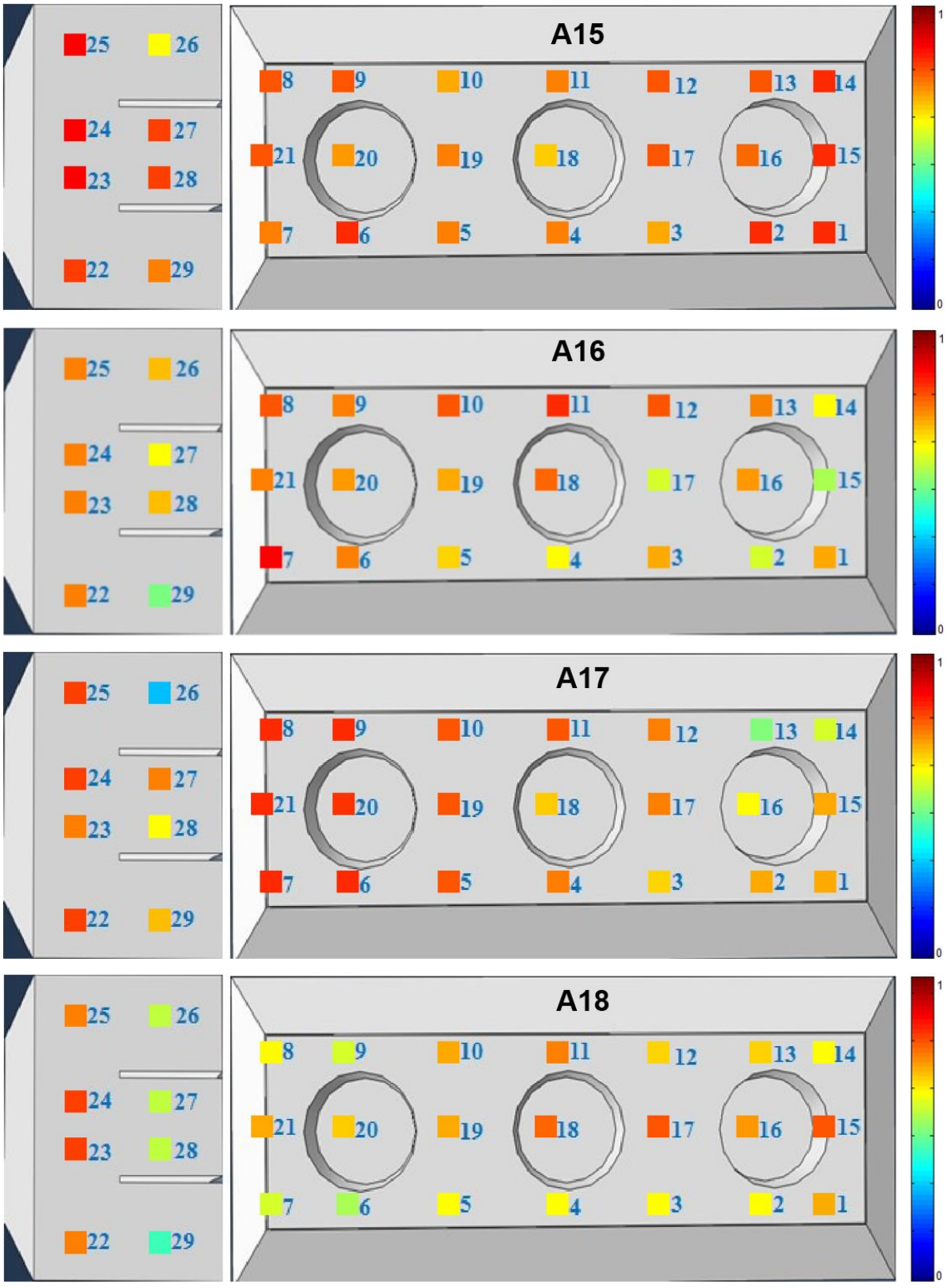
A15
25 26
24 27
23 28
22 29
8 9 10 11 12 13 14
21 20 19 18 17 16 15
7 6 5 4 3 2 1
1
0
A16
25 26
24 27
23 28
22 29
8 9 10 11 12 13 14
21 20 19 18 17 16 15
7 6 5 4 3 2 1
1
0
A17
25 26
24 27
23 28
22 29
8 9 10 11 12 13 14
21 20 19 18 17 16 15
7 6 5 4 3 2 1
1
0
A18
25 26
24 27
23 28
22 29
8 9 10 11 12 13 14
21 20 19 18 17 16 15
7 6 5 4 3 2 1
1
0

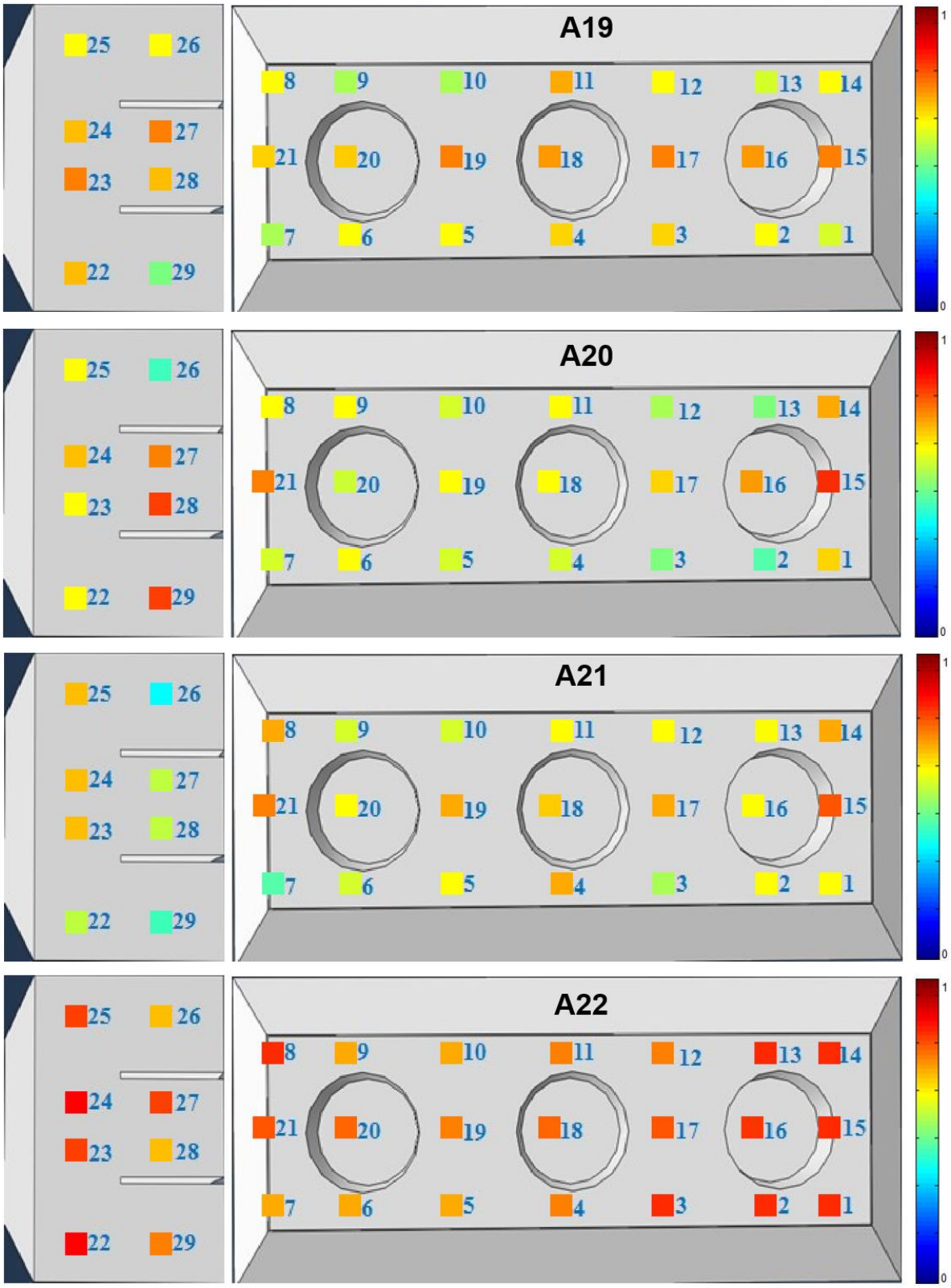
A19
25 26
24 27
23 28
22 29
8 9 10 11 12 13 14
21 20 19 18 17 16 15
7 6 5 4 3 2 1
1
0
A20
25 26
24 27
23 28
22 29
8 9 10 11 12 13 14
21 20 19 18 17 16 15
7 6 5 4 3 2 1
1
0
A21
25 26
24 27
23 28
22 29
8 9 10 11 12 13 14
21 20 19 18 17 16 15
7 6 5 4 3 2 1
1
0
A22
25 26
24 27
23 28
22 29
8 9 10 11 12 13 14
21 20 19 18 17 16 15
7 6 5 4 3 2 1
1
0

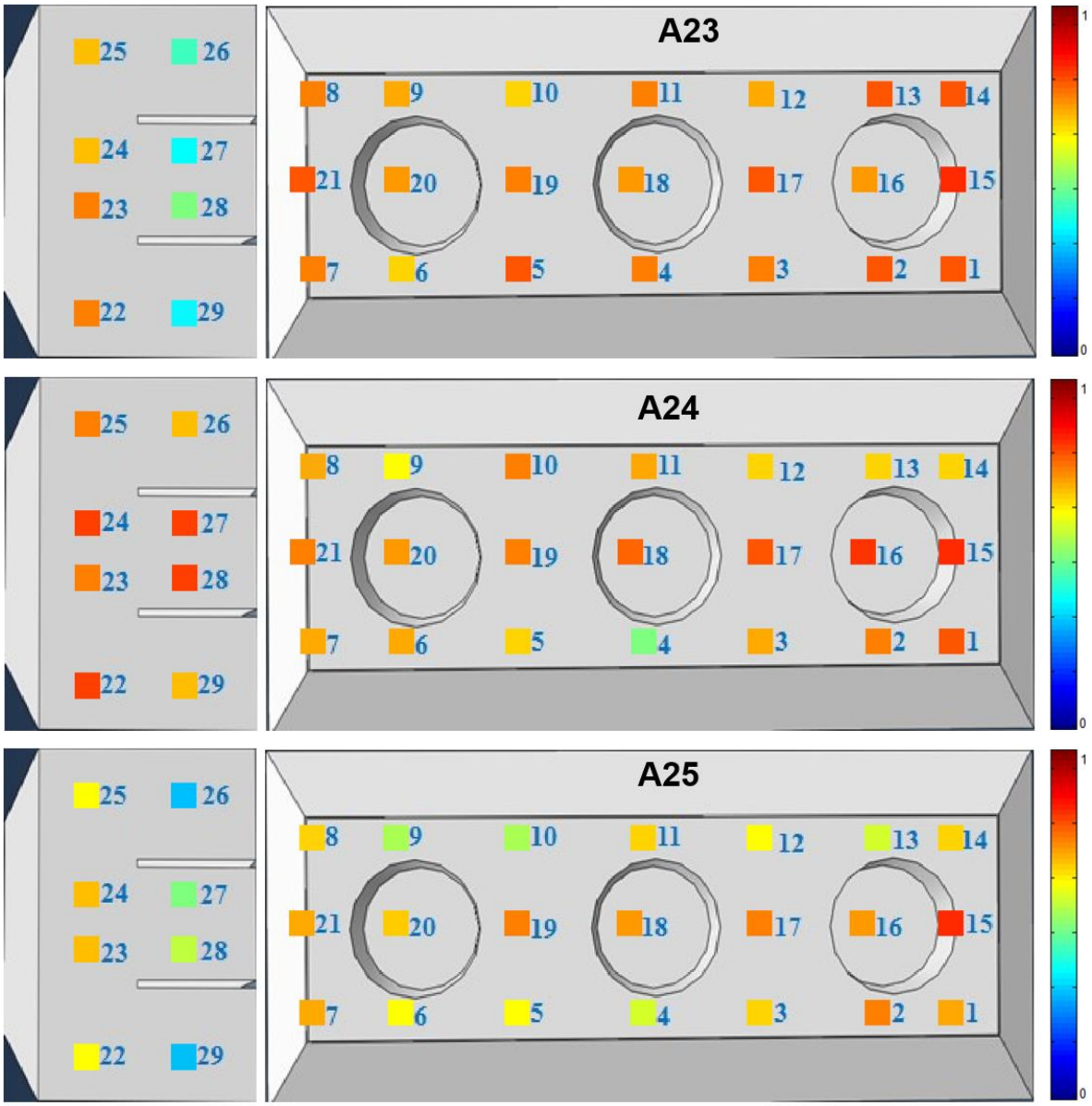
A23
25 26
24 27
23 28
22 29
8 9 10 11 12 13 14
21 20 19 18 17 16 15
7 6 5 4 3 2 1
1
0
A24
25 26
24 27
23 28
22 29
8 9 10 11 12 13 14
21 20 19 18 17 16 15
7 6 5 4 3 2 1
1
0
A25
25 26
24 27
23 28
22 29
8 9 10 11 12 13 14
21 20 19 18 17 16 15
7 6 5 4 3 2 1
1
0

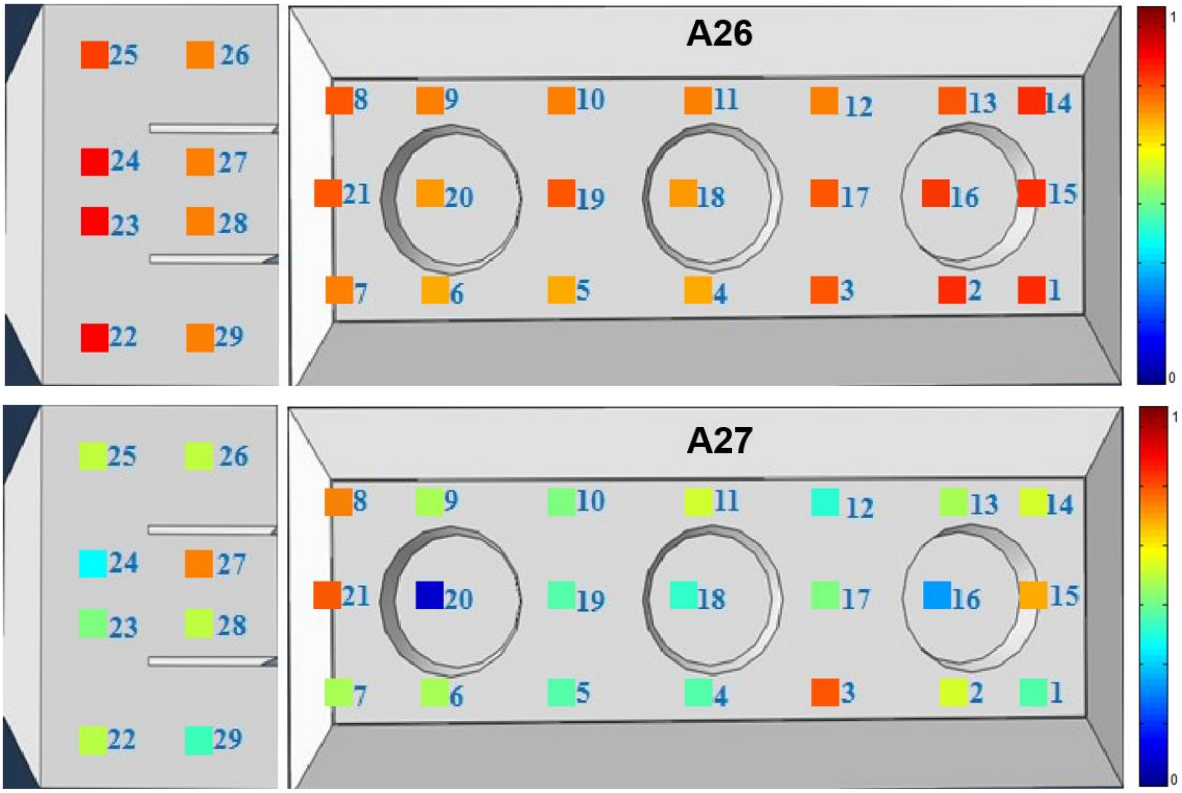

Figure A3-1 Maps of the t_1 score values associated with signal attenuation for all tested anodes. The color bar indicates the level of attenuation on relative scale, from low (dark blue) to high attenuation (dark red).

Appendix 4 Comparison of the numerical and experimental modal results

This section presents the work that has not been included in Chapter 6 due to the paper-format restrictions. It was added to better establish the link between the numerical modelling and experimental results. After choosing the two steel bar supports configuration, appropriate boundary conditions were applied at the contact line between the anode side and these supports. Especially, the translation in Y direction and rotations with respect of X and Z directions were restricted, as shown in Figure 6-2, where X, Y and Z correspond to the anode length, height and width directions, respectively. The "tie" constraint and the "hard contact" option were chosen as an interaction type between the anode and the supports.

The measured and calculated modes for ADQ's pre-baked anodes are presented in Table A4-1. The experimental and numerical modal frequencies are also showed in Figures A4-1-A4-3 and Figure A4-5, respectively. At this point is important to remind that only the responses of three faces are presented since the response of the front face (face R1 in Figure 6-6) is similar to that obtained when collecting the measurements between the anode slots (face R2 in Figure 6-6) for the first modes (modes between 0-500Hz). The experimental frequencies correspond to the mean of different anode responses, which are presented in Figures A4-1-A4-3. In these figures we have a total of 5 modes. Some of them are detected in some views (one face in Figure 6-6) and others are detected in other views. However it is difficult to discriminate the first two modes since they are very close to each other and are of very low amplitudes compared to the others. Indeed, Figure A4-4 was added to clarify this aspect. This figure represents a zoom (0-100Hz) of the left view response shown in Figure A4-2 but with a different location of excitation, especially the location that allows the simultaneous excitation of the first two modes. In this same figure we can clearly differentiate both of these two first modes at around 7 Hz and the other around 16 Hz.

The first significant numerical mode corresponds to the fourth mode in Figure A4-5 (7.21 Hz) because the boundary conditions consisting of one translation and two rotations restrict the model to give automatically three rigid body modes (two translation and one rotation not restricted by the boundary conditions). Therefore, the second, third, fourth and fifth significant numerical modes correspond to the fifth (16,63 Hz), sixth (61.20 Hz), seventh (355.79 Hz) and eighth (476.51 Hz) modes in Figure A4-4, respectively.

Table A4-1 Comparison of the measured and calculated anode responses

Number of the experimental mode	Experimental frequency (Hz)	Numerical Frequency of the corresponding mode (Hz)	Relative frequency error (%)
#1	7	7.21	3
#2	16	16.63	3.93
#3	60	61.20	2
#4	300	355.79	18.6
#5	400	476.51	19.12

The model predicts the first three modes with good accuracy (relative error between 2-4%). The prediction of the two higher order modes is not as precise. This is justified by the difficulty of the model to consider the physical phenomena involved when the mode shapes become more complex. The prediction of the model degrades when the energetic interactions between the sensitive zones of the structure, in particular the areas between anode slots and stub holes, are complex. In addition, material properties values were obtained from different works, made on anodes from other companies. These anodes do not have the same shape and the same sources of raw materials as those studied in this thesis.

Nevertheless, the first two modes in Table A4-1 (considered as global modes) of the structure have been correctly predicted by the model without implementation of any updating process. However, the main objective of the modeling part was to support the development of the experimental set up by allowing to determine the way to set the anodes on the supports, and the optimum excitation and measuring positions. Of course, these results can be considerably improved by implementing an updating process. In general, before the design phase and insertion of the material properties, especially for structures as porous as the anode material, it is also better to carry out characterization tests directly on the same type of anode (ADQ) to have the accurate values of Young's modulus and Poisson’s coefficient.

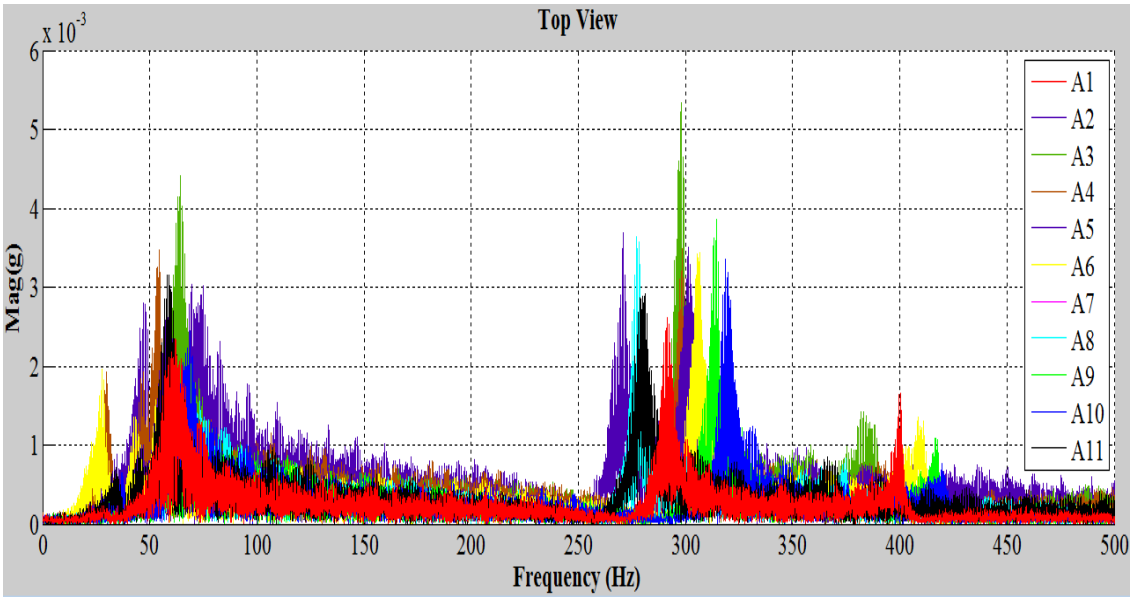

Figure A4-1 The first two peaks of the power spectrum of 11 anodes obtained from one accelerometer after excitation on the top face.

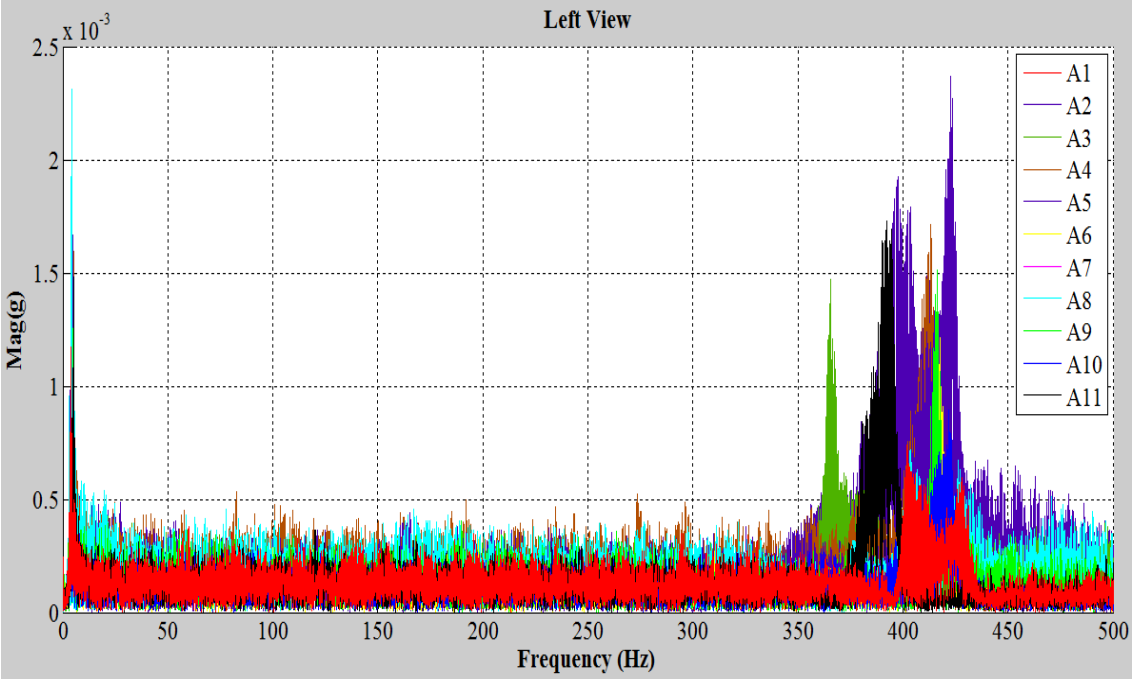

Figure A4-2 The first two peaks of the power spectrum of 11 anodes obtained from one accelerometer after excitation on the left face.

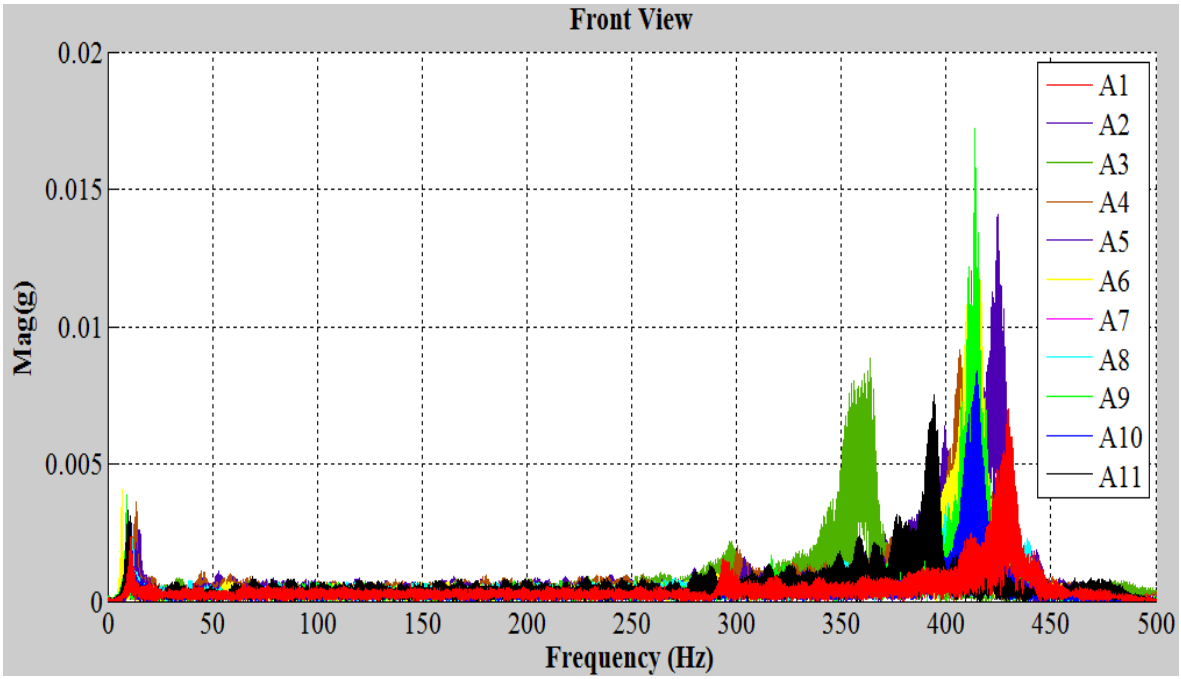

Figure A4-3 The first two peaks of the power spectrum of 11 anodes obtained from one accelerometer after excitation on the front face.

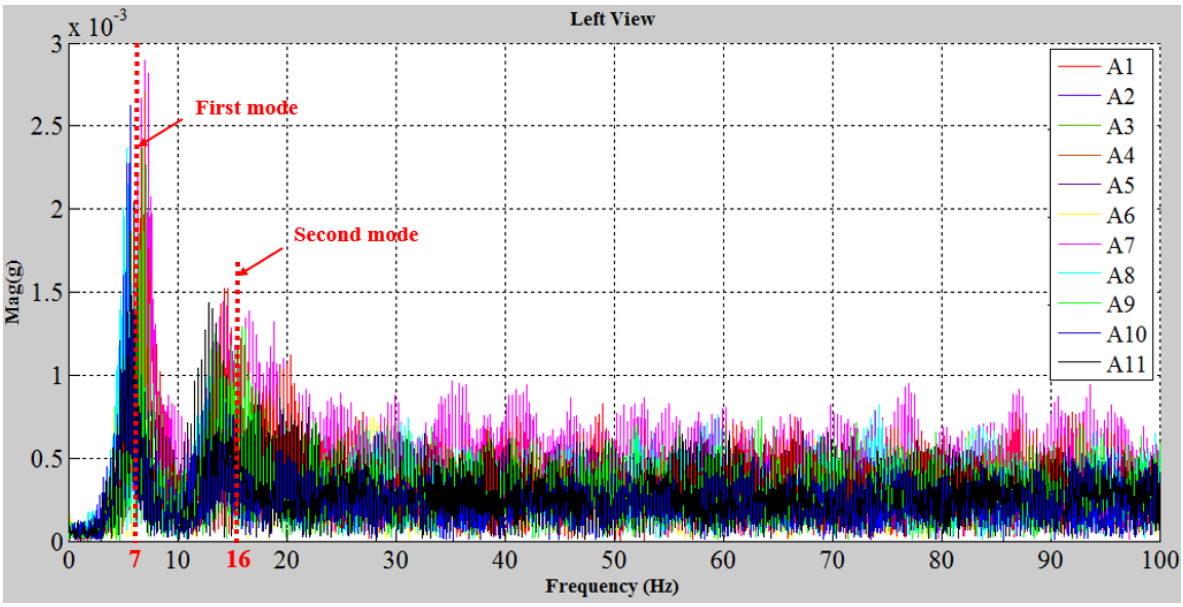

Figure A4-4 Zooming of the left view responses with another excitation point (different from that of Figure A4-2).

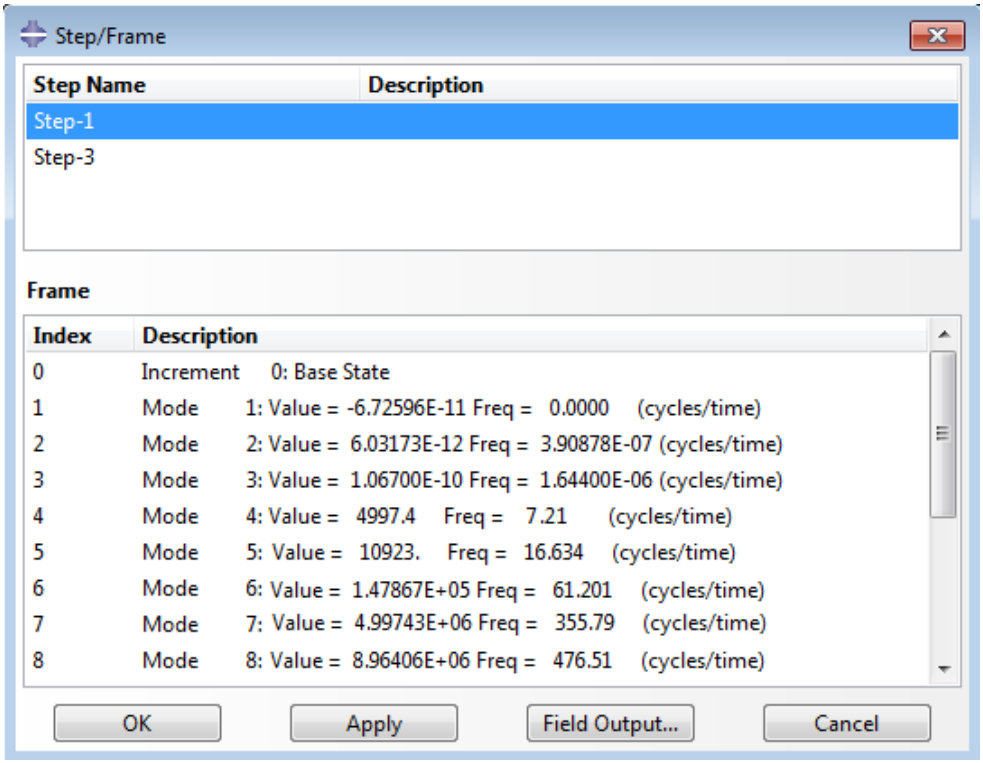

Figure A4-5 Numerical natural frequencies obtained by Abaqus software